POLITECNICO DI TORINO

Corso di Laurea Magistrale
in Ingegneria Aerospaziale

Tesi di Laurea Magistrale

Development of a ultrathin reaction wheel for modular nanosatellites

Relatore
prof. Leonardo M. Reyneri

Candidato
Giorgio Capovilla

Correlatore
prof. Giulio Romeo

A.A. 2018-2019

Contents

Introduction

A possible classification of miniaturized satellites is made according to their masses, and defines the following satellites categories:

- Microsatellites, having mass in the $10 - 100\,kg$ range;
- Nanosatellites, having mass in the $1 - 10\,kg$ range;
- Picosatellites, having mass in the $0.1 - 1\,kg$ range.

CubeSats are particular kinds of miniaturized satellites. This standard has been developed by Professor Robert Twiggs at Stanford University's Space Systems Development Laboratory in 1998. The standard defined the 1U CubeSat, which shall have a maximum mass of $1.33\,kg$ and a cubic shape with $10\,cm$ edges, and thus is a nanosatellite. Further standards have been defined, from 2U to 6U CubeSats, having maximum masses and dimensions multiples of the 1U standard.
This thesis concerns the development of part of the Attitude Determination and Control System (ADCS) of the AraMiS nanosatellite (acronym for modular architecture for satellites). The AraMiS project started in 2006 at Politecnico di Torino, after conclusion of the PICPOT project, which took its name from a previously developed nanosatellite.
The objective of the project is to design, produce, test and operate nanosatellites, whose development cost and time are strongly reduced with respect to traditional nanosatellites. The current version of AraMiS is a 1U CubeSat. Thus the main obstacle to space access for universities and small companies would be downsized. To achieve this result, the following strategies are adopted:

- Use of a highly modular architecture, for mechanical and electronic components and for testing. It allows to spread costs among a remarkable number of space missions, to reduce design cost, which represents 90% of total cost and to reduce testing and production time. In addition, modularity allows to easily implement satellite components redundancy;
- Use of Commercial Off-The-Shelf (COTS) components. These commercial level components allow components cost reduction, although their generally low reliability requires particular care during subsystem design. Components redundancy is employed to increase fault tolerance and keep performances decay at an acceptable level.

As a result, AraMiS bus is composed of small, distributed, intercommunicating units mounted on CubeSat structure external faces, called smart tiles or tiles, whose prototypes are shown in figure 1(a). Tile functions include all bus functions, although each subsystem components are normally distributed between two or more tiles. For example, the reaction wheel tile, object of the present thesis, contains the reaction wheel, its motor, a magnetic torquer and their electronic components, which are part of the ADCS system, and two solar cells with their electronic components and power conduits, which are part of the electrical power system. Hence subsystems components are distributed among CubeSat tiles.
While AraMiS payload has a different design for each mission and lies in the AraMis CubeSat interior, AraMiS bus (whose prototype is shown in figure 1(b)) is mounted on CubeSat structure external faces and is composed by a set of tiles that satisfies payload and mission requirements. The most appropriate tiles are chosen from a broader set which has previously been designed, produced and tested.

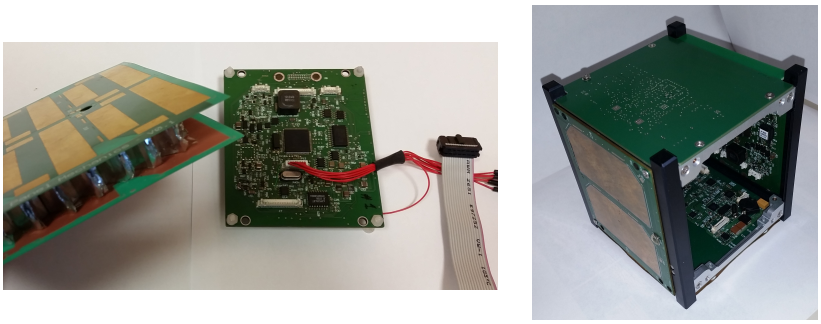

(a) (b)

Figure 1: AraMiS tiles prototypes (a) and tiles mounted on CubeSat structure, to form the bus prototype (b).

A further geometrical requirement is added. As is discussed in chapter 1, CubeSats mechanical requirements impose that no component shall protrude from structure external surface more than $6.5\,mm$. In addition, payload volume shall be maximized, hence tiles components shall protrude towards the interior of the CubeSat as little as possible. Consequently, tiles thickness shall be in the order of millimeters, which does not represent a problematic requirement for modern electronic systems, but for an electro-mechanical system as a reaction wheel it represents a challenging requirement.
In addition to reaction wheel tile, other kinds of tiles have been designed, built and tested. These are:

- Telecommunication tiles, encompassing a system of antennas, amplifiers for transmission and reception, a transceiver, a modem and a CPU;
- Power management tiles, encompassing sensors and actuators of the Attitude and Orbit Control System (AOCS), solar cells, a rechargeable battery, a battery charger and a housekeeping module.

As previously mentioned, the reaction wheel tile includes electrical power system components, two solar cells with their electronic components and power conduits, and ADCS components, magnetic torquers, the reaction wheel with its motor, along with their electronic components. The object of this thesis is the reaction wheel and its motor, while electrical power system, the magnetic torquer and all the electronic components are not considered.
An Axial Flux Permanent Magnet (AFPM) electric motor to drive the reaction wheel has been chosen. AFPM motors distinctive features are the use of permanent magnets in the rotor and the direction of magnetic field lines, that are mainly parallel to motor axis, while common electric motors have magnetic field lines which are mostly radial. As a consequence, AFPM motors have very compact geometries. The reason for this choice lies in the solid knowledge of this type of machines, in the adequacy of their performances for attitude control and in their usual compact "pancake" shape which is ideal to comply with AraMiS tiles geometric requirement discussed above.
The design of the tile and its analysis from a mechanical, electrical, thermal and structural point of view are proposed. In conclusion, the order and description of the analyses, along with chapters objects, is given in the following list:

1. Firstly, design and mechanical analysis have been performed. With the help of a CAD software, SOLIDWORKS, the reaction wheel tile geometrical configuration was chosen. This part of the work is deeply connected with electric motor design. It has been initially developed autonomously, and its performances, strongly depending on mechanical architecture, have been evaluated. A preliminary experimental work was done to verify geometrical design with this kind of motor. Once performances were evaluated, efficiency was found to be poor and a commercial motor was chosen. During this phase, the motor went out of production and another commercial motor was chosen. Mechanical design was deeply influenced by motor changes and once a satisfying motor was chosen, detailed mechanical dimensiong and tolerancing of the tile was performed and is described in chapter 1. Chapter 2 reports motor performances evaluation;

2. A preliminary thermal analysis is made and reported in chapter 3, adopting thermal resistors model. Tile equivalent thermal resistances are evaluated and components temperatures are evaluated when the tile is exposed to terrestrial albedo and when it is exposed to solar radiation, with the commercial motor operating in nominal conditions. Temperatures are evaluated with the help of the LTspice® software;

3. Finally, a preliminary structural finite elements analysis is performed with the help of MSC Nastran and Patran softwares and reported in chapter 4. Tile stresses and displacement are evaluated under recommended ultimate inertial loads for the Vega launch vehicle, after tile mass has been evaluated. Perfect bondings were assumed for the FEM model, and a separated, simplified evaluation of loads in the bondings is made.

Chapter 1

Problem statement and state of the art

1.1 Attitude control systems overview

Attitude can be defined as the angular position of spacecraft reference frame with respect to a datum reference frame. The ability to keep a certain attitude is essential for spacecrafts, and is required, for example, to point antennas, solar arrays and payloads or to keep components temperatures within nominal ranges. Space environment exerts disturbance torques that tend to modify spacecraft attitude and tumble it. Disturbances can be induced, for example, by solar radiation pressure, gravity, aerodynamic drag or magnetic fields, and can be classified as periodic, if torque sign is oscillating, or secular, if torque sign is constant.
Most of modern space vehicles need to perform attitude control, about one, two or three axes. Usually, spacecrafts adopt different kinds of sensors to determine their attitude, for example Earth, Sun or star sensors, magnetometers and global navigation satellite systems. The on-board computer system then combines data from sensors, evaluates spacecraft attitude and calculates commands that are sent to attitude actuators. These actuators provide torques to the spacecraft and are usually grouped in the following types:

- Thrusters. Clearly, thrusters can be employed to control spacecraft attitude along the three reference frame axes, as long as fuel is available;
- Magnetic torquers. Magnets can be used to produce a torque which is the outcome of the interaction between spacecraft magnetic field and environmental magnetic fields, e.g. Earth's magnetic field, when they have a relevant magnitude. With three orthogonal magnets, complete attitude control can be made, requiring current that is potentially umlimited, if provided by solar arrays for example;
- Momentum storage torquers. These devices are designed for angular momentum storage, and they consist of one or more wheels, in rotation about a fixed or movable axis, thanks to reliable ball bearings. They are driven by electric motors that are controlled by an electronic unit. Each wheel can store angular momentum about one axis, thus three axes control can be made with three wheels. Electrical power is required, that is potentially unlimited, but wheels can saturate and need another actuator to be desaturated. A detailed description of these actuators and saturation is given in section 1.1.1.

In addition, solar radiation pressure and gravity field gradients can be exploited to give torques. Solar radiation pressure can be collected on spacecraft surfaces to give torques about any axis and booms, for example, could be extended to obtain gravitational torques that tend to align spacecraft axis of minimum moment of inertia with the local vertical of the Earth, for example. Clearly, no torque around the local vertical axis can be generated. Obviously, these methods require the electrical energy to actuate the surfaces and the booms, which is potentially unlimited.

1.1.1 Momentum storage torquers

Momentum storage torquers can be divided in reaction wheels, momentum wheels and Control Moment Gyroscopes (CMGs). For spacecraft masses above the ton, wheel diameters are between 20 and $40\,cm$[1], the mass of the assembly is in the order of $3 - 10\,kg$[2] to give a momentum storage capacity of $5 - 70\,\frac{kg\,m^2}{s}$[3]. For nanosatellites, figures are different and are given in section 1.2.1.
Often, wheels have holes in the inner regions, acting as lightenings. This is done because their ability to store angular momentum is given by their moment of inertia, which is mainly increased by masses placed far from spin axis, while nearer masses add mass to the system without increasing performances significantly.
Wheel saturation happens when the wheel is at maximum allowable speed and is no longer able to compensate external disturbances. In this case, another kind of actuator is used, for example thrusters or magnetic torquers, to counteract disturbances and reduce wheel speed that becomes desaturated.
Reaction wheels, shown in figure 1.1[4], can spin in both directions and are designed for a null mean speed. However, at low or null angular speeds, system response is not linear due to "sticking friction". To avoid this problem, reaction wheel speed may be kept at low speed, usually $1 - 10\,RPM$[5].

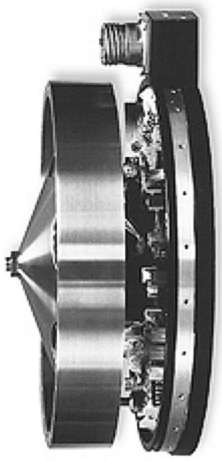

Figure 1.1: Example of reaction wheel.

Momentum wheels have a mean speed of $5000 - 10000\,RPM$[6] and momentum storage is obtained by accelerating and decelerating the wheel, typically in a $20\,\%$[7] range around mean speed.
Control moment gyroscopes represent an evolution of momentum wheels and consist of gyroscopes mounted on gimbals, able to rotate thanks to electric motors. Thus, a single wheel can provide momentum storage in all three axes. The alternative to have a three-axes attitude control is to employ at least three wheels whose rotation axes lie in three orthogonal directions. Often, a fourth wheel is added to provide redundancy.
The present trend is to integrate attitude sensors with these actuators.

1.2 CubeSats overview

CubeSat standard has been defined by Professor Robert Twiggs at Stanford University's Space Systems Development Laboratory in 1998, to encourage hands-on space education. In today's definition[8], the 1U form factor imposes a 10 x 10 x 10 cm cubic shape and a maximum mass of $1.33\,kg$, as main mechanical requirements. Their general shape, taken from CubeSat design specification[9] is reproduced in figure 1.2(a).

[1] Taken from [1, p. 308].
[2] ibidem.
[3] ibidem.
[4] Taken from https://en.wikipedia.org/wiki/Reaction_wheel.
[5] [1, p. 308].
[6] ibidem.
[7] ibidem.
[8] [2]
[9] [2, p. 23].

Since then, other form factors have been defined, their size and mass requirement are listed in table 1.1[10] and shown in figure 1.2[11]. While 1U-3U CubeSats are nanosatellites, 6U CubeSats are microsatellites.

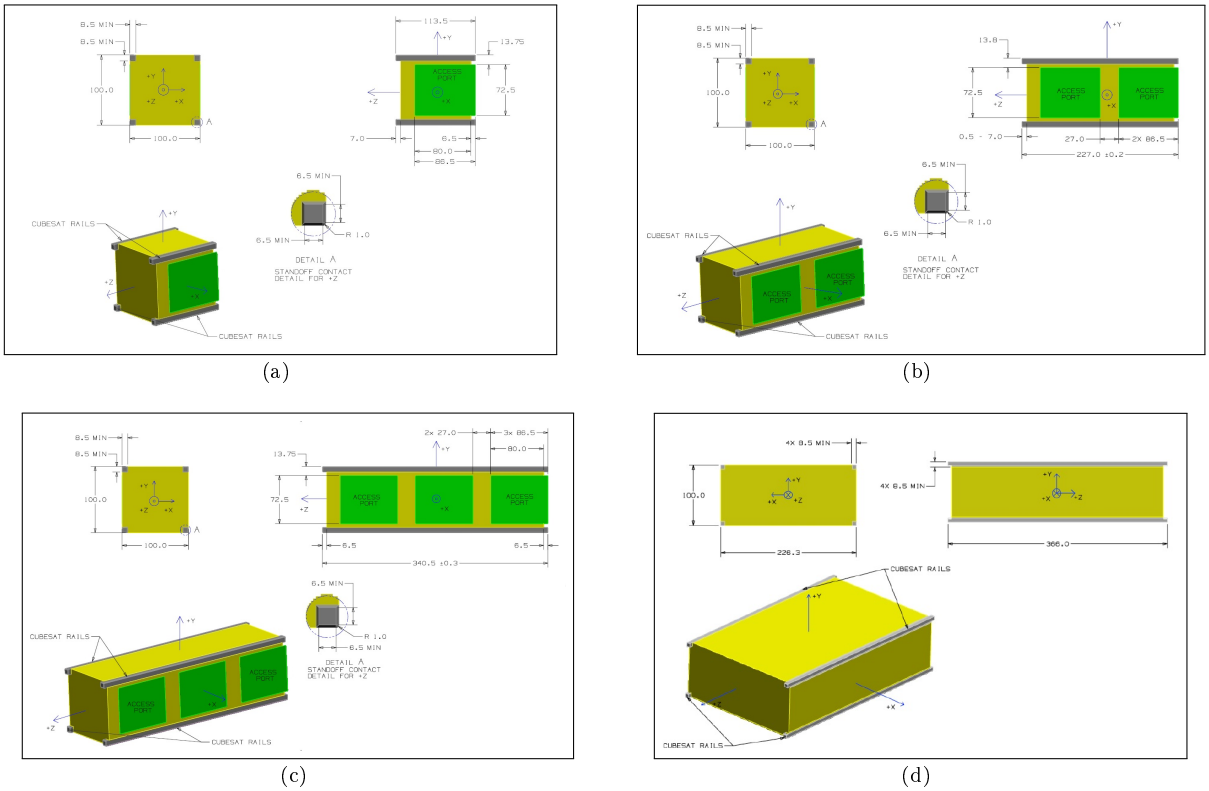

Figure 1.2: CubeSat design specification drawing for 1U form factor (a), 2U (b), 3U (c) and 6U (d).

Form factor	Size [cm]	Maximum mass [kg]
1U	10x10x10	1.330
1.5U	15x10x10	2.000
2U	20x10x10	2.660
3U	30x10x10	4.000
6U	10x20x30	12.000

Table 1.1: Size and maximum mass for CubeSats form factors.

CubeSats are launched directly by astronauts on the International Space Station or as a secondary payload on a launch vehicle. There are many types of adapters that accommodate CubeSats inside the launch vehicle, the one considered in this thesis is the Poly-Picosatellite Orbital Deployer (P-POD), developed by California Polytechnic State University and shown in figure 1.3[12]. Made in anodized aluminum, it can carry three 1U CubeSats or the equivalent of 3U, e.g. two 2U CubeSats and one 1U CubeSat. When the launch vehicle sends the deployment signal, torsion springs in the door hinge open the P-POD door (on the $+Z$ axis in figure). Cubesats are gently pulled by the main spring (shown in the cross section) and slide on rails to be deployed. The rails mechanically interface with CubeSat structure, made in aluminum alloy. Many commercial structures are available, the one considered in this thesis is a commercial ISIS 1U structure[13], shown in figure 1.4[14]. Due to the deployment procedure, a fundamental mechanical requirement imposes that no component shall protrude

[10] [2, pp. 9, 21-28] and [3, pp. 12, 24].
[11] ibidem.
[12] Reproduced from [2, pp. 7-8].
[13] Datasheet at the URL https://www.isispace.nl/product/1-unit-cubesat-structure/.
[14] Taken from the URL https://www.isispace.nl/product/1-unit-cubesat-structure/.

from CubeSat external surface for more than 6.5 mm.
At the moment, CubeSats are mostly used for education and technology demonstration, and all fly in Low Earth Orbit (LEO). Commercial CubeSat kits are available, and commercial use in LEO and scientific missions in LEO and Mars orbit are under development.

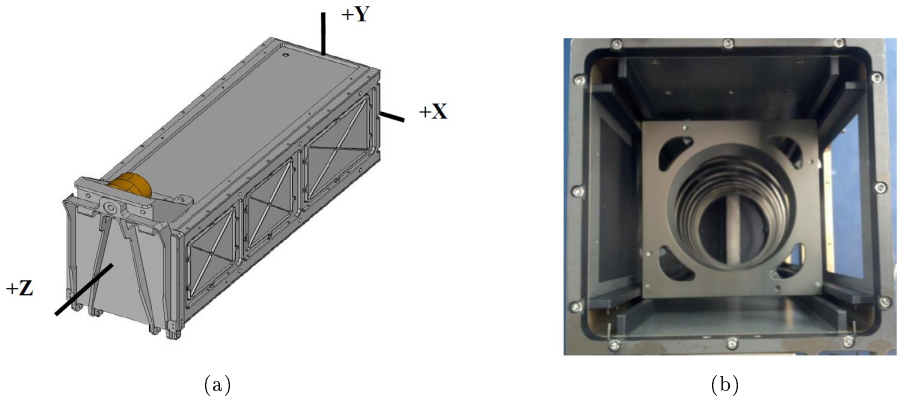

(a) (b)

Figure 1.3: Poly-picosatellite orbital deployer (a) and longitudinal cross section (b).

Figure 1.4: ISIS commercial 1U structure.

1.2.1 CubeSats attitude control overview

According to a 2010 worldwide pico- and nanosatellite survey[15], approximately 20% of all active pico- and nanosatellites have no attitude control, 40% has a passive attitude control system and the remaining 40% has an active system. In the emerging situation, attitude control appears to be not fully developed for these types of satellites, with momentum wheels, reaction wheels and thrusters still scarcely employed. These devices would allow precise remote sensing and ground station tracking, for example.
In particular, today's commercial offer of reaction wheels for 1U CubeSats can be represented by the three models shown in figure 1.5. Their characteristics and performances[16] are presented in tables 1.2 and 1.3. Nanoavionics

[15] [4, pp. 857-858].
[16] Images and data are taken from the URLs: http://bluecanyontech.com/microwheel/, https://www.cubesatshop.com/product/mai-400-reaction-wheel/ and https://n-avionics.com/subsystems/cubesat-reaction-wheels-control-system-satbus-4rw/.

data refer to a single reaction wheel. They have no integrated attitude sensors, and occupy volume in CubeSat interior, which should be left available to payload.

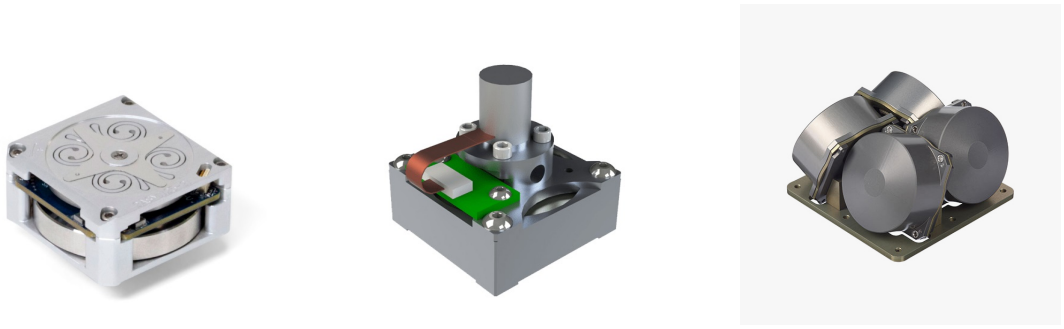

(a) (b) (c)

Figure 1.5: Commercial reaction wheels: proposals from Blue Canyon (a), CubeSatShop (b) and NanoAvionics (c).

Manufacturer	**Model**	**Dimensions** $[mm]$	**Weight** $[g]$	**Max input power** $[W]$
Blue Canyon	Microwheel (RWP015)	42x42x19	130	< 1.0
CubeSatShop	MAI-400	33x33x38.4	90	2.2
NanoAvionics	SatBus 4RW0	43.5x43.5x24	137	3.0

Table 1.2: Commercial reaction wheels characteristics.

Model	**Max speed** $[RPM]$	**Max torque** $[mNm]$	**Saturation momentum** $[mNms]$
Microwheel (RWP015)	—	4.000	15.000
MAI-400	10 000	0.635	9.350
SatBus 4RW0	6500	3.200	20.000

Table 1.3: Commercial reaction wheels performances. Torques are given in milli-newton-metres and saturation momenta in milli-newton-metre-seconds.

1.3 Problem statement

Based on examined state of the art for 1U commercial reaction wheels, the following improvements are proposed in 1U reaction wheel design reported in this thesis:

- The reaction wheel should be flat, to leave internal volume to the payload. It should be mounted on CubeSat external face;
- The reaction wheel shall integrate attitude sensors and possibly other subsystems components;
- The reaction wheel should be modular, so that three of them can be mounted on CubeSat orthogonal faces and work together in order to realize a three-axes attitude control;
- The reaction wheel should have weight, power consumption and performances comparable to state of the art devices.

In addition, reference space environment should be low Earth orbit. The flatness requirement, combined with the above mentioned maximum thickness of $6.5\,mm$ due to CubeSat mechanical requirements, makes the reaction wheel a ultrathin reaction wheel, with thickness in the order of millimeters.

Chapter 2

Reaction wheel tile sizing and tolerancing

In the present thesis, the reaction wheel tile is considered as the system. It is mounted on a commercial 1U aluminum alloy CubeSat structure[1] (shown in figure 2.1), which imposes requirements for tile mechanical and electrical connections. Other more general requirements are given in CubeSat Design Specification[2]. Section 2.1 provides a description of the entire system from a working principle and geometrical point of view. Tile sizing and tolerancing is described in the following section 2.2. Finally, preliminary experimental activity is described in section 2.3.
The sizing represents an essential input for the magnetic analysis described in chapter 3, where reaction wheel motor magnetic circuit is analyzed to make sure that magnetic saturation is avoided and then to estimate motor performances.

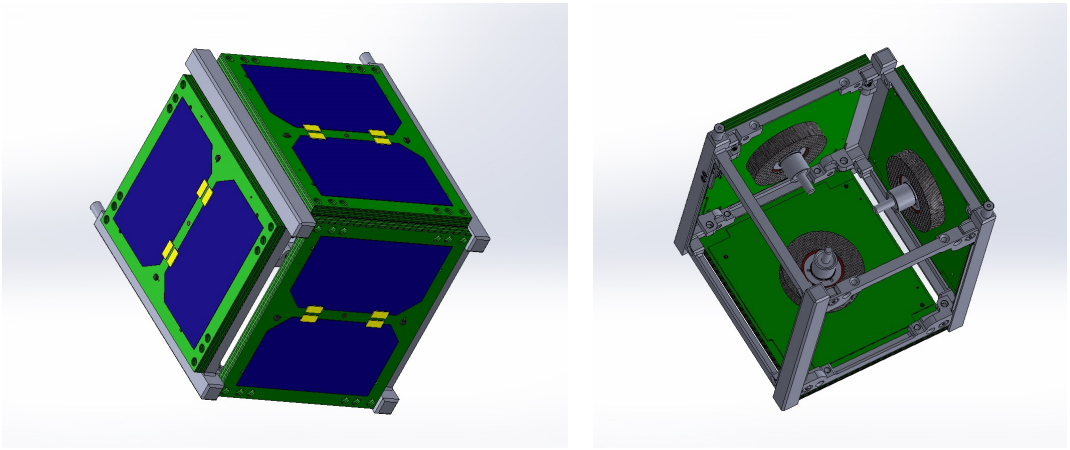

(a) (b)

Figure 2.1: Reaction wheel tiles (version 4) mounted on CubeSat ISIS 1U structure faces, seen from satellite exterior (a) and interior (b).

2.1 System description

The main requirements considered in this thesis are CubeSat Design Specification mechanical requirements 3.2.3 and 3.2.10[3]. The latter imposes a maximum CubeSat mass of $1.33\,kg$ for the 1U form factor, and transfers to reaction wheel tile as a requirement of minimum mass. Tile mass is estimated in the structural analysis chapter at section 5.2.2. The former requirement imposes that any component must not protrude from tile external surface more than $6.5\,mm$. An additional requirement has been set, and it states that as more volume

[1] https://www.isispace.nl/product/1-unit-cubesat-structure/.
[2] [2].
[3] [2, p. 9].

as possible in CubeSat interior shall be made available for the payload. As a result, a ultrathin reaction wheel has been developed.
Further important mechanical requirements are imposed by the above mentioned commercial 1U structure. Clearly, to assure an optimal mechanical connection, CubeSat structure dictates tile external dimensions and shape in its plane, along with fixing holes diameters and positions. Regardless of the tile version (described below), there are twelve smooth fixing holes, accommodating screws that fasten the tile to the aluminum alloy structure through helicoils. Depending on which face of the structure the tile is mounted on, different groups of four holes are employed for the screws. The fixing holes numbering in independent of tile version and is shown in figure 2.2(a). Fixing holes groups are composed by:

- Holes 1, 2, 11, 12, whose group is called internal holes group;
- Holes 3, 4, 9, 10, whose group is called intermediate holes group;
- Holes 5, 6, 7, 8, whose group is called internal holes group.

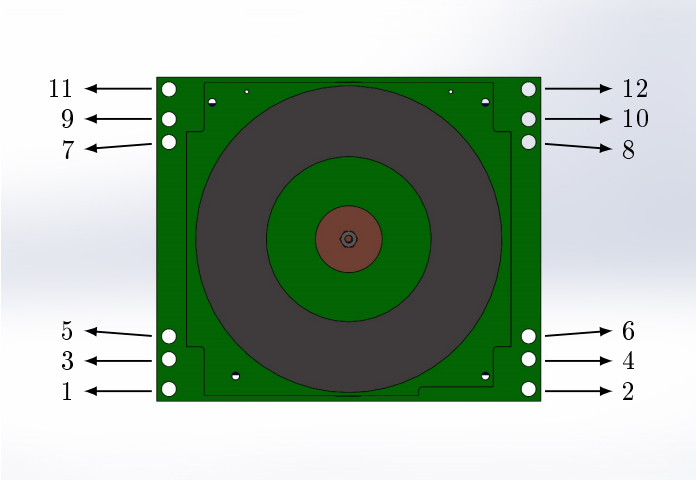

(a)

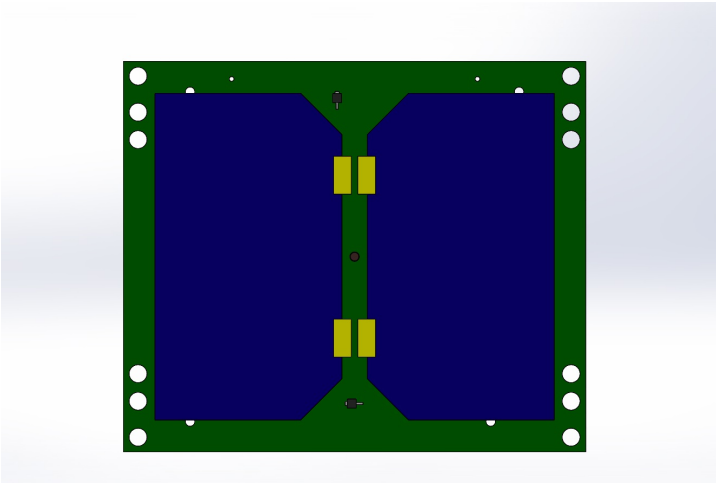

(b)

Figure 2.2: Tile version 1 seen from inner plate, with fixing holes numbering (a), and from outer plate (b).

2.1.1 Tile general concept

Four different tile versions have been developed, as a consequence of the results of electromagnetic, thermal and structural analyses described in the next chapters. However, there is a tile concept independent of tile versions (described in figure 2.4), which consists in a stack of printed circuit boards (PCBs), where the reaction wheel is embedded in an inner cavity and driven by an axial flux permanent magnet (AFPM) electric motor. External dimensions in tile plane are $97.8\,mm\,X\,82.4\,mm$. Two teflon rings are glued on PCBs, towards the wheel cavity, to protect them from possible impacts of the wheel edge, during wheel operation and launch. They have been obtained from a commercial PTFE G400 skived tape[4], supplied by Guarniflon®. In early versions of the wheel, teflon press-fits were used instead of teflon rings. These were abandoned for the teflon ring, to avoid malfunctions in which press-fits could enter wheel cavity and interfere with ball bearings operations. The PCBs in final version, number 4, are glued together with an epoxy resin and not soldered with a solder paste for electronic components, as for previous versions. Rationale of this decision are structural and are described in section 5.2.1. There are four PCB types, shown in figure 2.4:

- Inner plate, placed towards the interior of the CubeSat, facing the payload. Electronic components to drive and control the motor are soldered on the face of this PCB facing the payload. The motor is connected to the plate of this PCB in different ways, depending on the version. Sizing is presented in figure 2.3(a). Holes diameters and positions are identical to other PCBs and are presented in the following figure;

- Case body and case spacer, placed in the internal part of the stack and with an internal hole to accommodate the reaction wheel. Their shape is the same, except for the thickness. Their main function is to accomodate reaction wheel. Together with a silicon adhesive, case spacers have the additional function of blocking teflon rings (and iron ring for version 1). They do not have major electronic functions. Case body sizing is shown in figure 2.3(b). Case spacer is identical except for the central hole, whose diameter is $74\,mm$ and the thickness, which is $1\,mm$ instead of $0.63\,mm$;

- Outer plate, placed towards space. Two solar cells are glued on the external face of this PCB (shown in figure 2.2(b)), integrating components of the electrical power system. Other electronic components are soldered on this face and have electrical power regulation and control functions. Outer plate sizing is identical to case body sizing, except for the central hole which has a diameter of $2\,mm$. The thickness, as for case body, is $0.63\,mm$.

The teflon rings are bonded to the PCBs with a high temperature silicone adhesive[5], shown in red in figures. Junctions between PCB has been drawn with a gray layer, representing solder paste or epoxy resin.

Electric and electronic aspects are not the object of the present thesis. The connection among the wheel, the motor and the rest of the tile is dependent on tile version.
In the general concept, the four, asymmetric, $2\,mm$ diameter holes shown in figure are centering holes, accommodating four steel dowel pins to make sure that all PCBs are mounted correctly and always with the same orientation. The two $1\,mm$ diameter holes accommodate electrical conduits that deliver electrical power from the solar cells towards the electrical power bus.
When the tile is mounted on CubeSat structure, the surfaces of the tile in contact with the structure belong to a case body PCB, and the inner plate PCB is completely contained inside the structure. Thus the inner plate has a complex shape to adapt to the different ribs and side frames of each face of the 1U structure.

2.1.2 Tile versions

Tile versions numbering has a chronological sense and traces the evolution of tile design.
Version 1 general layout and specific components are shown in figure 2.5. A copper shaft is soldered on the outer plate central hole and soldered on a copper collar, which is soldered again on inner plate PCB, on the face towards CubeSat interior. Two commercial, miniaturized, stainless steel, flanged Sapporo F683 ball bearings[6] are splined on the shaft and allow aluminum wheel and permanent magnets rotation about the shaft. A pair of ball bearings are employed to allow gyroscopic torque transmission. They are held in position along the shaft with three commercial, spring steel cup springs[7]. The stack of springs is in contact with the collar and the

[4] Datasheet URL: http://www.guarniflon.com/en/materials/ptfe/ptfe-g400.
[5] Datasheet URL: https://docs-emea.rs-online.com/webdocs/0b64/0900766b80b644db.pdf.
[6] Datasheet URL: https://www.ezo-brg.co.jp/english/download/.
[7] Datasheet URL: http://www.gandini.it/www/molletazza_bauer.

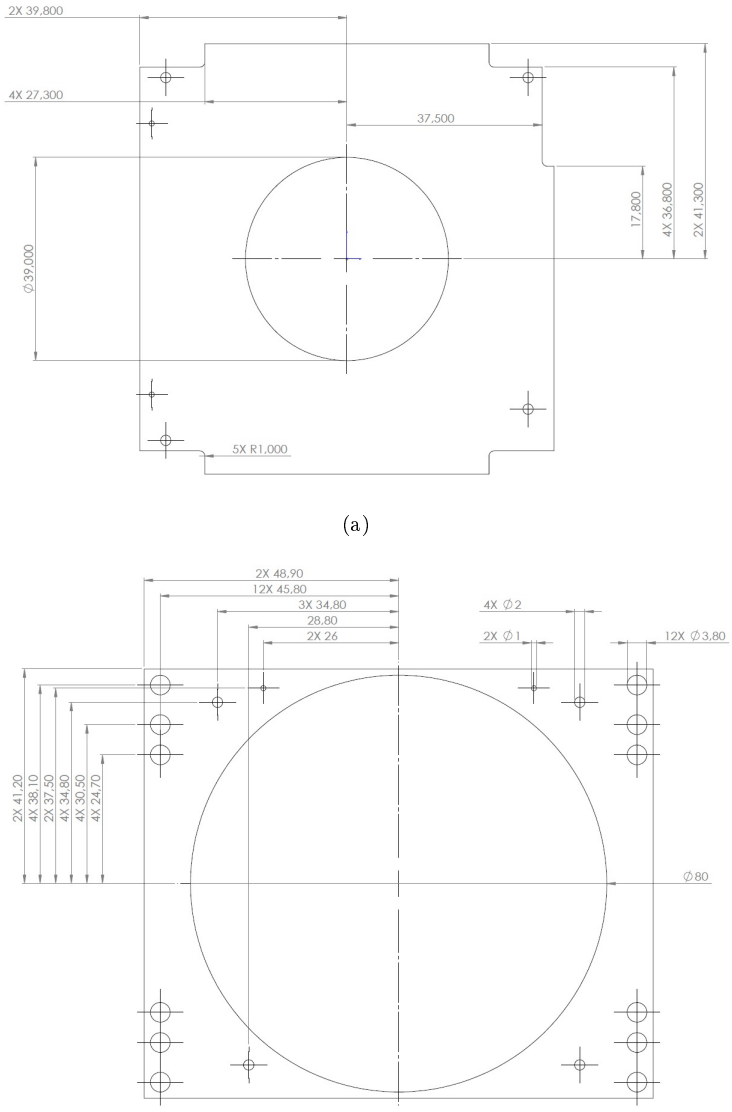

Figure 2.3: Inner plate (a) and case body sizing (b). Measures are given in millimeters.

inner ball bearing flange. A commercial, steel nut is screwed on the shaft threaded end to compress the springs. Shaft, wheel and collar are built autonomously with standard mechanical workshop equipment. The wheel and the shaft are made with a lathe starting respectively from a commercial aluminum sheet and from a commercial copper bar. The collar is made from a commercial copper sheet with a hole saw.
The AFPM motor has been developed autonomously, thus its components are distributed throughout the tile, instead of being concentrated in one assembly as for motors of other versions, which have been bought from Maxon Motor and treated as black boxes. On the contrary, version 1 motor has been analyzed to evaluate its performances and is the object of chapter 2. Its commercial level components are:

- Nine toroidal coils, made with copper wire, with internal cylindrical magnetic cores made with electrical steel sheet. They are placed on a circle on inner plate PCB, towards CubeSat interior, and have an even spacing of 40°;
- Six cylindrical NdFeB permanent magnets, buried in the aluminum wheel;
- Two identical, toroidal iron rings, made with the same electrical steel of the magnetic cores, to close motor magnetic circuit.

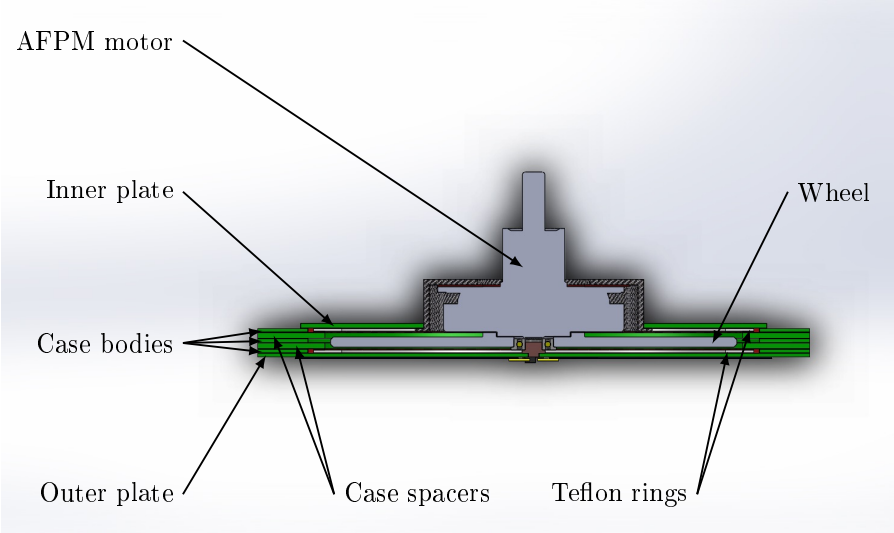

Figure 2.4: Tile general concept components shown on tile version 4.

Motor commercial components are indicated in chapter 3 and a description of motor operation involving the above mentioned components is given in section 3.2.
Version 2 has been developed after finding a poor efficiency for the autonomously built AFPM motor (see section 3.4) and its general layout and specific components are shown in figure 2.6. Since no internal iron ring is now needed, the outermost case spacer PCB has been moved to better block the outermost teflon ring. A Maxon EC 10 flat AFPM motor[8] was chosen, given its performances and dimensions. A second version of the aluminum wheel has been designed to assure an optimal mechanical connection with rotor. Since the motor has one internal ball bearing, one flanged ball bearing is adpoted, of the same kind of version 1 and is splined on the copper shaft. The shaft design is modified consequently and it is again soldered to the outer plate PCB. The wheel is bonded to the ball bearing and the rotor with the above mentioned high temperature silicone adhesive. The collar, in its second version, has been adapted to motor dimensions and has a hole to accommodate motor pins cables. Collar connection with the inner plate has not been designed, since during the project the motor has been retired from production. Autonomous production of wheel, shaft and collar employs the same materials and equipment of version 1 components.
Version 3 employs an EC 32 flat motor[9], and is shown in figure 2.7 along with its specific components. Motor performances are adequate, although its dimensions and mass, $32\,g$, are not optimal. The inner plate central hole diameter has been adapted to motor diameter. A new version of the aluminum wheel was designed, to accommodate the new rotor, the rest of the design is the same of version 2. The motor has one internal ball bearing, thus just one flanged ball bearing is adopted, of the same kind of version 1 bearing. Shaft material and design is the same of version 2. The copper collar has been adapted to motor dimensions. It is soldered to inner plate and bonded with the above mentioned high temperature adhesive to the motor. Other connections are made as for version 2. Equipment for production of shaft, collar and wheel is the same of previous versions. The design of these components is described in section 2.2 and its production is described in section 2.3.
In conclusion, version 4, the final version, has been developed and is shown in figure 2.8 with its specific components. The only difference with version 3 lies in the collar. From a structural point of view, the mass of previous copper collar resulted in excessive inertial loads at launch, thus it has been decided to use a lighter carbon-epoxy CFRP collar, with $0°/90°$ carbon fibers fabric plies. While it is still bonded to the motor with the above mentioned adhesive, connection with the inner plate has been modified. Bonding to the PCB with the high temperature adhesive was adopted, instead of soldering. Since bonding has a low resistance to traction stresses, compared to the higher resistance to compression stresses, a flange was designed to be bonded on inner plate PCB towards wheel cavity. Thus, the maximum inertial load from the shaft, the ball bearing, the wheel and the motor causes compression and not traction stresses on the bonding. Commercial motor axis, shown in figure 2.8(b), can be eliminated to save space for the payload, as shown in figure 2.9. Thickness of the part

[8] Datasheet URL: https://www.maxonmotor.com/medias/sys_master/root/8825428344862/17-EN-255.pdf.
[9] Datasheet URL: https://www.maxonmotor.com/medias/sys_master/root/8825434800158/17-EN-262.pdf.

towards CubeSat interior is thus reduced to 17.7 mm. However, the thicker cylindrical part contains the ball bearing and cannot be eliminated. Mass of version 4 is 102 g.

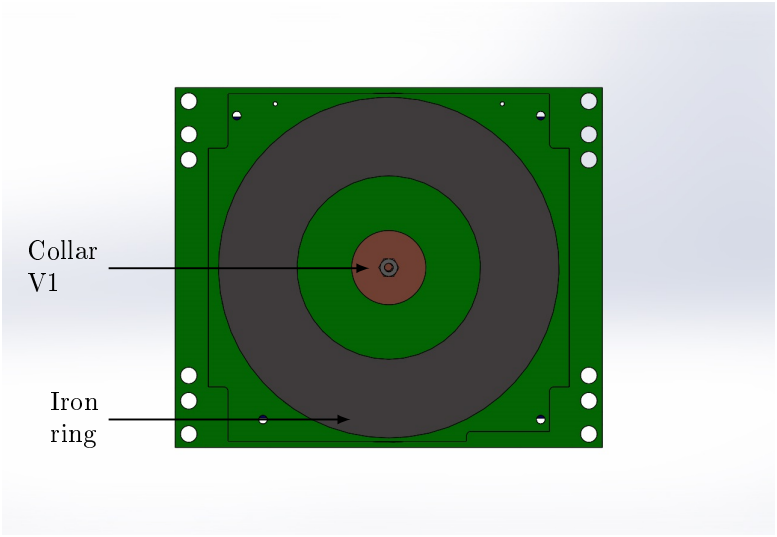

(a)

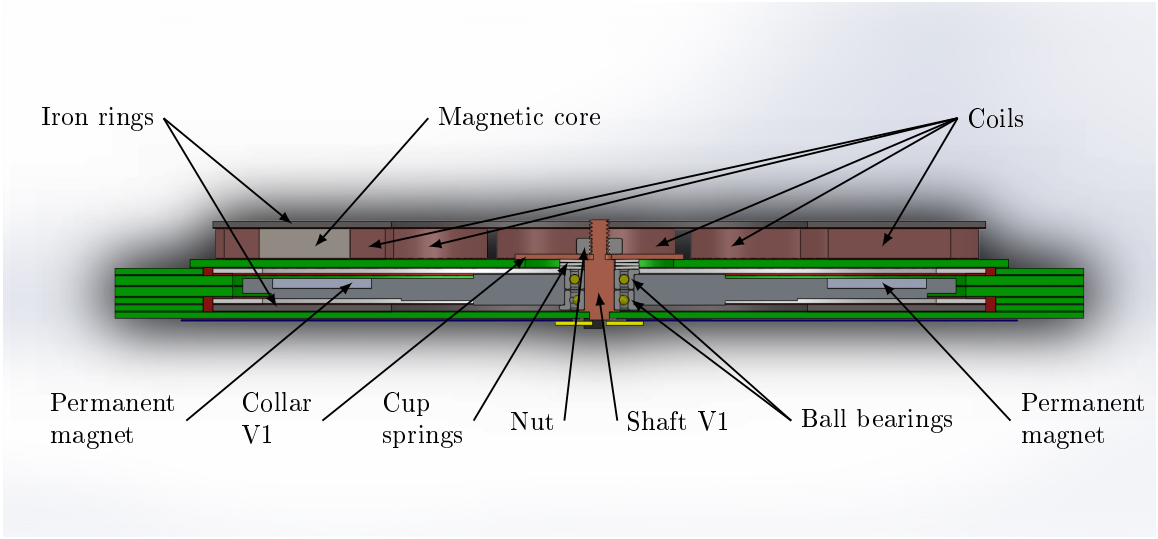

(b)

Figure 2.5: Tile version 1 seen from inner plate (a) and in section (b).

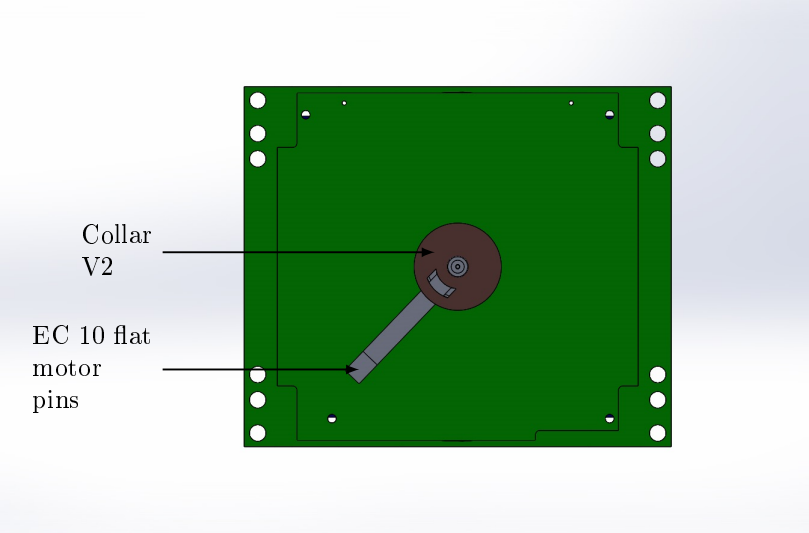

(a)

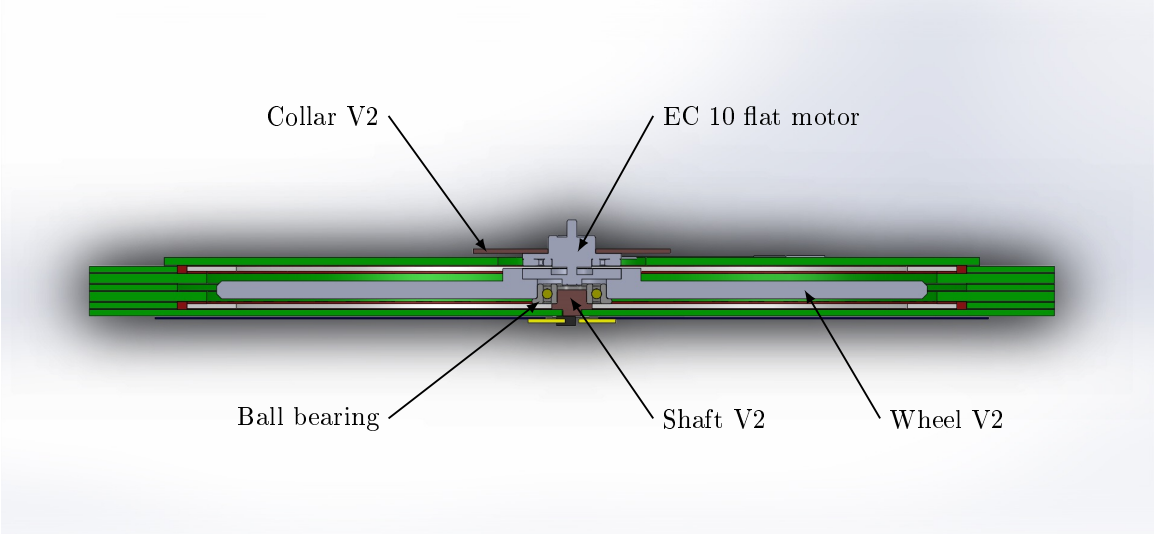

(b)

Figure 2.6: Tile version 2 seen from inner plate (a) and in section (b).

2.2 Tile sizing and tolerancing

Tile sizing and tolerancing has been essential to assure congruence of tile geometrical dimensions and has been introduced in version 2 of the reaction wheel tile. In particular, in designing the wheel and the shaft, tolerances imposed by PCB producer, PCBWay, have been taken into account to avoid interference among wheel cavity components. Little information is given on PCB tolerances by the producer[10], in particular:

- Dimensional tolerances on PCB thickness, which in the case of interest is $\pm 0.1\,mm$;
- Dimensional tolerances on PCB outline, which is $\pm 0.2\,mm$ in case of CNC routing, and $\pm 0.5\,mm$ in case of V-scoring;
- Dimensional tolerances on holes diameters, which is $\pm 0.08\,mm$.

Thicknesses taken into account are shown in figure 2.10, in particular:

[10] At the URL https://www.pcbway.com/capabilities.html.

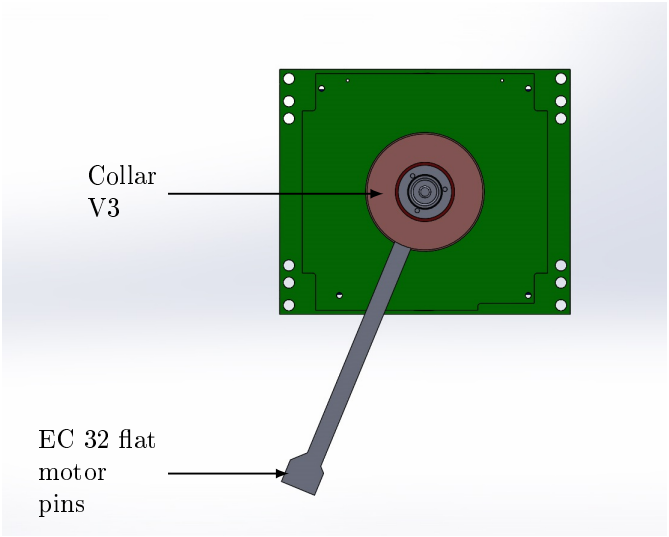

(a)

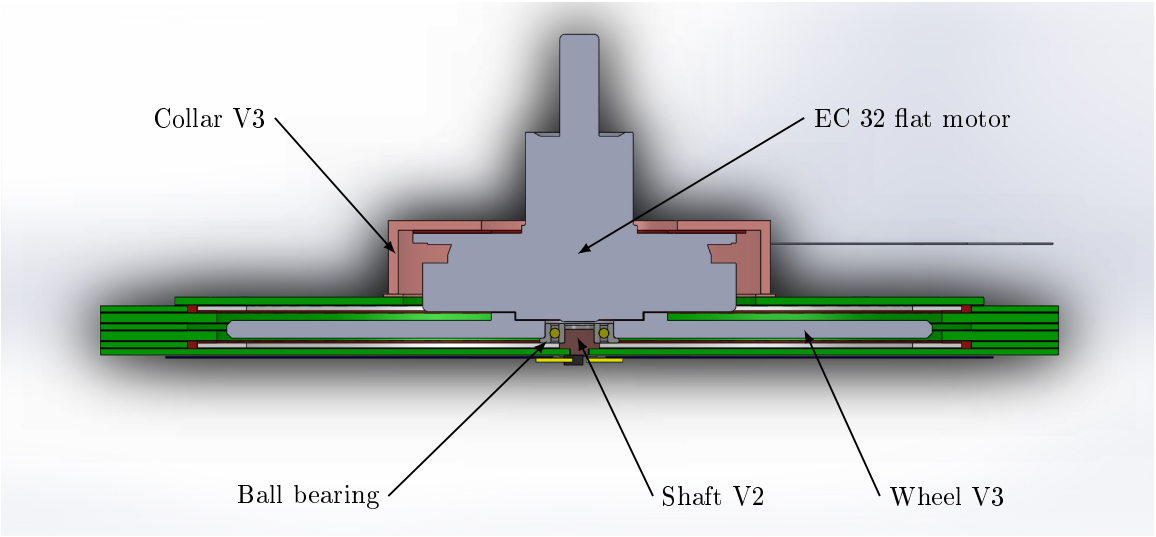

(b)

Figure 2.7: Tile version 3 seen from inner plate (a) and in section (b).

- T is total cavity thickness;
- t_s is the thickness of shaft flange;
- t_b is the thickness of ball bearing flange;
- t_t is the thickness of teflon rings;
- t_{cs} is the thickness of the case spacer;
- t_{cb} is the thickness of the case body;

Teflon rings thicknesses t_t are imposed by the PTFE skived tape producer[11]. In figure, it was not possible to show the following thicknesses, which have been taken into account:

- t_{sold}, the thickness of solderings or bondings among PCBs;

[11] Datasheet URL: http://www.guarniflon.com/en/materials/ptfe/ptfe-g400.

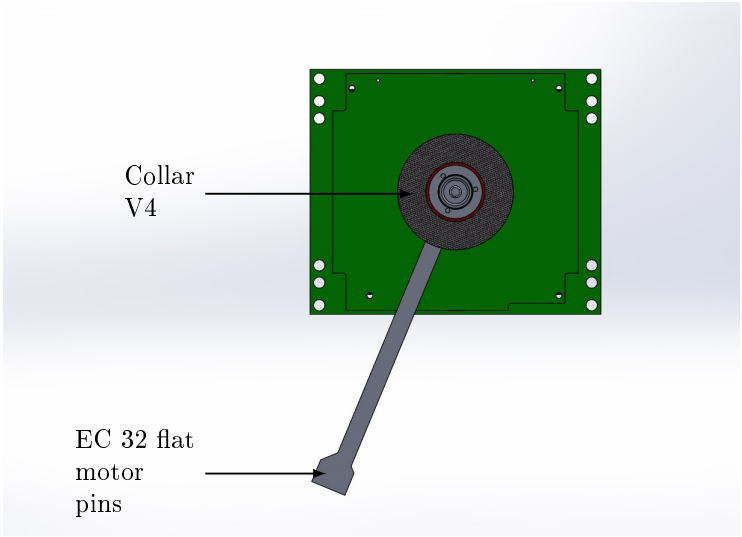

(a)

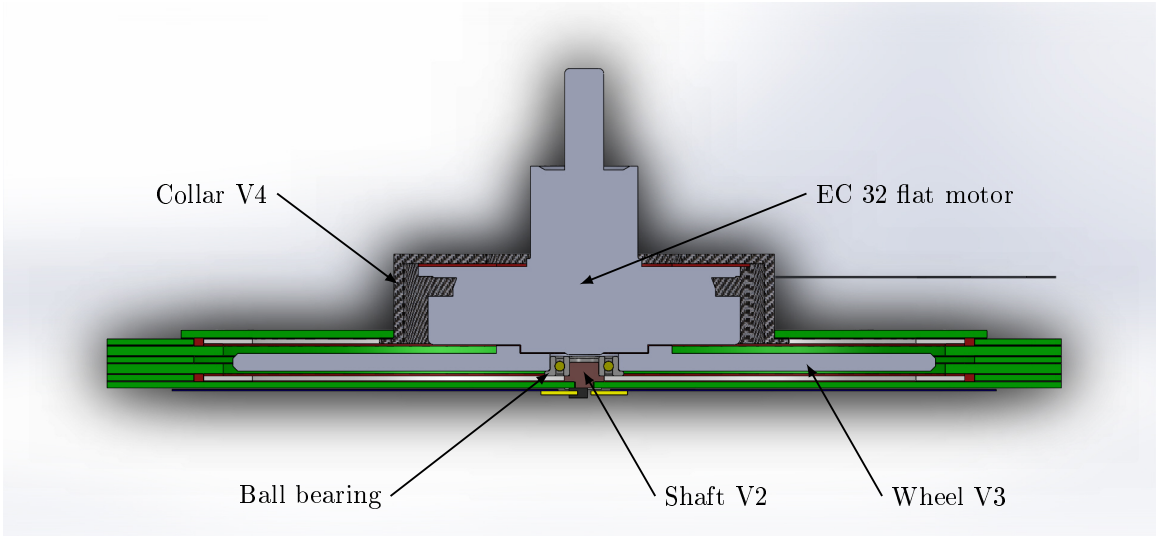

(b)

Figure 2.8: Tile version 4 seen from inner plate (a) and in section (b).

- $t_{sold,2}$, the thickness of the soldering between shaft flange and inner plate PCB;
- t_{glue}, the thickness of the bonding between teflon rings and inner or outer plate PCBs.

The analysis consists in the determination of the adequate thicknesses for the following gaps:

- a, the thickness of the gap between outer plate PCB and the wheel;
- b, the thickness of the gap between the outer teflon ring and the wheel;
- c, the thickness of the gap between the inner teflon ring and the wheel;
- d, the thickness of the gap between the inner plate PCB and the wheel.

In the first place, total thickness T is determined:

$$\begin{aligned} T &= 6 \cdot t_{sold} + 3 \cdot t_{cb} + 2 \cdot t_{cs} = \\ &= 6 \cdot 0.100 + 3 \cdot 0.630^{+0.100}_{-0.100} + 2 \cdot 1.000^{+0.100}_{-0.100} = 4.490^{+0.500}_{-0.500}\, mm \end{aligned} \tag{2.1}$$

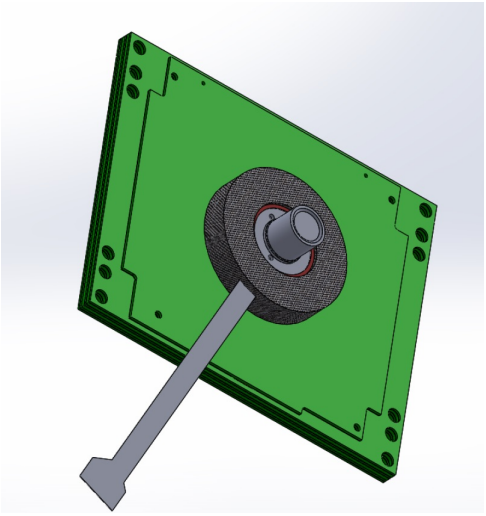

Figure 2.9: Tile version 4 without motor shaft.

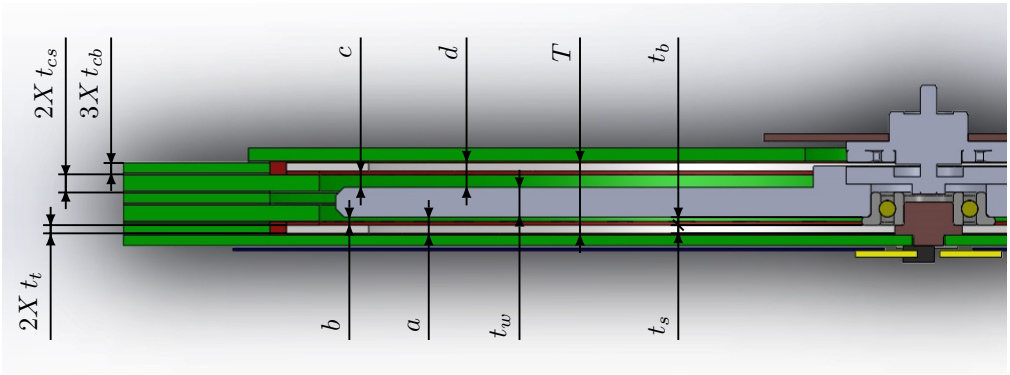

Figure 2.10: Tile version 2 dimensions for tolerancing.

To obtain a satisfying value for thicknesses a and b, the thickness of shaft flange t_s is imposed:

$$\begin{aligned} a &= t_s + t_b + t_{sold,2} = \\ &= 0.600^{+0.010\,+0.003}_{-0.010\,-0.003} + 0.500^{+0.000}_{-0.050} + 0.100 = 1.200^{+0.013}_{-0.063}\, mm \end{aligned} \tag{2.2}$$

$$\begin{aligned} b &= a - t_{glue} - t_t = \\ &= 1.200^{+0.013}_{-0.063} - 0.100 - \left(0.500^{-0.000}_{+0.030}\right) = 0.600^{+0.013}_{-0.093}\, mm \end{aligned} \tag{2.3}$$

Thicknesses c and d can then be calculated imposing wheel thickness t_w:

$$\begin{aligned} d &= T - a - t_w = \\ &= 4.490^{+0.500}_{-0.500} - \left(1.200^{-0.063}_{+0.013}\right) - \left(1.800^{-0.030-0.005}_{+0.030+0.005}\right) = 1.490^{+0.598}_{-0.548}\, mm \end{aligned} \tag{2.4}$$

$$\begin{aligned} c &= d - t_{glue} - t_t = \\ &= 1.490^{+0.598}_{-0.548} - 0.100 - \left(0.500^{-0.000}_{+0.030}\right) = 0.890^{+0.598}_{-0.578}\, mm \end{aligned} \tag{2.5}$$

And are considered satisfying. Gap thicknesses b and c are considered sufficient for usual wheel axis misalignment.
The above thicknesses analysis, made for the second version of wheel and shaft, has been adopted for version 3 of the wheel as well. A few modifications have been made to assure an optimal mechanical connection with the EC 32 flat motor, since the design of the second version of the wheel was made adopting the EC 10 flat motor. Mechanical schematics can be found in appendix B. Tolerances have been set according to present day standards. Clearly, most restrictive tolerances have been imposed along reaction wheel thickness.

2.3 Experimental activity

A preliminary experimental activity was conducted to verify tile layout, employing commercial equipment. As mentioned in system description at section 2.1.2, commercial level equipment was employed for components autonomous production. In particular, a Valex RX 5004 lathe, shown in figure 2.11(a), was used to produce the shaft and the wheel, shown in figure 2.11(c). A couple of aluminum adapters have been produced with the lathe from commercial aluminum bars, and are shown in figure. In an early version of the project, two identical adapters were needed to link the shaft with the aluminum wheel, which was a hard disk drive platter. Adapters were then integrated in wheel design in version 1. An OPTIMUM BF20 Vario milling machine, shown in figure 2.11(b), was employed to produce the collar, shown in figure 2.11(c).
Autonomously produced components congruence with the stack of printed circuit boards and permanent magnets was then verified. Permanent magnets and outer plate PCB, with solar cells pads, are shown in figure. Final version complete assembly could not be built and tested. However, testing is an essential aspect and is highly recommended for future work.

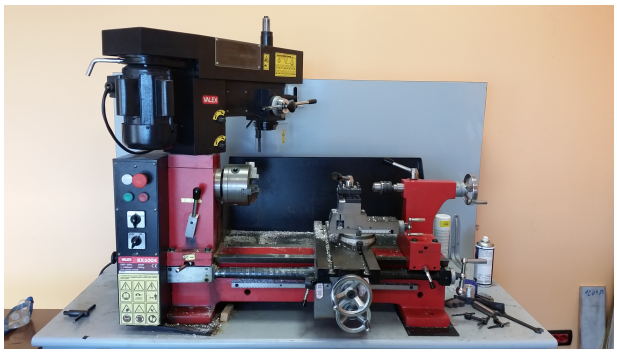

(a)

(b)

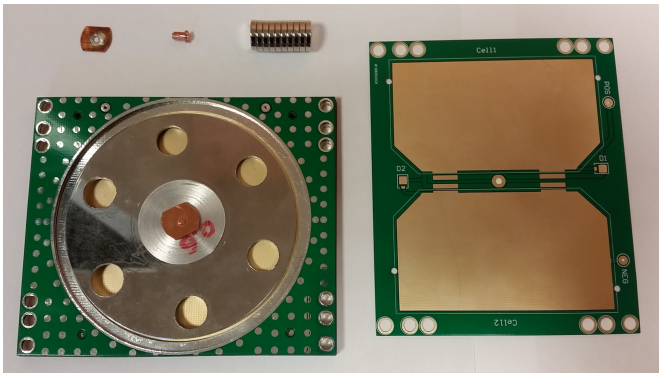

(c)

Figure 2.11: Lathe (a) and milling machine (b) employed in the experimental work. Shaft, collar, wheel and adapters have been produced and assembled with printed circuit boards (c).

Chapter 3

Brushless Motor Analysis

The present chapter reports the analysis of the autonomously built Axial Flux Permanent Magnet (AFPM) motor, whose objective is to evaluate its performances. Section 3.1 reports the theoretical work conducted to analyze motor magnetic circuit. The analysis of magnetic circuit is described at section 3.2. Coils voltage is set to avoid magnetic saturation in the iron rings, and then maximum magnetic flux induced by permanent magnets is evaluated. After theoretical deductions on counter-electromotive force in section 3.3, performances are evaluated in section 3.4, with the help of MATLAB scripts. In the conclusions section 3.5, the efficiency of the autonomously built motor is found to be poor, thus two commercial AFPM motors are selected and a performances comparison is made among the three solutions.

3.1 Magnetic Circuit Theory

The discussion in the present chapter is strictly valid if stationary conditions are considered, i.e. electromagnetic variables are constant in time. However results have an acceptable level of approximation if quasi-stationary conditions are considered, i.e. time variations of electromagnetic variables are low enough to make displacement currents (whose density is $\partial \boldsymbol{D}/\partial t$) negligible with respect to conductive currents (whose density is $\boldsymbol{j}$):

$$\left| \frac{\partial \boldsymbol{D}}{\partial t} \right| \ll |\boldsymbol{j}| \tag{3.1}$$

Where $\boldsymbol{D}$ is the electric displacement field and t is time. Relation between magnetic fields $\boldsymbol{B}$ and $\boldsymbol{H}$ is given by material's (or vacuum's) absolute permeability μ, which can be constant or variable with $\boldsymbol{H}$ field intensity (as is discussed below):

$$\boldsymbol{B} = \mu \boldsymbol{H} \tag{3.2}$$
$$\mu = \mu_0 \, \mu_r \tag{3.3}$$
$$\mu_0 = 4\pi \cdot 10^{-7} \, H/m \tag{3.4}$$

Where μ_0 is vacuum's permeability, μ_r is material's relative permeability and takes the unitary value for vacuum. In quasi-stationary conditions magnetic field is governed by Gauss's law and Ampère's circuital law. The former can be given for $\boldsymbol{B}$ and $\boldsymbol{H}$ fields both in differential form (showing $\boldsymbol{B}$ is a solenoidal vector field):

$$\boldsymbol{\nabla} \cdot \boldsymbol{B} = 0 \, ; \qquad \boldsymbol{\nabla} \cdot (\mu \boldsymbol{H}) = 0 \tag{3.5}$$

and in integral form:

$$\oint_A \boldsymbol{B} \cdot \boldsymbol{u_n} \, dA = 0 \, ; \qquad \oint_A \mu \boldsymbol{H} \cdot \boldsymbol{u_n} \, dA = 0 \tag{3.6}$$

Where integration is made over a closed, simply connected surface A, dA is an infinitesimal element of A and $\boldsymbol{u_n}$ is the unit vector outgoing and orthogonal with respect to A. Ampère's law can as well be written for $\boldsymbol{B}$ and $\boldsymbol{H}$ fields in differential form:

$$\boldsymbol{\nabla} \wedge \boldsymbol{B} = \mu_0 \, \boldsymbol{j} \, ; \qquad \boldsymbol{\nabla} \wedge \boldsymbol{H} = \boldsymbol{j} \tag{3.7}$$

and in integral form:

$$\oint_c \boldsymbol{B} \cdot \boldsymbol{u_c}\, dl = \mu_0\, i\,; \qquad \oint_c \boldsymbol{H} \cdot \boldsymbol{u_c}\, dl = i \tag{3.8}$$

Where $\boldsymbol{i}$ is the current inducing $\boldsymbol{B}$ and $\boldsymbol{H}$ magnetic fields and integration is made along a closed line c enclosed in the current $\boldsymbol{i}$. Direction of c is established by the current according to right-hand rule. dc is an infinitesimal segment on c and $\boldsymbol{u_c}$ is the unit vector tangent to c, with the same positive direction.

3.1.1 Hopkinson's law

The relation between a current $\boldsymbol{i}$ and its induced magnetic $\boldsymbol{H}$-field, integrated along the closed curve l enclosed in $\boldsymbol{i}$ is given by Ampère's law in integral form:

$$\oint_l \boldsymbol{H} \cdot \boldsymbol{u_l}\, dl = i$$

While magnetic $\boldsymbol{H}$-field is independent of the particular material (or the vacuum) the curve l is buried in, the $\boldsymbol{B}$-field is dependent on such material, since it is related to $\boldsymbol{H}$ field by material's or vacuum's permeability μ. Thus the second Ampère's law in equation 3.8 has the same form, regardless of different materials the closed curve l lies in. On the contrary, if the first integral form was considered, using $\boldsymbol{B}$-field, the correct value for $\boldsymbol{B}$-field would have to be found by adopting the proper value of μ for each portion of l corresponding to a particular material, so the first integral Ampère's law in equation 3.8 must be specified for each material.
The current $\boldsymbol{i}$ and the magnetic field induced in an enclosed ring made with magnetically isotropic, non homogeneous material can form an elementary magnetic circuit, a portion of which is shown in figure 3.1, where x is the curvilinear axis running along the ring. Obviously, the circuit will always be closed since $\boldsymbol{B}$ is solenoidal and the case of closure at infinity is excluded. By hypothesis, $\boldsymbol{B}$- and $\boldsymbol{H}$-magnetic fields must be completely contained on the material forming the circuit. As mentioned above, Ampère's law can be applied in the second form of equation 3.8 regardless of the particular point in the material. It can be simplified assuming that the closed curve l is coinciding with $\boldsymbol{H}$-magnetic field lines:

$$\oint \boldsymbol{H} \cdot \boldsymbol{u_l}\, dl = \oint H dl = i \tag{3.9}$$

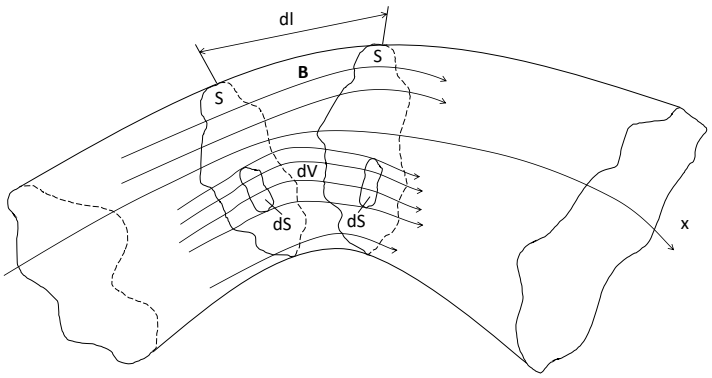

Figure 3.1: Generic magnetic circuit portion.

One can choose a section, whose area is S, such that it is everywhere orthogonal to $\boldsymbol{H}$-magnetic field lines (and thus orthogonal to $\boldsymbol{B}$-field lines as well) and such that magnetic fields $\boldsymbol{H}$ and $\boldsymbol{B}$ are constant over the section itself. An infinitesimal part of this section can be considered, whose area is dS. The infinitesimal flux $d\Phi$ of the $\boldsymbol{B}$-magnetic field over dS is then:

$$d\Phi = BdS \tag{3.10}$$

This flux is conserved in the streamtube whose walls are formed by magnetic field lines passing across the boundary of dS (shown in figure 3.1). Another infinitesimal section is identified along this streamtube at a

distance dl from the first section. It is assumed to have the same area dS and the same properties as the first section (it is locally orthogonal to magnetic fields and their intensity is constant over the section). Another finite section with the same area S can be identified starting from the second infinitesimal section. dS and dl are chosen such that the material inside the infinitesimal volume $dV = dl\,dS$ can be assumed to have homogeneous permeability μ. From conservation of the flux defined in 3.10 one can infer that the $\boldsymbol{B}$ and $\boldsymbol{H}$-magnetic field moduli inside dV are constant and H can be written as:

$$H = \frac{B}{\mu} = \frac{1}{\mu}\frac{d\Phi}{dS} \tag{3.11}$$

Solving for $d\Phi/H$ one obtains:

$$\frac{d\Phi}{H} = \mu dS \tag{3.12}$$

Equation 3.12 can be integrated over the entire slice whose axial length is dl (superior order variations of this distance will be neglected), between sections whose area is S. The total $\boldsymbol{B}$ flux is Φ and is obviously measured in webers (Wb) in SI units. By hypothesis it is completely contained in the material and it is conserved on each section since material walls form a streamtube which is the magnetic circuit itself.

$$\int_{\Phi} \frac{d\Phi}{H} = \int_S \mu dS \tag{3.13}$$

$$\frac{\Phi}{H} = \int_S \mu dS \tag{3.14}$$

Since field intensity H is constant on dV. Equation 3.14 can be integrated over the entire length l of the ring:

$$H = \frac{\Phi}{\int_S \mu dS} \tag{3.15}$$

$$\oint_l H dl = i = \oint_l \frac{\Phi}{\int_S \mu dS} dl \tag{3.16}$$

The total flux Φ is constant on each section of the ring, thus it can get out of the integral:

$$i = \Phi \oint_l \frac{dl}{\int_S \mu dS} \tag{3.17}$$

Equation 3.17 states that the magnetic flux Φ in the ring and the enclosed current i are proportional and their ratio is called magnetic reluctance $\mathcal{R}$, which is measured in inverse henrys (H^{-1}) in SI units:

$$i = \Phi \oint_l \frac{dl}{\int_S \mu dS} = \Phi\,\mathcal{R} = \Phi\,\frac{1}{\mathcal{P}} \tag{3.18}$$

The inverse of reluctance $\mathcal{P}$ is called magnetic permeance and is obviously measured in henrys (H). Equation 3.18 is the fundamental relation for magnetic circuits and is usually called Hopkinson's law. Reluctance and permeance are given in integral form for a magnetically isotropic and non homogeneous material. Clearly, they depend on material permeability μ, ring shape and dimensions, and $\boldsymbol{B}$-magnetic flux direction. If material has homogeneous permeability over each section their expressions can be simplified:

$$\mathcal{R} = \frac{1}{\mathcal{P}} = \oint_l \frac{dl}{\int_S \mu dS} = \oint_l \frac{dl}{\mu(x)S(x)} \tag{3.19}$$

Where x is the coordinate along the ring. If material permeability μ is everywhere homogeneous and its section S is constant further simplifications are possible:

$$\mathcal{R} = \frac{1}{\mathcal{P}} = \oint_l \frac{dl}{\mu(x)S(x)} = \frac{l}{\mu S} \tag{3.20}$$

Magnetic flux Φ in Hopkinson's law 3.18 can obtained not only by calculation of the flux on sections with particular properties as the ones defined above, it can be obtained from flux calculation on sections with any orientation and shape, since magnetic circuit can be considered as the streamtube containing the entire magnetic

field generated by the current $\boldsymbol{i}$.
This current from a magnetic point of view represents a magnetomotive force $\mathcal{F}$. Magnetomotive force is obtained, in normal practice, by means of a permanent magnet or a coil with a number N of turns in which a stationary current $\mathcal{I}$ flows, thus total enclosed current modulus is $i = N\,\mathcal{I} = \mathcal{F}$ and is measured in ampere-turns (At). Hence Hopkinson's law 3.18 can be written as:

$$\mathcal{F} = \mathcal{R}\,\Phi = \frac{\Phi}{\mathcal{P}} \tag{3.21}$$

The unit of measure of reluctance, inverse henry, can be thought as ampere-turn per weber (At/Wb), and the unit of measure of permeance, henry, can be thought as weber per ampere-turn (Wb/At). The physical arrangement of the elementary magnetic circuit becomes the typical one shown in figure 3.2. Flux direction is given by enclosed current $\mathcal{I}$ according to right-hand rule. Magnetomotive force $\mathcal{F}$ has the same direction as Φ since it comes from a generator. It is absorbed by circuit material which has an equal and opposite magnetic voltage drop $\mathcal{F}_d = \mathcal{R}\,\Phi$.
Given the derivation above, Hopkinson's law can be applied to a magnetic circuit or a generic streamtube, for example a smaller streamtube contained inside (whose axis can be the black dashed line in figure) or partially outside the magnetic circuit (whose axis can be the blue dashed line in figure).

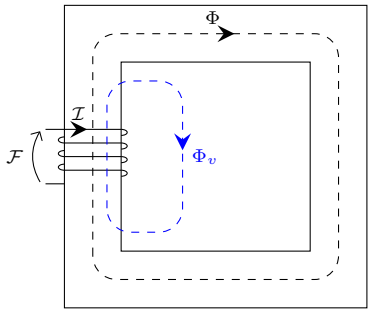

Figure 3.2: Physical diagram of elementary magnetic circuit. The black dashed line represents streamtubes whose axis is completely buried in the material, the blue dashed line represents streamtubes whose axis partially crosses vacuum.

Hopkinson's law 3.21 has been given for a circuit (or a generic streamtube), whose properties are varying in a continuous way, then it can be easily adapted to the case of a circuit (or a streamtube) with discrete properties. Considering a whole circuit, with a number Z of discrete segments whose lengths are l_k, with constant permeabilities μ_k and sections S_k, Hopkinson's law can easily be developed starting from equation 3.17:

$$i = N\,\mathcal{I} = \mathcal{F} = \Phi \oint_l \frac{dl}{\int_S \mu dS} = \Phi \sum_{k=1}^{Z} \frac{l_k}{\mu_k\,S_k} = \Phi \sum_{k=1}^{Z} \mathcal{R}_k = \Phi\,\mathcal{R}_{eq} \tag{3.22}$$

Thus circuit equivalent reluctance $\mathcal{R}_{eq}$ is the sum of reluctances of single segments $\mathcal{R}_k$. The sum of segments reluctances $\mathcal{R}_k$ multiplied by their flux Φ can be interpreted as the sum of magnetic voltage drops $\mathcal{F}_{d,\,k}$ of each segment:

$$\mathcal{F} = \Phi \sum_{k=1}^{Z} \mathcal{R}_k = \sum_{k=1}^{Z} \Phi\,\mathcal{R}_k = \sum_{k=1}^{Z} \mathcal{F}_{d,\,k} \tag{3.23}$$

In the present case, the sum of magnetic voltage drops equals magnetomotive force $\mathcal{F}$ (see also section 3.1.3). In particular, the sum of magnetic voltage drops includes magnetic voltage drop in generator segment as well, accounting for its reluctance, which in lumped parameter models is represented separately from the generator function, as happens for real electromotive force generators in electric circuits.
A discrete variation of properties is verified for the streamtube in figure 3.2 which partially crosses vacuum. Assuming a constant section S, segment m, buried in material, can have continuously or discretely varying permeability, the mean value being $\mu_1 = \mu_0\,\mu_{rm}$, while segment v in vacuum has constant permeability μ_0. Thus Hopkinson's law becomes:

$$N\,\mathcal{I} = \Phi_v \left(\frac{l_m}{\mu_0\,\mu_{rm}\,S} + \frac{l_v}{\mu_0\,S} \right) \simeq \Phi_v\,\frac{l_v}{\mu_0\,S} \tag{3.24}$$

Since for usual materials $\mu_{rm} \gg 1$ and lengths have the same order of magnitude. A second streamtube is considered, its axis is represented by the black dashed line in figure 3.2. It is completely buried in the material, with length l, section S and mean relative permeability μ_{rM} (it can vary in a continuous or discrete way). μ_{rM} has the same order of magnitude as μ_{rm}. Currents enclosed by streamtubes are the same and thus:

$$N\mathcal{I} = \Phi \frac{l}{\mu_0 \mu_{rM} S} = \Phi_v \frac{l_v}{\mu_0 S} \tag{3.25}$$

Since lengths l and l_v have the same orders of magnitude, an important inequality is obtained:

$$\frac{\Phi}{\mu_{rM}} \simeq \Phi_v \tag{3.26}$$

$$\Phi \gg \Phi_v \tag{3.27}$$

Thus the assumption of a $\boldsymbol{B}$-magnetic field completely contained in circuit material (or null leakage flux), made in the above derivation of Hopkinson's law, is well verified as long as μ_{rM} is orders of magnitude bigger than unity. In usual materials, flux leakages are negligible and μ_{rM} can reach orders of magnitude of millions.
The entire discussion above is formally similar to the corresponding one for electric conductors in electrically stationary conditions leading to Ohm's law, which is formally comparable to Hopkinson's law. Ohm's law establishes a relation between the current I flowing through an electric conductor and the electric potential difference V between its ends:

$$V = R\,I = \frac{I}{G} \tag{3.28}$$

According to the formal analogy, the flux Φ in Hopkinson's law 3.21 can be compared with current I in Ohm's law 4.8. Similarly, electric resistance R can be compared to magnetic reluctance $\mathcal{R}$, electric conductance G can be compared to magnetic permeance $\mathcal{P}$, and the role of the electric potential difference V is taken by the magnetomotive force $\mathcal{F}$. It is possible to study magnetic circuits behaviour with a lumped parameter model and to represent the lumped parameters as discrete components, that are connected and interact among themselves to represent the real magnetic circuit, as is made for electric circuits. The example of elementary magnetic circuit described above is represented with lumped parameters in figure 3.3(b), where it is compared to its electric counterpart shown in figure 3.3(a). The current I flowing in the electric circuit 3.3(a) corresponds to the $\boldsymbol{B}$-field flux Φ, the resistor whose electric resistance is R is equivalent to the element whose magnetic reluctance is $\mathcal{R}$ and the voltage generator that produces the electric potential difference V is the equivalent of the magnetomotive force generator that produces the magnetomotive force $\mathcal{F}$. In the remainder of the present chapter, magnetomotive force generator is considered to be ideal, i.e. it is able to produce a constant magnetomotive force at every flux intensity.

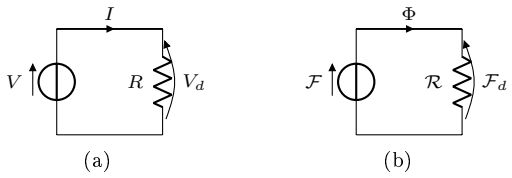

Figure 3.3: Lumped parameters diagram of elementary electric circuit (a) and magnetic circuit (b).

3.1.2 Magnetic circuit materials

An important aspect of magnetic circuits can be pointed out assuming the same hypotheses of previous section: a magnetic circuit with a number Z of discrete circuit segments, whose sections are S_k, lengths are l_k and permeabilities μ_k are assumed to be constant. If a further assumption is made, assuming that $\boldsymbol{B}$- and $\boldsymbol{H}$-fields have axial field lines for the whole circuit and $\boldsymbol{B}$-field is constant on each segment, simple relations between circuit flux Φ and $\boldsymbol{B}$-fields and between circuit magnetomotive force $\mathcal{F}$ and $\boldsymbol{H}$-field can be found:

$$\Phi = \int_S \boldsymbol{B} \cdot \boldsymbol{n}\, dS = B_k\, S_k = \Phi_k = B^*\, \overline{S} \qquad k = 1, 2, \ldots, Z \tag{3.29}$$

$$\mathcal{F} = N\mathcal{I} = \sum_{k=1}^{Z} \int_{l_k} \boldsymbol{H} \cdot \boldsymbol{u}_{\boldsymbol{l_k}}\, dl = \sum_{k=1}^{Z} H\, l_k = \sum_{k=1}^{Z} \mathcal{F}_{d,\,k} \tag{3.30}$$

Where the classical definition of flux Φ is calculated on a generic surface S whose normal vector in direction of $\boldsymbol{B}$-field is $\boldsymbol{n}$ and the general expression of magnetic voltage drop is calculated with the projection of $\boldsymbol{H}$-field on unit vector $\boldsymbol{u}_{l_k}$, tangent to circuit axis in k-th segment. Defining circuit mean section $\overline{S}$, it is possible to find a magnetic field modulus value B^* which gives circuit flux Φ.

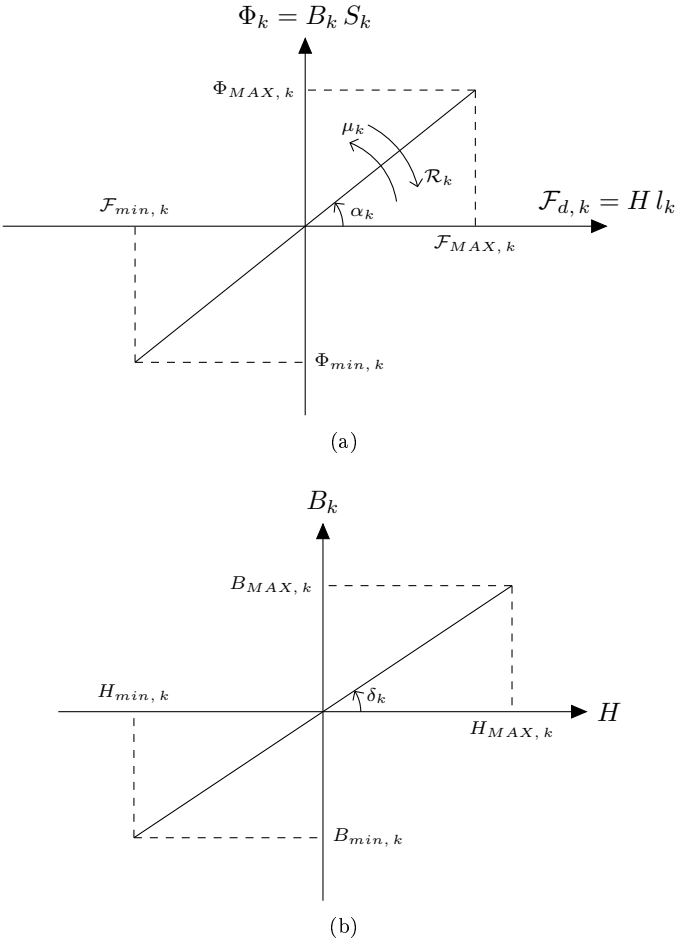

Figure 3.4: Magnet circuit k-th segment $\Phi - \mathcal{F}$ curve (a) and correspondent linear material magnetization curve (b).

The relation between flux Φ and each segment's magnetic voltage drop $\mathcal{F}_{d,\,k}$ is given by Hopkinson's law and is linear:

$$\mathcal{F}_{d,\,k} = \Phi\, \mathcal{R}_k = \Phi_k\, \mathcal{R}_k \qquad\qquad k = 1, 2, \ldots, Z \tag{3.31}$$

it is shown in a $\Phi - \mathcal{F}$ diagram in figure 3.4(a). Straight line's constant slope is clearly affected by reluctance $\mathcal{R}_k$:

$$\frac{\Phi_k}{\mathcal{F}_{d,\,k}} = \frac{1}{\mathcal{R}_k} = \frac{\mu_k S_k}{l_k} = \frac{d\Phi_k}{d\mathcal{F}_{d,\,k}} = \tan\alpha_k \tag{3.32}$$

The line shown in figure is limited to a segment. Maximum (minimum) magnetomotive force $\mathcal{F}_{MAX}$ ($\mathcal{F}_{min}$) is limited, once number of coil turns N is fixed, by the maximum (minimum) current $\mathcal{I}$ that can flow through the coil (see figure 3.2), thus maximum (minimum) magnetic voltage drop $\mathcal{F}_{MAX,\,k}$ ($\mathcal{F}_{min,\,k}$) in k-th segment is limited as well, as the sum of magnetic voltage drops has to be equal to magnetomotive force $\mathcal{F}$ (equation 3.30). Corresponding maximum (minimum) k-th segment flux $\Phi_{MAX,\,k}$ ($\Phi_{min,\,k}$) would be:

$$\Phi_{MAX,\,k} = \mu_k \frac{\mathcal{F}_{MAX,\,k}}{l_k} S_k = \mu_k\, H_{MAX,\,k}\, S_k \tag{3.33}$$

$$\Phi_{min,\,k} = \mu_k \frac{\mathcal{F}_{min,\,k}}{l_k} S_k = \mu_k\, H_{min,\,k}\, S_k \tag{3.34}$$

Where maximum (minimum) $\boldsymbol{H}$-field intensity $H_{MAX,\,k}$ ($H_{min,\,k}$) corresponds to $\mathcal{F}_{MAX,\,k}$ ($\mathcal{F}_{min,\,k}$). Since magnetic flux Φ has to have a unique value for all segments, it is limited by maximum (minimum) flux that can be reached in a critical section:

$$\Phi_{MAX} = \min_{1\leq k\leq Z} \Phi_{MAX,\,k} \tag{3.35}$$

$$\Phi_{min} = \max_{1\leq k\leq Z} \Phi_{min,\,k} \tag{3.36}$$

$$\Phi_{min} \leq \Phi \leq \Phi_{MAX} \tag{3.37}$$

Thus for k-th segment $\Phi - \mathcal{F}$ curve extreme points in first quadrant $(\mathcal{F}_{MAX,\,k}, \Phi_{MAX,\,k})$ and third quadrant $(\mathcal{F}_{min,\,k}, \Phi_{min,\,k})$ are set. Material magnetization curve underlying graph in figure 3.4(a) can easily be obtained with equations 3.29 and 3.30. The resulting material magnetization curve, shown in figure 3.4(b), is then linear and the material is usually defined as magnetically linear material. Vacuum, for example, is magnetically linear. Linearity is due to the hypothesis of constant relative magnetic permeability $\mu_{r,\,k}$ and then constant absolute magnetic permeability $\mu_k = \mu_0\,\mu_{r,\,k}$. This leads to a magnetization curve with constant slope:

$$\frac{B_k}{H} = \mu_k = \frac{dB_k}{dH} = \tan\delta_k \tag{3.38}$$

However, ferromagnetic materials are usually employed to build magnetic circuits, whose typical magnetization curve is shown in figure 3.5(a). In the present chapter, ferromagnetic materials magnetization curves are assumed to be symmetric. Due to Weiss domains rigidity, they clearly feature a non linear, hysteretic behaviour, where relative and absolute magnetic permeabilities are not constant. Indeed, permeabilities and **B**-field intensities have a non linear dependence on applied **H**-magnetic fields intensities and depend on magnetization histories of materials. General equation 3.2, relating $\boldsymbol{B_k}$ and $\boldsymbol{H}$, still holds, although a variable permeability μ_k must be considered:

$$\frac{dB_k}{dH} = \tan\delta_k = \mu_k(H,\ k\text{-th magnetization history}) \tag{3.39}$$

B_k and H intensities in figure 3.5(a) are usually limited by material positive and negative magnetic saturation which is discussed below. When material is not magnetized it is at the origin of the $B-H$ plane in figure 3.5(a). When a positive field intensity H is applied, the central curve in first quadrant is followed according to the arrow (first magnetization curve), until a field value $H_{MAX,\,k}$ is reached, leading to maximum positive intensity of material magnetization and to $\boldsymbol{B}$-field intensity $B_{MAX,\,k}$, called positive saturation induction. Any increase of $\boldsymbol{H}$ field intensity beyond $H_{MAX,\,k}$ would not increase magnetization intensity, already at its maximum value, while would increase $\boldsymbol{B}$-field intensity due to enclosed current increase, thus magnetization curve would follow a straight line whose slope is μ_0. When $\boldsymbol{H}$ field intensity is decreased from positive saturation to zero, the uppermost curve starting from first quadrant is followed (demagnetization curve). B decreases to $B_{r,\,k}$ (called positive remanence) but does not reach zero, due to magnetic domains rigidity which gives residual magnetization. When negative H is applied with increasing magnitude the curve enters the second quadrant in which $\boldsymbol{B}$ field reaches zero intensity for a negative value of H whose modulus is $H_{c,\,k}$ (negative coercivity). Material then reaches minimum (maximum negative) magnetization intensity for $H = H_{min,\,k} = -H_{MAX,\,k}$ (it is exactly the opposite of $H_{MAX,\,k}$ due to magnetization curve symmetry), reaching the corresponding $\boldsymbol{B}$-field intensity value $B_{min,\,k} = -B_{MAX,\,k}$, opposite to $B_{MAX,\,k}$ due to curve symmetry. As for positive saturation, a further decrease of $\boldsymbol{H}$-field intensity would not decrease magnetization intensity while would decrease $\boldsymbol{B}$-field intensity due to enclosed current decrease, following a straight line whose slope is μ_0. If $\boldsymbol{H}$-field intensity is increased from $H_{min,\,k}$ up to $H_{MAX,\,k}$, lowermost curve (magnetization curve) is followed with similar phenomena: for $H = 0$, there is a negative $\boldsymbol{B}$-field intensity in the material $-B_{r\,k}$ (negative remanence, the opposite of positive remanence due to curve symmetry) due to magnetic domains rigidity, and B_k remains negative until a certain positive value of H is reached. This value corresponds to positive coercivity $H_{c,\,k}$, the opposite of negative coercivity due to curve symmetry. When H returns to $H_{MAX,\,k}$ again, material returns to $(H_{MAX,\,k}, B_{MAX,\,k})$ point, tracing a closed and symmetric curve which represents the hysteresis cycle. It is clear that magnetic behaviour cannot be considered globally linear although a linear $B-H$ curve can be assumed locally, in a neighbourhood of a certain value of H and for a specific magnetization history.

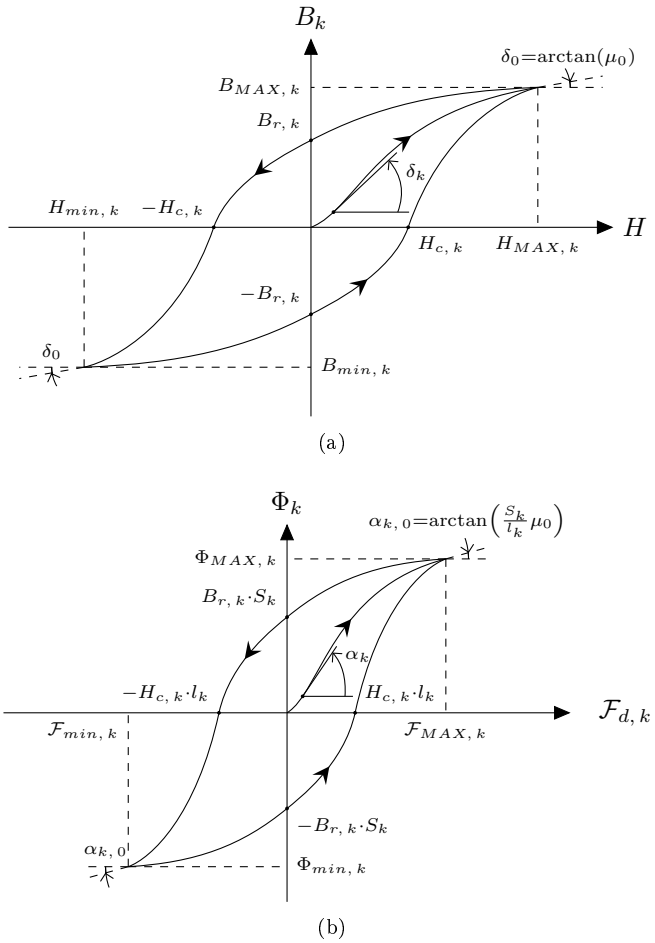

Figure 3.5: Ferromagnetic material magnetization curve (a) and corresponding $\Phi - \mathcal{F}$ curve for k-th segment of magnetic circuit (b).

Equations 3.29 and 3.30 allow to consider k-th segment $\Phi - \mathcal{F}$ curve when it is made of ferromagnetic material. The result is shown in figure 3.5(b): non linear, hysteretic behaviour is transposed to magnetic circuit segment. As a consequence, $\Phi - \mathcal{F}$ curve becomes non linear, dependent on magnetization history and, due to magnetic domains rigidity, it is now able to access to second and fourth quadrant, that were not reached with the linear curve in figure 3.4(a). Thus following the uppermost (lowermost) curve, flux remains at positive (negative) value $B_{r,\,k}\,S_k$ ($-B_{r,\,k}\,S_k$) with no magnetic voltage drop, it is possible to have positive (negative) flux Φ_k with negative (positive) magnetic voltage drop $\mathcal{F}_{d,\,k}$ in the second (fourth) quadrant, and flux reaches zero with the negative (positive) magnetic voltage drop $-H_{c,\,k}\,l_k$ ($H_{c,\,k}\,l_k$). Clearly, due to segment's variable permeability μ_k (3.39), its reluctance $\mathcal{R}_k$ must be variable as well:

$$\frac{d\Phi_k}{d\mathcal{F}_{d,\,k}} = \tan\alpha_k = \frac{1}{\mathcal{R}_k} = \frac{S_k}{l_k}\,\mu_k(H,\ k\text{-th magnetization history}) \tag{3.40}$$

And angle between magnetization curve and H axis beyond (below) maximum positive (negative) material magnetization is $\alpha_{k,\,0}$. Obviously, the discussion and limitations on magnetic flux given in equations 3.33-3.37 have to account for non linearity and hysteretic behaviour of absolute permeability μ_k.
Another remark about ideal magnetomotive force generators can be done using the $\Phi - \mathcal{F}$ plane. It is clear that such a generator is represented, by definition, by a vertical line in the $\Phi - \mathcal{F}$ plane and thus has a constant and null reluctance according to equation 3.40.

3.1.3 Magnetic components networks

It is possible to evaluate magnetic circuit parameters for more complex networks exploiting the formal analogy with electric circuits. Indeed all the laws of electrotechnics for tensions and currents can be transposed for their magnetic counterparts, respectively magnetomotive forces and fluxes, under equivalent hypotheses.
Kirchhoff's laws, for example, are transposed to magnetomotive forces and fluxes given the hypothesis of instantaneous propagation of magnetic signals. The law for magnetic fluxes is obtained considering equation 3.6 for $\boldsymbol{B}$ field, i.e. $\boldsymbol{B}$ flux through a closed, simply connected surface A is null. Considering a surface A including a finite segment of the circuit with no nodes, conservation of flux Φ along the segment, at any time t, is obtained. If the same fundamental equation is applied with a surface including a node of the circuit with N concurrent segments, conservation of flux in the node is obtained, i.e. the sum of N_i fluxes $\Phi_{i,k}$ incoming to the node equals the sum of N_o fluxes $\Phi_{o,k}$ outgoing from the node, or the algebraic sum of the N fluxes Φ_k is null at any time t:

$$\sum_{k=1}^{N_i} \Phi_{i,k} = \sum_{k=1}^{N_o} \Phi_{o,k} \quad \Longleftrightarrow \quad \sum_{k=1}^{N} \Phi_k = 0 \qquad \forall\, t \tag{3.41}$$

Since the equation is homogeneous, incoming or outgoing fluxes with respect to the node can equally be taken as positive.
Magnetic voltages direction must follow indications given in section 3.1.1, i.e. for a generator, flux direction is given according to direction of enclosed current, magnetomotive force direction is concordant with flux. For circuit segments, magnetic voltage drops direction must be opposite to direction of flux crossing the segment. In case no generator is present on the segment, an arbitrary direction for the flux can be chosen. The equivalent of Kirchhoff's voltage law is obtained considering a generic loop in the magnetic circuit as a streamtube, to which Hopkinson's law can be applied, in the version of equation 3.16. Discrete variations of circuit physical parameters must be considered, i.e. there is a number Z_d of discrete segments, with lengths l_k, constant permeabilities μ_k and constant sections S_k. Different fluxes Φ_k are considered as well, as in general the loop can contain nodes, in which case flux law 3.41 applies. A number Z_g of magnetomotive force generators, producing magnetomotive forces $\mathcal{F}_{g,k}$, is considered. Total magnetomotive force $\mathcal{F}$ is clearly the algebraic sum of single magnetomotive forces, with respect to an arbitrary positive direction:

$$\oint_l H dl = i = \sum_{k=1}^{Z_g} \mathcal{I}_k = \sum_{k=1}^{Z_g} \mathcal{F}_{g,k} = \mathcal{F} = \oint_l \frac{\Phi}{\int_S \mu dS} dl = \sum_{k=1}^{Z_d} \Phi_k \frac{l_k}{\mu_k S_k} = \sum_{k=1}^{Z_d} \Phi_k \mathcal{R}_k = \sum_{k=1}^{Z_d} \mathcal{F}_{d,k} = \mathcal{F}_d \tag{3.42}$$

Thus the algebraic sum of magnetomotive forces $\mathcal{F}$ equals the sum of the Z_d magnetic voltage drops $\mathcal{F}_{d,k} = \Phi_k \mathcal{R}_k$. These drops are clearly always negative. In other words, algebraic sum of the Z magnetic voltage drops and magnetomotive forces $\mathcal{F}_k$ in the same closed loop is zero at any moment t:

$$\sum_{k=1}^{Z_g} \mathcal{F}_{g,k} = \sum_{k=1}^{Z_d} \mathcal{F}_{d,k} \quad \Longleftrightarrow \quad \sum_{k=1}^{Z} \mathcal{F}_k = 0 \qquad \forall\, t \tag{3.43}$$

Again, since the equation is homogeneous, positive direction for magnetomotive forces can be decided to be both clockwise or anticlockwise. As for electric networks, topology laws assure that flux law 3.41 and magnetic voltage law 3.43 provide enough independent equations to solve any magnetic network, i.e. it is possible to find fluxes and magnetic voltages for every discrete element.

3.1.3.1 Series magnetic circuit

A few magnetic circuits will be solved, considering their lumped parameters models and the corresponding schematic representations, to describe some aspects which are peculiar with respect to electrical circuits. The physical diagram in figure 3.6(a) represents a circuit with two components in series (called series magnetic circuit in the remainder of the chapter).
The resolution is based on lumped parameter model shown in figure 3.6(b) and formally similar to the commmonly adopted procedure for the equivalent electric circuit. Applying Hopkinson's law 3.21 magnetic voltage drops $\mathcal{F}_1$ and $\mathcal{F}_2$ can be found:

$$\mathcal{F}_1 = \mathcal{R}_1 \Phi \tag{3.44}$$

$$\mathcal{F}_2 = \mathcal{R}_2 \Phi \tag{3.45}$$

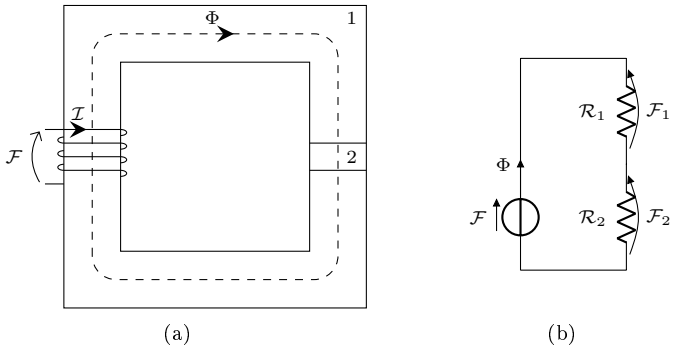

Figure 3.6: Series magnetic circuit physical diagram (a) and schematic (b). Regions 1 and 2 in physical diagram are identified by the black solid line.

Applying magnetic voltage law 3.43 to the only loop, circuit equivalent reluctance $\mathcal{R}_{eq}$ and flux Φ can be found:

$$\mathcal{F} = \mathcal{F}_1 + \mathcal{F}_2 = \mathcal{R}_1\Phi + \mathcal{R}_2\Phi = (\mathcal{R}_1 + \mathcal{R}_2)\Phi \tag{3.46}$$

$$\Phi = \frac{\mathcal{F}}{\mathcal{R}_1 + \mathcal{R}_2} = \frac{\mathcal{F}}{\mathcal{R}_{eq}} \tag{3.47}$$

$$\mathcal{R}_{eq} = \mathcal{R}_1 + \mathcal{R}_2 \tag{3.48}$$

Obviously, in case the number of components is $Z > 2$ Hopkinson's law is applied:

$$\mathcal{F}_k = \mathcal{R}_k\Phi \qquad\qquad k = 1, 2, \ldots, Z \tag{3.49}$$

And the above mentioned laws apply to give a similar result:

$$\mathcal{F} = \sum_{k=1}^{Z} \mathcal{F}_k = \sum_{k=1}^{Z} \mathcal{R}_k\Phi = \Phi \sum_{k=1}^{Z} \mathcal{R}_k \tag{3.50}$$

$$\Phi = \frac{\mathcal{F}}{\sum_{k=1}^{Z} \mathcal{R}_k} = \frac{\mathcal{F}}{\mathcal{R}_{eq}} \tag{3.51}$$

$$\mathcal{R}_{eq} = \sum_{k=1}^{Z} \mathcal{R}_k \tag{3.52}$$

The same equations were obtained during discussion of Hopkinson's law (3.22 and 3.23).
As a first example a series circuit with two linear magnetic materials is considered. Regions 1 and 2 have different relative magnetic permeabilities $\mu_{r\,1}$ and $\mu_{r\,2}$ and different lengths l_1 and l_2, respectively and thus different reluctances $\mathcal{R}_1$ and $\mathcal{R}_2$, respectively (equation 3.20). Thus in the $\Phi - \mathcal{F}$ plane in figure 3.7(a), due to equation 3.32, curves for region 1 and 2 have different slopes α_1 and α_2, respectively. The slope of the curve corresponding to equivalent component (*eq* curve in figure) can be obtained from equation 3.48:

$$\tan\alpha_{eq} = \frac{1}{\mathcal{R}_{eq}} = \frac{1}{\mathcal{R}_1 + \mathcal{R}_2} = \frac{\tan\alpha_1 \tan\alpha_2}{\tan\alpha_1 + \tan\alpha_2} \tag{3.53}$$

Or, correspondingly, *eq* curve points coordinates can be obtained by sum of the abscissae of points on curves 1 and 2 at a given ordinate. Resolution can also be obtained graphically on the $\Phi - \mathcal{F}$ plane, by intersecting *eq* curve with the ideal magnetomotive force generator curve. The only intersection point P represents circuit working point in the $\Phi - \mathcal{F}$ plane, and its ordinate indicates the flux running in the circuit. Working points of components 1 and 2 are identified as well as P_1 and P_2, respectively. Flux law 3.41 is found again, since ordinates of P_1 and P_2 are the same and equal to the ordinate of P, i.e. since there are no nodes the flux is conserved. Magnetic voltage law 3.43 is found again as well, since the sum of the abscissae of P_1 and P_2 gives exactly the abscissa of point P, i.e. magnetomotive force is equal and opposite to the sum of magnetic voltage drops.

Another example corresponding to diagrams in figure 3.6 can be considered. Its physical arrangement, dimensions and magnetomotive force $\mathcal{F}$ are the same as the linear material case. Now material in region 1 is ferromagnetic, instead of being a linear magnetic material, and material in region 2 is the same linear material as in the above case. As a result, $B-H$ curve for material 1 is not linear (see figure 3.5(a)), its relative magnetic permeability μ_{r1} is variable with $\boldsymbol{H}$-magnetic field intensity and both $B-H$ curve and μ_{r1} depend on magnetization history. In the example, material magnetization curve in the first quadrant is considered and positive coercivity H_c is neglected since it has a small value with respect to magnetomotive forces and magnetic voltage drops considered in these examples. Hence $\Phi-\mathcal{F}$ curve for material 1 is fixed (selected by choice of the magnetization curve) and non linear (equations 3.29 and 3.30). The curve has a slope α_1 which depends on flux, corresponding to a reluctance $\mathcal{R}_1$ variable with flux as well (equation 3.40).
Equations 3.44-3.47 for circuit analytic resolution are still valid, although in this case $\mathcal{R}_1$ is variable. Circuit $\Phi-\mathcal{F}$ curves can be drawn and are shown in figure 3.7(b) with a non linear curve 1. *eq* curve points and slope can be obtained as in the above case (equation 3.53), but due to non linearity of ferromagnetic material $\Phi-\mathcal{F}$ curve, *eq* curve slope and corresponding reluctance $\mathcal{R}_{eq}$ are now variable with magnetomotive force. Graphic method can be applied to identify working points P, P_1 and P_2. An important difference can be noticed between *eq* curves in figures 3.7(a) and 3.7(b). While for the former case *eq* curve grows linearly, due to material 1 linear $B-H$ curve, in the latter case circuit flux Φ grows with magnetomotive force with a decreasing slope, due to ferromagnetic material 1 $B-H$ curve which has a decreasing slope (which is the tangent of relative magnetic permeability μ_{r1}) as it approaches positive saturation. Thus in a series magnetic circuit, for a given magnetomotive force and under the same conditions, flux is limited by ferromagnetic material saturation, a sitation which is not common in electric circuits.

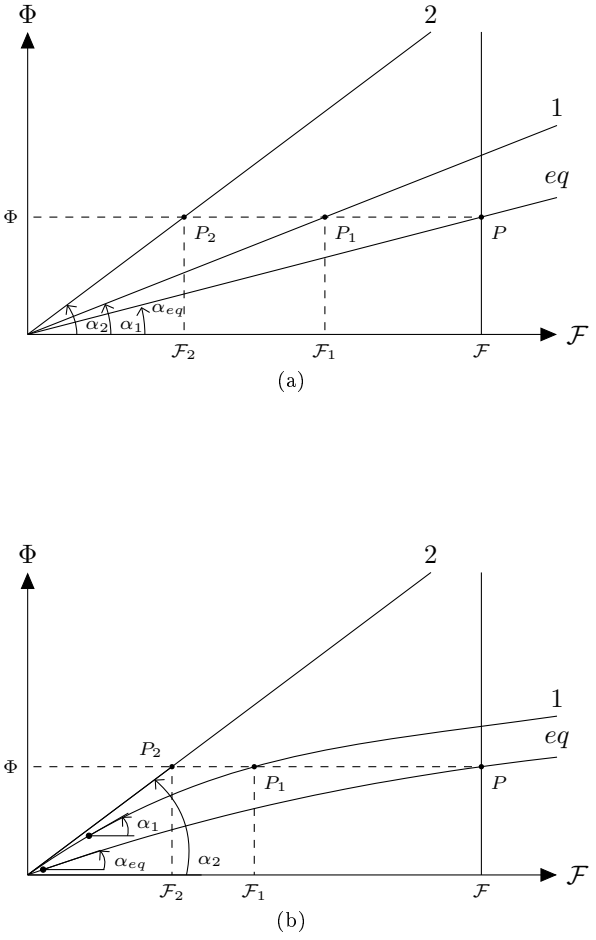

Figure 3.7: Series magnetic circuit $\Phi-\mathcal{F}$ curves for linear magnetic materials (a) and ferromagnetic material (b).

Region 2 still has a linear magnetic behaviour when it is made with vacuum or air. Since for common magnetic circuit applications air is found, the term air gap is used. The main difference with other magnetic materials lies in the order of magnitude of relative magnetic permeability. While for common materials it is $10^3 - 10^6$, for vacuum relative permeability is unitary. As a consequence, reluctance of the air gap $\mathcal{R}_g$ is much bigger than reluctance in region 2. Lengths of the air gap l_g are usually much inferior to lengths l_1 of region 1, so air gap reluctance is slightly reduced by this factor.

$$\mathcal{R}_1 = \frac{1}{\mu_0 \mu_{r1}} \frac{l_1}{S_1} \tag{3.54}$$

$$\mathcal{R}_g = \frac{1}{\mu_0 \cdot 1} \frac{l_g}{S'_g} \tag{3.55}$$

$$\mathcal{R}_g \gg \mathcal{R}_1 \tag{3.56}$$

Another important phenomenon affects air gaps reluctance $\mathcal{R}_g$. Typical behaviour of $\boldsymbol{B}$-magnetic field is shown in figure 3.8. Field lines crossing the air gap protrude outside of the magnetic circuit causing a fringing of magnetic field, thus while flux Φ running in the magnetic circuit is conserved, air gap cross section cannot be considered constant in any case. A number of empirical methods have been conceived to account for fringing of magnetic field in air gap reluctance, the most common of whom is used in equation 3.55. It consists in adopting a constant mean gap section S'_g with the same shape of the sections facing the gap and whose side lengths are given by physical sides lengths of sections facing the gap, incremented by gap length l_g. Thus if section S_g is circular with diameter d_g, mean section S'_g is:

$$S_g = \pi \frac{d_g^2}{4} \tag{3.57}$$

$$S'_g = \pi \frac{(d_g + l_g)^2}{4} \tag{3.58}$$

Clearly fringing of magnetic field tends to slightly reduce air gap reluctance, as air gap shortening does. However, the most important factor by far is given by unitary relative permeability, which increases reluctance. Analytic and graphic procedures can always be applied to circuits with air gaps, with the discussed modification.

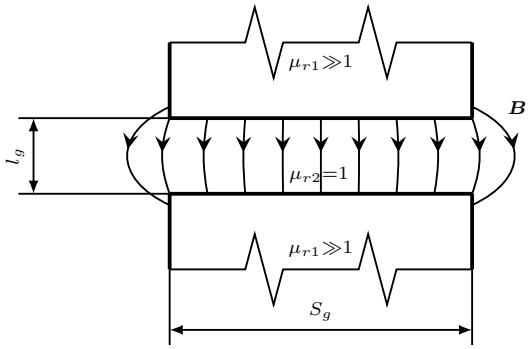

Figure 3.8: Fringing of magnetic field crossing an air gap.

A similar graphic procedure can be adopted for a magnetic circuit with three or more components in series. In such a case flux limitation at a certain magnetomotive force is still given by saturation of ferromagnetic material. In case there are more ferromagnetic sections with different relative magnetic permeabilities, sections and lengths, the most critical component is the one with the lowest $\Phi - \mathcal{F}$ curve. Obviously it tends to be the lowest when the corresponding $B - H$ curve is lowered, i.e. when reluctance is higher (equation 3.40). Features that tend to lower $B - H$ curve are:

1. low section S;
2. high length l;
3. low relative magnetic permeability μ_r in the considered $\boldsymbol{H}$-field intensity range.

Equations 3.29-3.30 then lead to $\Phi - \mathcal{F}$ curve, then for a given $B - H$ curve:

1. Decreasing section S lowers $\Phi - \mathcal{F}$ curve;
2. To decrease ferromagnetic section length l produces saturation for lower levels of magnetic voltage.

3.1.3.2 Parallel magnetic circuit

Similar analytic and graphic resolutions can be made for a magnetic circuit with two components in parallel. A possible physical diagram is shown in figure 3.9(a). Regions 0, 1 and 2 are identified by blue dashed lines. There are exactly two components in parallel if reluctance in region 0 is neglected and the corresponding schematic is shown in figure 3.9(b).
Hopkinson's law 3.21 is applied to find magnetic voltage drops:

$$\mathcal{F}_1 = \mathcal{R}_1\Phi_1 \tag{3.59}$$
$$\mathcal{F}_2 = \mathcal{R}_2\Phi_2 \tag{3.60}$$

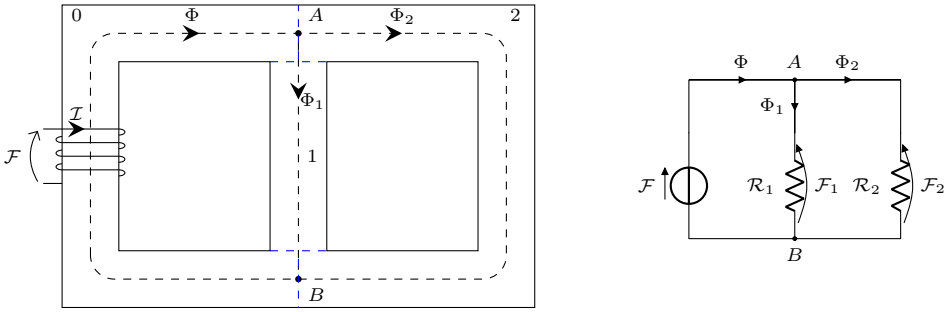

Figure 3.9: Parallel magnetic circuit physical diagram (a) and schematic (b). Regions 0, 1 and 2 in physical diagram are identified by blue dashed lines.

Magnetic voltage law 3.43 is applied to left loop and external loop:

$$\mathcal{F} = \mathcal{F}_1 \tag{3.61}$$
$$\mathcal{F} = \mathcal{F}_2 \tag{3.62}$$

And finally flux law 3.41 is applied to node A to find total flux Φ and circuit equivalent reluctance $\mathcal{R}_{eq}$:

$$\Phi = \Phi_1 + \Phi_2 \tag{3.63}$$
$$\Phi = \frac{\mathcal{F}_1}{\mathcal{R}_1} + \frac{\mathcal{F}_2}{\mathcal{R}_2} = \mathcal{F}\left(\frac{1}{\mathcal{R}_1} + \frac{1}{\mathcal{R}_2}\right) = \frac{\mathcal{F}}{\mathcal{R}_{eq}} \tag{3.64}$$
$$\mathcal{R}_{eq} = \left(\frac{1}{\mathcal{R}_1} + \frac{1}{\mathcal{R}_2}\right)^{-1} = \frac{\mathcal{R}_1\mathcal{R}_2}{\mathcal{R}_1 + \mathcal{R}_2} \tag{3.65}$$

If the number of components in parallel is $Z > 2$, Hopkinson's law is applied:

$$\mathcal{F} = \mathcal{F}_k = \mathcal{R}_k\Phi_k \qquad k = 1, 2, \ldots, Z \tag{3.66}$$

Then the same laws are applied to give:

$$\Phi = \sum_{k=1}^{Z} \Phi_k \tag{3.67}$$
$$\Phi = \sum_{k=1}^{Z} \frac{\mathcal{F}_k}{\mathcal{R}_k} = \mathcal{F}\sum_{k=1}^{Z} \frac{1}{\mathcal{R}_k} = \frac{\mathcal{F}}{\mathcal{R}_{eq}} \tag{3.68}$$
$$\mathcal{R}_{eq} = \left(\sum_{k=1}^{Z} \frac{1}{\mathcal{R}_k}\right)^{-1} \tag{3.69}$$

As for the series case, equations 3.59-3.65 can be applied regardless of the particular materials in the circuit. In particular, they can be applied with linear magnetic materials in regions 1 and 2 and with linear magnetic material in region 2 and ferromagnetic material in region 1. $\Phi - \mathcal{F}$ curves for both cases are represented in figure 3.10. In the former case in figure 3.10(a), regions 1 and 2 have again different relative magnetic permeabilities μ_{r1} and μ_{r2} and different legths l_1 and l_2, respectively and thus different reluctances $\mathcal{R}_1$ and $\mathcal{R}_2$, respectively. Hence $\Phi - \mathcal{F}$ curves for these regions have different slopes, α_1 and α_2 respectively. The slope of the curve of the equivalent component can be obtained from equation 3.65:

$$\tan \alpha_{eq} = \frac{1}{\mathcal{R}_{eq}} = \frac{\mathcal{R}_1 + \mathcal{R}_2}{\mathcal{R}_1 \mathcal{R}_2} = \tan \alpha_1 + \tan \alpha_2 \tag{3.70}$$

Or, correspondingly, *eq* curve points coordinates can be obtained by the sum of the ordinates of points on curves 1 and 2 at a given abscissa. Resolution can be obtained graphically as well, on $\Phi - \mathcal{F}$ plane, by intersecting *eq* curve with with the ideal magnetomotive force generator curve. The only intersection point P represents circuit working point, its ordinate indicates the total flux Φ running in circuit's left loop. Working points of components 1 and 2 can be identified as P_1 and P_2, respectively. Flux law 3.41 is found again, since the sum of the ordinates of P_1 and P_2 gives the ordinate of P, i.e. the algebraic sum of fluxes concurrent to node A is zero at any time. Magnetic voltage law 3.43 is found again as well, since the abscissae of points P_1, P_2 and P are the same, i.e. magnetomotive force is equal and opposite to magnetic voltage drops in components 1 and 2. The second case, as for the series circuit, considers the same physical arrangement, dimensions and magnetomotive force $\mathcal{F}$ as in the linear materials case. Now material in region 1 is ferromagnetic, and material in region 2 remains magnetically linear, as for the above parallel circuit case. Again, similar to homologous case for series circuit, for material 1 magnetization curve in the first quadrant is considered in $B - H$ plane, and positive coercivity H_c is neglected, since it is a small value with respect to magnetomotive forces and magnetic voltage drops under consideration. Thus $\Phi - \mathcal{F}$ curve for component 1 is non linear, with a variable slope α_1 and a variable reluctance $\mathcal{R}_1$. Relative magnetic permeability μ_{r1} is now variable with magnetomotive force. Equations 3.59-3.65 can always be applied, but now reluctance $\mathcal{R}_1$ is variable. $\Phi - \mathcal{F}$ curves can be drawn again and are shown in figure 3.10(b). *eq* curve points and slope can be obtained as for the linear materials case (equation 3.70) and its slope and corresponding reluctance $\mathcal{R}_{eq}$ are now variable with magnetomotive force. Graphic method can be applied to identify working points P_1, P_2 and P and it allows to notice the same phenomenon as for the series circuit. While for linear materials case *eq* curve grows linearly, with a ferromagnetic material in region 1, *eq* curve has a decreasing slope for increasing magnetomotive force. This is due to material 1 $B - H$ curve, which has a decreasing slope (which is the tangent of relative magnetic permeability μ_{r1}) as it approaches positive saturation. Thus in a parallel magnetic circuit, for a given magnetomotive force and under the same conditions, flux is limited by ferromagnetic material saturation, as for the series magnetic circuit.

A similar graphic procedure can be used for a magnetic circuit with three or more components in parallel. In such cases flux limitation can still exist due to saturation of ferromagnetic material. In case there are two or more ferromagnetic sections with different geometries and relative permeabilities, the same conclusion for series circuits can be drawn.

3.1.3.3 Magnetic circuit with ferromagnetic segment as a magnetomotive force generator

A segment of ferromagnetic material can be used as a magnetomotive force generator, in this case graphical method employed in electrotechnics can be used to find magnetic circuit working point. Circuit schematic is shown in figure 3.11(a), where ferromagnetic segment is represented with magnetomotive force generator symbol and the rest of the circuit is represented as an equivalent reluctance $\mathcal{R}_{eq}$. The ferromagnetic segment is not exactly a magnetomotive force generator and thus its circuital variables have opposite signs, as for passive components.
Possible circuit working points A and B are located at intersections of components $\Phi - \mathcal{F}$ curves and are shown in figure 3.11(b). Their location in second and fourth quadrant implies that ferromagnetic segment flux and magnetic voltage have opposite signs, thus it works as a generator. Equivalent reluctance flux and magnetic voltage drop have the same signs in second and fourth quadrant, thus the rest of the circuit remains a passive load.

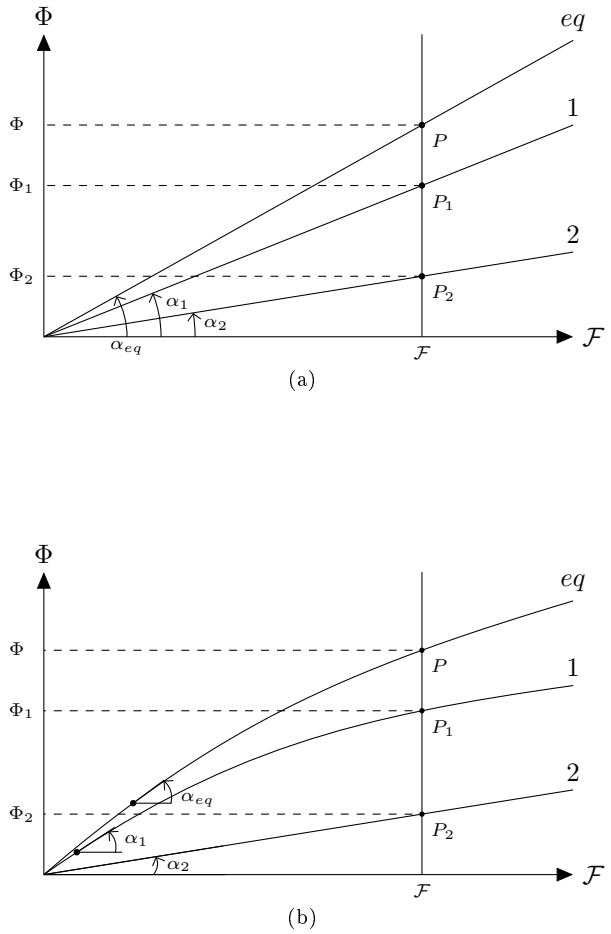

Figure 3.10: Parallel magnetic circuit $\Phi - \mathcal{F}$ curves for linear magnetic materials (a) and ferromagnetic material (b).

Prior to circuit insertion, ferromagnetic material is assumed to be at negative coercivity point C in the $\Phi - \mathcal{F}$ plane and circuit load is at the origin O. When ferromagnetic segment is inserted, magnetic load assumes magnetic voltage drop modulus equal to point C magnetic voltage. It produces a positive magnetic flux which is received by ferromagnetic segment, which, according to its $\Phi - \mathcal{F}$ curve, imposes a different value for magnetic voltage. Its absolute value is assumed by load magnetic voltage drop, which, according to its $\Phi - \mathcal{F}$ curve, leads to a different magnetic flux value. This transient phase, represented by the magnified spiral in figure, ends when load and generator reach the same value of magnetic flux Φ_A and equal modulus for magnetic voltage and magnetic voltage drop $\mathcal{F}_A$. Working point B cannot be reached because ferromagnetic segment is not able to get to first and third quadrant without absorbing energy.
Since ferromagnetic material magnetization curve may not be known in detail, an approximate working point A' is found by adopting an approximate magnetization curve, shown in blue in figure 3.11(c). The approximate curve simply consists in joining positive remanence and negative coercivity points in the second quadrant. Thus true flux and magnetomotive force are approximated:

$$\mathcal{F}_A \simeq \mathcal{F}_{A'} = -H_c \cdot l \tag{3.71}$$

$$\Phi_A \simeq \Phi_{A'} \tag{3.72}$$

$$0 \leq \Phi_{A'} < B_r \cdot S \tag{3.73}$$

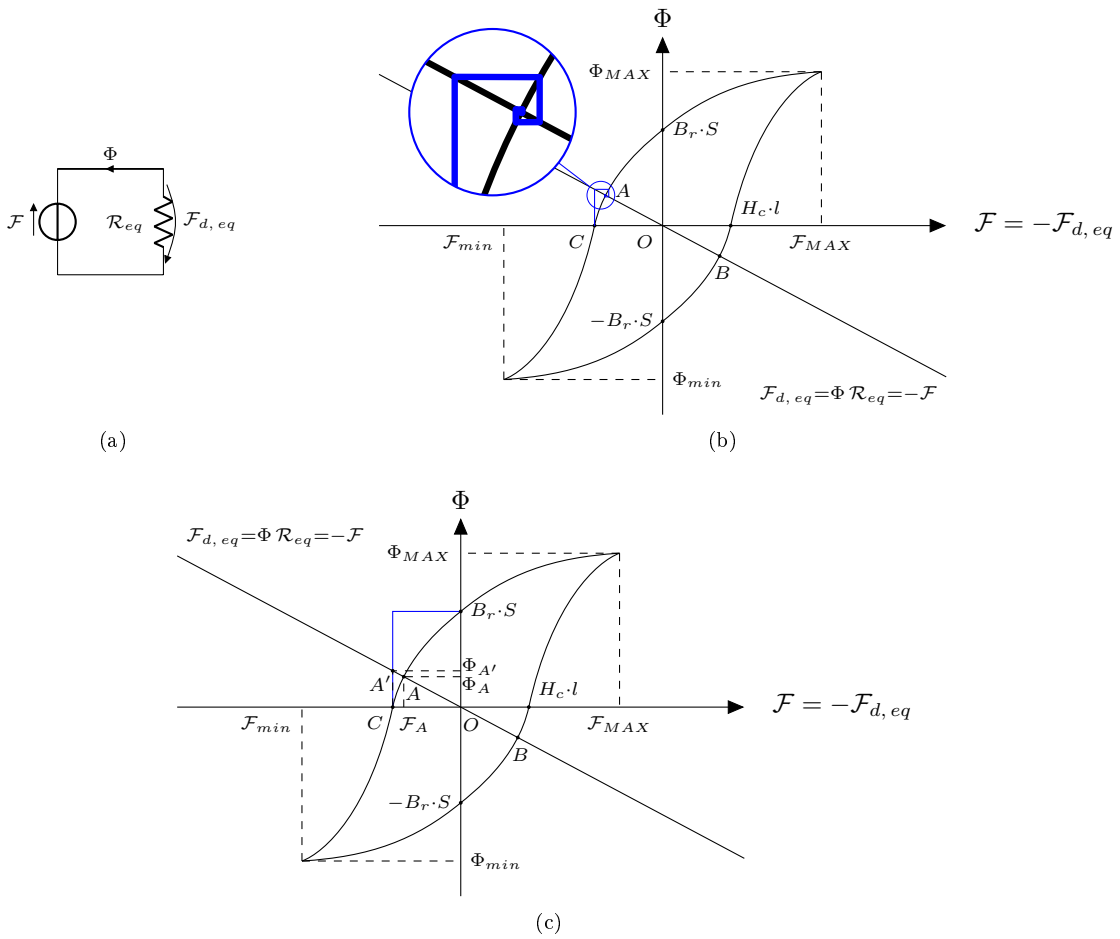

Figure 3.11: Magnetic circuit with ferromagnetic segment as a generator schematic (a), correspondent $\Phi - \mathcal{F}$ diagram (b) and ferromagnetic curve approximation (c).

If approximate intersection A' were on the horizontal blue segment, clearly approximate working point coordinates would be:

$$\mathcal{F}_A \simeq \mathcal{F}_{A'} \tag{3.74}$$

$$0 \geq \mathcal{F}_{A'} > -H_c \cdot l \tag{3.75}$$

$$\Phi_A \simeq \Phi_{A'} = B_r \cdot S \tag{3.76}$$

Approximate working point coordinates can be found with the following formulas, that work on both cases mentioned above:

$$\Phi_{A'} = \min\left\{\frac{|-H_c|\,l}{\mathcal{R}_{eq}}\,,\, B_r\,S\right\} \geq 0 \tag{3.77}$$

$$\mathcal{F}_{A'} = \max\left\{-H_c\,l\,,\, -\mathcal{R}_{eq}\,B_r\,S\right\} \leq 0 \tag{3.78}$$

3.1.4 Energy balance

3.1.4.1 Magnetic circuit with single magnetomotive force generator

The simple magnetic circuit in figure 3.12(b) is thought to be driven by the electric circuit in figure 3.12(a). In the electric schematic, the coil generating magnetic flux Φ, in which the current $\mathcal{I}$ flows, is represented as an inductor whose coefficient of self-inductance is L. In general, magnetic circuit reluctance can be imagined as the equivalent magnetic reluctance resulting from a network of magnetic segments.
In the electric schematic, resistance R represents coil wire resistance and resistance R_e represents resistance encountered by eddy currents. Time-varying voltage V is given by voltage generator on left side.

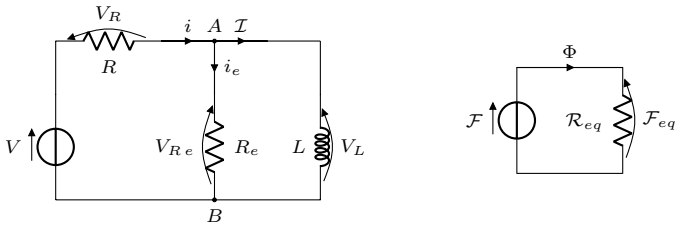

(a) (b)

Figure 3.12: Electric schematic (a) and magnetic schematic (b) for magnetic circuit with one magnetomotive force generator.

Kirchhoff's current law applied to node A allows to write immediately:

$$i = i_e + \mathcal{I} \tag{3.79}$$

And Kirchhoff's voltage law applied to all three loops allows to find remaining equations:

$$V = R\,i + L\,\frac{d\mathcal{I}}{dt} \tag{3.80}$$

$$V = R\,i + R_e\,i_e \tag{3.81}$$

$$L\,\frac{d\mathcal{I}}{dt} = R_e\,i_e = V - R\,i \tag{3.82}$$

Equations 3.80 and 3.81 are multiplied by current modulus i:

$$Vi = R\,i^2 + L\,\frac{d\mathcal{I}}{dt}\,(i_e + \mathcal{I}) \tag{3.83}$$

$$Vi = R\,i^2 + R_e\,i_e\,(i_e + \mathcal{I}) \tag{3.84}$$

$$\tag{3.85}$$

And are then summed to find total power balance 3.88:

$$2Vi = 2R\,i^2 + L\,\frac{d\mathcal{I}}{dt}\,\mathcal{I} + R_e\,i_e^2 + L\,\frac{d\mathcal{I}}{dt}\,i_e + R_e\,i_e\,\mathcal{I} \tag{3.86}$$

$$L\,\frac{d\mathcal{I}}{dt}\,i_e + R_e\,i_e\,\mathcal{I} = L\,\frac{d\mathcal{I}}{dt}\,(i_e + \mathcal{I}) = (V - R\,i)\,i \tag{3.87}$$

$$Vi = R\,i^2 + L\,\frac{d\mathcal{I}}{dt}\,\mathcal{I} + R_e\,i_e^2 \tag{3.88}$$

Thus power Vi given by voltage generator is dissipated as Joule effect by resistors representing coil wire, $R\,i^2$, and eddy currents, $R_e\,i_e^2$, and is spent by the inductor, $L\,\frac{d\mathcal{I}}{dt}\,\mathcal{I}$, to vary magnetic flux enclosed with electric circuit in time. In the remainder of present section, only magnetic flux included in magnetic circuit will be considered. The remaining magnetic flux, self-induced and enclosed by the electric circuit, is neglected. Energy balance is immediately obtained by integrating power balance 3.88 in the generic time interval $[t_0,\, t_1]$:

$$\int_{t_0}^{t_1} Vi\,dt = \int_{t_0}^{t_1} R\,i^2\,dt + \int_{t_0}^{t_1} L\,\frac{d\mathcal{I}}{dt}\,\mathcal{I}\,dt + \int_{t_0}^{t_1} R_e\,i_e^2\,dt \tag{3.89}$$

Some conclusions can be drawn on power P_L absorbed by inductor recalling the classical definition of self-inductance coefficient L:

$$\Phi_e = N\,\Phi = L\,\mathcal{I} \tag{3.90}$$

Where Φ_e is the magnetic flux, included in magnetic circuit, enclosed in electric circuit. Application of Hopkinson's law allows to find the expression of coefficient L for the present case:

$$\Phi = \frac{\mathcal{F}}{\mathcal{R}_{eq}} = \frac{N\mathcal{I}}{\mathcal{R}_{eq}} \tag{3.91}$$

$$\Phi_e = N\Phi = \frac{N^2}{\mathcal{R}_{eq}}\mathcal{I} = L\mathcal{I} \tag{3.92}$$

$$L = \frac{N^2}{\mathcal{R}_{eq}} \tag{3.93}$$

Absorbed power P_L can then be written as a function of magnetic circuit variables:

$$V_L = L\frac{d\mathcal{I}}{dt} = \frac{d(L\mathcal{I})}{dt} = \frac{d\Phi_e}{dt} = N\frac{d\Phi}{dt} \tag{3.94}$$

$$P_L = L\frac{d\mathcal{I}}{dt}\,\mathcal{I} = N\frac{d\Phi}{dt}\,\mathcal{I} = \mathcal{F}\,\frac{d\Phi}{dt} = \mathcal{R}\Phi\frac{d\Phi}{dt} \tag{3.95}$$

In case the magnetic circuit is made with a linear magnetic material, reluctance is constant in the $\Phi - \mathcal{F}$ plane and power $P_L = P_{L,\,lin}$ can be written as:

$$P_{L,\,lin} = \mathcal{R}_{eq}\Phi\frac{d\Phi}{dt} = \frac{d}{dt}\left(\frac{1}{2}\mathcal{R}_{eq}\Phi^2\right) = \frac{d}{dt}\left(\frac{1}{2}\Phi\mathcal{F}\right) = \frac{d}{dt}\left(\frac{1}{2}\frac{\mathcal{F}^2}{\mathcal{R}_{eq}}\right) \tag{3.96}$$

The argument of time derivative can be interpreted as the energy E_f of the magnetic field stored inside the magnetic circuit. Recalling general equation 3.8, which represents the definition of magnetomotive force, and the definition of $\boldsymbol{B}$-field flux on a generic surface S whose normal unit vector in direction of magnetic flux is $\boldsymbol{n}$:

$$\Phi = \int_S \boldsymbol{B}\cdot\boldsymbol{n}\,dS \tag{3.97}$$

Quantity $\frac{1}{2}\Phi\mathcal{F}$ can be written as:

$$\begin{aligned}\frac{1}{2}\mathcal{F}\Phi &= \frac{1}{2}\oint_c \boldsymbol{H}\cdot\boldsymbol{u_c}\,dl\cdot\int_S \boldsymbol{B}\cdot\boldsymbol{n}\,dS = \int_S\oint_c \frac{1}{2}\boldsymbol{B}\cdot\boldsymbol{H}\,\boldsymbol{u_c}\cdot\boldsymbol{n}\,dl dS = \\ &= \int_V \frac{1}{2}\boldsymbol{B}\cdot\boldsymbol{H}\,dV = \int_V \mathcal{E}\,dV = E_f\end{aligned} \tag{3.98}$$

Where dV is the infinitesimal volume identified by dl and dS and $\mathcal{E}$ is the classical expression of magnetic field energy per unit volume. Thus power absorbed by the inductor is spent to change energy of magnetic field stored inside the magnetic circuit. Classical expression of magnetic field energy can be found as well:

$$E_f = \frac{1}{2}\int_S \boldsymbol{B}\cdot\boldsymbol{n}\,dS\cdot\oint_c \boldsymbol{H}\cdot\boldsymbol{u_c}\,dl = \frac{1}{2}\,\frac{L\mathcal{I}}{N}\cdot N\mathcal{I} = \frac{1}{2}L\mathcal{I}^2 \tag{3.99}$$

Energy variation $\Delta E_{L,\,lin}$ due to absorbed power in linear case is easily found:

$$\begin{aligned}\Delta E_{L,\,lin} &= \int_{t_0}^{t_1} P_{L,\,lin}\,dt = \int_{t_0}^{t_1}\mathcal{R}_{eq}\Phi\frac{d\Phi}{dt}\,dt = \int_{\Phi_0}^{\Phi_1}\mathcal{R}_{eq}\Phi d\Phi = \\ &= \int_{\Phi_0}^{\Phi_1}\mathcal{F}d\Phi = \int_{\frac{1}{2}\mathcal{R}_{eq}\Phi_0^2}^{\frac{1}{2}\mathcal{R}_{eq}\Phi_1^2} d\left(\frac{1}{2}\mathcal{R}_{eq}\Phi^2\right) = \frac{1}{2}\mathcal{R}_{eq}\left[\Phi^2\right]_{\Phi_0}^{\Phi_1} = E_{f\,1} - E_{f\,0} = \Delta E_f\end{aligned} \tag{3.100}$$

Hence area between the portion of $\Phi - \mathcal{F}$ curve corresponding to states 0 and 1 and Φ axis represents energy absorbed by the magnetic circuit to vary magnetic field intensity. Geometrical interpretation of equation 3.100, supposing states 1 and 0 in the first quadrant of $\Phi - \mathcal{F}$ curve and $\Phi_1 > \Phi_0$, is presented in figure 3.13. The area bounded by the $0-1$ segment and the Φ axis (which represents absorbed energy) can be obtained as the

difference of areas of triangles bounded by Φ axis and the segments between origin and points 1 and 0 (which represent magnetic field energy of correspondent states). Thus absorbed energy is positive and magnetic field energy is increased. The opposite transformation (from state 1 to state 0) implies a negative bounded area (and a reduction of magnetic field energy) since the area of the triangle whose vertex is 0 is positive and minor than the positive area of the triangle whose vertex is 1 (and magnetic energy of state 0 is minor than energy of state 1). It is important to notice that the transformation starting from state 0, reaching 1 and then again zero implies that absorbed energy is completely returned to electric circuit and magnetic energy returns to the original value. Symmetrical conclusions can be drawn with states in the third quadrant.
For linear magnetic materials energetic deductions given above can be made with areas bounded by material curve and $\mathcal{F}$ axis as well, as can be deduced geometrically and analytically:

$$\begin{aligned}\Delta E_{L,\,lin} &= \int_{\Phi_0}^{\Phi_1} \mathcal{R}_{eq}\Phi d\Phi = \int_{\mathcal{R}_{eq}\Phi_0}^{\mathcal{R}_{eq}\Phi_1} \Phi d(\mathcal{R}_{eq}\Phi) = \int_{\mathcal{F}_0}^{\mathcal{F}_1} \Phi d\mathcal{F} = \\ &= \int_{\mathcal{F}_0}^{\mathcal{F}_1} \frac{\mathcal{F}}{\mathcal{R}_{eq}} d\mathcal{F} = \int_{\frac{1}{2}\frac{\mathcal{F}_0^2}{\mathcal{R}_{eq}}}^{\frac{1}{2}\frac{\mathcal{F}_1^2}{\mathcal{R}_{eq}}} d\left(\frac{1}{2}\frac{\mathcal{F}^2}{\mathcal{R}_{eq}}\right) = \frac{1}{2}\frac{\left[\mathcal{F}^2\right]_{\mathcal{F}_0}^{\mathcal{F}_1}}{\mathcal{R}_{eq}} = \Delta E_f \end{aligned} \tag{3.101}$$

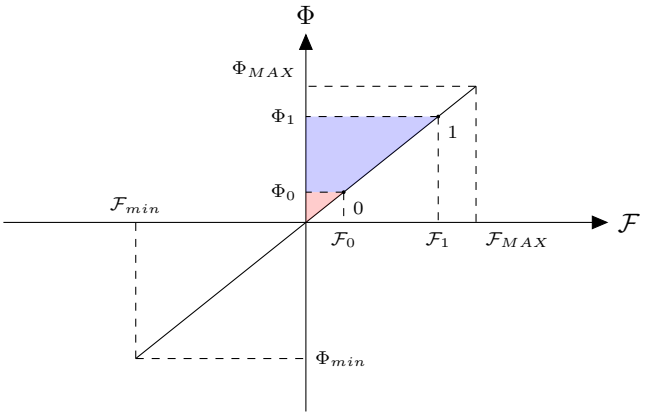

Figure 3.13: Geometrical interpretation of magnetic circuit energetic exchanges. Coloured areas represent energy absorbed or released by magnetic circuit. Red area represents energy of the magnetic field in state 0 and blue area represents energy absorbed (released) in transformation $0 \to 1$ ($1 \to 0$).

If magnetic circuit material is not magnetically linear, as for ferromagnetic materials, reluctance is not constant on $\Phi - \mathcal{F}$ plane and absorbed power P_L becomes:

$$P_L = \mathcal{R}_{eq}\Phi\frac{d\Phi}{dt} = \frac{d}{dt}\left(\frac{1}{2}\mathcal{R}_{eq}\Phi^2\right) - \frac{1}{2}\Phi^2\frac{d\mathcal{R}_{eq}}{dt} = \frac{dE_f}{dt} + P_\mu \tag{3.102}$$

The term P_μ represents power spent to change the relative magnetic permeability of the material, and thus its reluctance. Variation of relative permeability requires external work to modify Weiss domains which becomes heat. If relative permeability is increased, reluctance is decreased and thus P_μ is positive, representing absorbed power.
Energy ΔE_L absorbed by the material in the generic time interval $[t_0,\, t_1]$ becomes:

$$\begin{aligned}\Delta E_L &= \int_{t_0}^{t_1} P_L\, dt = \int_{t_0}^{t_1} \mathcal{R}_{eq}\Phi\frac{d\Phi}{dt}dt = \int_{\Phi_0}^{\Phi_1} \mathcal{F} d\Phi = \int_{t_0}^{t_1} \frac{d}{dt}\left(\frac{1}{2}\mathcal{R}_{eq}\Phi^2\right) dt + \\ &+ \int_{t_0}^{t_1} -\frac{1}{2}\Phi^2\frac{d\mathcal{R}_{eq}}{dt}\, dt = \int_{t_0}^{t_1} \frac{dE_f}{dt}\, dt + \int_{t_0}^{t_1} P_\mu\, dt = \Delta E_f + E_\mu \end{aligned} \tag{3.103}$$

Thus absorbed energy ΔE_L is spent in part to change magnetic field energy (term ΔE_f) and in part to change material relative permeability (term E_μ). Geometrically, absorbed energy ΔE_L is represented by area bounded by $\Phi - \mathcal{F}$ curve and the Φ axis only and not by the area between $\Phi - \mathcal{F}$ curve and the $\mathcal{F}$ axis as well, as is for

linear materials.
An important consequence of ferromagnetic materials $\Phi - \mathcal{F}$ curve can be presented with equation 3.103 and is shown in figure 3.14. Considering transformation from state 0 to state 1, shown in figure 3.14(a), equation 3.103 can be applied. The result is:

$$\Delta E_{L\,0\to1} = \Delta E_{f\,0\to1} + E_{\mu\,0\to1} \tag{3.104}$$

Positive contributions to $\Delta E_{L\,0\to1}$ are shown in blue, and negative ones in red. The same can be done with transformation from 1 to 0 (figure 3.14(b)), which does not follow the same curve on $\Phi - \mathcal{F}$ plane due to Weiss domains rigidity. Energy balance equation is:

$$\Delta E_{L\,1\to0} = \Delta E_{f\,1\to0} + E_{\mu\,1\to0} \tag{3.105}$$

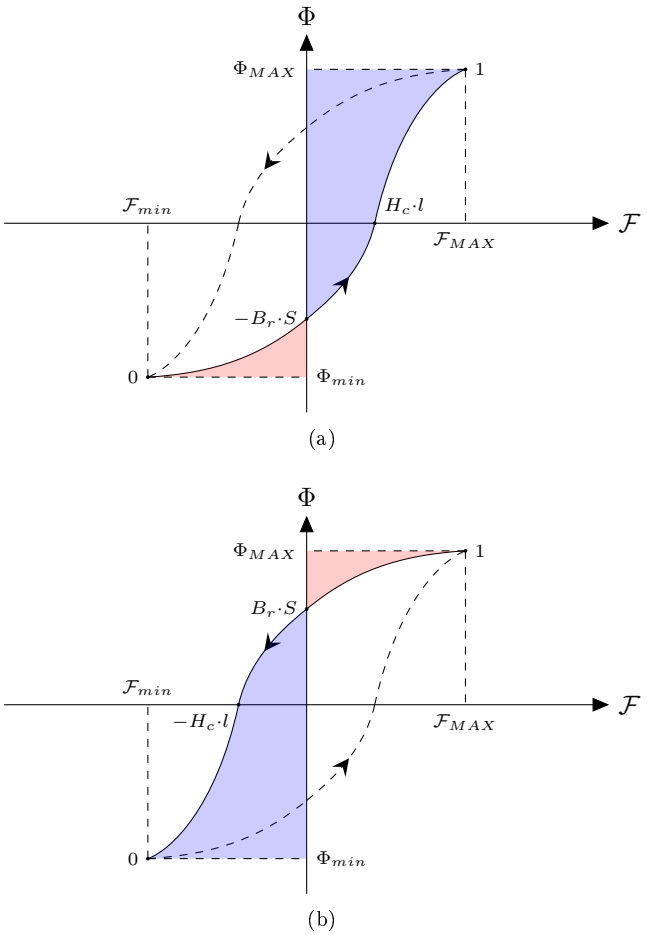

Figure 3.14: Energy absorbed by ferromagnetic material during a symmetric hysteresis cycle. Positive (absorbed) energy is coloured in blue and negative (released) energy is coloured in red.

From figures it can be deduced that the area enclosed by the cycle $0 \to 1 \to 0$, which represents energy absorbed by material $\Delta E_{L\,0\to1\to0}$, is positive. Variation of magnetic field energy for the whole cycle $\Delta E_{f\,0\to1\to0}$ must be null, given its geometrical meaning. Thus it must be:

$$\begin{aligned} \Delta E_{L\,0\to1} + \Delta E_{L\,1\to0} &= \Delta E_{L\,0\to1\to0} = \Delta E_{f\,0\to1} + \Delta E_{f\,1\to0} + E_{\mu\,0\to1} + E_{\mu\,1\to0} = \\ &= \Delta E_{f\,0\to1\to0} + E_{\mu\,0\to1\to0} = E_{\mu\,0\to1\to0} > 0 \end{aligned} \tag{3.106}$$

Hence the amount of energy absorbed during a complete hysteresis cycle, $E_{\mu\,0\to1\to0}$, is spent to modify Weiss domains to vary material relative permeability and thus its reluctance.
E_μ losses are inevitable with ferromagnetic materials, but these are able to concentrate most of the magnetic field inside the circuit with few magnetic flux leakages, so that the fundamental hypothesis made above in the

discussion is satisfied. Thus they provide high levels of $\boldsymbol{B}$-magnetic field intensity for a given input field intensity H.
Magnetic circuit considered in the present section may consist of a network of N magnetic components with $N_{fe} \leq N$ ferromagnetic components.
If the N components are in series (as in schematic in figure 3.6(b) with N components), given the analysis in section 3.1.3, energy and power balances are easily found:

$$E_f = \frac{1}{2}\Phi^2 \sum_{k=1}^{N} \mathcal{R}_k = \sum_{k=1}^{N} \frac{1}{2}\mathcal{R}_k \Phi^2 = \sum_{k=1}^{N} E_{f\,k} \tag{3.107}$$

$$P_\mu = -\frac{1}{2}\Phi^2 \frac{d}{dt} \sum_{k=1}^{N_{fe}} \mathcal{R}_k = \sum_{k=1}^{N_{fe}} -\frac{1}{2}\Phi^2 \frac{d\mathcal{R}_k}{dt} = \sum_{k=1}^{N_{fe}} P_{\mu\,k} \tag{3.108}$$

$$P_L = \frac{d}{dt} \sum_{k=1}^{N} E_{f\,k} + \sum_{k=1}^{N_{fe}} P_{\mu\,k} = \sum_{k=1}^{N} \frac{dE_{f\,k}}{dt} + \sum_{k=1}^{N_{fe}} P_{\mu\,k} \tag{3.109}$$

$$\begin{aligned} \Delta E_L &= \int_{t_0}^{t_1} \frac{dE_f}{dt}\,dt + \int_{t_0}^{t_1} P_\mu\,dt = \int_{t_0}^{t_1} \sum_{k=1}^{N} \frac{dE_{f\,k}}{dt}\,dt + \int_{t_0}^{t_1} \sum_{k=1}^{N_{fe}} P_{\mu\,k}\,dt = \\ &= \sum_{k=1}^{N} \int_{t_0}^{t_1} \frac{dE_{f\,k}}{dt}\,dt + \sum_{k=1}^{N_{fe}} \int_{t_0}^{t_1} P_{\mu\,k}\,dt = \sum_{k=1}^{N} \Delta E_{f\,k} + \sum_{k=1}^{N_{fe}} E_{\mu\,k} \end{aligned} \tag{3.110}$$

If the N components are in parallel (as for schematic in figure 3.9(b) with N components), with the help of the analysis in section 3.1.3, total field energy E_f and total power P_μ spent to vary reluctances are found:

$$E_f = \frac{1}{2}\frac{\mathcal{F}^2}{\mathcal{R}_{eq}} = \frac{1}{2}\mathcal{F}^2 \sum_{k=1}^{N} \frac{1}{\mathcal{R}_k} = \sum_{k=1}^{N} \frac{1}{2}\frac{\mathcal{F}^2}{\mathcal{R}_k} = \sum_{k=1}^{N} E_{f\,k} \tag{3.111}$$

$$\begin{aligned} P_\mu &= -\frac{1}{2}\frac{\mathcal{F}^2}{\mathcal{R}_{eq}^2}\frac{d\mathcal{R}_{eq}}{dt} = \frac{1}{2}\mathcal{F}^2 \frac{d}{dt}\frac{1}{\mathcal{R}_{eq}} = \\ &= \frac{1}{2}\mathcal{F}^2 \frac{d}{dt} \sum_{k=1}^{N_{fe}} \frac{1}{\mathcal{R}_k} = \sum_{k=1}^{N_{fe}} \frac{1}{2}\mathcal{F}^2 \frac{d}{dt}\frac{1}{\mathcal{R}_k} = \sum_{k=1}^{N_{fe}} P_{\mu\,k} \end{aligned} \tag{3.112}$$

Given the similarity with homologous equations 3.107 and 3.108 for series case, power and energy balance equations are identical to series case equations 3.109 and 3.110. Thus, for any magnetic circuit topology, power balance 3.102 applies to sum of absorbed powers in the N components P_L, time derivative of the sum of magnetic fields energies in N components E_f and sum of powers required to change reluctances in N_{fe} ferromagnetic components P_μ. Energy balance 3.103 applies to the sum of absorbed energies in N components, ΔE_L, to sum of fields energies variations in N components, ΔE_f, and to sum of energies spent to change reluctances in N_{fe} ferromagnetic components, E_μ.

3.1.4.2 Magnetic circuit with two magnetomotive force generators

In case there are two magnetomotive force generators as in figure 3.15(b), their currents $\mathcal{I}_1$ and $\mathcal{I}_2$ are driven by the similar electric circuits 1 and 2, shown in figure 3.15(a), coupled by mutual inductance whose coefficient is M. Circuit resolution is similar to previous case, currents balance is obtained with Kirchhoff's current law applied to nodes A_1 and A_2:

$$i_1 = i_{e\,1} + \mathcal{I}_1 \tag{3.113}$$

$$i_2 = i_{e\,2} + \mathcal{I}_2 \tag{3.114}$$

As for previous case, self- and mutually induced magnetic fluxes enclosed by electric circuit are assumed to be given only by fluxes included in the magnetic circuit, other enclosed fluxes are neglected. Thus fluxes $\Phi_{e\,1}$ and $\Phi_{e\,2}$, enclosed respectively with circuit 1 and 2, are given by magnetic flux Φ multiplied by respective inductors' number of turns N_1 and N_2, and are proportional to currents $\mathcal{I}_1$ and $\mathcal{I}_2$:

$$\Phi_{e\,1} = N_1\Phi = L_1\mathcal{I}_1 + M\mathcal{I}_2 \tag{3.115}$$

$$\Phi_{e\,2} = N_2\Phi = L_2\mathcal{I}_2 + M\mathcal{I}_1 \tag{3.116}$$

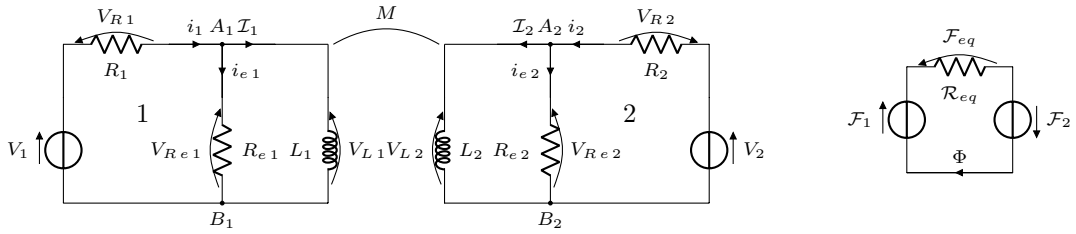

Figure 3.15: Electric schematic (a) and magnetic schematic (b) for magnetic circuit with two magnetomotive force generators.

Since self- and mutual induction coefficients are constant in time, enclosed fluxes time derivatives are:

$$\frac{d\Phi_{e\,1}}{dt} = N_1\frac{d\Phi}{dt} = L_1\frac{d\mathcal{I}_1}{dt} + M\frac{d\mathcal{I}_2}{dt} \tag{3.117}$$

$$\frac{d\Phi_{e\,2}}{dt} = N_2\frac{d\Phi}{dt} = L_2\frac{d\mathcal{I}_2}{dt} + M\frac{d\mathcal{I}_1}{dt} \tag{3.118}$$

Expressions of induction coefficients L_1, L_2 and M are easily obtained from Hopkinson's law:

$$\Phi = \frac{\mathcal{F}_1 + \mathcal{F}_2}{\mathcal{R}_{eq}} = \frac{N_1\mathcal{I}_1 + N_2\mathcal{I}_2}{\mathcal{R}_{eq}} \tag{3.119}$$

$$\Phi_{e\,1} = N_1\Phi = \frac{N_1^2}{\mathcal{R}_{eq}}\mathcal{I}_1 + \frac{N_1\,N_2}{\mathcal{R}_{eq}}\mathcal{I}_2 \tag{3.120}$$

$$\Phi_{e\,2} = N_2\Phi = \frac{N_1\,N_2}{\mathcal{R}_{eq}}\mathcal{I}_1 + \frac{N_2^2}{\mathcal{R}_{eq}}\mathcal{I}_2 \tag{3.121}$$

Thus their expressions are:

$$L_1 = \frac{N_1^2}{\mathcal{R}_{eq}} \tag{3.122}$$

$$L_2 = \frac{N_2^2}{\mathcal{R}_{eq}} \tag{3.123}$$

$$M = \frac{N_1\,N_2}{\mathcal{R}_{eq}} \tag{3.124}$$

Focusing on circuit 1 (leftmost circuit in figure 3.15(a)), Kirchhoff's voltage law applied to all three loops leads to:

$$V_1 = R_1 i_1 + R_{e\,1} i_{e\,1} \tag{3.125}$$

$$V_1 = R_1 i_1 + \frac{d\Phi_{e\,1}}{dt} = R_1 i_1 + L_1\frac{d\mathcal{I}_1}{dt} + M\frac{d\mathcal{I}_2}{dt} \tag{3.126}$$

$$R_{e\,1} i_{e\,1} = \frac{d\Phi_{e\,1}}{dt} = L_1\frac{d\mathcal{I}_1}{dt} + M\frac{d\mathcal{I}_2}{dt} \tag{3.127}$$

Multiplying equations 3.125 and 3.126 by current i_1, power equations are obtained:

$$V_1 i_1 = R_1 i_1^2 + R_{e\,1} i_{e\,1}(\mathcal{I}_1 + i_{e\,1}) \tag{3.128}$$

$$V_1 i_1 = R_1 i_1^2 + L_1\frac{d\mathcal{I}_1}{dt}(\mathcal{I}_1 + i_{e\,1}) + M\frac{d\mathcal{I}_2}{dt}(\mathcal{I}_1 + i_{e\,1}) \tag{3.129}$$

The sum of the above equations leads to:

$$2V_1 i_1 = 2R_1 i_1^2 + R_{e\,1} i_{e\,1}^2 + R_{e\,1} i_{e\,1}\mathcal{I}_1 + L_1\frac{d\mathcal{I}_1}{dt} i_{e\,1} + L_1\frac{d\mathcal{I}_1}{dt}\mathcal{I}_1 + M\frac{d\mathcal{I}_2}{dt}\mathcal{I}_1 + M\frac{d\mathcal{I}_2}{dt} i_{e\,1} \tag{3.130}$$

Recalling voltage equation 3.127 the final form of combined power equations for circuit 1 is obtained:

$$\begin{aligned} R_{e\,1} i_{e\,1} \mathcal{I}_1 + L_1 \frac{d\mathcal{I}_1}{dt} i_{e\,1} + M \frac{d\mathcal{I}_2}{dt} i_{e\,1} &= R_{e\,1} i_{e\,1} (\mathcal{I}_1 + i_{e\,1}) = R_{e\,1} i_{e\,1} i_1 = (V_1 - R_1 i_1) i_1 \qquad (3.131) \\ V_1 i_1 &= R_1 i_1^2 + R_{e\,1} i_{e\,1}^2 + L_1 \frac{d\mathcal{I}_1}{dt} \mathcal{I}_1 + M \frac{d\mathcal{I}_2}{dt} \mathcal{I}_1 = \\ &= R_1 i_1^2 + R_{e\,1} i_{e\,1}^2 + \mathcal{I}_1 \left(L_1 \frac{d\mathcal{I}_1}{dt} + M \frac{d\mathcal{I}_2}{dt} \right) = \\ &= R_1 i_1^2 + R_{e\,1} i_{e\,1}^2 + \mathcal{I}_1 \frac{d\Phi_{e\,1}}{dt} \qquad (3.132) \end{aligned}$$

Thus entering power $V_1 i_1$ is spent as Joule effect in the resistors, $R_1 i_1^2$ and $R_{e\,1} i_{e\,1}^2$, and is spent by the inductor to vary enclosed magnetic flux $\Phi_{e\,1}$ in time. The term $\mathcal{I}_1 \frac{d\Phi_{e\,1}}{dt}$ can be written with magnetic circuit parameters:

$$\mathcal{I}_1 \frac{d\Phi_{e\,1}}{dt} = N_1 \mathcal{I}_1 \frac{d\Phi}{dt} = \mathcal{F}_1 \frac{d\Phi}{dt} \qquad (3.133)$$

The same steps can be followed for circuit 2 (rightmost circuit in figure 3.15(a)), leading to correspondent power equation:

$$\begin{aligned} V_2 i_2 &= R_2 i_2^2 + R_{e\,2} i_{e\,2}^2 + \mathcal{I}_2 \left(L_2 \frac{d\mathcal{I}_2}{dt} + M \frac{d\mathcal{I}_1}{dt} \right) = \\ &= R_2 i_2^2 + R_{e\,2} i_{e\,2}^2 + \mathcal{I}_2 \frac{d\Phi_{e\,2}}{dt} \qquad (3.134) \end{aligned}$$

With the same meaning of terms, corresponding to powers that are injected in circuit 2 or spent by its components. The term $\mathcal{I}_2 \frac{d\Phi_{e\,2}}{dt}$ can be written in terms of magnetic circuit parameters as well:

$$\mathcal{I}_2 \frac{d\Phi_{e\,2}}{dt} = N_2 \mathcal{I}_2 \frac{d\Phi}{dt} = \mathcal{F}_2 \frac{d\Phi}{dt} \qquad (3.135)$$

Total power equation is the sum of power equations for circuit 1, 3.132, and 2, 3.134:

$$V_1 i_1 + V_2 i_2 = R_1 i_1^2 + R_2 i_2^2 + R_{e\,1} i_{e\,1}^2 + R_{e\,2} i_{e\,2}^2 + (\mathcal{F}_1 + \mathcal{F}_2) \frac{d\Phi}{dt} \qquad (3.136)$$

In which the sum $(\mathcal{F}_1 + \mathcal{F}_2)$ can be interpreted as a total magnetomotive force $\mathcal{F}$ given by a single magnetomotive force generator, thus the same conclusions of previous section for a single magnetomotive force generator can be drawn. Energy balance is found by integrating power balance equation in the generic time interval $[t_0,\, t_1]$:

$$\begin{aligned} \int_{t_0}^{t_1} V_1 i_1 \, dt + \int_{t_0}^{t_1} V_2 i_2 \, dt &= \int_{t_0}^{t_1} R_1 i_1^2 \, dt + \int_{t_0}^{t_1} R_2 i_2^2 \, dt + \int_{t_0}^{t_1} R_{e\,1} i_{e\,1}^2 \, dt + \int_{t_0}^{t_1} R_{e\,2} i_{e\,2}^2 \, dt + \\ &\quad + \int_{\Phi_0}^{\Phi_1} (\mathcal{F}_1 + \mathcal{F}_2) \, d\Phi \qquad (3.137) \end{aligned}$$

Thus entering energy $\int_{t_0}^{t_1} V_1 i_1 \, dt + \int_{t_0}^{t_1} V_2 i_2 \, dt$ is dissipated by Joule effect, $\int_{t_0}^{t_1} R_1 i_1^2 \, dt + \int_{t_0}^{t_1} R_2 i_2^2 \, dt + \int_{t_0}^{t_1} R_{e\,1} i_{e\,1}^2 \, dt + \int_{t_0}^{t_1} R_{e\,2} i_{e\,2}^2 \, dt$ and spent to vary magnetic circuit flux, $\int_{\Phi_0}^{\Phi_1} (\mathcal{F}_1 + \mathcal{F}_2) \, d\Phi$.
Expression for total field energy E_f is modified with respect to previous case with a single magnetomotive force generator. Total $\boldsymbol{B}$-magnetic field is now given by the sum $\boldsymbol{B} = \boldsymbol{B_1} + \boldsymbol{B_2}$, and total $\boldsymbol{H}$-magnetic field is given by the sum $\boldsymbol{H} = \boldsymbol{H_1} + \boldsymbol{H_2}$. Thus field energy becomes:

$$\begin{aligned} E_f &= \frac{1}{2} \Phi (\mathcal{F}_1 + \mathcal{F}_2) = \frac{1}{2} \int_S (\boldsymbol{B_1} + \boldsymbol{B_2}) \cdot \boldsymbol{n} \, dS \cdot \oint_c (\boldsymbol{H_1} + \boldsymbol{H_2}) \cdot \boldsymbol{u_c} \, dl = \\ &= \int_S \oint_c \frac{1}{2} (\boldsymbol{B_1} + \boldsymbol{B_2}) \cdot (\boldsymbol{H_1} + \boldsymbol{H_2}) \, \boldsymbol{u_c} \cdot \boldsymbol{n} \, dl dS = \\ &= \int_S \oint_c \frac{1}{2} \boldsymbol{B_1} \cdot \boldsymbol{H_1} \, \boldsymbol{u_c} \cdot \boldsymbol{n} \, dl dS + \int_S \oint_c \frac{1}{2} \boldsymbol{B_2} \cdot \boldsymbol{H_2} \, \boldsymbol{u_c} \cdot \boldsymbol{n} \, dl dS + \int_S \oint_c \frac{1}{2} (\boldsymbol{B_1} \cdot \boldsymbol{H_2} + \boldsymbol{B_2} \cdot \boldsymbol{H_1}) \, \boldsymbol{u_c} \cdot \boldsymbol{n} \, dl dS = \\ &= \int_V \mathcal{E}_1 \, dV + \int_V \mathcal{E}_2 \, dV + \int_V \frac{1}{2} (\boldsymbol{B_1} \cdot \boldsymbol{H_2} + \boldsymbol{B_2} \cdot \boldsymbol{H_1}) \, dV \qquad (3.138) \end{aligned}$$

The first two terms on the last line represent energy of fields 1 and 2 when isolated, and their classical expressions are easily found:

$$\begin{aligned} E_{f\,1} &= \int_V \mathcal{E}_1\,dV = \frac{1}{2}\int_S \boldsymbol{B_1}\cdot\boldsymbol{n}\,dS\cdot\oint_c \boldsymbol{H_1}\cdot\boldsymbol{u_c}\,dl = \\ &= \frac{1}{2}\,\frac{\Phi_{e\,1}-M\mathcal{I}_2}{N_1}\cdot N_1\mathcal{I}_1 = \frac{1}{2}\,\frac{L_1\mathcal{I}_1}{N_1}\cdot N_1\mathcal{I}_1 = \frac{1}{2}\,L_1\mathcal{I}_1^2 \end{aligned} \tag{3.139}$$

$$\begin{aligned} E_{f\,2} &= \int_V \mathcal{E}_2\,dV = \frac{1}{2}\int_S \boldsymbol{B_2}\cdot\boldsymbol{n}\,dS\cdot\oint_c \boldsymbol{H_2}\cdot\boldsymbol{u_c}\,dl = \\ &= \frac{1}{2}\,\frac{\Phi_{e\,2}-M\mathcal{I}_1}{N_2}\cdot N_2\mathcal{I}_2 = \frac{1}{2}\,\frac{L_2\mathcal{I}_2}{N_2}\cdot N_2\mathcal{I}_2 = \frac{1}{2}\,L_2\mathcal{I}_2^2 \end{aligned} \tag{3.140}$$

The integrand in the last term on the last line is given by the sum of the two cross products. Thus the last integral can be split and the integrals of cross products can be calculated as previous terms:

$$\begin{aligned} \int_V \frac{1}{2}\boldsymbol{B_1}\cdot\boldsymbol{H_2}\,dV &= \frac{1}{2}\int_S \boldsymbol{B_1}\cdot\boldsymbol{n}\,dS\cdot\oint_c \boldsymbol{H_2}\cdot\boldsymbol{u_c}\,dl = \frac{1}{2}\,\frac{\Phi_{e\,1}-M\mathcal{I}_2}{N_1}\cdot N_2\mathcal{I}_2 = \\ &= \frac{1}{2}\,\frac{L_1\mathcal{I}_1}{N_1}\cdot N_2\mathcal{I}_2 = \frac{1}{2}\,\frac{N_1\mathcal{I}_1}{\mathcal{R}_{eq}}\cdot N_2\mathcal{I}_2 = \frac{1}{2}\,M\mathcal{I}_1\mathcal{I}_2 \end{aligned} \tag{3.141}$$

$$\begin{aligned} \int_V \frac{1}{2}\boldsymbol{B_2}\cdot\boldsymbol{H_1}\,dV &= \frac{1}{2}\int_S \boldsymbol{B_2}\cdot\boldsymbol{n}\,dS\cdot\oint_c \boldsymbol{H_1}\cdot\boldsymbol{u_c}\,dl = \frac{1}{2}\,\frac{\Phi_{e\,2}-M\mathcal{I}_1}{N_2}\cdot N_1\mathcal{I}_1 = \\ &= \frac{1}{2}\,\frac{L_2\mathcal{I}_2}{N_2}\cdot N_1\mathcal{I}_1 = \frac{1}{2}\,\frac{N_2\mathcal{I}_2}{\mathcal{R}_{eq}}\cdot N_1\mathcal{I}_1 = \frac{1}{2}\,M\mathcal{I}_1\mathcal{I}_2 \end{aligned} \tag{3.142}$$

$$\begin{aligned} \int_V \frac{1}{2}(\boldsymbol{B_1}\cdot\boldsymbol{H_2}+\boldsymbol{B_2}\cdot\boldsymbol{H_1})\,dV &= \int_V \frac{1}{\mu}\boldsymbol{B_1}\cdot\boldsymbol{B_2}\,dV = \int_V \mu\boldsymbol{H_1}\cdot\boldsymbol{H_2}\,dV = \\ &= \int_V \mathcal{E}_{12}\,dV = M\mathcal{I}_1\mathcal{I}_2 = E_{f\,12} \end{aligned} \tag{3.143}$$

Hence the last term on last line of equation 3.138 represents the classical interaction energy between the fields. Finally, total field energy E_f can be written as:

$$E_f = \int_V \mathcal{E}_1\,dV + \int_V \mathcal{E}_2\,dV + \int_V \mathcal{E}_{12}\,dV = E_{f\,1} + E_{f\,2} + E_{f\,12} = \frac{1}{2}\,L_1\mathcal{I}_1^2 + \frac{1}{2}\,L_2\mathcal{I}_2^2 + M\mathcal{I}_1\mathcal{I}_2 \tag{3.144}$$

3.1.4.3 Magnetic circuit with N_g magnetomotive force generators

In case the magnetic circuit has $N_g > 2$ magnetomotive force generators, its equations are given by generalization of the previous case with two generators. Hopkinson's law is immediately written:

$$\Phi = \frac{\sum_{j=1}^{N_g}\mathcal{F}_j}{\mathcal{R}_{eq}} = \frac{\sum_{j=1}^{N_g}N_j\mathcal{I}_j}{\mathcal{R}_{eq}} \tag{3.145}$$

Where Φ is the total magnetic flux running in the magnetic circuit, N_j and $\mathcal{I}_j$ are respectively the number of turns and current running in the j-th generator. Magnetic flux $\Phi_{e\,j}$, enclosed with j-th electric circuit, is given by:

$$\Phi_{e\,j} = N_j\Phi = L_j\mathcal{I}_j + \sum_{\substack{k=1\\k\neq j}}^{N_g} M_{jk}\mathcal{I}_k \qquad\qquad j = 1, 2, \ldots, N_g \tag{3.146}$$

In the usual hypothesis that the flux enclosed with j-th electric circuit is given only by magnetic circuit and other enclosed fluxes are neglected. Enclosed flux time derivative is:

$$\frac{d\Phi_{e\,j}}{dt} = N_j\frac{d\Phi}{dt} = L_j\frac{d\mathcal{I}_j}{dt} + \sum_{\substack{k=1\\k\neq j}}^{N_g} M_{jk}\frac{d\mathcal{I}_k}{dt} \qquad\qquad j = 1, 2, \ldots, N_g \tag{3.147}$$

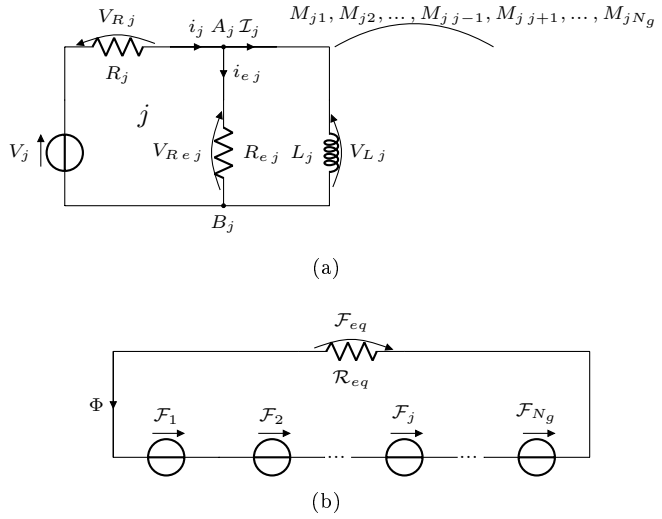

Figure 3.16: Electric schematic (a) and magnetic schematic (b) for magnetic circuit with N_g magnetomotive force generators.

Substitution of Hopkinson's law 3.145 in enclosed flux equation 3.146 leads to:

$$\Phi_{e\,j} = N_j \Phi = \frac{N_j}{\mathcal{R}_{eq}} \sum_{k=1}^{N_g} N_k \mathcal{I}_k = \frac{N_j^2}{\mathcal{R}_{eq}} \mathcal{I}_j + \sum_{\substack{k=1 \\ k \neq j}}^{N_g} \frac{N_k N_j}{\mathcal{R}_{eq}} \mathcal{I}_k \qquad j = 1, 2, \ldots, N_g \tag{3.148}$$

Thus expressions of self- and mutual induction coefficients are:

$$L_j = \frac{N_j^2}{\mathcal{R}_{eq}} \qquad j = 1, 2, \ldots, N_g \tag{3.149}$$

$$M_{jk} = M_{kj} = \frac{N_j N_k}{\mathcal{R}_{eq}} \qquad j, k = 1, 2, \ldots, N_g\,, \quad j \neq k \tag{3.150}$$

j-th electric circuit equations are similar to previous case for two generators:

$$i_j = i_{e\,j} + \mathcal{I}_j \tag{3.151}$$

$$V_j = R_j i_j + R_{e\,j} i_{e\,j} \tag{3.152}$$

$$V_j = R_j i_j + \frac{d\Phi_{e\,j}}{dt} = R_j i_j + L_j \frac{d\mathcal{I}_j}{dt} + \sum_{\substack{k=1 \\ k \neq j}}^{N_g} M_{jk} \frac{d\mathcal{I}_k}{dt} \tag{3.153}$$

$$R_{e\,j} i_{e\,j} = \frac{d\Phi_{e\,j}}{dt} = L_j \frac{d\mathcal{I}_j}{dt} + \sum_{\substack{k=1 \\ k \neq j}}^{N_g} M_{jk} \frac{d\mathcal{I}_k}{dt} \tag{3.154}$$

And power equation for j-th circuit is obtained in the same way:

$$\begin{aligned} V_j i_j &= R_j i_j^2 + R_{e\,j} i_{e\,j}^2 + \mathcal{I}_j \frac{d\Phi_{e\,j}}{dt} = R_j i_j^2 + R_{e\,j} i_{e\,j}^2 + \mathcal{F}_j \frac{d\Phi}{dt} = \\ &= R_j i_j^2 + R_{e\,j} i_{e\,j}^2 + \mathcal{I}_j \left(L_j \frac{d\mathcal{I}_j}{dt} + \sum_{\substack{k=1 \\ k \neq j}}^{N_g} M_{jk} \frac{d\mathcal{I}_k}{dt} \right) \end{aligned} \tag{3.155}$$

Energy equation for j-th circuit is obviously obtained by integration in the generic $[t_0,\, t_1]$ time interval:

$$\begin{aligned}\int_{t_0}^{t_1} V_j i_j\, dt &= \int_{t_0}^{t_1} R_j i_j^2\, dt + \int_{t_0}^{t_1} R_{e\,j} i_{e\,j}^2\, dt + \int_{t_0}^{t_1} \mathcal{F}_j \frac{d\Phi}{dt}\, dt = \\ &= \int_{t_0}^{t_1} R_j i_j^2\, dt + \int_{t_0}^{t_1} R_{e\,j} i_{e\,j}^2\, dt + \int_{\Phi_0}^{\Phi_1} \mathcal{F}_j\, d\Phi \end{aligned} \tag{3.156}$$

Where the meanings of terms in power and energy equations are the same as in the above cases. Total power equation is then obtained by summation of the N_g power equations:

$$\sum_{j=1}^{N_g} V_j i_j = \sum_{j=1}^{N_g} R_j i_j^2 + \sum_{j=1}^{N_g} R_{e\,j} i_{e\,j}^2 + \sum_{j=1}^{N_g} \mathcal{I}_j \frac{d\Phi_{e\,j}}{dt} = \sum_{j=1}^{N_g} R_j i_j^2 + \sum_{j=1}^{N_g} R_{e\,j} i_{e\,j}^2 + \sum_{j=1}^{N_g} \mathcal{F}_j \frac{d\Phi}{dt} \tag{3.157}$$

Total energy balance is found, as usual, by integration in the generic $[t_0,\, t_1]$ time interval:

$$\begin{aligned}\int_{t_0}^{t_1} \sum_{j=1}^{N_g} V_j i_j\, dt &= \int_{t_0}^{t_1} \sum_{j=1}^{N_g} R_j i_j^2\, dt + \int_{t_0}^{t_1} \sum_{j=1}^{N_g} R_{e\,j} i_{e\,j}^2\, dt + \int_{t_0}^{t_1} \sum_{j=1}^{N_g} \mathcal{F}_j \frac{d\Phi}{dt}\, dt = \\ &= \int_{t_0}^{t_1} \sum_{j=1}^{N_g} R_j i_j^2\, dt + \int_{t_0}^{t_1} \sum_{j=1}^{N_g} R_{e\,j} i_{e\,j}^2\, dt + \int_{\Phi_0}^{\Phi_1} \sum_{j=1}^{N_g} \mathcal{F}_j\, d\Phi \end{aligned} \tag{3.158}$$

Where integral and sum order in each term can be inverted:

$$\sum_{j=1}^{N_g} \int_{t_0}^{t_1} V_j i_j\, dt = \sum_{j=1}^{N_g} \int_{t_0}^{t_1} R_j i_j^2\, dt + \sum_{j=1}^{N_g} \int_{t_0}^{t_1} R_{e\,j} i_{e\,j}^2\, dt + \sum_{j=1}^{N_g} \int_{\Phi_0}^{\Phi_1} \mathcal{F}_j\, d\Phi \tag{3.159}$$

Thus entering energy (leftmost term) is the sum of energies given to each electric circuit. It is absorbed by resistors and dissipated as Joule effect (first and second term in right side) and by inductors and thus spent to vary magnetic flux (rightmost term).
Total field energy E_f is affected by contributions of N_g $\boldsymbol{B}$-magnetic fields and N_g $\boldsymbol{H}$-magnetic fields:

$$\begin{aligned} E_f &= \frac{1}{2}\Phi \sum_{j=1}^{N_g} \mathcal{F}_j = \frac{1}{2} \int_S \sum_{j=1}^{N_g} \boldsymbol{B_j} \cdot \boldsymbol{n}\, dS \cdot \oint_c \sum_{k=1}^{N_g} \boldsymbol{H_k} \cdot \boldsymbol{u_c}\, dl = \int_S \oint_c \frac{1}{2} \sum_{j=1}^{N_g} \sum_{k=1}^{N_g} \boldsymbol{B_j} \cdot \boldsymbol{H_k}\, \boldsymbol{n} \cdot \boldsymbol{u_c}\, dl dS = \\ &= \sum_{j=1}^{N_g} \int_V \frac{1}{2} \boldsymbol{B_j} \cdot \boldsymbol{H_j} dV + \sum_{j=1}^{N_g} \sum_{\substack{k=1 \\ k \neq j}}^{N_g} \int_V \frac{1}{2} \boldsymbol{B_j} \cdot \boldsymbol{H_k} dV = \sum_{j=1}^{N_g} \left(E_j + \sum_{\substack{k=1 \\ k \neq j}}^{N_g} E_{jk} \right) \end{aligned} \tag{3.160}$$

Where E_j represents j-th field energy when isolated and E_{jk} represents interaction energy between j-th and k-th fields. Energies can be expressed in terms of self- and mutual induction coefficients:

$$\begin{aligned} E_j &= \int_V \frac{1}{2} \boldsymbol{B_j} \cdot \boldsymbol{H_j} dV = \frac{1}{2} \int_S \sum_{j=1}^{N_g} \boldsymbol{B_j} \cdot \boldsymbol{n}\, dS \cdot \oint_c \sum_{k=1}^{N_g} \boldsymbol{H_j} \cdot \boldsymbol{u_c}\, dl = \\ &= \frac{1}{2} \frac{\Phi_{e\,j} - \sum_{k=1,\, k \neq j}^{N_g} M_{jk} \mathcal{I}_k}{N_j} N_j \mathcal{I}_j = \frac{1}{2} L_j \mathcal{I}_j^2 \end{aligned} \tag{3.161}$$

$$\begin{aligned} E_{jk} &= \int_V \frac{1}{2} \boldsymbol{B_j} \cdot \boldsymbol{H_k} dV = \frac{1}{2} \int_S \sum_{j=1}^{N_g} \boldsymbol{B_j} \cdot \boldsymbol{n}\, dS \cdot \oint_c \sum_{k=1}^{N_g} \boldsymbol{H_k} \cdot \boldsymbol{u_c}\, dl = \\ &= \frac{1}{2} \frac{\Phi_{e\,j} - \sum_{k=1,\, k \neq j}^{N_g} M_{jk} \mathcal{I}_k}{N_j} N_k \mathcal{I}_k = \frac{1}{2} \frac{L_j \mathcal{I}_j}{N_j} N_k \mathcal{I}_k = \frac{1}{2} \frac{N_j N_k}{\mathcal{R}_{eq}} \mathcal{I}_j \mathcal{I}_k = \frac{1}{2} M_{jk} \mathcal{I}_j \mathcal{I}_k \end{aligned} \tag{3.162}$$

The expression for E_{jk} is obviously symmetrical with respect to j and k indices, as for its definition:

$$E_{jk} = E_{kj} = \frac{1}{2} M_{jk} \mathcal{I}_j \mathcal{I}_k \tag{3.163}$$

$$E_{jk} + E_{kj} = 2\, E_{jk} = 2\, E_{kj} = M_{jk} \mathcal{I}_j \mathcal{I}_k \tag{3.164}$$

Finally, total field energy can be written as:

$$E_f = \frac{1}{2}\Phi\sum_{j=1}^{N_g}\mathcal{F}_j = \frac{1}{2}\int_S\sum_{j=1}^{N_g}\boldsymbol{B_j}\cdot\boldsymbol{n}\,dS\cdot\oint_c\sum_{k=1}^{N_g}\boldsymbol{H_k}\cdot\boldsymbol{u_c}\,dl = \frac{1}{2}\sum_{j=1}^{N_g}\left(L_j\mathcal{I}_j^2 + \sum_{\substack{k=1\\k\neq j}}^{N_g}M_{jk}\mathcal{I}_j\mathcal{I}_k\right) \tag{3.165}$$

3.2 Motor magnetic circuit analysis

An approximate, preliminary analysis of brushless motor magnetic circuit is performed to assess maximum entity of magnetic flux circulating in a critical working condition. This value is then compared to motor materials $B-H$ curves to verify saturation avoidance and flux leakages containment (i.e. to have appropriate materials' relative permeabilities).

3.2.1 Magnetic circuit and working principle description

Brushless motor magnetic circuit is shown in figure 3.17 without nearby components. Some components are placed on reaction wheel inner plate, thus they form magnetic circuit inner part, others are placed on the outer plate, thus they form magnetic circuit outer part and the rest of the components are placed inside the case body. Components forming magnetic circuit and their functions are:

1. Nine rectangular section, toroidal coils (shown in dark orange in figure 3.17) glued on inner plate PCB on payload side. The current circulating within each coil wire produces an axisymmetric magnetic field, whose symmetry axis is orthogonal to inner plate PCB plane;

2. Nine cylindrical magnetic cores (shown in light gray in figure 3.17) glued on inner plate PCB on payload side. Concentric to coils, they concentrate the magnetic fields generated by coils;

3. One rectangular section iron ring (shown in dark gray in figure 3.17(a), named inner iron ring) glued on coils and magnetic cores. Its function is to drive magnetic field lines, generated by coils and permanent magnets, on a plane parallel to inner plate PCB plane. The iron ring and the above mentioned components form magnetic circuit inner part;

4. Six cylindrical permanent magnets (shown in dark gray in figure 3.17(a)), glued within through holes in the HDD dish with alternating polarities. They generate axisymmetric magnetic fields whose symmetry axis is orthogonal to inner plate PCB plane. These fields interact with magnetic fields generated by coils, producing magnetic forces which give moments that allow mutual rotation between HDD dish and reaction wheel tile;

5. One rectangular section HDD dish (shown in gray in figure 3.17) located inside the case body and splined to a pair of ball bearings. The plane of the dish is parallel to inner plate PCB plane. Magnetic forces acting on permanent magnets produce moments on HDD dish about shaft axis and its rotation about the shaft is allowed by ball bearings;

6. One additional rectangular section iron ring (shown in dark gray in figure 3.17(b), named outer iron ring) identical to inner iron ring and glued on outer plate PCB on case body side. As its homologous component on circuit inner part, it drives magnetic field lines, generated by coils and permanent magnets, on a plane parallel to inner plate PCB plane. It forms magnetic circuit outer part.

Magnetic cores and iron rings should have cuts to reduce eddy currents intensities due to temporal variations of magnetic fields induced by time-varying currents circulating in coils and permanent magnets rotation with respect to the rest of magnetic circuit. Iron rings should be cut along concentric circumferences and magnetic cores cuts should be along their cross sections, they will be implemented on future versions of reaction wheel. Coils are placed on PCB along a circumference concentric with iron rings and HDD dish and circumference centre is coincident with shaft axis. Coils are evenly spaced 40° apart. Permanent magnets are as well placed in HDD dish along a circumference whose centre lies on shaft axis and they are evenly spaced 60° apart. The circular symmetry of magnetic circuit is evident.

(a) (b)

Figure 3.17: Brushless motor magnetic circuit inner side (a) and outer side (b) shown without other reaction wheel components.

A possible motor working principle has been proposed but not thoroughly examined yet. It mirrors magnetic circuit geometrical circular symmetry and is shown in figure 3.18. Coils are divided in three identical coil groups in which three coils (numbers 1 to 3 in figure 3.18(a)) interact magnetically with the nearest permanent magnets. Working cycle is the same for all coil groups and is described by diagram shown in figure 3.18(b). Configuration in figure 3.18(a) is taken arbitrarily as the initial angular position, where the dish has null angular velocity and acceleration with respect to coils and magnetic cores and corresponds to angular position in stage I. From electrical point of view, during stage I a current i flows in the wire in coil 1 (this is arbitrarily chosen as the positive current sign) and thus coil 1 and its core become equivalent to a magnet whose poles orientation is shown in figure. During the same stage, wire in coil 3 is crossed by an opposite current $-i$, with the same magnitude and opposite direction with respect to i, while there is no current in coil 2 wire. Coil 3 and its core then act as a magnet whose poles orientation is opposite to poles orientation for coil 1. Ideal resulting magnetic field lines are represented in figure, where uppermost and lowermost horizontal field lines would be included in inner and outer iron rings respectively but are represented outside of them for clarity. In the remainder of this chapter, angular motion of HDD dish and permanent magnets with respect to coils, magnetic cores and iron rings will be considered, thus the former group of components, corresponding to magnetic circuit inner and outer parts, is called stator group and the latter is called rotor group. Permanent magnets experience forces of attraction given by coils and magnetic cores (and vice versa). Components of these forces producing rotor rotation are considered in the remainder and shown as red vectors in figure. Coil 2 receives no current since it has a magnet right below it, i.e. their axes are coincident. The leftmost permanent magnet in figure is exactly between coil 1 of coil group in picture and coil 3 of adjacent coil group on the left, i.e. magnet axis is 20° far from each coil axis. Coil 1 in picture is crossed by current i in order to attract leftmost magnet, which is 20° far and experiences the magnetic force of attraction F. Similarly, the central magnet in figure experiences an attraction force F' given by coil 3, which is minor than F since angular distance between coil and magnet is 40°, major than in previous case. Forces F and F' exerted on HDD dish and magnets give a moment about shaft axis and thus rotor begins angular acceleration. Clearly all three coil groups in HDD dish are in the same stage at a given time. Only attraction forces with nearest active coil is taken into account, if repulsion forces with nearest coil were considered,, they would have given the same result. Thus repulsion forces and other magnetic forces are not considered here, since attraction forces are sufficient to illustrate the working principle.
HDD dish and magnets rotate with respect to stator until they reach angular position for stage II, in which currents in coils have switched. Relation between rotor angular displacement $\Delta\theta$ in successive stages and coil number N is:

$$\Delta\theta = \frac{1}{2} \cdot \frac{360°}{N} = 20° \tag{3.166}$$

Current in coil 3 remains the same as the permanent magnet attracted by coil 3 in stage I can still be attracted by the same coil now with a force of major intensity since angular distance between their axes is 20°, thus force

exerted is F. Current in coil 1 is null since the nearest permanent magnet is right below it. That magnet is attracted by coil 2, which now undergoes current i, with a force F' since their angular distance is 40°. Hence forces are exerted again on permanent magnets, and give a moment about shaft axis to rotor group. Thus it keeps accelerating with respect to stator group, arriving to configuration of stage III.
In stage III, coil 2 is still undergoing current i since the magnet it was attracting in stage II is still 20° far. This current exerts force F on the magnet. Coil 1 receives current $-i$ to attract a permanent magnet which is exiting the adjacent coil group on the left and is 40° far, thus exerted attraction force is F'. Similarly, rightmost permanent magnet is attracted by coil 1 of adjacent coil group on the right. This coil is clearly crossed by current $-i$ and exerts force F' on rightmost magnet which is 40° far. Thus rotor group keeps accelerating and reaches stage IV, where its angular position is equal to stage I with reversed magnet polarities (while rotor angular acceleration and velocity are not null). Thus in stages IV - VI angular positions of magnets are repeated, but their polarities are reversed, so currents sequences are equal to the ones in stages I - III but with opposite signs, as shown in table 3.19(a). Clearly, stages IV - VI have an explanation of magnetic and mechanical aspects of operations similar to stages I - III illustrated above. At stage VI the leftmost magnet in stage I in figure 3.18(b) is exactly below coil 3 and rotor rotation in stages I - VI is 100°.

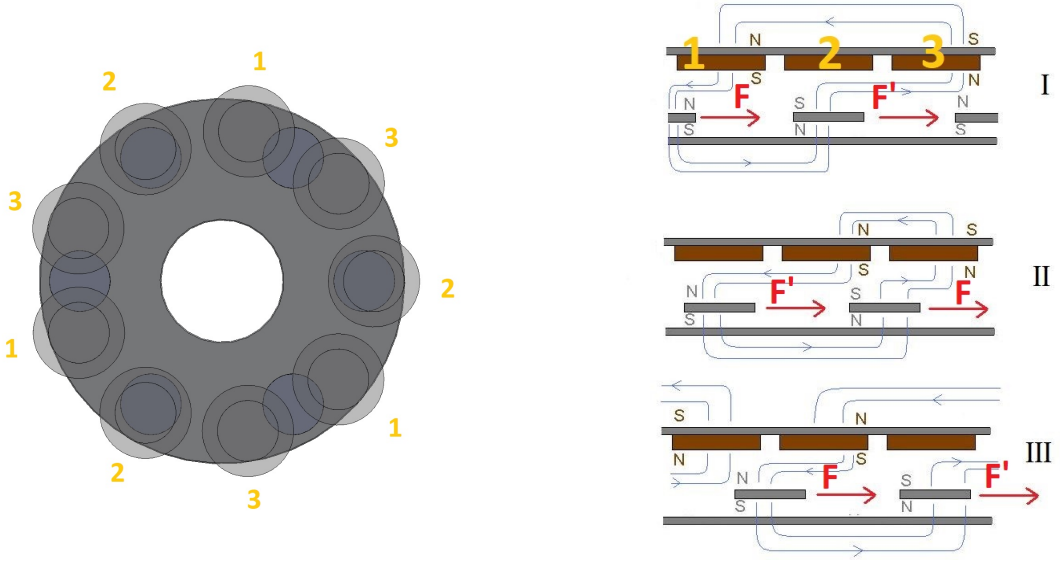

(a) (b)

Figure 3.18: Possible motor working principle. Rotor group is represented as seen from payload side along a direction orthogonal to inner plate PCB plane with coils in transparency, in stage I (a). Numbers refer to coil numbering in coil groups. Magnetic circuit in stages I - III is represented as seen from a direction parallel to inner plate PCB plane (b), with red vectors representing attraction forces acting on permanent magnets and blue lines representing ideal $\boldsymbol{B}$-field lines. Uppermost and lowermost horizontal field lines should lie inside inner and outer iron rings respectively and are represented outside of iron rings for clarity.

After a further currents commutation from stage VI to stage I, it becomes 120° and currents working cycle is complete: magnets that were under adjacent coil group on the left of figure 3.18(b) now undergo the same working cycle, this time driven by coils in figure and starting from non null angular acceleration and velocity of dish. After three complete current cycles a complete rotation of HDD dish and permanent magnets is performed.
An ideal time diagram of coil currents is shown in figure 3.19(b). They appear as square waves where duration of interval at null current is one half of duration of intervals on $\pm i$. Moreover, the three time diagrams have the same structure but are shifted in time: curve for coil 2 (coil 3) can be obtained by shifting curve for coil 1 (coil 2) two stages forward. Furthermore, in the ideal time diagram in figure, all stages have the same temporal extension, which is not true since rotor is accelerating. Supposing coils current curves remain as in figure (thus rotor is accelerating), stages temporal lengths are different within the same working cycle and between homologous stages from different cycles, since stages duration becomes shorter as rotor accelerates. In any case, current cycle period is always one third of rotor rotation cycle period.

Stage	Coil 1	Coil 2	Coil 3
I	$+i$	0	$-i$
II	0	$+i$	$-i$
III	$-i$	$+i$	0
IV	$-i$	0	$+i$
V	0	$-i$	$+i$
VI	$+i$	$-i$	0

(a)

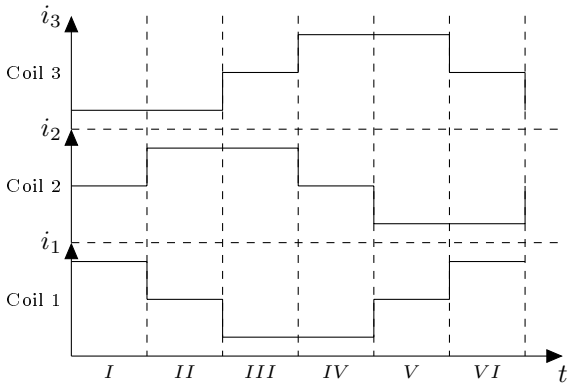

(b)

Figure 3.19: Possible time table (a) and ideal time diagram (b) of currents working cycle.

3.2.2 Magnetic circuit model and maximum flux evaluation

The simplified magnetic circuit model has been developed starting from simplifying assumptions on magnetic field:

1. Quasi-stationary magnetic conditions are assumed, i.e. displacement currents are negligible with respect to conductive currents (see section 3.1);
2. Magnetic field is completely contained between iron rings and does not leak outside of reaction wheel;
3. Inside iron rings, $\boldsymbol{B}$-field lines are circular, concentric to iron rings and parallel to their planes;
4. In the rectangular section toroid between iron rings, $\boldsymbol{B}$-field lines are straight lines orthogonal to iron rings themselves and field is null elsewhere.

Coils with their cores and permanent magnets are treated as magnetomotive force generators and their contributions to magnetic flux are evaluated separately within the same overall magnetic schematic and then summed to obtain total flux thanks to superposition principle. Coils can be considered as ideal generators while permanent magnets cannot and the approximate analysis shown in section 3.1.3.3 shall be applied. Circular symmetry of magnetic circuit allows to conceive magnetic circuit schematic for a single coil group and then describe magnetic interactions among coil groups in overall magnetic schematic.
Coil group mechanical diagrams are represented in figure 3.20 without contribution of permanent magnets and HDD dish. Iron rings are split into six annulus sectors whose length of mean arc is l_1. Streamtube segments in which magnetic field is supposed to flow, in present simplified model, are shown in mechanical diagrams with colored areas and numbers. They are represented by:

- The internal volumes of iron rings sectors. Further divisions of these segments are considered, which consist in the volumes of the above mentioned annulus sectors whose mean length is l_1. These segments are shown in red in figure 3.20 and identified with number 1;
- The right circular cylinder whose height is l_3 and cross section is equal to magnetic cores' cross section. This segment is shown in blue in figure 3.20 and identified with number 3;
- The volume contained between iron rings in sectors whose mean length is $2\,l_1$, excluding adjacent cylindrical segments. This segment is shown in yellow in figure 3.20 and identified with number 4.

Reaction wheel components not belonging to magnetic circuit, not shown in mechanical diagram, are supposed to be magnetically transparent and are then considered as vacuum in following calculations. Reluctance of coil cores has been neglected.

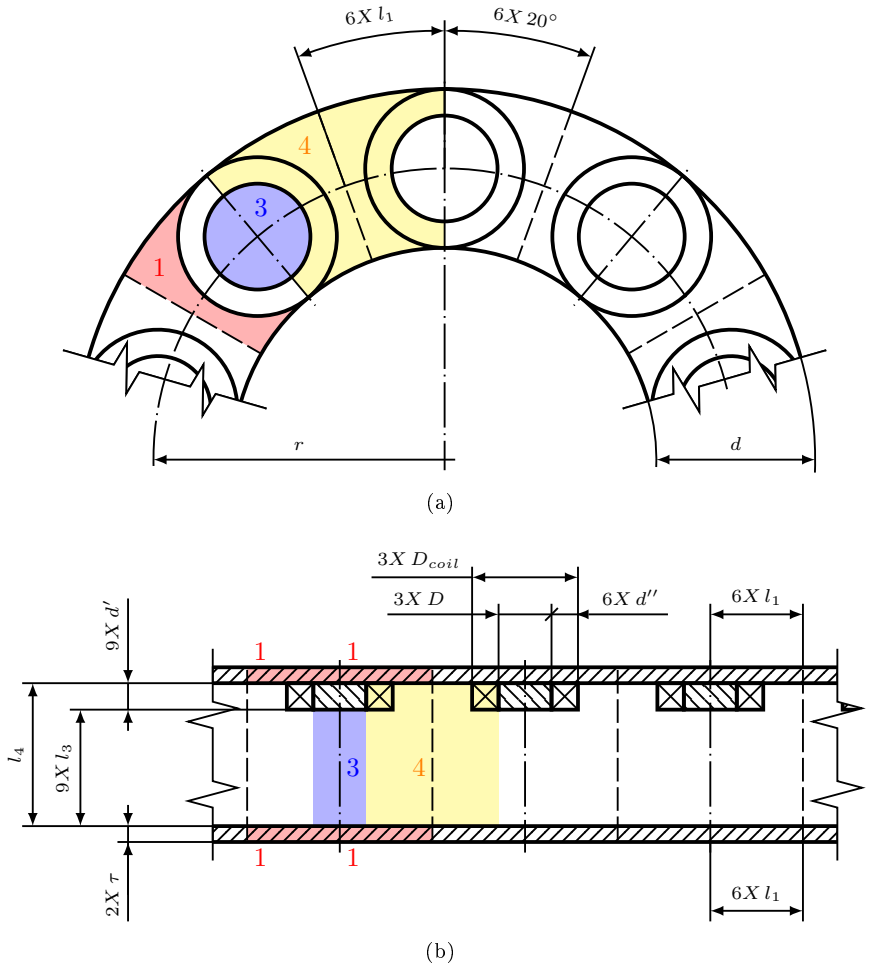

Figure 3.20: Mechanical diagrams (not to scale) of a single coil group without contribution of HDD dish and permanent magnets. Coil group is seen from space side along a direction orthogonal to inner plate PCB plane, without outer iron ring (a) and from a direction parallel to inner plate PCB plane, once sectioned along iron rings mean radii (b). Each colored area and number identifies a separate streamtube segment for magnetic field.

Magnetic schematic of each coil group, corresponding to mechanical diagrams in figure 3.20, is shown in figure 3.22(a). The outermost segments of iron rings in mechanical diagrams have been left out of coil group definition for magnetic schematic to highlight coil groups magnetic interaction among themselves. Coils undergo currents with opposite signs or null currents, thus values of resulting magnetic voltages $\mathcal{F}_A$, $\mathcal{F}_B$ and $\mathcal{F}_C$ will be imposed depending on which stage of currents working cycle is examined. Reluctances of streamtubes segments 1, 3 and 4 are calculated as shown in section 3.1.1 with the following dimensions, taken from CAD model and indicated in figure 3.20:

- N is the number of coils, as in previous section;
- D is magnetic cores diameter, coincident with coils inner diameter d_{coil};
- d is the difference between iron rings external and internal radii;
- r is iron rings mean radius;
- τ is iron rings thickness;
- d' is the distance between cores outermost surface and outermost surface of inner iron ring. It is equal to coil thickness c, summed to glue thickness;
- l_3 is the distance between innermost surface of outer iron ring and cores outermost surface.

Dimensions are indicated in table 3.2. Lengths l_3 and l_4 are relative to an early version of the reaction wheel, before version 1. However, results are valid for version 1. They are exploited for reluctances calculation according to equations 3.168-3.172.

$$\mathcal{R}_i = \frac{1}{\mu_0 \, \mu_{r\,i}} \frac{l_i}{S_i} \qquad i = 1, 3, 4 \tag{3.167}$$

$$l_1 = \frac{2\,\pi\,r}{2\,N} \tag{3.168}$$

$$S_1 = \tau \cdot d \tag{3.169}$$

$$S_3 = \pi \left(\frac{D}{2} \right)^2 \tag{3.170}$$

$$l_4 = l_3 + d' \tag{3.171}$$

$$S_4 = 2\,\frac{2\,\pi\,r}{2\,N}\,d - \pi \left(\frac{D}{2} \right)^2 \tag{3.172}$$

Relative permeabilities $\mu_{r\,3}$ and $\mu_{r\,4}$ are unitary, since streamtubes segments 3 and 4 are assumed to be in vacuum. Relative permeability $\mu_{r\,1}$ can be found with the help of M530-65A electrical steel datasheet[1], from which magnetic performance are extracted and indicated in table 3.1. The first segment of the curve is chosen, i.e. saturation is avoided, by hypothesis and permeability $\mu_{r\,1}$ becomes:

$$\mu_{r\,1} = \frac{1}{\mu_0} \frac{1.54\,T}{2500\,A/m} = 490.197 \tag{3.173}$$

Clearly, this assumption must be verified by checking that the maximum flux $\Phi_{1\,MAX}$ in the iron rings, given by coils and permanent magnets, at every time t, remains inferior to limit flux Φ_{lim}:

$$\Phi_{lim} = 1.54 \cdot S_1 = 18.018 \cdot 10^{-6} Wb \tag{3.174}$$

$$|\Phi_{1\,MAX}| \leq \Phi_{lim} \qquad \forall t \tag{3.175}$$

This condition will be verified in the remainder of the chapter.

[1] Available at the URL https://www.thyssenkrupp-steel.com/media/content_1/publikationen/lieferprogramme/thyssenkrupp_product-range_no-electrical-steel_powercore_steel_en.pdf.

$B\,[T]$	$H\,[A/m]$
0.000	0
1.540	2500
1.640	5000
1.740	10000

Table 3.1: M530-65A electrical steel magnetization parameters table.

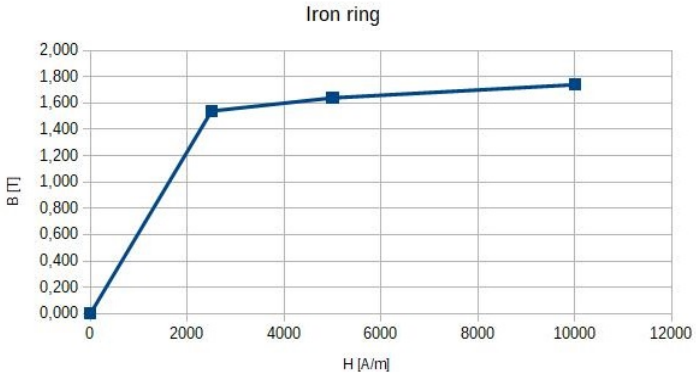

Figure 3.21: M530-65A electrical steel magnetization curve.

N	[ ]	9	l_3	$[mm]$	5.290
d	$[mm]$	18.000	r	$[mm]$	30.000
d'	$[mm]$	3.100	τ	$[mm]$	0.650
D	$[mm]$	12.000			

Table 3.2: Streamtubes physical dimensions without contribution of permanent magnets.

	$l\,[mm]$	$S\,[mm^2]$	μ_r [ ]	$\mathcal{R}\,[1/H]$
1	10.472	11.700	490.197	1.453×10^6
3	5.290	113.097	1.000	3.722×10^7
4	8.390	263.894	1.000	2.530×10^7

Table 3.3: Reluctances of magnetic circuits with contribution of coils alone.

Coil groups are magnetically connected as described in figure 3.22(b), where they are represented as black boxes. Focusing on uppermost loop, applying flux law 3.41 to each node, it is clear that fluxes leaving one coil group and entering the adjacent coil group are equal:

$$\Phi_2 = \Phi_3 \tag{3.176}$$
$$\Phi_4 = \Phi_5 \tag{3.177}$$
$$\Phi_1 = \Phi_6 \tag{3.178}$$

Applying flux law to upper sections of coil groups, imagined as nodes, it becomes clear that total fluxes Φ_{CG} leaving uppermost loop must be null. Flux law leads to:

$$\Phi_1 = \Phi_{CG} + \Phi_2 \tag{3.179}$$
$$\Phi_2 = \Phi_{CG} + \Phi_4 \tag{3.180}$$
$$\Phi_4 = \Phi_{CG} + \Phi_1 \tag{3.181}$$

Expression for flux Φ_1 then becomes:

$$\Phi_1 = 3\Phi_{CG} + \Phi_1 \tag{3.182}$$

Leading to:

$$\Phi_{CG} = 0 \tag{3.183}$$

This happens because all coil groups magnetic parameters are the same at a given time, since they are in the same stage. Thus all fluxes in uppermost loop have the same value Φ:

$$\Phi_1 = \Phi_2 = \Phi_3 = \Phi_4 = \Phi_5 = \Phi_6 = \Phi \tag{3.184}$$

Due to flux conservation in uppermost loop, all magnetic voltage drops between coil groups have the same value and are equal to $\mathcal{F}_1$. Considering then circuit symmetry, all coil groups voltage drops in horizontal direction

must have the same value $\mathcal{F}_{CG}$. Applying magnetic voltage law 3.43 to upper loop, it is evident that total magnetic voltage drop $\mathcal{F}_{CG}$ on a coil group is equal and opposite to $\mathcal{F}_1$:

$$3\mathcal{F}_{CG} + 3\mathcal{F}_1 = 0 \tag{3.185}$$
$$\mathcal{F}_{CG} = -\mathcal{F}_1 \tag{3.186}$$

The same principles can be applied to lowermost loop magnetic parameters, to draw the same conclusions about magnetic fluxes:

$$\Phi'_1 = \Phi'_2 = \Phi'_3 = \Phi'_4 = \Phi'_5 = \Phi'_6 = \Phi' \tag{3.187}$$
$$\Phi'_{CG} = 0 \tag{3.188}$$

Thus all fluxes in lowermost loop have the same value, Φ'. Due to conservation of flux in lowermost loop and to its symmetry, voltage drops between coil groups have the same value $\mathcal{F}'_1$ and horizontal voltage drops across coil groups are all equal to $\mathcal{F}'_{CG}$. Voltage drop $\mathcal{F}'_{CG}$ can be found to be equal and opposite to $\mathcal{F}'_1$:

$$\mathcal{F}'_{CG} = -\mathcal{F}'_1 \tag{3.189}$$

Applying magnetic voltage law 3.43 to coil groups leads to the following equations:

$$\mathcal{F}_{CG\,1} - \mathcal{F}_{CG} - \mathcal{F}_{CG\,2} + \mathcal{F}'_{CG} = 0 \tag{3.190}$$
$$\mathcal{F}_{CG\,3} - \mathcal{F}_{CG} - \mathcal{F}_{CG\,4} + \mathcal{F}'_{CG} = 0 \tag{3.191}$$
$$\mathcal{F}_{CG\,5} - \mathcal{F}_{CG} - \mathcal{F}_{CG\,6} + \mathcal{F}'_{CG} = 0 \tag{3.192}$$

That, combined with the following magnetic voltage balances, from loops between coil groups:

$$\mathcal{F}_{CG\,2} + \mathcal{F}_{CG} - \mathcal{F}_{CG\,3} - \mathcal{F}'_{CG} = 0 \tag{3.193}$$
$$\mathcal{F}_{CG\,4} + \mathcal{F}_{CG} - \mathcal{F}_{CG\,5} - \mathcal{F}'_{CG} = 0 \tag{3.194}$$
$$\mathcal{F}_{CG\,6} + \mathcal{F}_{CG} - \mathcal{F}_{CG\,1} - \mathcal{F}'_{CG} = 0 \tag{3.195}$$

Lead to the equalities:

$$\mathcal{F}_{CG\,1} = \mathcal{F}_{CG\,3} = \mathcal{F}_{CG\,5} \tag{3.196}$$
$$\mathcal{F}_{CG\,2} = \mathcal{F}_{CG\,4} = \mathcal{F}_{CG\,6} \tag{3.197}$$

Thus all coil groups have the same circuital variables values at a given stage. Uppermost and lowermost coil group terminals in figure 3.22(a) can then be connected with a short circuit, as in figure 3.24(a), to represent a generic coil group working condition under the input of coils or permanent magnets.
Contributions of permanent magnets must be introduced as well. Coil group mechanical diagrams with HDD dish and permanent magnets are shown in figure 3.23. In the following calculations, the distance between permanent magnets geometrical centers and shaft axis is supposed to be the same distance between coil cores geometrical centers and shaft axis.
From magnetic schematic point of view (see schematic at figure 3.22(a)), leftmost magnet (called permanent magnet 1 in the remainder) can be imagined to lie between nodes A and A' giving a magnetomotive force $\mathcal{F}_{M1}$ while the rightmost magnet lies between nodes M and M', gives a magnetomotive force $\mathcal{F}_{M2}$ and is called permanent magnet 2 in the remainder. Aluminum in HDD dish is supposed to be magnetically transparent and thus is considered as vacuum for magnetic field calculations. Streamtube segment 3 is now replaced by segment 5, shown in mechanical diagram. It has the same shape of segment 3 but its length l_5 is modified with respect to l_3 due to magnets thickness τ_{PM}, given by component datasheet:

$$l_5 = l_3 - \tau_{PM} = 4.290\,mm \tag{3.198}$$

This represents a simplification since permanent magnet does not occupy the entire section of streamtube segment 3. Segment reluctance is named $\mathcal{R}_5$ and calculated with magnet section S_5, taken from component datasheet:

$$S_5 = S_3 = 113.097\,mm^2 \tag{3.199}$$
$$\mu_{r\,5} = \mu_{r\,3} = 1.000 \tag{3.200}$$
$$\mathcal{R}_5 = \frac{1}{\mu_5}\frac{l_5}{S_5} = 3.019 \cdot 10^7\,H^{-1} \tag{3.201}$$

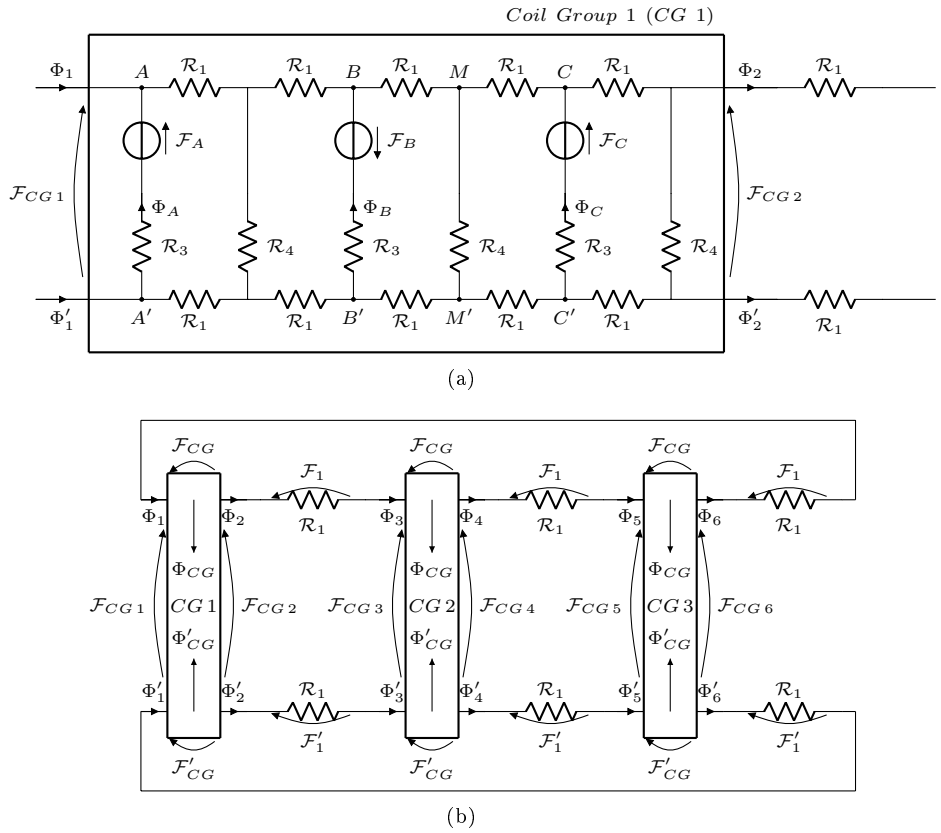

Figure 3.22: Magnetic circuit schematics for coil group 1 ($CG\,1$) with contribution of coils only (a) and for coil groups assembly ($CG\,1$ to $CG\,3$) with contribution of coils or permanent magnets (b).

Streamtube segment 6 is introduced as well and is shown in mechanical diagram. It has the same shape of segment 4 except for its length, which is equal to distance between iron rings l_4 minus magnets thickness τ_{PM}.

$$l_6 = l_4 - \tau_{PM} = l_5 + d' = 7.390\,mm \tag{3.202}$$

$$S_6 = S_4 = 263.894\,mm^2 \tag{3.203}$$

$$\mu_{r\,6} = 1.000 \tag{3.204}$$

$$\mathcal{R}_6 = \frac{1}{\mu_6}\frac{l_6}{S_6} = 2.228 \cdot 10^7\,H^{-1} \tag{3.205}$$

As for segment 5, this is a simplifying assumption since permanent magnet does not occupy the entire section of streamtube segment 4. Reluctances of magnetic circuits with permanent magnets are listed in table 3.5.

$\boldsymbol{N}$	[ ]	9	$\boldsymbol{l_3}$	$[mm]$	5.290
$\boldsymbol{d}$	$[mm]$	18.000	$\boldsymbol{r}$	$[mm]$	30.000
$\boldsymbol{d'}$	$[mm]$	3.100	$\boldsymbol{\tau}$	$[mm]$	0.650
$\boldsymbol{D}$	$[mm]$	12.000	$\boldsymbol{\tau_{PM}}$	$[mm]$	1.000

Table 3.4: Streamtubes physical dimensions with contribution of permanent magnets.

	$\boldsymbol{l}\,[mm]$	$\boldsymbol{S}\,[mm^2]$	$\boldsymbol{\mu_r}$ [ ]	$\boldsymbol{\mathcal{R}}\,[1/H]$
1	10.472	11.700	490.197	1.453×10^6
3	5.290	113.097	1.000	3.722×10^7
4	8.390	263.894	1.000	2.530×10^7
5	4.290	113.097	1.000	3.019×10^7
6	7.390	263.894	1.000	2.228×10^7

Table 3.5: Reluctances of magnetic circuits with contribution of permanent magnets alone.

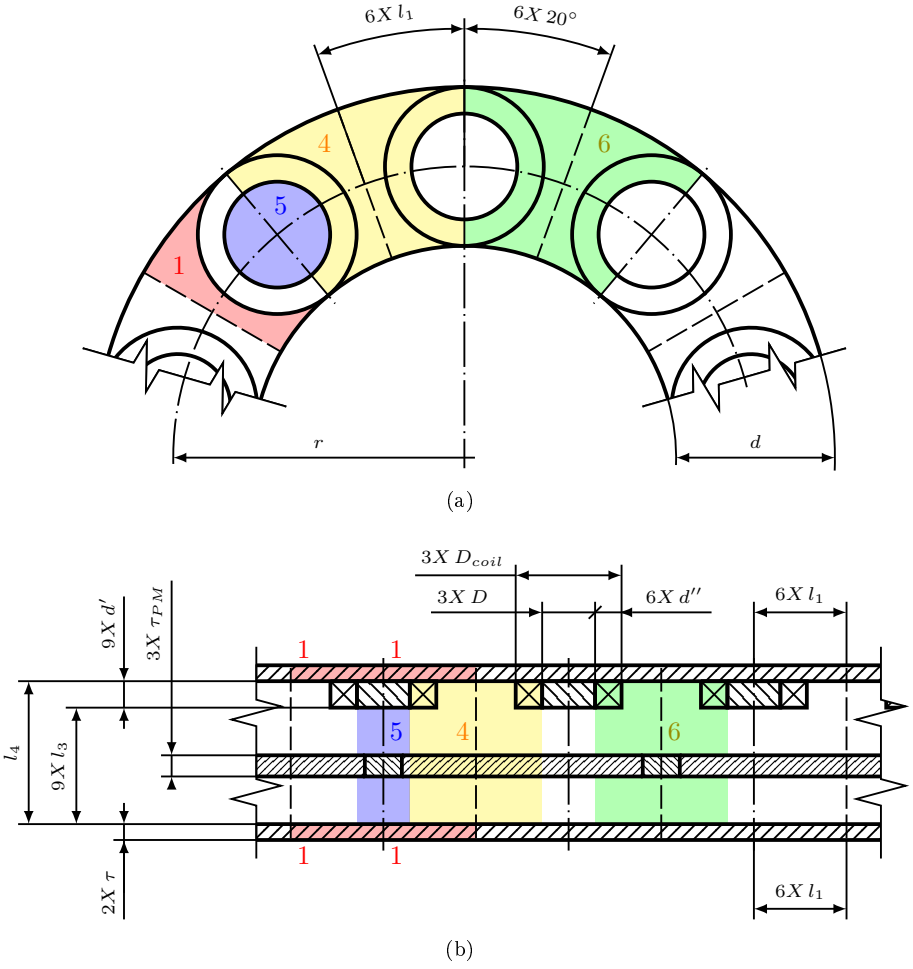

Figure 3.23: Mechanical diagrams (not to scale) of a single coil group with contribution of HDD dish and permanent magnets. Coil group is seen from space side along a direction orthogonal to inner plate PCB plane, without outer iron ring (a) and from a direction parallel to inner plate PCB plane, once sectioned along iron rings mean radii (b). Each colored area and number identifies a separate streamtube segment for magnetic field.

The above deductions leading from general magnetic schematics in figure 3.22 to schematics in figure 3.24(a), considering contribution of coils, can be drawn when contribution of permanent magnets is considered as well. These lead to magnetic schematic for coil group with permanent magnets drawn in figure 3.24(b).

As mentioned above, magnetic flux evaluation must account for contributions of coils and permanent magnets. For coils, stage VI is chosen thus magnetomotive forces intensities are:

$$\mathcal{F}_B = -\mathcal{F}_A \tag{3.206}$$

$$\mathcal{F}_C = 0\,At \tag{3.207}$$

Flux to evaluate is chosen to be Φ_A (see schematics in figure 3.24). Angular position of permanent magnets does not correspond to stage VI position, chosen for coils, but gives maximum flux Φ_A which can occur out of nominal working conditions. Flux contributions to Φ_A from each generator are evaluated separately and have an additional subscript corresponding to origin:

- Φ_{AA} from magnetomotive force $\mathcal{F}_A$, corresponding to coil 1;
- Φ_{AB} from magnetomotive force $\mathcal{F}_B$, corresponding to coil 2;
- Φ_{AC} from magnetomotive force $\mathcal{F}_C$, corresponding to coil 3;
- Φ_{AM1} from magnetomotive force $\mathcal{F}_{M1}$, corresponding to permanent magnet 1;

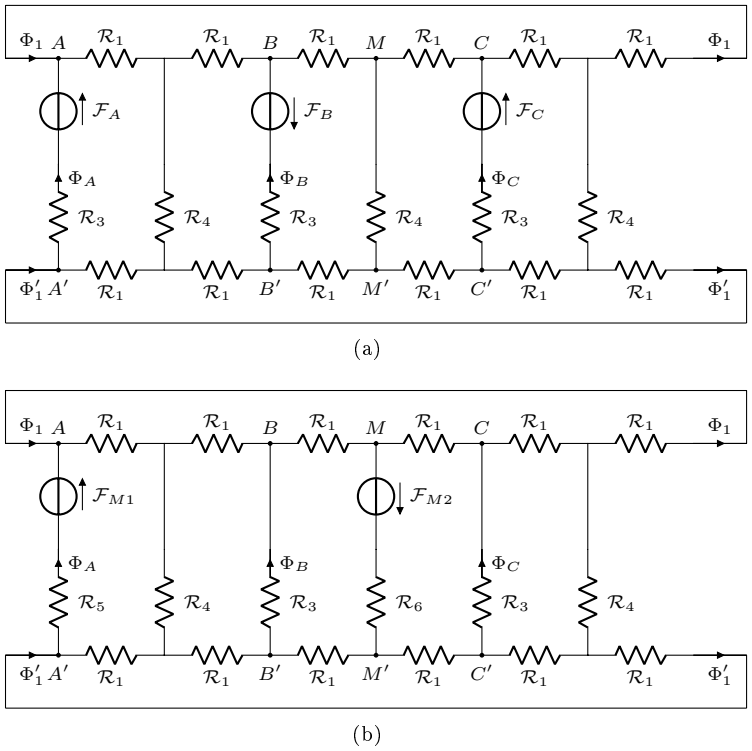

Figure 3.24: Magnetic circuit schematic of coil group with contribution of coils only (a) and with contribution of reaction wheel magnets only (b).

- Φ_{AM2} from magnetomotive force $\mathcal{F}_{M2}$, corresponding to permanent magnet 2.

Thus total flux Φ_A is given by the sum of each of the above terms thanks to superposition principle:

$$\Phi_A = \Phi_{AA} + \Phi_{AB} + \Phi_{AC} + \Phi_{AM1} + \Phi_{AM2} \tag{3.208}$$

Each flux contribution is imagined to be given by elementary circuits shown in figure 3.25, where generators correspond to active coils and their cores or permanent magnets, and reluctances are equivalent reluctances calculated below for each case. Their additional subscript corresponds to magnetomotive force considered. For schematics in figures 3.25(a) - 3.25(c) equivalent reluctances are calculated starting from schematic in figure 3.24(a), equivalent reluctances for schematics in figures 3.25(d) and 3.25(e) are calculated starting from schematic in figure 3.24(b).

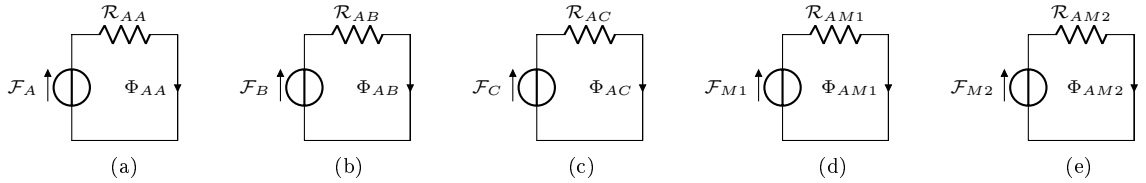

Figure 3.25: Contributions to magnetic flux Φ_A, consisting in flux Φ_{AA} given by magnetomotive force $\mathcal{F}_A$ (a), Φ_{AB} given by $\mathcal{F}_B$ (b), Φ_{AC} given by $\mathcal{F}_C$ (c), Φ_{AM1} given by $\mathcal{F}_{M1}$ (d) and Φ_{AM2} given by $\mathcal{F}_{M2}$ (e). Reluctances are equivalent reluctances resulting in each case from magnetic circuit configuration.

Thus total flux expression becomes:

$$\Phi_A = \Phi_{AA} + \Phi_{AB} + \Phi_{AC} + \Phi_{AM1} + \Phi_{AM2} = \frac{\mathcal{F}_A}{\mathcal{R}_{AA}} + \frac{\mathcal{F}_B}{\mathcal{R}_{AB}} + \frac{\mathcal{F}_C}{\mathcal{R}_{AC}} + \frac{\mathcal{F}_{M1}}{\mathcal{R}_{AM1}} + \frac{\mathcal{F}_{M2}}{\mathcal{R}_{AM2}} \tag{3.209}$$

Clearly, contribution Φ_{AC} is null since correspondent magnetomotive force $\mathcal{F}_C$ is null for the present case, and expression for Φ_A is then simplified:

$$\Phi_{AC} = \frac{\mathcal{F}_C}{\mathcal{R}_{AC}} = 0 \tag{3.210}$$

$$\Phi_A = \Phi_{AA} + \Phi_{AB} + \Phi_{AM1} + \Phi_{AM2} = \frac{\mathcal{F}_A}{\mathcal{R}_{AA}} + \frac{\mathcal{F}_B}{\mathcal{R}_{AB}} + \frac{\mathcal{F}_{M1}}{\mathcal{R}_{AM1}} + \frac{\mathcal{F}_{M2}}{\mathcal{R}_{AM2}} \tag{3.211}$$

In the first place coils magnetomotive forces must be calculated. The maximum number of turns n_{MAX} in each coil is evaluated from the following geometrical parameters, taken from CAD model and components datasheets:

- d'', difference between coils outer and inner radii (shown in figure 3.20(b));
- c, coil thickness, equal to distance d' minus glue thickness;
- ϕ_{wire}, total diameter of coil wire, including conductor and insulation.

$$n_{MAX} \simeq \left\lceil \frac{d''\,c}{\phi_{wire}^2} \right\rceil = 166 \tag{3.212}$$

Further considerations about motor maximum speed (see section 3.4) led to adopt a number of turns per coil n inferior to n_{MAX}:

$$n = 9 \tag{3.213}$$

Electrical resistance of coil wire R_{coil} can be estimated with Ohm's law, once its cross section area S_{coil} and material resistivity ρ_c are known. Wire length l_{coil} is estimated using coil average diameter $\overline{d}_{coil}$. Necessary geometrical parameters are taken from CAD model and components datasheets:

- $\phi_c < \phi_{wire}$, diameter of coil wire conductor alone;
- d_{coil}, coil inner diameter, coincident with magnetic cores diameter D shown in figure 3.20(b);
- D_{coil}, coil outer diameter.

$$d_{coil} = 12.000\,mm \tag{3.214}$$

$$D_{coil} = 18.000\,mm \tag{3.215}$$

$$\overline{d}_{coil} = \frac{d_{coil} + D_{coil}}{2} = 15.000\,mm \tag{3.216}$$

$$l_{coil} \simeq n\,2\pi\,\frac{\overline{d}_{coil}}{2} = 0.424\,m \tag{3.217}$$

$$S_{coil} = \pi\,\frac{\phi_c^2}{4} = 0.031\,mm^2 \tag{3.218}$$

$$\rho_c = 1.678 \cdot 10^{-8}\,\Omega\,m \tag{3.219}$$

$$R_{coil} \simeq \rho_c \frac{l_{coil}}{S_{coil}} = 0.227\,\Omega \tag{3.220}$$

Once total phase voltage V is decided, coil voltage V_{coil} can be found dividing total voltage V by the number of coils per phase n_c. Current circulating in each coil I_{coil} and coil magnetomotive force, $\mathcal{F}_A$ or $\mathcal{F}_B$ (depending on current sign) can then be estimated. Total phase voltage V is the maximum possible voltage that avoids saturation of electrical steel of the iron rings (calculation of maximum flux in iron rings is given below).

$$V = 2\,V \tag{3.221}$$

$$n_c = 3 \tag{3.222}$$

$$V_{coil} = \frac{V}{n_c} = 0.667\,V \tag{3.223}$$

$$I_{coil} = \frac{V_{coil}}{R_{coil}} = 2.943\,A \tag{3.224}$$

$$\mathcal{F}_A = n\,I_{coil} = 26.487\,At \tag{3.225}$$

$$\mathcal{F}_B = -\mathcal{F}_A = -26.487\,At \tag{3.226}$$

Magnetomotive forces and magnetic fluxes given by S-10-01-N permanent magnets depend on equivalent reluctances seen by magnets (see section 3.1.3.3), and will be discussed later. Their magnetization curve parameters, in particular coercivity H_c and remanence B_r, can be read on the datasheet[2]:

$$B_r = 1.210\,T \tag{3.227}$$

$$H_c = 9.150 \cdot 10^5\,A/m \tag{3.228}$$

Contributions to magnetic flux Φ_A given by coils and permanent magnets can now be estimated. In following calculations, positive directions of fluxes and magnetic voltages are taken as depicted in figures 3.26-3.29.

3.2.2.1 Calculation of Φ_{AA}

Magnetic circuit producing contribution Φ_{AA} is obtained from general schematic in figure 3.24(a) and shown in figure 3.26(a). To calculate equivalent reluctance $\mathcal{R}_{AA}$ as indicated in schematic at figure 3.25(a), circuit is modified to get to the symmetric form in figure 3.26(c) from which final form, in figure 3.26(d), is obtained exploiting schematic symmetry. Equivalent reluctance $\mathcal{R}_{AA}$ is then:

$$\mathcal{R}_{AA} = \mathcal{R}_1 + \mathcal{R}_3 + \frac{1}{\frac{1}{\mathcal{R}_1 + \left((\mathcal{R}_3/2)^{-1} + (\mathcal{R}_1 + \mathcal{R}_4)^{-1}\right)^{-1}} + \frac{1}{\mathcal{R}_4/2}} = 4.494 \cdot 10^7\,H^{-1} \tag{3.229}$$

Contribution to flux Φ_A due to magnetomotive force $\mathcal{F}_A$ is then:

$$\Phi_{AA} = \frac{\mathcal{F}_A}{\mathcal{R}_{AA}} = 5.893 \cdot 10^{-7}\,Wb \tag{3.230}$$

3.2.2.2 Calculation of Φ_{AB}

Magnetic circuit producing contribution Φ_{AB} is obtained again from general schematic in figure 3.24(a) and shown in figure 3.27(a). With some modifications, its symmetry is highlighted in figure 3.27(c) and then exploited to get to a simpler schematic, shown in figure 3.27(d). Flux Φ_{A+C} is calculated, which is the double of Φ_A:

$$\Phi_{A+C} = 2\,\Phi_{AB} = 2\,\Phi_{CB} = \Phi_{AB} + \Phi_{CB} \tag{3.231}$$

First of all, applying the equivalent of Thévenin's theorem for magnetic circuits, circuit portion between nodes D and D' is replaced with an equivalent magnetomotive force generator $\mathcal{F}'_B$ and an equivalent reluctance $\mathcal{R}_{eq\,1}$:

$$\mathcal{F}'_B = \mathcal{F}_B \frac{\mathcal{R}_4/2}{\mathcal{R}_1 + \mathcal{R}_3 + \mathcal{R}_4/2} \tag{3.232}$$

$$\mathcal{R}_{eq\,1} = \frac{1}{\frac{1}{\mathcal{R}_1 + \mathcal{R}_3} + \frac{1}{\mathcal{R}_4/2}} = 9.532 \cdot 10^6\,H^{-1} \tag{3.233}$$

Then the same theorem is applied to circuit portion between nodes E and E', which is replaced with equivalent reluctance $\mathcal{R}_{eq\,2}$:

$$\mathcal{R}_{eq\,2} = \frac{1}{\frac{1}{\mathcal{R}_1 + \mathcal{R}_4} + \frac{1}{\mathcal{R}_3/2}} = 1.098 \cdot 10^7\,H^{-1} \tag{3.234}$$

To get to schematic in figure 3.27(e). Then magnetic voltage drop for $\mathcal{R}_{eq\,2}$, $\mathcal{F}_E$, can easily be evaluated:

$$\mathcal{F}_E = \mathcal{F}'_B \frac{\mathcal{R}_{eq\,2}}{\mathcal{R}_1 + \mathcal{R}_{eq\,1} + \mathcal{R}_{eq\,2}} = \mathcal{F}_B \frac{\mathcal{R}_4/2}{\mathcal{R}_1 + \mathcal{R}_3 + \mathcal{R}_4/2} \frac{\mathcal{R}_{eq\,2}}{\mathcal{R}_1 + \mathcal{R}_{eq\,1} + \mathcal{R}_{eq\,2}} \tag{3.235}$$

And flux Φ_{AB} can be written as:

$$\Phi_{AB} = \frac{1}{2}\,\Phi_{A+C} = \frac{1}{2}\,\frac{\mathcal{F}_E}{\mathcal{R}_3/2} = \frac{\mathcal{F}_E}{\mathcal{R}_3} = \mathcal{F}_B \frac{\mathcal{R}_4/2}{\mathcal{R}_1 + \mathcal{R}_3 + \mathcal{R}_4/2} \frac{\mathcal{R}_{eq\,2}}{\mathcal{R}_1 + \mathcal{R}_{eq\,1} + \mathcal{R}_{eq\,2}} \frac{1}{\mathcal{R}_3} = \frac{\mathcal{F}_B}{\mathcal{R}_{AB}} \tag{3.236}$$

$$\mathcal{R}_{AB} = \mathcal{R}_3 \frac{\mathcal{R}_1 + \mathcal{R}_{eq\,1} + \mathcal{R}_{eq\,2}}{\mathcal{R}_{eq\,2}} \frac{\mathcal{R}_1 + \mathcal{R}_3 + \mathcal{R}_4/2}{\mathcal{R}_4/2} = 3.022 \cdot 10^8\,H^{-1} \tag{3.237}$$

[2] Available at the URL https://www.supermagnete.it/data_sheet_S-10-01-N.pdf.

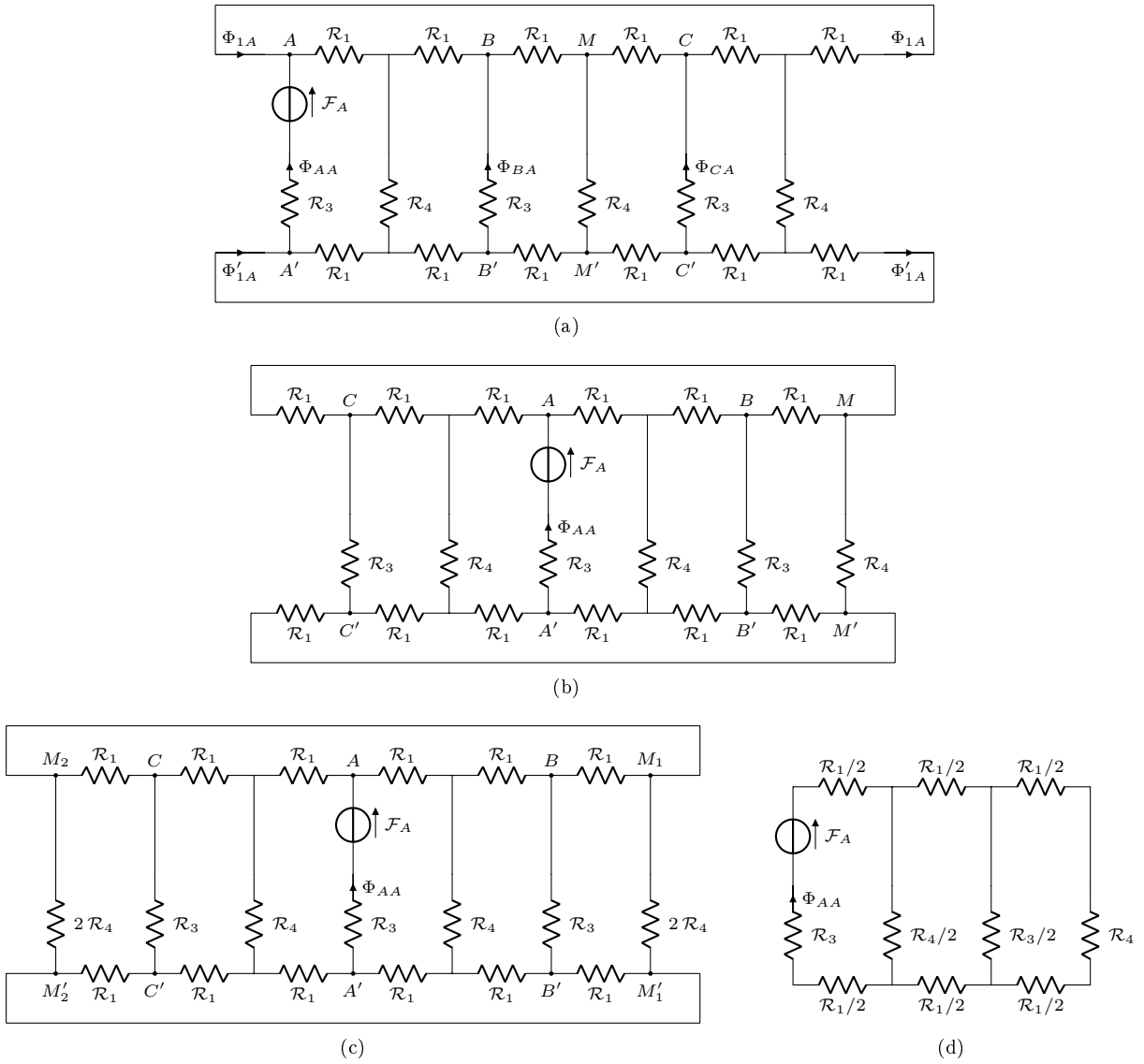

Figure 3.26: Magnetic schematic for contribution of coil 1 to magnetic flux Φ_A. Schematic is given as in general case (a) and is then modified to highlight its symmetry (b to c) to get to the final form (d).

Clearly $\mathcal{R}_{AB}$ can be interpreted as the equivalent reluctance for contribution from coil 2. Finally, flux Φ_{AB} can be evaluated:

$$\Phi_{AB} = \frac{\mathcal{F}_B}{\mathcal{R}_{AB}} = 8.766 \cdot 10^{-8}\, Wb \tag{3.238}$$

The remaining contributions to Φ_A, given by permanent magnets, are evaluated below.

3.2.2.3 Calculation of Φ_{AM1}

Reference magnetic schematic is obtained from general schematic in figure 3.24(b) and shown in figure 3.28(a). It clearly has the same topology as the one for contribution Φ_{AA} in figure 3.26(a), while magnetomotive force is now $\mathcal{F}_{M1}$ and reluctances in sides with permanent magnets are now $\mathcal{R}_5$. Hence, the same steps made for coil 1 contribution are taken in figures 3.28(b) to 3.28(d) to get to the final form for the schematic. Equivalent reluctance $\mathcal{R}_{AM1}$ can then be calculated:

$$\mathcal{R}_{AM1} = \mathcal{R}_1 + \mathcal{R}_5 + \frac{1}{\frac{1}{\mathcal{R}_1 + ((\mathcal{R}_1+\mathcal{R}_6)^{-1} + (\mathcal{R}_3/2)^{-1})^{-1}} + \frac{1}{\mathcal{R}_4/2}} = 3.777 \cdot 10^{7}\, H^{-1} \tag{3.239}$$

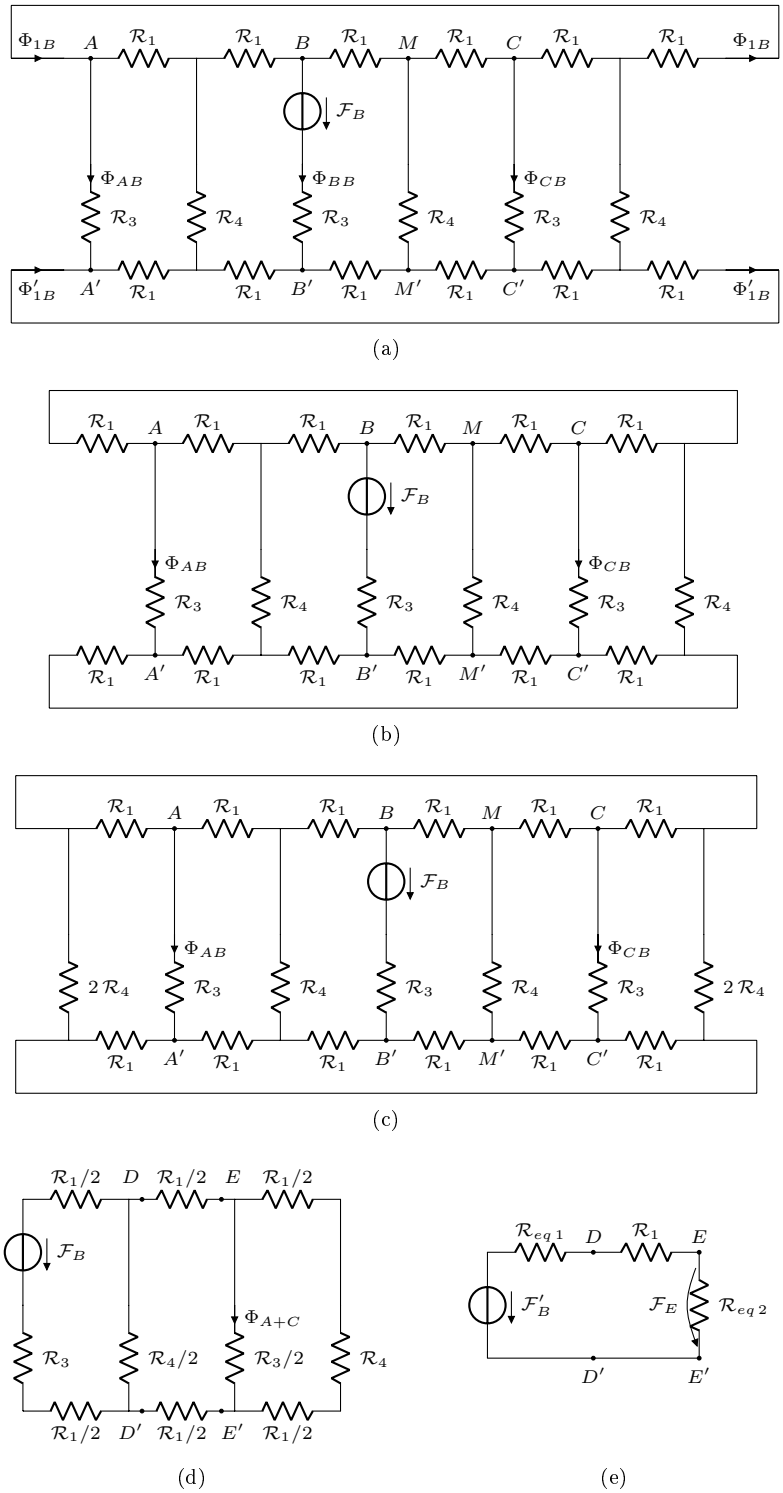

Figure 3.27: Magnetic schematic for contribution of coil 2 to magnetic flux Φ_A. Schematic is given as in general case (a) and is then modified to highlight its symmetry (b to c) which is then exploited to simplify the schematic (d) and the final form is obtained applying the magnetic equivalent of Thévenin's theorem (e).

As permanent magnet material is ferromagnetic, analysis developed in section 3.1.3.3 can be applied to find circuit approximate working point in the $\Phi - \mathcal{F}$ plane. In particular, the intersection between approximate magnet curve and the linear curve representing the rest of the circuit is find, as in figure 3.11(c). It must

be noticed that magnetomotive force $\mathcal{F}_{M1}$ at schematic in figure 3.28(a), following active components sign convention, has opposite sign with respect to magnetomotive force $\mathcal{F}$ in schematic at figure 3.11(a) which follows passive components sign convention. An approximation of flux at intersection Φ_{AM1} is given by equation 3.77:

$$B_r\, S_5 = 1.368 \cdot 10^{-4}\, Wb \tag{3.240}$$

$$\Phi_{AM1} \simeq \min\left\{ \frac{H_c\, \tau_{PM}}{\mathcal{R}_{AM1}}\, ,\, B_r\, S_5 \right\} = 2.423 \cdot 10^{-5}\, Wb \tag{3.241}$$

Where H_c is permanent magnet coercivity and B_r is its remanence. It must be noticed that, since $\Phi_{AM1} < B_r\, S_5$, recalling the $\Phi - \mathcal{F}$ plane in figure 3.11(c), it is confirmed that permanent magnet behaves, with the approximate analysis, as an ideal magnetic voltage generator, as it has been represented in present chapter.

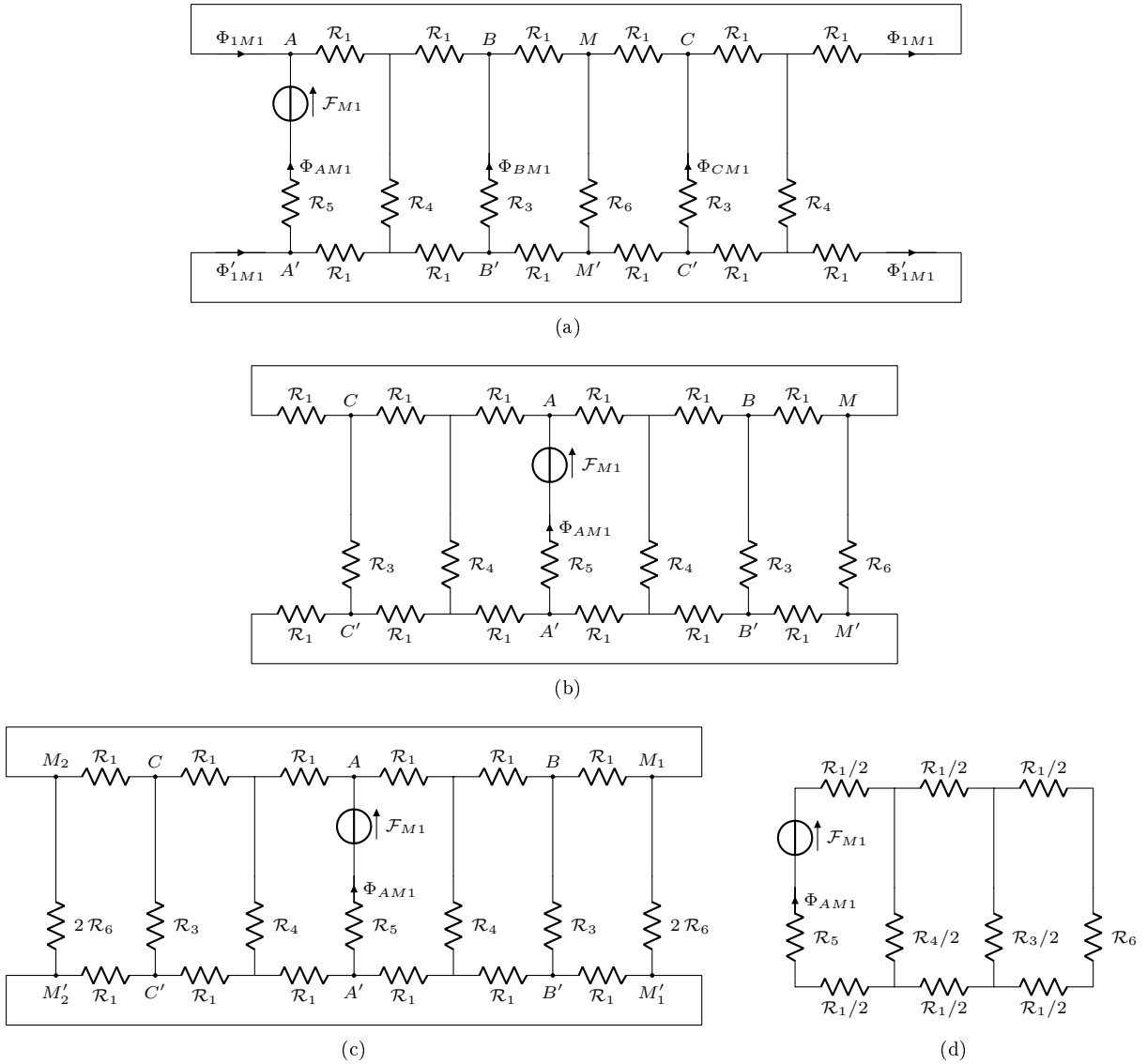

Figure 3.28: Magnetic schematic for contribution of permanent magnet 1 to magnetic flux Φ_A. Schematic is given as in general case (a) and then modified to highlight its symmetry (b to c) to get to the final form (d).

3.2.2.4 Calculation of Φ_{AM2}

Reference magnetic schematic is obtained again from general schematic in figure 3.24(b) and shown in figure 3.29(a). As in previous cases, its symmetry is exploited to get to final form in figure 3.29(c).

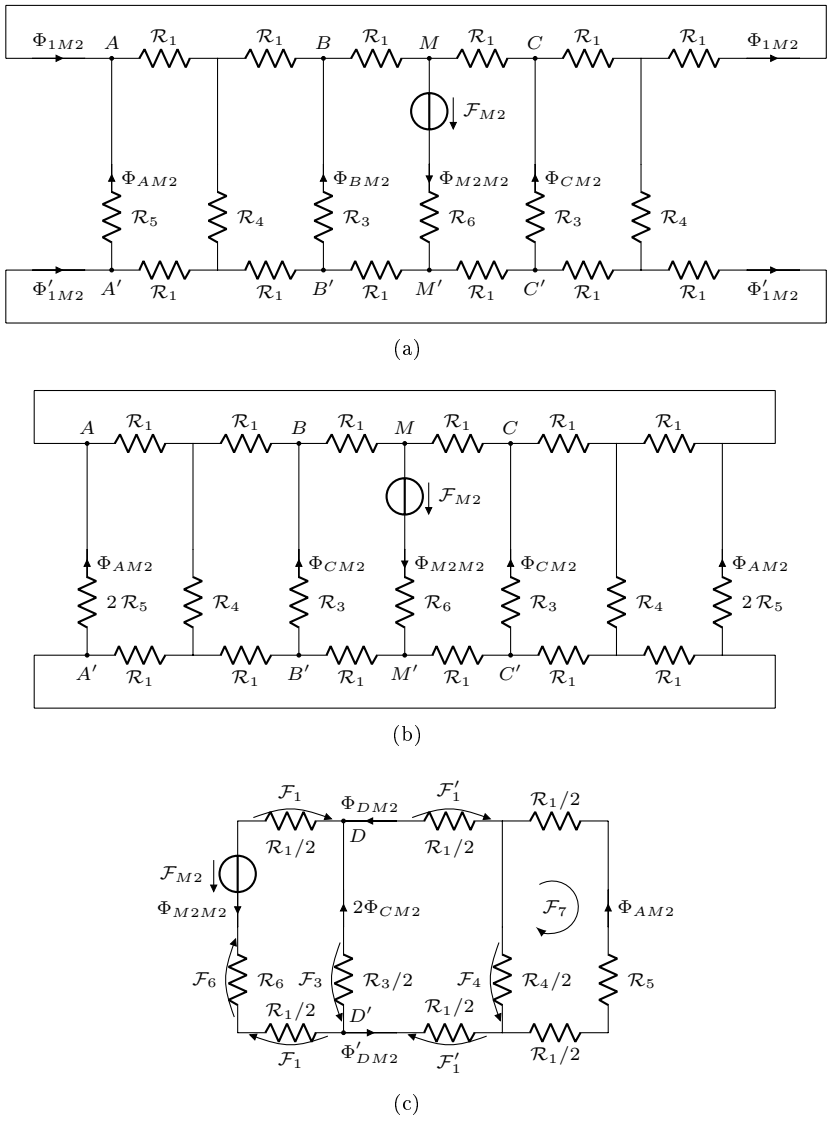

Figure 3.29: Magnetic schematic for contribution of permanent magnet 2 to magnetic flux Φ_A. Schematic is given as in general case (a) and then modified to highlight its symmetry (b) to get to the final form (c).

Equivalent reluctance $\mathcal{R}_{AM2}$, shown in figure 3.25(e), is then calculated:

$$\mathcal{R}_{eq\,1} = \mathcal{R}_1 + \frac{1}{\frac{1}{\mathcal{R}_1+\mathcal{R}_5} + \frac{1}{\mathcal{R}_4/2}} = 1.049 \cdot 10^7\, H^{-1} \tag{3.242}$$

$$\mathcal{R}_{AM2} = \mathcal{R}_1 + \mathcal{R}_6 + \frac{1}{\left((\mathcal{R}_3/2)^{-1} + \mathcal{R}_{eq\,1}^{-1}\right)^{-1}} = 3.045 \cdot 10^7\, H^{-1} \tag{3.243}$$

And equation 3.77 can be used again to find approximate flux Φ_{M2M2}:

$$\begin{aligned} B_r\, S_5 &= 1.368 \cdot 10^{-4}\, Wb \\ \Phi_{M2M2} &\simeq \min\left\{ \frac{H_c\, \tau_{PM}}{\mathcal{R}_{AM2}}\, ,\, B_r\, S_5 \right\} = 3.005 \cdot 10^{-5}\, Wb \end{aligned} \tag{3.244}$$

Where H_c is again magnet's coercivity and B_r its remanence. As for previous case, the fact that $\Phi_{M2M2} < B_r\, S_5$ means that, in the approximate analysis leading to figure 3.11(c), the permanent magnet behaves as an ideal magnetic voltage generator, as it has been represented in the present chapter. Magnetic voltage law is applied

to leftmost loop:

$$\mathcal{F}_{M2} - 2\,\mathcal{F}_1 - \mathcal{F}_3 - \mathcal{F}_6 = 0 \tag{3.245}$$

Magnetic voltage $\mathcal{F}_{M2}$ can be computed exploiting equation 3.78

$$\mathcal{F}_{M2} \simeq |\max\{-H_c\,\tau_{PM}\,,\,-\mathcal{R}_{AM2}\,B_r\,S_5\}| = 9.150 \cdot 10^2\,At \tag{3.246}$$

And magnetic voltage drop $\mathcal{F}_3$ can be reckoned:

$$\mathcal{F}_3 = \mathcal{F}_{M2} - 2\,\mathcal{F}_1 - \mathcal{F}_6 = \mathcal{F}_{M2} - \Phi_{M2M2}\,(\mathcal{R}_1 + \mathcal{R}_6) = 2.016 \cdot 10^2\,At \tag{3.247}$$

And flux $2\Phi_{CM2}$ is then given by Hopkinson's law:

$$2\Phi_{CM2} = \frac{\mathcal{F}_3}{\mathcal{R}_3/2} \tag{3.248}$$

Applying magnetic flux law to nodes D and D', fluxes Φ_{DM2} and Φ'_{DM2} can be obtained:

$$\Phi_{DM2} = \Phi_{M2M2} - 2\Phi_{CM2} = 1.922 \cdot 10^{-5}\,Wb \tag{3.249}$$

$$\Phi'_{DM2} = \Phi_{M2M2} - 2\Phi_{CM2} = \Phi_{DM2} \tag{3.250}$$

Then magnetic voltage law can be applied to central loop:

$$-2\mathcal{F}'_1 + \mathcal{F}_3 - \mathcal{F}_4 = 0 \tag{3.251}$$

And magnetic voltage drop $\mathcal{F}_4$ is found:

$$\mathcal{F}_4 = -2\mathcal{F}'_1 + \mathcal{F}_3 = -\mathcal{R}_1\Phi_{DM2} + \mathcal{F}_3 = 173.687\,At \tag{3.252}$$

Finally, flux Φ_{AM2} can be calculated applying magnetic voltage law to rightmost loop and then Hopkinson's law to rightmost circuit side:

$$\mathcal{F}_4 = \mathcal{F}_7 \tag{3.253}$$

$$\Phi_{AM2} = \frac{\mathcal{F}_7}{\mathcal{R}_1 + \mathcal{R}_5} = 5.490 \cdot 10^{-6}\,Wb \tag{3.254}$$

In conclusion, total magnetic flux Φ_A is given by the sum of partial contributions. Unlike previous calculations, fluxes are considered positive if pointing upwards:

$$\Phi_A = \Phi_{AA} - \Phi_{AB} + \Phi_{AM1} - \Phi_{AM2} = 1.924 \cdot 10^{-5}\,Wb \tag{3.255}$$

Results are summarized in table 3.6. Fluxes and magnetic voltages are considered positive if pointing upwards.

		$\boldsymbol{AA}$	$\boldsymbol{AB}$	$\boldsymbol{AM1}$	$\boldsymbol{AM2}$	$\boldsymbol{A}$
$\boldsymbol{\mathcal{F}}$	$[\boldsymbol{At}]$	26.487	−26.487	—	−915.000	—
$\boldsymbol{\mathcal{R}}$	$[\boldsymbol{10^6\,H^{-1}}]$	44.940	302.200	37.770	30.450	—
$\boldsymbol{\Phi}$	$[\boldsymbol{10^{-6}\,Wb}]$	0.589	−0.088	24.230	−5.490	19.240

Table 3.6: Main results for calculation of flux Φ_A. Magnetic parameters refer to elementary circuits represented in figure 3.25.

3.2.2.5 Iron rings saturation check

The intensity of magnetic fluxes in iron rings has been evaluated with the LTspice® software. The fluxes obtained are then compared with maximum flux Φ_{lim} of equation 3.174 to make sure that saturation of iron rings is avoided, as was mentioned above with equation 3.175:

$$\Phi_{lim} = 1.54 \cdot S_1 = 18.018 \cdot 10^{-6}\, Wb$$
$$|\Phi_{1\,MAX}| \leq \Phi_{lim} \qquad \forall t$$

Contributions of coils and permanent magnets have been separated, according to schematics in figures 3.24(a) and 3.24(b). Correspondent fluxes in iron rings are then summed thanks to superposition principle. Coils contributions have been calculated simulating schematic in figure 3.24(a), with magnetomotive forces $\mathcal{F}_A$ and $\mathcal{F}_B$ corresponding to a total phase voltage V of $2\,V$, as reckoned in equations 3.221-3.226:

$$\mathcal{F}_A = n\, I_{coil} = 26.487\, At$$
$$\mathcal{F}_B = -\mathcal{F}_A = -26.487\, At$$
$$\mathcal{F}_C = 0\, At$$

Clearly, magnetomotive forces are considered positive if pointing upwards. Results are shown in figure 3.30.

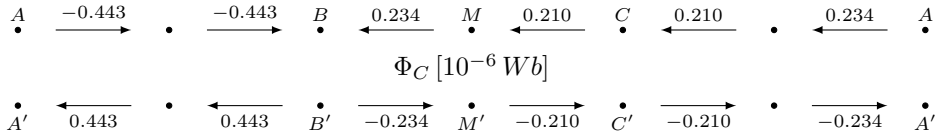

Figure 3.30: Fluxes in iron rings Φ_C due to coils.

To find contributions given by permanent magnets with the schematic in figure 3.24(b), it must be remembered that, in the approximate analysis developed at section 3.1.3.3, they are equivalent to ideal magnetomotive force generators, as it has been shown during calculation of fluxes Φ_{AM1} and Φ_{M2M2} at equations 3.240, 3.241 and 3.244. Thus their magnetomotive forces $\mathcal{F}_{M1}$ and $\mathcal{F}_{M2}$ are given by:

$$\mathcal{F}_{M1} = H_c\, \tau_{PM} = 915\, At \tag{3.256}$$
$$\mathcal{F}_{M2} = -\,H_c\, \tau_{PM} = -915\, At \tag{3.257}$$

Where magnetomotive force is positive when pointing upwards. Simulation of schematic 3.24(b) leads to fluxes shown in figure 3.31.

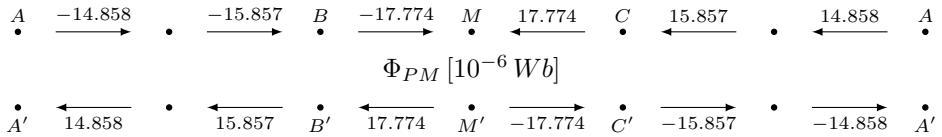

Figure 3.31: Fluxes in iron rings Φ_{PM} due to permanent magnets.

The total magnetic fluxes circulating in iron rings are obtained with the sum of contributions from coils and permanent magnets, thanks to superposition principle. Results are shown in figure 3.32.

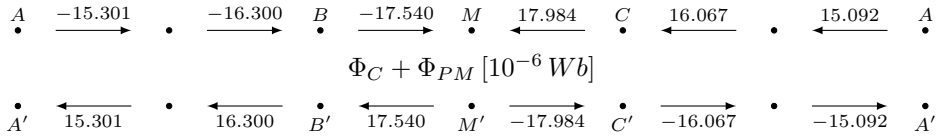

Figure 3.32: Total fluxes in iron rings $\Phi_C + \Phi_{PM}$ due to coils and permanent magnets.

In conclusion, fluxes with maximum modulus $|\Phi_{1\,MAX}|$ occur between nodes M and C and M' and C' and saturation flux intensity Φ_{lim} in iron rings is avoided:

$$\begin{aligned} \Phi_{lim} &= 18.018 \cdot 10^{-6}\, Wb \\ |\Phi_{1\,MAX}| &= 17.984 \cdot 10^{-6}\, Wb \leq \Phi_{lim} \end{aligned} \tag{3.258}$$

As already observed in the present section, the condition under examination does not correspond to a nominal working condition, in terms of permanent magnets angular positions, but produces maximum magnetic fluxes in iron rings.

3.3 Motor electric circuits analysis

In the present section, governing equations for stator electric circuits are found.
According to Axial Flux Permanent Magnet (AFPM) brushless machines standards, stator windings can be defined as single-layer, non-overlap (concentrated coil), iron-cored, salient-pole windings [3]. The number of coils Q_c, the number of phases m_1, the number of pole pairs p and the number of coils per phase n_c is found by CAD model and working principle examination:

$$Q_c = 9 \tag{3.259}$$
$$m_1 = 3 \tag{3.260}$$
$$p = 3 \tag{3.261}$$
$$n_c = 3 \tag{3.262}$$

It is important to recall the working cycle discussed in section 3.2.1, where rotor angle θ was defined. Angle Θ, swept by rotor during one complete currents working cycle was inferred to be 120°. This can also be deduced independently of the particular electric working cycle by observing that coils with the same number belong to the same phase, thus for example coils with number 1 belong to phase 1. Since there are three pole pairs P for each phase, the relation between rotor mechanical angle θ and electrical angle θ_e is:

$$\theta_e = p\,\theta = 3\,\theta \tag{3.263}$$

Thus the mechanical angle $\Theta = 120°$ in electrical degrees is $\Theta_e = 3 \cdot 120°$, corresponding to a complete electrical rotation or a complete currents working cycle, and a complete mechanical rotation $\theta = 360°$ corresponds to three currents working cycles. In the present section null value of mechanical angle θ is arbitrarily chosen to be met when the axes of permanent magnets with south poles towards the inner plate PCB are coincident with the axes of coils of phase 1 (independently from their radii with respect to inner plate PCB), i.e. when rotor is in stage V referring to description in section 3.2.1. Rotor speed ω is obviously the time derivative of mechanical angle θ. Similarly, an electrical angular speed ω_e can be defined as the time derivative of electrical angle θ_e:

$$\omega = \frac{d\theta}{dt} \tag{3.264}$$
$$\omega_e = \frac{d\theta_e}{dt} = p\,\frac{d\theta}{dt} = p\,\omega \tag{3.265}$$

In case of constant angular velocity ω, rotor period T and currents working cycle period T_e can be defined:

$$T = \frac{360°}{\omega} \tag{3.266}$$
$$T_e = \frac{\Theta}{\omega} = \frac{\Theta_e}{\omega_e} = \frac{120°}{\omega} \tag{3.267}$$

Having clarified windings configuration, it is possible to analyze counter-electromotive force, in nominal working conditions, which is essential to evaluate motor performances.

[3] [5, p. 38-40].

3.3.1 Counter-electromotive force

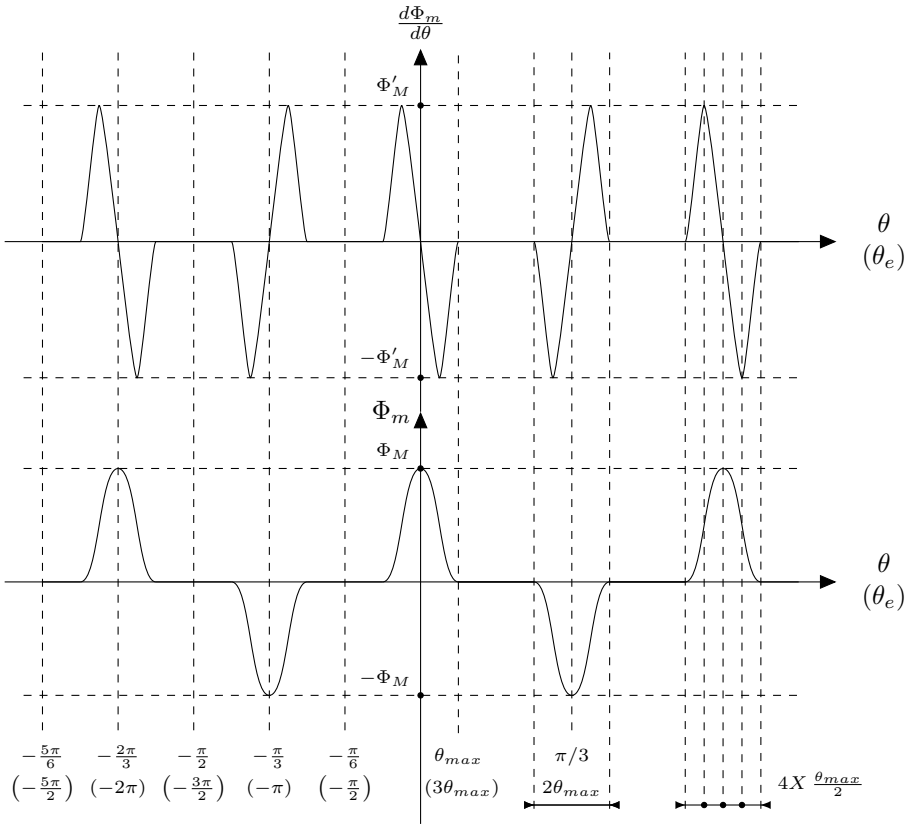

Figure 3.33: Diagrams showing effects of permanent magnets as a function of rotor mechanical angle θ and electrical angle θ_e. Lowermost diagram shows the assumed shape for magnetic flux Φ_m received by one turn of a coil. Uppermost diagram shows flux derivative $d\Phi_m/d\theta$.

Counter-electromotive force is due to time variation of magnetic flux Φ_m induced by permanent magnets in one turn of stator coil. It is useful to represent magnetic flux Φ_m as a function of mechanical and electrical angles. The assumed behaviour for magnetic flux is qualitatively represented in figure 3.33. The correspondent expression is given in equation 3.268 in mechanical angles and in equation 3.269 in electrical angles.

$$\Phi_m \simeq \begin{cases} \frac{1}{2}\,\Phi_M \left[1+\cos\left(\frac{\pi}{\theta_{max}}\theta\right)\right] & \text{if} \quad 0 \le \theta \le \theta_{max} \\ -\frac{1}{2}\,\Phi_M \left\{1+\cos\left[\frac{\pi}{\theta_{max}}\left(\theta-\frac{\pi}{3}\right)\right]\right\} & \text{if} \quad \frac{\pi}{3}-\theta_{max} \le \theta \le \frac{\pi}{3}+\theta_{max} \\ \frac{1}{2}\,\Phi_M \left\{1+\cos\left[\frac{\pi}{\theta_{max}}\left(\theta-\frac{2\pi}{3}\right)\right]\right\} & \text{if} \quad \frac{2\pi}{3}-\theta_{max} \le \theta \le \frac{2\pi}{3} \\ 0 & \text{elsewhere} \end{cases} \tag{3.268}$$

$$\Phi_m \simeq \begin{cases} \frac{1}{2}\,\Phi_M \left[1+\cos\left(\frac{\pi}{\theta_{max,\,e}}\theta_e\right)\right] & \text{if} \quad 0 \le \theta_e \le \theta_{max,\,e} \\ -\frac{1}{2}\,\Phi_M \left\{1+\cos\left[\frac{\pi}{\theta_{max,\,e}}(\theta_e-\pi)\right]\right\} & \text{if} \quad \pi-\theta_{max,\,e} \le \theta_e \le \pi+\theta_{max,\,e} \\ \frac{1}{2}\,\Phi_M \left\{1+\cos\left[\frac{\pi}{\theta_{max,\,e}}(\theta_e-2\pi)\right]\right\} & \text{if} \quad 2\pi-\theta_{max,\,e} \le \theta_e \le 2\pi \\ 0 & \text{elsewhere} \end{cases} \tag{3.269}$$

Φ_M is the maximum positive magnetic flux induced by permanent magnets in one turn of the coil, and

it is assumed to be equal to the sum of the fluxes Φ_{AM1} and Φ_{AM2} found in section 3.2.2:

$$\Phi_M = \Phi_{AM1} + \Phi_{AM2} = 2.9715 \cdot 10^{-5}\, Wb \tag{3.270}$$

Derivatives of flux Φ_m, with respect to mechanical angle θ and electrical angle θ_e are given in equations 3.271 and 3.272 respectively:

$$\frac{d\Phi_m}{d\theta} \simeq \begin{cases} -\frac{1}{2}\Phi_M \frac{\pi}{\theta_{max}} \sin\left(\frac{\pi}{\theta_{max}}\theta\right) & \text{if} \quad 0 \le \theta \le \theta_{max} \\ \frac{1}{2}\Phi_M \frac{\pi}{\theta_{max}} \sin\left[\frac{\pi}{\theta_{max}}\left(\theta - \frac{\pi}{3}\right)\right] & \text{if} \quad \frac{\pi}{3} - \theta_{max} \le \theta \le \frac{\pi}{3} + \theta_{max} \\ -\frac{1}{2}\Phi_M \frac{\pi}{\theta_{max}} \sin\left[\frac{\pi}{\theta_{max}}\left(\theta - \frac{2\pi}{3}\right)\right] & \text{if} \quad \frac{2\pi}{3} - \theta_{max} \le \theta \le \frac{2\pi}{3} \\ 0 & \text{elsewhere} \end{cases} \tag{3.271}$$

$$\frac{d\Phi_m}{d\theta_e} = \frac{1}{p}\frac{d\Phi_m}{d\theta} \tag{3.272}$$

The counter-electromotive force for the whole phase V_{cem} is given by the product of number of coils per phase n_c and number of turns per coil n multiplied by temporal derivative of flux Φ_m:

$$V_{cem} = n_c\, n\, \frac{d\Phi_m}{dt} \tag{3.273}$$

If rotor angular velocity ω is constant, then expression for rotor mechanical angle and counter-electromotive force become:

$$\theta = \omega\, t \tag{3.274}$$

$$V_{cem} = n_c\, n\, \omega \frac{d\Phi_m}{d\theta} = \\ = n_c\, n\, \omega \begin{cases} -\frac{1}{2}\Phi_M \frac{\pi}{\theta_{max}} \sin\left(\frac{\pi}{\theta_{max}}\omega\, t\right) & \text{if} \quad 0 \le t \le \theta_{max}/\omega \\ \frac{1}{2}\Phi_M \frac{\pi}{\theta_{max}} \sin\left[\frac{\pi}{\theta_{max}}\left(\omega\, t - \frac{\pi}{3}\right)\right] & \text{if} \quad \frac{\pi/3 - \theta_{max}}{\omega} \le t \le \frac{\pi/3 + \theta_{max}}{\omega} \\ -\frac{1}{2}\Phi_M \frac{\pi}{\theta_{max}} \sin\left[\frac{\pi}{\theta_{max}}\left(\omega\, t - \frac{2\pi}{3}\right)\right] & \text{if} \quad \frac{2\pi/3 - \theta_{max}}{\omega} \le t \le \frac{2\pi/3}{\omega} \\ 0 & \text{elsewhere} \end{cases} \tag{3.275}$$

Knowing counter-electromotive force expression, stator circuits equations can be written. In order to do this, coils self-inductances $L_{coil\,1,2,3}$ and mutual inductances M are needed. They can be evaluated with the results of section 3.2.2. Self-inductances turn out to be equal among coils:

$$L_{coil\,1} = n\,\frac{\Phi_{AA}}{i_1} = 1.802 \cdot 10^{-6}\, H \tag{3.276}$$

$$L_{coil\,2} = n\,\frac{\Phi_{BB}}{i_2} = n\,\frac{\Phi_{AA}}{i_1} \tag{3.277}$$

$$L_{coil\,3} = n\,\frac{\Phi_{CC}}{i_3} = n\,\frac{\Phi_{AA}}{i_1} \tag{3.278}$$

$$L_{coil\,1} = L_{coil\,2} = L_{coil\,3} = L_{coil} = 1.802 \cdot 10^{-6}\, H \tag{3.279}$$

To be able to write stator circuits equations, phases total self-inductances are needed. Their expression and values are easily found:

$$L = n_c\, L_{coil} = 5.407 \cdot 10^{-6}\, H \tag{3.280}$$

Coils mutual inductances turn out to be all equal:

$$|M_{12}| = \left| n \frac{\Phi_{AB}}{i_2} \right| = 2.681 \cdot 10^{-7}\, H \tag{3.281}$$

$$|M_{13}| = \left| n \frac{\Phi_{AC}}{i_3} \right| = \left| n \frac{\Phi_{CA}}{i_1} \right| = \left| n \frac{\Phi_{AB}}{i_1} \right| = |M_{12}| \tag{3.282}$$

$$|M_{23}| = \left| n \frac{\Phi_{BC}}{i_3} \right| = \left| n \frac{\Phi_{CB}}{i_1} \right| = \left| n \frac{\Phi_{AB}}{i_1} \right| = |M_{12}| \tag{3.283}$$

$$|M_{12}| = |M_{13}| = |M_{23}| = |M| \tag{3.284}$$

Moreover, they are considered to be negligible with respect to self-inductances:

$$M \simeq 0 \tag{3.285}$$

However, stator circuits general equations are obtained, without neglecting mutual inductances. These will be neglected for performances evaluation in next section. The enclosed magnetic fluxes for each stator circuit $\Phi_{e\,1,2,3}$ are clearly given by:

$$\Phi_{e\,1} = L\, i_1 + M(i_2 + i_3) \tag{3.286}$$

$$\Phi_{e\,2} = L\, i_2 + M(i_1 + i_3) \tag{3.287}$$

$$\Phi_{e\,3} = L\, i_3 + M(i_1 + i_2) \tag{3.288}$$

Where numbers in the subscripts represent a stator circuit and not each stator's coils, as for self-inductances at equations 3.276-3.279. Stator circuits are represented in figure 3.34, where coil voltages for the three phases are represented with $V_{1,2,3}$ generators.

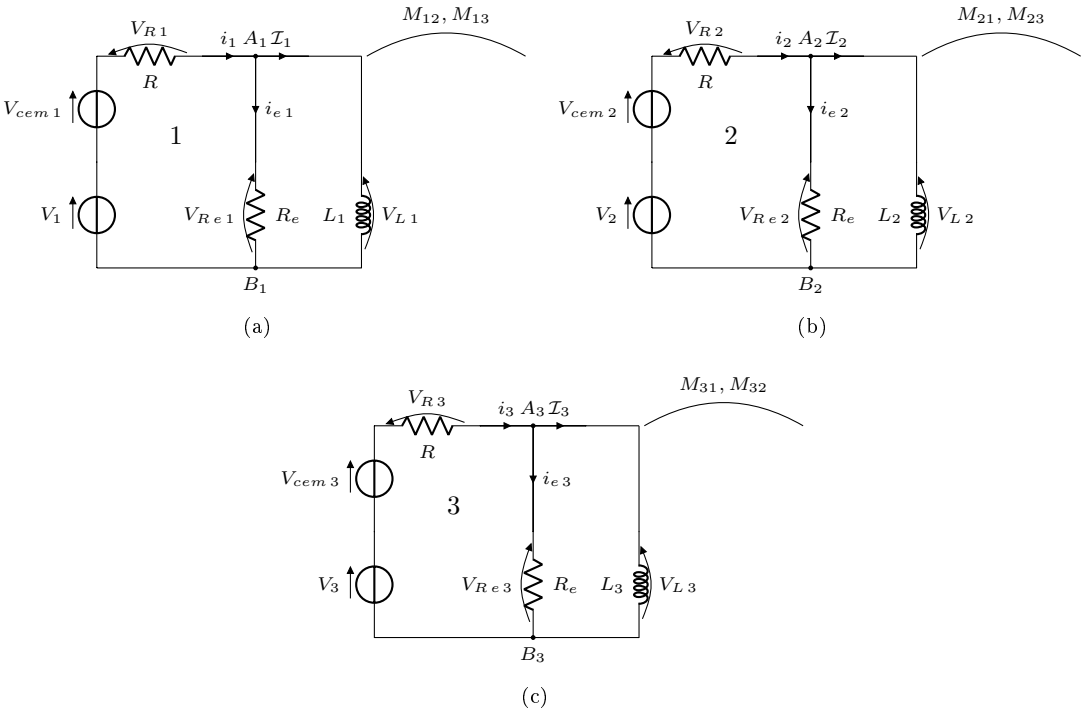

Figure 3.34: Electric schematics for stator circuits.

In conclusion, equations for generic j-th stator circuit are easily found:

$$i_j = i_{e\,j} + \mathcal{I}_j \qquad j = 1,2,3 \tag{3.289}$$

$$V_j + V_{cem\,j} = Ri_j + R_e i_{e\,j} \tag{3.290}$$

$$V_j + V_{cem\,j} = Ri_j + \frac{d\Phi_{e\,j}}{dt} = R_j i_j + L\frac{d\mathcal{I}_j}{dt} + M\sum_{\substack{k=1\\k\neq j}}^{3}\frac{d\mathcal{I}_k}{dt} \tag{3.291}$$

$$R_e i_{e\,j} = \frac{d\Phi_{e\,j}}{dt} = L\frac{d\mathcal{I}_j}{dt} + M\sum_{\substack{k=1\\k\neq j}}^{3}\frac{d\mathcal{I}_k}{dt} \tag{3.292}$$

The phasing between voltages from coils $V_{1,2,3}$ and counter-electromotive force $V_{cem\,1,2,3}$ emerges from working principle examination given at section 3.2.1. A simplifying assumption is made on the angle subtended by permanent magnets θ_{MAX}. According to CAD model, permanent magnets radius is $5\,mm$ and the distance between magnets centers and wheel center is $28\,mm$. Simple geometrical deductions lead to the value for θ_{MAX}:

$$\theta_{MAX} = 2\,\arcsin\left(\frac{5\,mm}{28\,mm}\right) = 20.573^\circ \simeq 20^\circ \tag{3.293}$$

In present section θ_{MAX} has been assumed to be equal to 20°. However this simplification can be avoided in the evaluation of motor performances at the following section, except where specified. Phasing for phase 1 is represented in figure 3.35, with a qualitative representation of V_1 and $V_{cem\,1}$. The correct graphs are calculated and shown in the following section. Phase 2 and 3 have respectively a 40° and 80° lag with respect to phase 1.

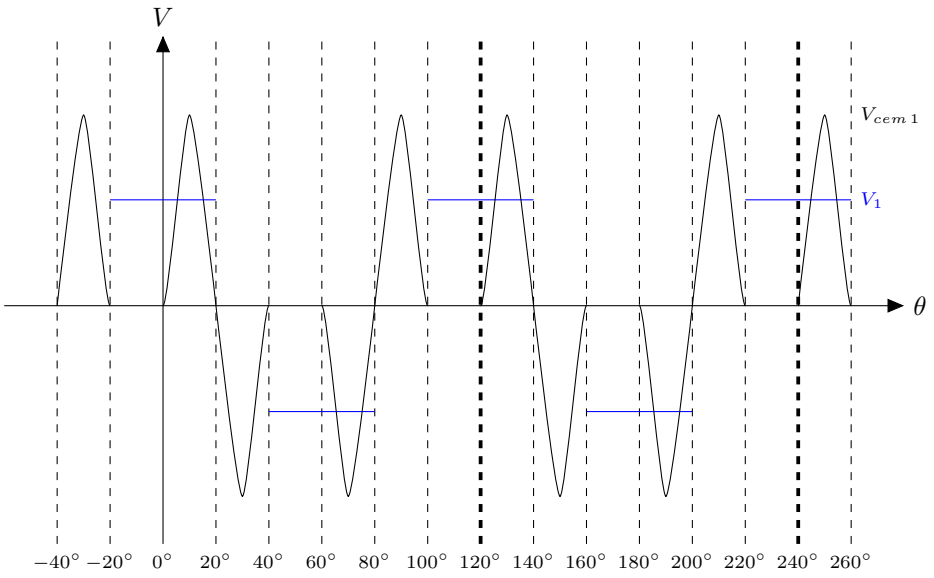

Figure 3.35: Qualitative representation of counter-electromotive force $V_{cem\,1}$ and coil voltage V_1 for phase 1 as a function of mechanical angle θ. Bold dashed lines indicate currents working cycles.

3.4 Performances evaluation

Firstly, fundamental parameters used in present section are recalled:

$$n = 9$$
$$R_{coil} = 0.227\,\Omega$$
$$L_{coil} = 1.802\cdot 10^{-6}\,H$$
$$V = V_{ext} = 2\,V$$

The number of turns per coil n is chosen according to conclusions given below. Coil resistance R_{coil} is calculated according to equation 3.220 at section 3.2.2, coil inductance L_{coil} is taken from equation 3.279 at section 3.3.1. Total phase voltage V is taken according to magnetic circuit analysis at section 3.2.2.
The generic stator electrical circuit can be conceived as in figure 3.36(a). It includes three coils belonging to the generic phase (see figure 3.18). Resulting resistance R and inductance L due to coils were calculated in previous section respectively from coils resistance R_{coil} and inductance L_{coil}:

$$R = n_c\, R_{coil} = 0.681\,\Omega$$
$$L = n_c\, L_{coil} = 5.407 \cdot 10^{-6}\, H$$

Other contributions to circuit resistance and inductance are neglected. As a consequence, circuit time constant τ can be calculated:

$$\tau = L/R = 7.940 \cdot 10^{-6}\, s \tag{3.294}$$

The generator V_{ext} represents external voltage given to coils. Its temporal evolution is represented by a square wave between its peak value, the total phase voltage V, and null voltage. The second generator V_{cem} represents counterelectromotive force described at previous section, with a sinusoidal temporal evolution. It is the sum of the three counterelectromotive forces given by the three coils, as shown in previous section.
Thanks to superposition principle, the total current I can be conceived as the sum of current I_C, given by the square wave generator and due to coils external voltage supply, and the current I_{PM}, given by the sinusoidal wave generator and due to counterelectromotive force induced by permanent magnets:

$$I\,(t) = I_C\,(t) - I_{PM}\,(t) \tag{3.295}$$

Circuits bringing the currents I_C and I_{PM} are represented in figures 3.36(b) and 3.36(c), respectively.

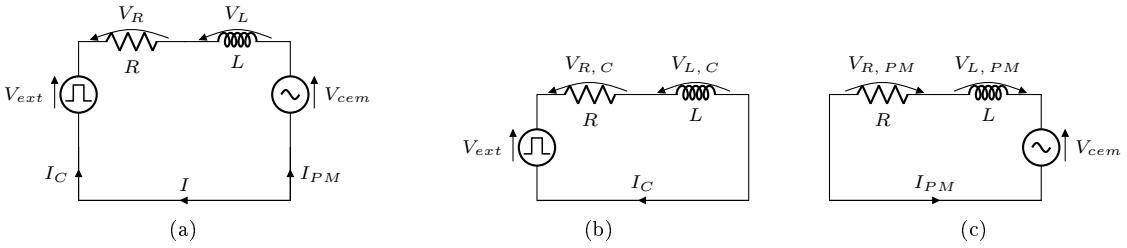

Figure 3.36: Generic stator electric circuit (a) and relative contribution given by coils (b) and permanent magnets (c).

Expressions for current I_C can be immediately found, being the response of an elementary RL circuit undergoing stepwise voltage changes. Supposing that at time $t = 0^-$ voltage is null and at time $t = 0$ the voltage is equal to $V_{ext} = V$, temporal evolution of current I_C is described by the following expression:

$$I_C\,(t) = \frac{V_{ext}}{R} + C_C\, e^{-t/\tau} \tag{3.296}$$

Clearly, the constant C_C depends on current at initial time $I_C(0)$ and on external voltage V_{ext}:

$$C_C = I_C\,(0) - \frac{V_{ext}}{R} \tag{3.297}$$

$$I_C\,(t) = I_C\,(0)\, e^{-\frac{t}{\tau}} + \frac{V_{ext}}{R}\left(1 - e^{-\frac{t}{\tau}}\right) \tag{3.298}$$

If initial current $I_C\,(0)$ is null, clearly final expression is:

$$I_C\,(t) = \frac{V_{ext}}{R}\left(1 - e^{-\frac{t}{\tau}}\right) \tag{3.299}$$

If external voltage is lowered from $V = V_{ext}$ at $t = 0^-$ to null voltage at $t = 0$, clearly the final expression becomes:

$$I_C\,(0) \quad = V_{ext}/R \tag{3.300}$$
$$I_C\,(t) \quad = \tfrac{V_{ext}}{R}\, e^{-\frac{t}{\tau}} \tag{3.301}$$

The expression for counterelectromotive force V_{cem} is recalled and constants K and K_ω are defined:

$$V_{cem} = n_c\, n\, \frac{1}{2}\, \Phi_M \frac{\pi\, \omega}{\theta_{MAX}}\, \sin\left(\frac{\pi}{\theta_{MAX}}\, \omega t\right) = K\, \sin\left(\frac{\pi}{\theta_{MAX}}\, \omega t\right) \tag{3.302}$$

$$K = n_c\, n\, \frac{1}{2}\, \Phi_M \frac{\pi\, \omega}{\theta_{MAX}} = K_\omega\, \omega \tag{3.303}$$

Expression for current I_{PM} has to be found by integration of circuit differential equation:

$$V_{cem} = R\, I + L\, \frac{dI}{dt} \tag{3.304}$$

The general expression can be found, defining the constants K', K'_ω and $\hat{K}$:

$$K' = \frac{1}{\tau}\, \frac{\theta_{MAX}}{\pi\, \omega} = \frac{K'_\omega}{\omega} \tag{3.305}$$

$$\begin{aligned} I_{PM}(t) &= e^{-\frac{t}{\tau}} \left(C_{PM} + \int \frac{V_{cem}}{L} e^{\frac{t}{\tau}}\right) = \\ &= C_{PM}\, e^{-\frac{t}{\tau}} + \frac{K}{L}\, \frac{\frac{\theta_{MAX}}{\pi\, \omega}}{1 + K'^2} \left[-\cos\left(\frac{\pi}{\theta_{MAX}}\, \omega t\right) + K'\, \sin\left(\frac{\pi}{\theta_{MAX}}\, \omega t\right)\right] = \\ &= C_{PM}\, e^{-\frac{t}{\tau}} + \hat{K} \left[-cos\left(\frac{\pi}{\theta_{MAX}}\, \omega t\right) + K'\, sin\left(\frac{\pi}{\theta_{MAX}}\, \omega t\right)\right] \end{aligned} \tag{3.306}$$

Clearly, constant C_{PM} depends on initial current $I_{PM}(0)$ and constant $\hat{K}$, and the final expression becomes:

$$C_{PM} = I_{PM}(0) + \hat{K} \tag{3.307}$$

$$I_{PM}(t) = I_{PM}(0)\, e^{-\frac{t}{\tau}} + \hat{K} \left[e^{-\frac{t}{\tau}} - cos\left(\frac{\pi}{\theta_{MAX}}\, \omega t\right) + K'\, sin\left(\frac{\pi}{\theta_{MAX}}\, \omega t\right)\right] \tag{3.308}$$

If initial current $I_{PM}(0)$ is null, the expression becomes:

$$I_{PM}(t) = \hat{K} \left[e^{-\frac{t}{\tau}} - cos\left(\frac{\pi}{\theta_{MAX}}\, \omega t\right) + K'\, sin\left(\frac{\pi}{\theta_{MAX}}\, \omega t\right)\right] \tag{3.309}$$

If initial current $I_{PM}(0)$ is not null and the voltage V_{cem} becomes null from $t = 0$ on, the expression clearly becomes:

$$I_{PM}(t) = I_{PM}(0)\, e^{-\frac{t}{\tau}} \tag{3.310}$$

As for an ordinary RL transient with a null voltage generator. The above equations will be used in the remainder of present chapter, to evaluate brushless motor performances.

3.4.1 Constant angular velocity

The hypothesis for present section is that motor has a constant angular velocity ω, thus its relation with time t and rotor angle θ is simple:

$$\theta = \omega\, t \tag{3.311}$$

In all equations concerning current I derived above, time t can be easily substituted with rotor angle θ, starting from current contributions:

$$I(\theta) = I_C(\theta) - I_{PM}(\theta) \tag{3.312}$$

General expression for current I_C at equation 3.296 can be given as a function of θ:

$$I_C(\theta) = I_C(0)\, e^{-\frac{\theta}{\omega\, \tau}} + \frac{V_{ext}}{R} \left(1 - e^{-\frac{\theta}{\omega\, \tau}}\right) \tag{3.313}$$

As a consequence, the two particular cases at equations 3.299 and 3.301 become:

$$I_C(\theta) = \frac{V_{ext}}{R} \left(1 - e^{-\frac{\theta}{\omega\, \tau}}\right) \tag{3.314}$$

$$I_C(\theta) = \frac{V_{ext}}{R}\, e^{-\frac{\theta}{\omega\, \tau}} \tag{3.315}$$

The same can be done for current I_{PM}, substituting time t with rotor angle θ in equations 3.308 and 3.309:

$$I_{PM}(\theta) = I_{PM}(0)\, e^{-\frac{\theta}{\omega\,\tau}} + \hat{K}\left[e^{-\frac{\theta}{\omega\,\tau}} - cos\left(\frac{\pi}{\theta_{MAX}}\,\theta\right) + K'\, sin\left(\frac{\pi}{\theta_{MAX}}\,\theta\right)\right] \tag{3.316}$$

$$I_{PM}(\theta) = \hat{K}\left[e^{-\frac{\theta}{\omega\,\tau}} - cos\left(\frac{\pi}{\theta_{MAX}}\,\theta\right) + K'\, sin\left(\frac{\pi}{\theta_{MAX}}\,\theta\right)\right] \tag{3.317}$$

Finally, substitution for counterelectromotive force V_{cem} is straightforward:

$$V_{cem} = K\, \sin\left(\frac{\pi}{\theta_{MAX}}\,\theta\right) \tag{3.318}$$

$$K = K_\omega\,\omega = n_c\, n\, \frac{1}{2}\, \Phi_M\, \frac{\pi\,\omega}{\theta_{MAX}}$$

The above mentioned currents and counterelectromotive force for phase 1 are shown in figure 3.37 for different angular speeds, which are limited to motor maximum speed of $3434\,RPM$. Maximum speed will be identified below and will be used for the rest of the chapter. As mentioned in previous section, for phases 2 and 3 the parameters shown in figure and the respective coil voltages $V_{cem\,2}$ and $V_{cem\,3}$ have a lag of 40° and 80° respectively.

Components powers can then be defined from classical electrotechnics definitions. Powers associated with resistor, inductor, coils and counterelectromotive force are respectively P_R, P_L, P_C and P_{cem} and are defined as:

$$P_R = R\, I^2 = R\,(I_C - I_{PM})^2 \tag{3.319}$$

$$P_L = L\, I\, \frac{dI}{dt} \tag{3.320}$$

$$P_C = V_{ext}\, I \tag{3.321}$$

$$P_{cem} = V_{cem}\, I \tag{3.322}$$

Instantaneous values of power P_R can be evaluated with equation 3.319 and are shown for phase 1 in figure 3.38(c). Thus generic phase circuit power balance can be written:

$$V_{ext}\, I = V_{cem}\, I + L\, I\, \frac{dI}{dt} + R\, I^2 \tag{3.323}$$

The sum of power balances in the three phases circuits can then be written (equation 3.324, where subscripts indicate phases). A simplified power balance for the whole reaction wheel is presented in equation 3.325. It neglects power losses in the iron components, due to magnetic hysteresis, and power losses due to ball bearings friction. Entering power given by coils, $P_C = \sum_{i=1}^{3}(V_{ext}\, I)_i$, is dissipated into heat in the resistor, $R\sum_{i=1}^{3} I_i^2$ and produces mechanical power, expressed as the product of wheel angular velocity ω and torque absorbed by the wheel, T.

$$\sum_{i=1}^{3}(V_{ext}\, I)_i = \sum_{i=1}^{3}(V_{cem}\, I)_i + L\sum_{i=1}^{3}\left(I\,\frac{dI}{dt}\right)_i + R\sum_{i=1}^{3} I_i^2 \tag{3.324}$$

$$P_C = \sum_{i=1}^{3}(V_{ext}\, I)_i = R\sum_{i=1}^{3} I_i^2 + T\,\omega \tag{3.325}$$

The above expressions can be combined together to obtain an equation that expresses mechanical power P_M as a function of electrical parameters:

$$P_M = T\,\omega = \sum_{i=1}^{3}(V_{cem}\, I)_i + L\sum_{i=1}^{3}\left(I\,\frac{dI}{dt}\right)_i \tag{3.326}$$

It is useful to express the mean value in time of mechanical power $\overline{P}_M$. The average value is indicated with a bar and is evaluated in a time interval whose duration is $T = \Delta\theta/\omega = 20°/\omega$, the time required to rotor to

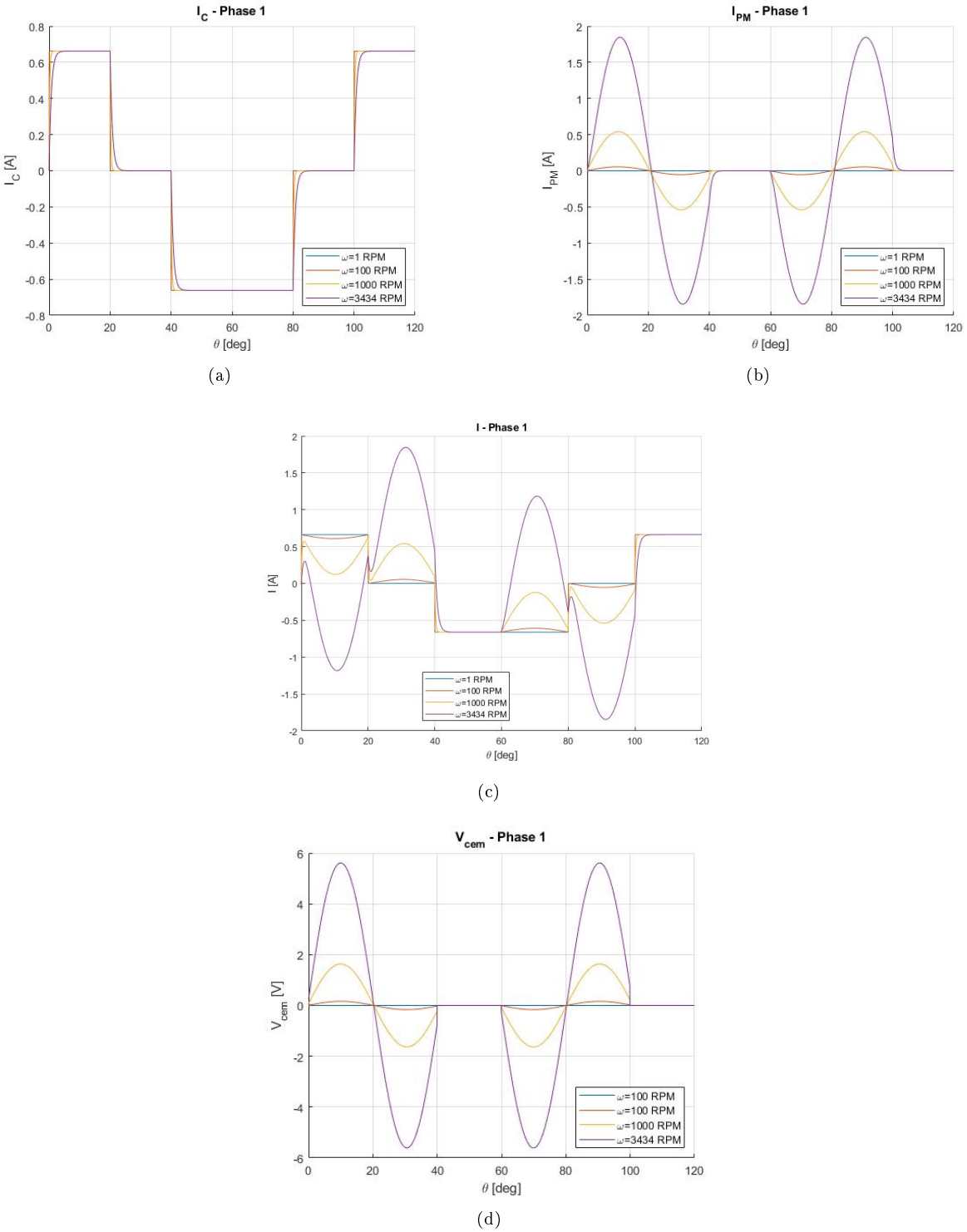

Figure 3.37: Time histories of electrical parameters for phase 1: current due to coils (a) and permanent magnets (b), total current (c) and counterelectromotive force (d).

move between successive stages (defined in equation 3.166):

$$\frac{1}{T}\int_{t=0}^{t=T} T\,\omega\,dt = \frac{1}{T}\int_{t=0}^{t=T}\sum_{i=1}^{3}(V_{cem}\,I)_i\,dt + \frac{1}{T}\int_{t=0}^{t=T} L\sum_{i=1}^{3}\left(I\,\frac{dI}{dt}\right)_i dt \tag{3.327}$$

$$\overline{P}_M = \overline{P}_{cem} + \overline{P}_L \tag{3.328}$$

Mean mechanical power $\overline{P}_M$ is now estimated in the $0° - 20°$ interval, evaluating terms of the equation given above. The angle θ_{MAX} is assumed to be equal to 20°, as explained at section 3.3.1:

$$\theta_{MAX} \simeq 20° \tag{3.329}$$

Firstly, mean power due to counterelectromotive force $\overline{P}_{cem}$ is evaluated. It is the sum of powers from the three phases. However, since currents and voltages in the phases are equal except for a temporal shift, phases 2 and 3 electrical parameters are equal to those of phase 1 in $80° - 100°$ and $40° - 60°$ intervals, respectively. Thus total power due to counterelectromotive force is given by the sum of three terms, that can be referred to phase 1 parameters: the first, $\overline{P}_{cem\,0-20}$, for phase 1, obtained considering the $0° - 20°$ interval parameters and the others, $\overline{P}_{cem\,40-60}$ for phase 3 and $\overline{P}_{cem\,80-100}$ for phase 2 considering the $40° - 60°$ and $80° - 100°$ intervals parameters respectively:

$$\overline{P}_{cem} = \frac{1}{T} \int_{t=0}^{t=T} \sum_{i=1}^{3} (V_{cem}\, I)_i \, dt = \overline{P}_{cem\,0-20} + \overline{P}_{cem\,40-60} + \overline{P}_{cem\,80-100} \tag{3.330}$$

It is clear from figure 3.35 that phase 3 power $\overline{P}_{cem\,40-60}$ is null, since counterelectromotive force is null:

$$\overline{P}_{cem\,40-60} = 0 \tag{3.331}$$

Phase 1 power $\overline{P}_{cem\,0-20}$ can be evaluated with simplified expressions for voltage V_{cem} and current I:

$$\begin{aligned} \overline{P}_{cem\,0-20} &= \frac{1}{T} \int_{t=0}^{t=T} V_{cem}(t)\, I(t)\, dt \simeq \\ &\simeq \frac{1}{T} \int_{t=0}^{t=T} -K \sin\left(\frac{\pi}{\theta_{MAX}}\,\omega t\right) \left\{ \frac{V_{ext}}{R} - \hat{K} \left[-\cos\left(\frac{\pi}{\theta_{MAX}}\,\omega t\right) + K' \sin\left(\frac{\pi}{\theta_{MAX}}\,\omega t\right) \right] \right\} dt \end{aligned} \tag{3.332}$$

The integrals are easily calculated:

$$\begin{aligned} \frac{1}{T} \int_{t=0}^{t=T} -\frac{V_{ext}}{R}\, K \sin\left(\frac{\pi}{\theta_{MAX}}\,\omega t\right) dt &= -\frac{1}{T}\,\frac{V_{ext}}{R}\, K \left[-\cos\left(\frac{\pi}{\theta_{MAX}}\,\omega t\right) \right]_{t=0}^{t=T} \frac{\theta_{MAX}}{\pi\,\omega} = \\ &= -\frac{2}{\pi}\,\frac{V_{ext}}{R}\, K \end{aligned} \tag{3.333}$$

$$\frac{1}{T}\, K\, K'\, \hat{K} \int_{t=0}^{t=T} \sin^2\left(\frac{\pi}{\theta_{MAX}}\,\omega t\right) dt = \frac{1}{2}\, K\, K'\, \hat{K} \tag{3.334}$$

$$-\frac{1}{T}\, K\, \hat{K} \int_{t=0}^{t=T} \sin\left(\frac{\pi}{\theta_{MAX}}\,\omega t\right) \cos\left(\frac{\pi}{\theta_{MAX}}\,\omega t\right) dt = 0 \tag{3.335}$$

Phase 2 power $\overline{P}_{cem\,80-100}$ can be evaluated with the same simplifications:

$$\begin{aligned} \overline{P}_{cem\,80-100} &= \frac{1}{T} \int_{t=0}^{t=T} V_{cem}(t)\, I(t)\, dt \simeq \\ &\simeq \frac{1}{T} \int_{t=0}^{t=T} K \sin\left(\frac{\pi}{\theta_{MAX}}\,\omega t\right) \hat{K} \left[-\cos\left(\frac{\pi}{\theta_{MAX}}\,\omega t\right) + K' \sin\left(\frac{\pi}{\theta_{MAX}}\,\omega t\right) \right] dt \end{aligned} \tag{3.336}$$

The required integrals are trivial:

$$-\frac{1}{T}\, K\, \hat{K} \int_{t=0}^{t=T} \sin\left(\frac{\pi}{\theta_{MAX}}\,\omega t\right) \cos\left(\frac{\pi}{\theta_{MAX}}\,\omega t\right) dt = 0 \tag{3.337}$$

$$\frac{1}{T}\, K\, K'\, \hat{K} \int_{t=0}^{t=T} \sin^2\left(\frac{\pi}{\theta_{MAX}}\,\omega t\right) dt = \frac{1}{2}\, K\, K'\, \hat{K} \tag{3.338}$$

Thus the expression for power $\overline{P}_{cem}$ is:

$$\overline{P}_{cem} \simeq -\frac{2}{\pi}\,\frac{V_{ext}}{R}\, K + K\, K'\, \hat{K} = K \left(-\frac{2}{\pi}\,\frac{V_{ext}}{R} + K'\, \hat{K} \right) \tag{3.339}$$

It can be shown that the neglected terms in voltage V_{cem} and current I produce negligible terms. The neglected power for phase 3 is $\overline{P}_{cem\,40-60\,II}$ and is clearly null:

$$\overline{P}_{cem\,40-60\,II} = 0 \tag{3.340}$$

Neglected power for phase 1, $\overline{P}_{cem\,0-20\,II}$, is given by:

$$\overline{P}_{cem\,0-20\,II} = \frac{1}{T}\,\hat{K}\,K\int_{t=0}^{t=T} e^{-\frac{t}{\tau}}\,\sin\left(\frac{\pi}{\theta_{MAX}}\,\omega t\right)\,dt + \frac{1}{T}\,\frac{V_{ext}}{R}\,K\int_{t=0}^{t=T} e^{-\frac{t+T}{\tau}}\,\sin\left(\frac{\pi}{\theta_{MAX}}\,\omega t\right)\,dt \tag{3.341}$$

Neglected power for phase 2, $\overline{P}_{cem\,80-100\,II}$, is given by:

$$\begin{aligned}\overline{P}_{cem\,80-100\,II} = &-\frac{1}{T}\,\hat{K}\,K\int_{t=0}^{t=T} e^{-\frac{t+T}{\tau}}\,\sin\left(\frac{\pi}{\theta_{MAX}}\,\omega t\right)\,dt + \\ &+\frac{1}{T}\,\frac{V_{ext}}{R}\,K\left(1-e^{-2\frac{T}{\tau}}\right)\int_{t=0}^{t=T} e^{-\frac{t}{\tau}}\,\sin\left(\frac{\pi}{\theta_{MAX}}\,\omega t\right)\,dt\end{aligned} \tag{3.342}$$

Thus total neglected power is given by:

$$\begin{aligned}\overline{P}_{cem\,II} &= \overline{P}_{cem\,0-20\,II} + \overline{P}_{cem\,40-60\,II} + \overline{P}_{cem\,80-100\,II} = \\ &= \frac{K}{\pi}\,\frac{1}{1+\left(\frac{T}{\pi\,\tau}\right)^2}\left(1+e^{-\frac{T}{\tau}}\right)\left[\frac{V_{ext}}{R}\left(1+e^{-\frac{T}{\tau}}-e^{-2\frac{T}{\tau}}\right)+\hat{K}\left(1-e^{-\frac{T}{\tau}}\right)\right] \simeq 0\end{aligned} \tag{3.343}$$

Instantaneous power P_{cem} for phase 1 is represented in figure 3.38(a), and the total instantaneous power is represented in figure 3.39(a). Mean power $\overline{P}_{cem\,II}$ is shown in figure 3.40(c). Clearly, the corresponding mean term $\overline{P}_{cem\,II}$ can be considered negligible. Figure 3.40(a) reports mean power $\overline{P}_{cem}$ as a function of angular velocity ω for different numbers of turns per coil n. This figure has been used to choose n, since $n = 9$ gives an acceptable maximum angular speed without excessive currents in the coils. The maximum speed can be estimated from this figure to be $\omega_{MAX} = 3434\,RPM$.
Mean power due to inductors $\overline{P}_L$, as for power $\overline{P}_{cem}$, is given by the sum of contributions from the three phases: $\overline{P}_{L\,0-20}$ from phase 1, $\overline{P}_{L\,80-100}$ from phase 2 and $\overline{P}_{L\,40-60}$ for phase 3:

$$\overline{P}_L = \frac{1}{T}\int_{t=0}^{t=T} L\sum_{i=1}^{3}\left(I\,\frac{dI}{dt}\right)_i\,dt = \overline{P}_{L\,0-20} + \overline{P}_{L\,40-60} + \overline{P}_{L\,80-100} \tag{3.344}$$

Power from phase 1 turns out to be negligible:

$$\overline{P}_{L\,0-20} = \frac{1}{T}\int_{t=0}^{t=T} L\,I\,\frac{dI}{dt}\,dt = \frac{1}{T}\,\frac{L}{2}\left(I^2(T) - I^2(0)\right) \simeq 0 \tag{3.345}$$

And so is for the other terms:

$$\overline{P}_{L\,40-60} \simeq 0 \tag{3.346}$$

$$\overline{P}_{L\,80-100} \simeq 0 \tag{3.347}$$

With the exact expressions for the currents, the expression for $\overline{P}_{L\,0-20}$ would be:

$$I_C(0) = I_C(T) = \frac{V_{ext}}{R} \tag{3.348}$$

$$I_{PM}(0) \simeq 0 \tag{3.349}$$

$$I_{PM}(T) = -\hat{K}\left(1+e^{-\frac{T}{\tau}}\right) \tag{3.350}$$

$$\overline{P}_{L\,0-20} = \frac{L}{2\,T}\left[\hat{K}^2\left(1+e^{-\frac{T}{\tau}}\right)^2 - 2\,\frac{V_{ext}}{R}\,\hat{K}\left(1+e^{-\frac{T}{\tau}}\right)\right] \tag{3.351}$$

And the expression for $\overline{P}_{L\,40-60}$ would be:

$$I_C(0) = I_{PM}(T) \simeq 0 \tag{3.352}$$

$$I_C(T) = \frac{V_{ext}}{R} \tag{3.353}$$

$$I_{PM}(0) = \hat{K}\left(1 - e^{-2\frac{T}{\tau}}\right) \tag{3.354}$$

$$\overline{P}_{L\,40-60} = \frac{L}{2\,T}\left[\left(\frac{V_{ext}}{R}\right)^2 - \hat{K}^2\left(1 - e^{-2\frac{T}{\tau}}\right)^2\right] \tag{3.355}$$

Finally, expression for $\overline{P}_{L\,80-100}$ would be:

$$I_C(0) = -\frac{V_{ext}}{R} \tag{3.356}$$

$$I_C(T) \simeq 0 \tag{3.357}$$

$$I_{PM}(0) = \hat{K}\left(1 + e^{-\frac{T}{\tau}}\right) \tag{3.358}$$

$$I_{PM}(T) = -\hat{K}\left(1 - e^{-2\frac{T}{\tau}}\right) \tag{3.359}$$

$$\overline{P}_{L\,80-100} = \frac{L}{2\,T}\left[-\left(\frac{V_{ext}}{R}\right)^2 + \hat{K}^2\left(1 - e^{-2\frac{T}{\tau}}\right)^2 - \hat{K}^2\left(1 - e^{-\frac{T}{\tau}}\right)^2 + 2\,\frac{V_{ext}}{R}\,\hat{K}\left(1 + e^{-\frac{T}{\tau}}\right)\right] \tag{3.360}$$

So that the exact expression for mean inductors power $\overline{P}_L$ would be:

$$\overline{P}_L = \overline{P}_{L\,0-20} + \overline{P}_{L\,40-60} + \overline{P}_{L\,80-100} = \frac{L}{2\,T}\,\hat{K}^2\left[\left(1 + e^{-\frac{T}{\tau}}\right)^2 - \left(1 - e^{-\frac{T}{\tau}}\right)^2\right] =$$

$$= 2\,\frac{L}{\Delta\theta}\,\omega\,\hat{K}^2\,e^{-\frac{\Delta\theta}{\omega\,\tau}} \simeq 0 \tag{3.361}$$

Phase 1 contribution to power P_L is represented in figure 3.38(b), and the instantaneous total power is shown in figure 3.39(b). Its mean values as a function of angular speed ω are represented in figure 3.40(b). As can be seen, this term is negligible. Total instantaneous power P_R can be obtained with the sum of phases contributions, which are equal except for a shift in angle θ, and is shown in figure 3.39(c).
Thus complete expression for mean mechanical power $\overline{P}_M$ is:

$$\overline{P}_M \simeq K\left(-\frac{2}{\pi}\,\frac{V_{ext}}{R} + K'\,\hat{K}\right) \tag{3.362}$$

Recalling the terms defined above:

$$K = K_\omega\,\omega \tag{3.363}$$

$$K_\omega = \frac{1}{2}\,n_c\,n\,\Phi_M\,\frac{\pi}{\theta_{MAX}} \tag{3.364}$$

$$K' = K'_\omega/\omega \tag{3.365}$$

$$K'_\omega = \frac{\theta_{MAX}}{\tau\,\pi} \tag{3.366}$$

The expression becomes:

$$\overline{P}_M \simeq -\frac{2}{\pi}\,\frac{V_{ext}}{R}\,K_\omega\,\omega + \frac{K'_\omega}{L}\,K_\omega^2\,\frac{\theta_{MAX}/\pi}{1 + \frac{K'^2_\omega}{\omega^2}} =$$

$$= P_1\,\omega + \frac{P_2}{1 + \frac{K'^2_\omega}{\omega^2}} \tag{3.367}$$

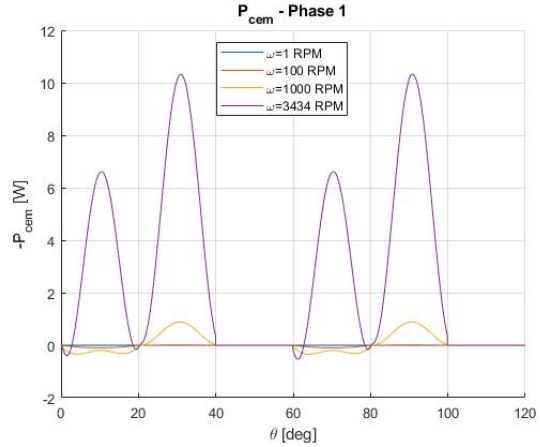

(a)

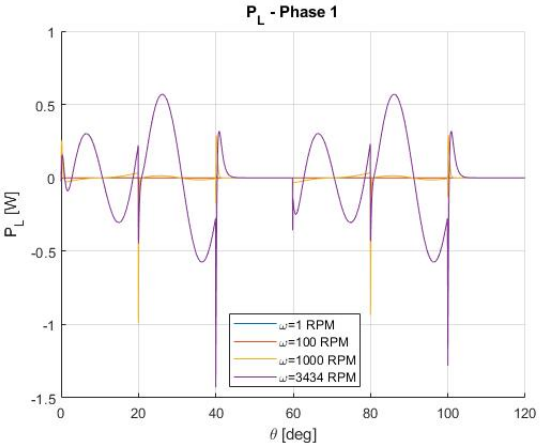

(b)

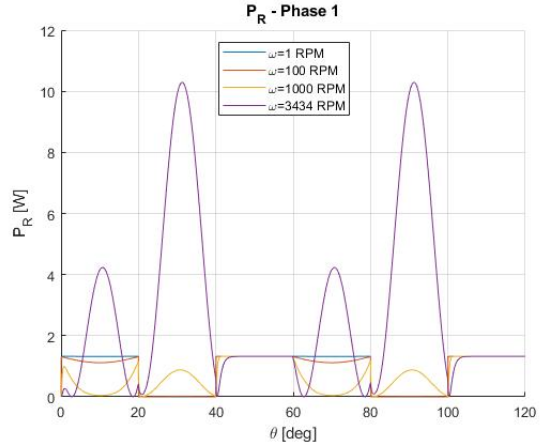

(c)

Figure 3.38: Instantaneous electrical powers for phase 1: counterelectromotive force power (a), inductor power (b) and resistor power (c).

For the MATLAB script described below, it is useful to have an average value of mean power $\overline{P}_M$ between an initial angular velocity ω_{in} and a final angular velocity ω_{fin}. It can be easily reckoned:

$$\Delta\omega = \omega_{fin} - \omega_{in} \tag{3.368}$$

$$\begin{aligned}\overline{P}_{M,\,\omega} &= \frac{1}{\Delta\omega}\int_{\omega=\omega_{in}}^{\omega=\omega_{fin}} \overline{P}_M\, d\omega = \\ &= -\frac{K_\omega}{\pi}\frac{V_{ext}}{R}\,(\omega_{in}+\omega_{fin}) + K'_\omega\frac{K_\omega^2}{L}\frac{\theta_{MAX}}{\pi}\left[1+\frac{K'_\omega}{\Delta\omega}\left(\arctan\frac{\omega_{in}}{K'_\omega} - \arctan\frac{\omega_{fin}}{K'_\omega}\right)\right]\end{aligned} \tag{3.369}$$

Motor efficiency η can be defined as the ratio of mean mechanical power $\overline{P}_M$ and mean power given by coils $\overline{P}_C$:

$$\eta = \frac{\overline{P}_M}{\overline{P}_C} \tag{3.370}$$

$$\overline{P}_C = \frac{1}{T}\int_{t=0}^{t=T}\sum_{i=1}^{3}(V_{ext}\,I)_i\,dt = \overline{P}_{C\,0-20} + \overline{P}_{C\,40-60} + \overline{P}_{C\,80-100} \tag{3.371}$$

Mean power $\overline{P}_C$ can be evaluated as was done with the other mean powers, estimating contributions from each phase. Thus $\overline{P}_C$ can be split in the terms $\overline{P}_{C\,0-20}$, the contribution from phase 1, $\overline{P}_{C\,40-60}$, the contribution from phase 3, and $\overline{P}_{C\,80-100}$, the contribution from phase 2. It is clear from figure 3.35 that mean power $\overline{P}_{C\,80-100}$ is null, since coils voltage is null:

$$\overline{P}_{C\,80-100} = 0 \tag{3.372}$$

The remaining terms $\overline{P}_{C\,0-20}$ and $\overline{P}_{C\,40-60}$ can be estimated evaluating the outcoming integrals:

$$\overline{P}_{C\,0-20} = \frac{1}{T}\int_{t=0}^{t=T} V_{ext}\,(I_C + I_{PM})\,dt \tag{3.373}$$

$$\frac{V_{ext}}{T}\int_{t=0}^{t=T} I_C\,dt = \frac{V_{ext}}{T}\int_{t=0}^{t=T}\frac{V_{ext}}{R}\left(1-e^{-t/\tau}\right)dt = \frac{V_{ext}^2}{RT}\left[T+\tau\left(e^{-\frac{T}{\tau}}-1\right)\right] \tag{3.374}$$

$$\begin{aligned}\frac{V_{ext}}{T}\int_{t=0}^{t=T} I_{PM}\,dt &= \frac{V_{ext}}{T}\int_{t=0}^{t=T} -\hat{K}\left[e^{-\frac{t}{\tau}} - \cos\left(\frac{\pi}{\theta_{MAX}}\,\omega t\right) + K'\sin\left(\frac{\pi}{\theta_{MAX}}\,\omega t\right)\right]dt = \\ &= -\frac{V_{ext}}{T}\,\hat{K}\left[\tau\left(1-e^{-\frac{T}{\tau}}\right) + K'\frac{2\,\theta_{MAX}}{\pi\,\omega}\right]\end{aligned} \tag{3.375}$$

$$\overline{P}_{C\,40-60} = \frac{1}{T}\int_{t=0}^{t=T} -V_{ext}\,(I_C + I_{PM})\,dt \tag{3.376}$$

$$-\frac{V_{ext}}{T}\int_{t=0}^{t=T} I_C\,dt = \frac{V_{ext}^2}{RT}\left[T+\tau\left(e^{-\frac{T}{\tau}}-1\right)\right] \tag{3.377}$$

$$\begin{aligned}-\frac{V_{ext}}{T}\int_{t=0}^{t=T} I_{PM}\,dt &= -\frac{V_{ext}}{T}\int_{t=0}^{t=T}\hat{K}\left(1-e^{-\frac{2\,T}{\tau}}\right)e^{-\frac{t}{\tau}}\,dt = \\ &= -\frac{V_{ext}}{T}\,\hat{K}\,\tau\left(1-e^{-\frac{T}{\tau}}\right)\left(1-e^{-\frac{2\,T}{\tau}}\right)\end{aligned} \tag{3.378}$$

Thus total mean entering power $\overline{P}_C$ expression is:

$$\overline{P}_C = 2\,\frac{V_{ext}^2}{RT}\left[T+\tau\left(e^{-\frac{T}{\tau}}-1\right)\right] - \frac{V_{ext}}{T}\,\hat{K}\left[K'\frac{2\,\theta_{MAX}}{\pi\,\omega} + \tau\left(1-e^{-\frac{T}{\tau}}\right)\left(2-e^{-\frac{2\,T}{\tau}}\right)\right] \tag{3.379}$$

And motor efficiency η can be estimated.
A MATLAB script, reproduced in appendix A, has been prepared to evaluate motor performances, in terms of achievable torques, angular velocities and efficiencies. The correspondent flow chart is reported in figure 3.44. The following phases are considered in the computation:

- Inital inputs are given and initializations are made. Motor parameters include rotor moment of inertia J;
- The inner cycle evaluates motor working point in the $T-\omega$ plane. Computation is made for a swept angle of $20° = \Delta\theta$. Given initial and final angular velocities ω_{in} and ω_f respectively, the mean mechanical power $\overline{P}_{M,\omega}$ is evaluated with equation 3.369. With simple mechanics and kinematics equations, torque T and angular acceleration $\dot{\omega}$ are estimated. The final velocity $\omega_{f,2}$ is estimated and compared to given final velocity ω_f. Depending on the sign of their difference Δ, mean angular velocity $\overline{\omega}$ is corrected for the next cycle of calculation. If the difference Δ is acceptable, the initial velocity ω_{in} is increased by the quantity ω_+, given as an input. Number of iterations it to complete the cycle is recorded, and mean power due to inductors $\overline{P}_L$ is evaluated with equation 3.361 and efficiency η is reckoned, with equations 3.370 and 3.379;
- The outer cycle increments the inital angular speed ω_{in} from its minimum value ω_{MIN} to its maximum value, ω_{MAX}, both given as initial inputs, and initializes variables for the inner cycle. Working points are given considering mean angular velocity $\overline{\omega}$.

Results are given in figures 3.41(a), 3.42(c), 3.42(b) and 3.43.

3.4.2 Constant angular acceleration

A second model assuming rotor in constant angular acceleration was made to verify results of previous model. Rotor angular velocity ω and angular position θ are then influenced by angular acceleration $\dot{\omega}$:

$$\omega = \omega_0 + \dot{\omega}\, t \tag{3.380}$$

$$\theta = \omega_0\, t + \frac{1}{2}\,\dot{\omega}\, t^2 \tag{3.381}$$

Where ω_0 is initial angular velocity. A considerable increase in problem complexity arises from these assumptions, since magnetic flux for one turn of a coil $\Phi_m(t)$ has the following expression:

$$\Phi_m(t) = \Phi_M \cos\left[\frac{\pi}{\theta_{MAX}}\left(\omega_0\, t + \frac{1}{2}\,\dot{\omega}\, t^2\right)\right] \tag{3.382}$$

Consequently, counterelctromotive force assumes the following expression:

$$\begin{aligned} V_{cem}(t) &= n_c\, n\, \frac{1}{2}\,\Phi_M \frac{d}{dt} \cos\left[\frac{\pi}{\theta_{MAX}}\left(\omega_0\, t + \frac{1}{2}\,\dot{\omega}\, t^2\right)\right] = \\ &= n_c\, n\, \frac{1}{2}\,\Phi_M \left\{-\sin\left[\frac{\pi}{\theta_{MAX}}\left(\omega_0\, t + \frac{1}{2}\,\dot{\omega}\, t^2\right)\right] \frac{\pi}{\theta_{MAX}}\,(\omega_0 + \dot{\omega}\, t)\right\} = \\ &= -K_\omega\,\,(\omega_0 + \dot{\omega}\, t)\,\sin\left[\frac{\pi}{\theta_{MAX}}\left(\omega_0\, t + \frac{1}{2}\,\dot{\omega}\, t^2\right)\right] \end{aligned} \tag{3.383}$$

As a consequence, equation 3.304:

$$V_{cem} = R\, I + L\,\frac{dI}{dt}$$

Cannot be solved analytically to obtain current I_{PM} and has to be solved numerically, and represents a stiff numerical problem. Therefore, the MATLAB script, given in appendix A, has been written directly and the correspondent flow chart is reported in figure 3.45. It can be divided in the following stages:

- Initializations are made and inputs are given. In particular, rotor moment of inertia J is given as a motor input;
- In the inner cycle, motor working point in the $T-\omega$ plane and mean powers $\overline{P}_{cem}$ and $\overline{P}_L$ are evaluated. The computation is always made for a swept angle of $20° = \Delta\theta$. Final angular velocity ω_{fin} is obtained from the initial velocity ω_{in} and angular acceleration $\dot{\omega}$. Time $\Delta\, t$ to sweep the angle $\Delta\,\theta$ is calculated according to the following equations:

$$0 = \frac{1}{2}\dot{\omega}\Delta t^2 + \omega_{in}\,\Delta t - \Delta\theta \tag{3.384}$$

$$\Delta = \omega_{in}^2 + 2\dot{\omega}\,\Delta\,\theta \tag{3.385}$$

$$\Delta t = \frac{-\omega_{in} + \sqrt{\Delta}}{\dot{\omega}} \tag{3.386}$$

Then current $I_{PM\,0-20}$ is evaluated numerically with the ode15s solver, then the solution is interpolated with a global polynomial. Spurious oscillation of the polynomial have been monitored and are considered negligible. Mean power P_{cem} is then evaluated by numerical integration with the following expression:

$$\overline{P}_{cem} \simeq \frac{1}{\Delta t} \int_{t=0}^{t=\Delta t} V_{cem} \left(I_{PM\,0-20} + V_{ext,\,P}/R \right) dt \tag{3.387}$$

$$V_{ext,\,P} = 2\,V \tag{3.388}$$

Where $V_{ext,\,P}$ is the peak value for voltage given to coils V_{ext}. Then, with equations similar to those given above, time interval Δt_2 is estimated. It is the time required to sweep a further angle $\Delta\theta$ starting from speed ω_f. This quantity is required to numerically evaluate the current $I_{PM\,20-40}$ with the ode15s solver. This current is then interpolated with a global polynomial and used to evaluate average power $\overline{P}_L$ with the following expression:

$$\overline{P}_L = \frac{1}{2}\frac{L}{\Delta t}\left[2I_{PM\,f1}^2 + I_{PM\,f2}^2 \left(e^{-2\frac{\Delta t}{\tau}} - 1 \right) + 2\frac{V_{ext,\,P}}{R} \left(-I_{PM\,f1} + I_{PM\,f2}\, e^{-\frac{\Delta t}{\tau}} \right) \right] \tag{3.389}$$

$$I_{PM\,f1} = I_{PM}(\Delta t) \tag{3.390}$$

$$I_{PM\,f2} = I_{PM}(\Delta t + \Delta t_2) \tag{3.391}$$

Then, with simple mechanics and kinematics equations, torque T and angular acceleration $\dot{\omega}_2$ are obtained. The difference $diff_2$ between the final velocity ω_{fin} and $\omega_{in} + \dot{\omega}_2 \Delta t$ is evaluated. The difference $diff$ between $\dot{\omega}_2$ and $\dot{\omega}$ is evaluated as well, and angular acceleration $\dot{\omega}$ is corrected according to the sign of $diff$. If $diff$ has an acceptable value, the cycle is completed. The number of iterations it is computed and efficiency η is evaluated as in previous algorithm, however mean power $\overline{P}_C$ is approximated:

$$\overline{P}_C \simeq 2\,\frac{V_{ext}^2}{RT}\left[T + \tau \left(e^{-\frac{T}{\tau}} - 1 \right) \right] \tag{3.392}$$

- The outer cycle increments initial angular velocity ω_{in} from minimum value ω'_{MIN}, to maximum value ω'_{MAX}, both given as initial inputs, and initializes variables for the inner cycle. Working points are given considering mean angular velocity $\overline{\omega}$.

Results are presented in figures 3.41(b), 3.41(c), 3.42 and 3.43.

3.5 Conclusions

Figure 3.43 assures that computation cycles for the two models, with constant angular angular velocity and constant angular acceleration, have converged correctly, as the numbers of iterations are always inferior to maximum allowed value. The constant angular acceleration model, correctly, did not converge for a velocity $\omega_{in} = 3500\,RPM$, as motor maximum angular speed, as can be inferred from figure 3.40(a), is $\omega_{MAX} = 3434\,RPM$. Moreover, the figure shows clearly that computational cost for the constant angular acceleration model is major than cost of the other model, especially recalling that each iteration of the constant acceleration model involves two numerical integrations. Figures 3.41(a) and 3.41(b) confirm that error has always been under maximum values, except for the above mentioned speed in the case of constant angular acceleration. For this model, difference $diff_2$ between angular velocities in each computation cycle is shown in figure 3.41(c) and is considered acceptable.
Figure 3.42(a) shows that mean power due to inductors $\overline{P}_L$ is negligible with respect to mean power due to counterelectromotive force $\overline{P}_{cem}$ for the case of constant angular acceleration, as was for the constant angular velocity analysis. Working curves and efficiencies for both models, shown in figures 3.42(c) and 3.42(b) respectively, appear to be in good agreement. Two important performance parameters can be identified, maximum angular velocity or no load speed ω_{MAX} and maximum torque or stall torque T_{MAX}:

$$\omega_{MAX} = 3434\,RPM \tag{3.393}$$

$$T_{MAX} = 6.525 \cdot 10^{-3}\,Nm \tag{3.394}$$

Clearly, the wheel can be spun in the opposite direction, thus it has a minimum angular speed ω_{min} which is the opposite of ω_{MAX}:

$$\omega_{min} = -3434\,RPM \tag{3.395}$$

Saturation momentum H_{sat} is given by the product of wheel moment of inertia, J and its maximum speed:

$$H_{sat} = J\,\omega_{MAX} = 5.636 \cdot 10^{-3}\,Nms \tag{3.396}$$

Which is comparable with present, commercial, 1U CubeSats reaction wheels saturation momenta.
However, motor efficiency is very poor. For the constant angular velocity case, maximum efficiency η_{MAX} and the corresponding angular velocity $\omega_{\eta\,MAX}$ are the following:

$$\eta_{MAX} = 5.704\% \tag{3.397}$$

$$\omega_{\eta\,MAX} = 1836\,RPM \tag{3.398}$$

While maximum efficiency should be around 40%. The reason lies in equation 3.312:

$$I\,(\theta) = I_C\,(\theta) - I_{PM}\,(\theta)$$

And in the shapes of voltages V_{cem}, due to counterelectromotive force, and V, given to coils, shown for phase 1 in figure 3.35. Considering phase 1 and one complete cycle between 0° and 120°, there is no coil voltage to compensate counterelectromotive force in the intervals $20° - 40°$ and $80° - 100°$. As a consequence, the total current I in these intervals is major than in the rest of the cycle, as can be seen in figure 3.37(c). The large current, passing through the resistor, causes a considerable power P_R, with respect to the rest of the cycle, as shown in figure 3.38(c). This power is dissipated and does not produce mechanical power (equation 3.325). A possible solution would be to adopt the voltages scheme qualitatively shown in figure 3.46: This scheme requires more permanent magnets than the six in version 1. Thus magnetic circuit analysis should be repeated, and performances must be evaluated again. This option is not adopted, although it could be possible for future work.
Instead, Maxon commercial AFPM motors are chosen. As mentioned in chapter 1, at section 1.1.2, the EC 10 flat[4] motor has been initially chosen, and went out of production during design phase. Thus the EC 32 flat[5] motor has been adopted for the rest of the project, although it is not optimal from a mass and dimensions point of view. Their maximum efficiencies are 41% and 55%, respectively. Their maximum speeds and torques are given below:

$$\omega_{MAX\,EC10} = 16600\,RPM \tag{3.399}$$

$$\omega_{MAX\,EC32} = 9210\,RPM \tag{3.400}$$

$$T_{MAX\,EC10} = 0.202 \cdot 10^{-3}\,Nm \tag{3.401}$$

$$T_{MAX\,EC32} = 15.500 \cdot 10^{-3}\,Nm \tag{3.402}$$

To evaluate saturation momenta, rotors moments of inertia J_R have to be taken into account:

$$J_{R\,EC10} = 0.080 \cdot 10^{-7}\,kgm^2 \tag{3.403}$$

$$J_{R\,EC32} = 13.900 \cdot 10^{-7}\,kgm^2 \tag{3.404}$$

Thus saturation momenta can be obtained:

$$H_{sat\,EC10} = (J + J_{R\,EC10})\,\omega_{MAX\,EC10} = 27.257 \cdot 10^{-3}\,Nms \tag{3.405}$$

$$H_{sat\,EC32} = (J + J_{R\,EC32})\,\omega_{MAX\,EC32} = 16.455 \cdot 10^{-3}\,Nms \tag{3.406}$$

They are clearly satisfying, although the mass of EC 32 flat motor can be considered excessive, as shown in tile mass breakdown at section 4.2.2. Indeed, the mass of EC 32 flat motor is major than the mass of the wheel. For future work, it would be advantageous to modify autonomously built motor as explained above.
In conclusion, motors working curves are presented in figure 3.47.

[4] Datasheet URL: https://www.maxonmotor.com/medias/sys_master/root/8825428344862/17-EN-255.pdf.
[5] Datasheet URL: https://www.maxonmotor.com/medias/sys_master/root/8825434800158/17-EN-262.pdf.

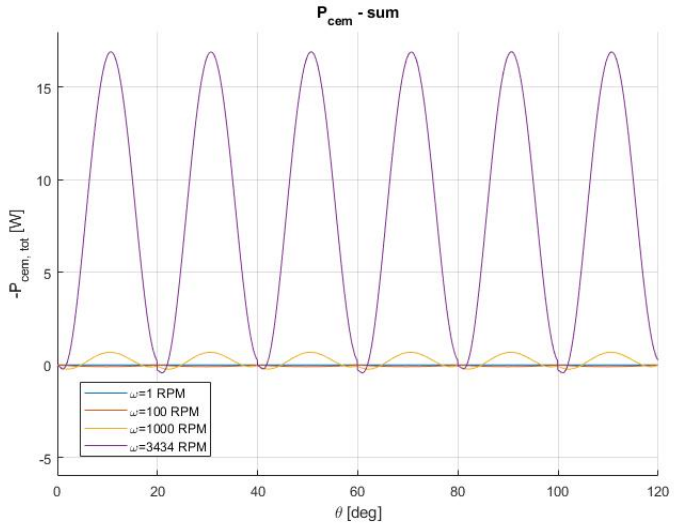

(a)

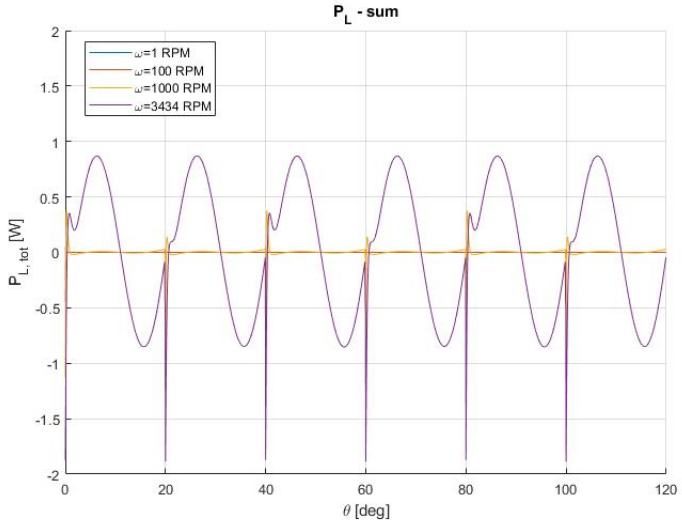

(b)

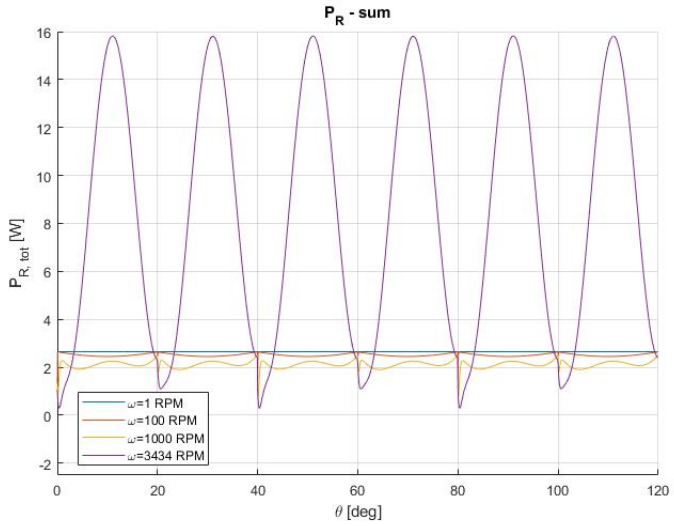

(c)

Figure 3.39: Instantaneous total electrical powers: counterelectromotive force power (a), inductor power (b) and resistor power (c).

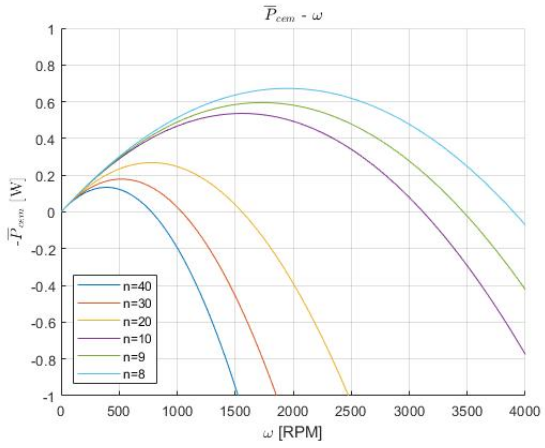

(a)

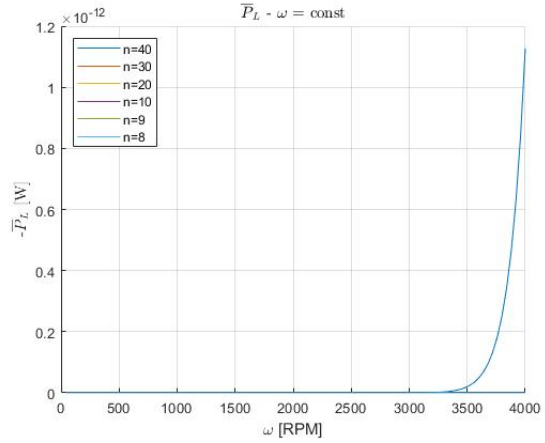

(b)

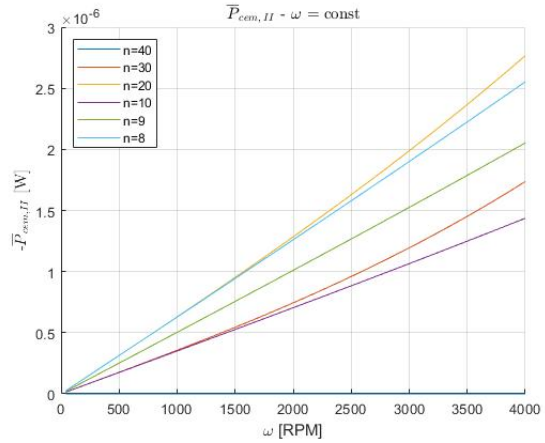

(c)

Figure 3.40: Mean total electrical powers for constant angular velocity case: counterelectromotive power (a), inductive power (b) and complementary term for counterelectromotive power (c).

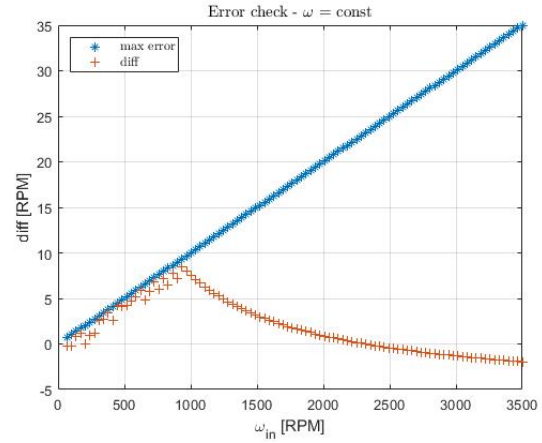

(a)

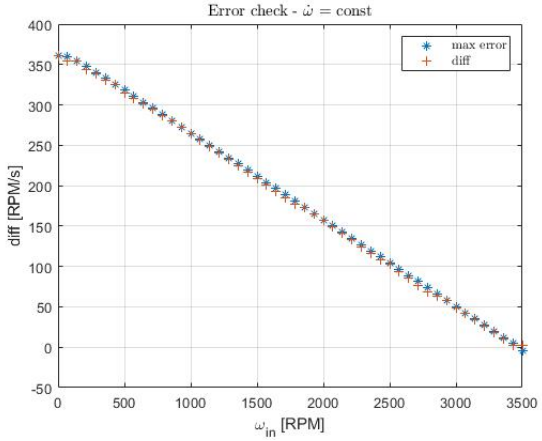

(b)

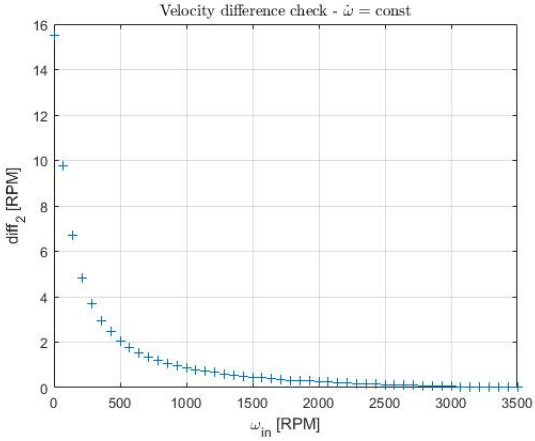

(c)

Figure 3.41: Error checks for constant angular velocity case (a) and constant angular acceleration case (b) and velocity difference check for constant angular acceleration case (c).

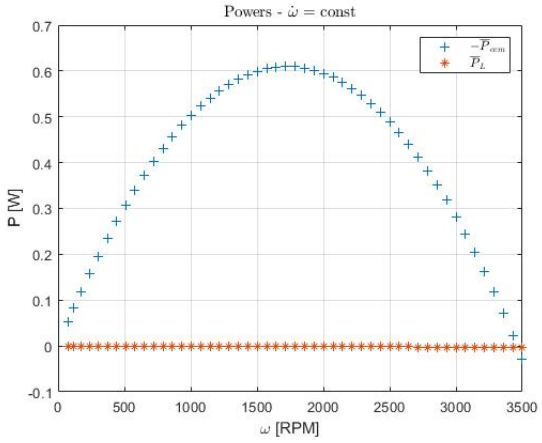

(a)

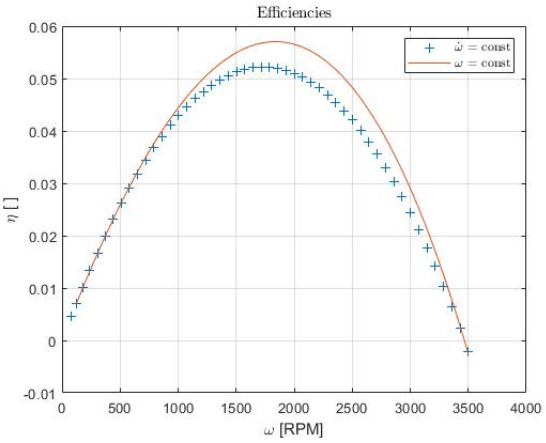

(b)

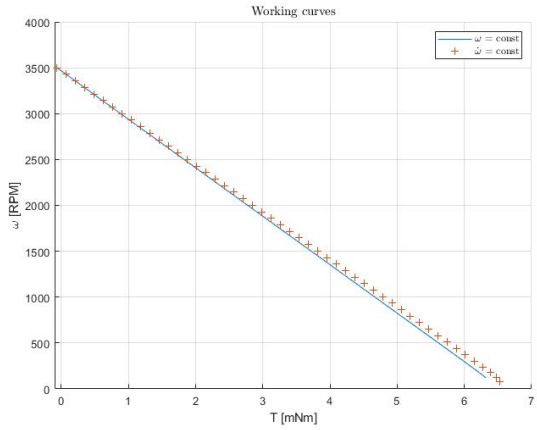

(c)

Figure 3.42: Results for constant angular velocity and acceleration cases: electrical powers for constant angular acceleration case (a), efficiencies (b) and working curves (c) for both cases. Torque T is given in milli-newton-metres.

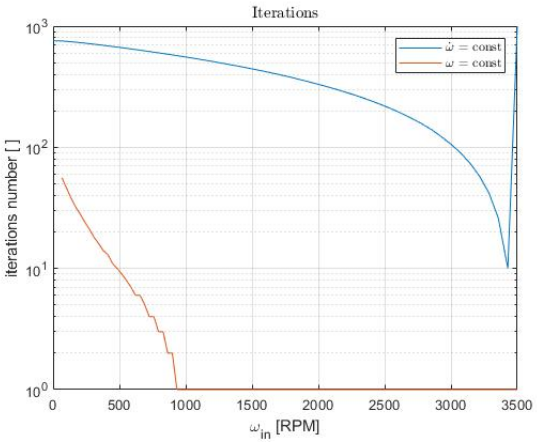

Figure 3.43: Number of iterations as a function of initial angular velocities for constant angular velocity and acceleration cases.

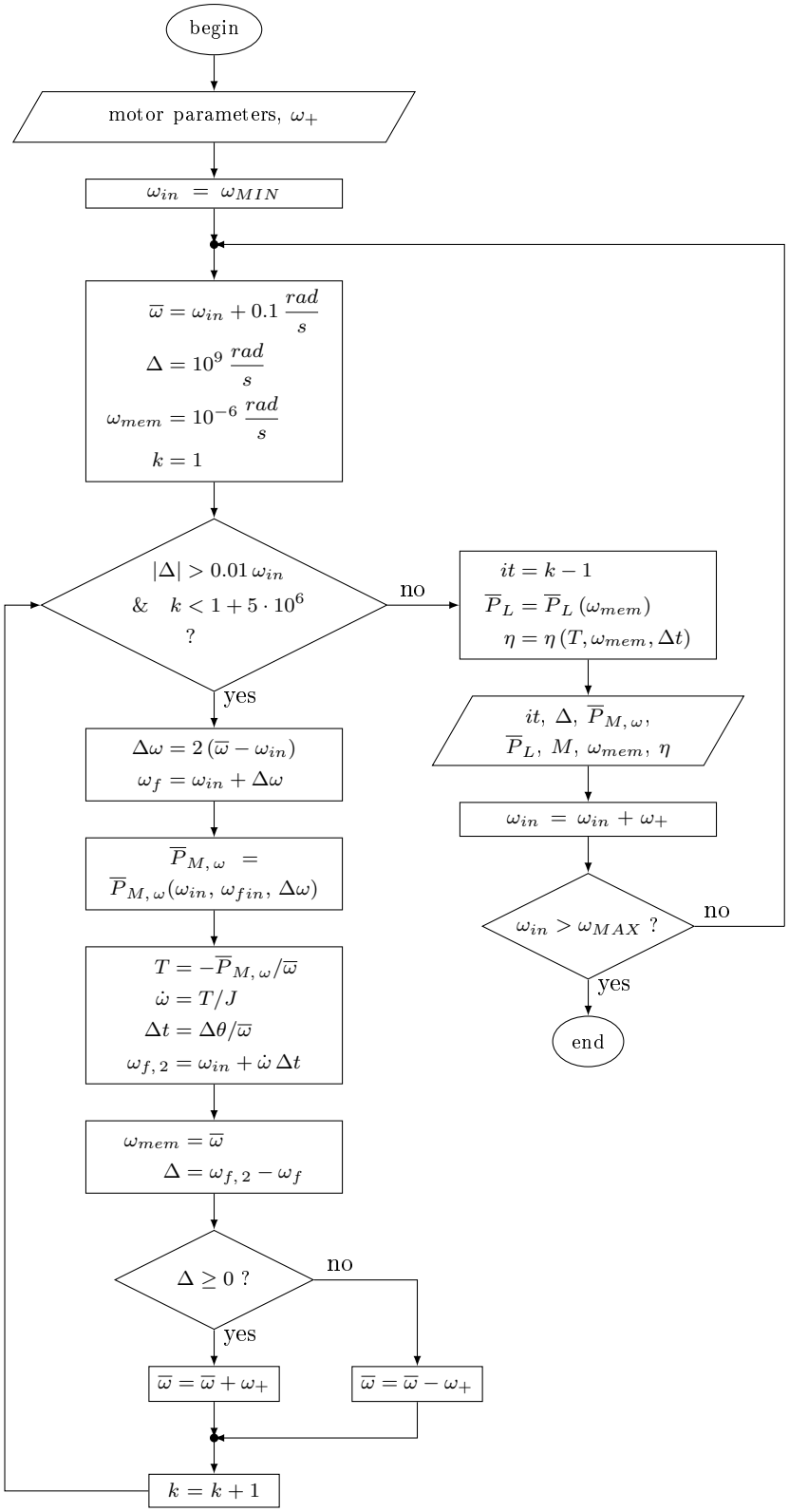

Figure 3.44: Flow chart for motor performance evaluation algorithm, for constant angular velocity case.

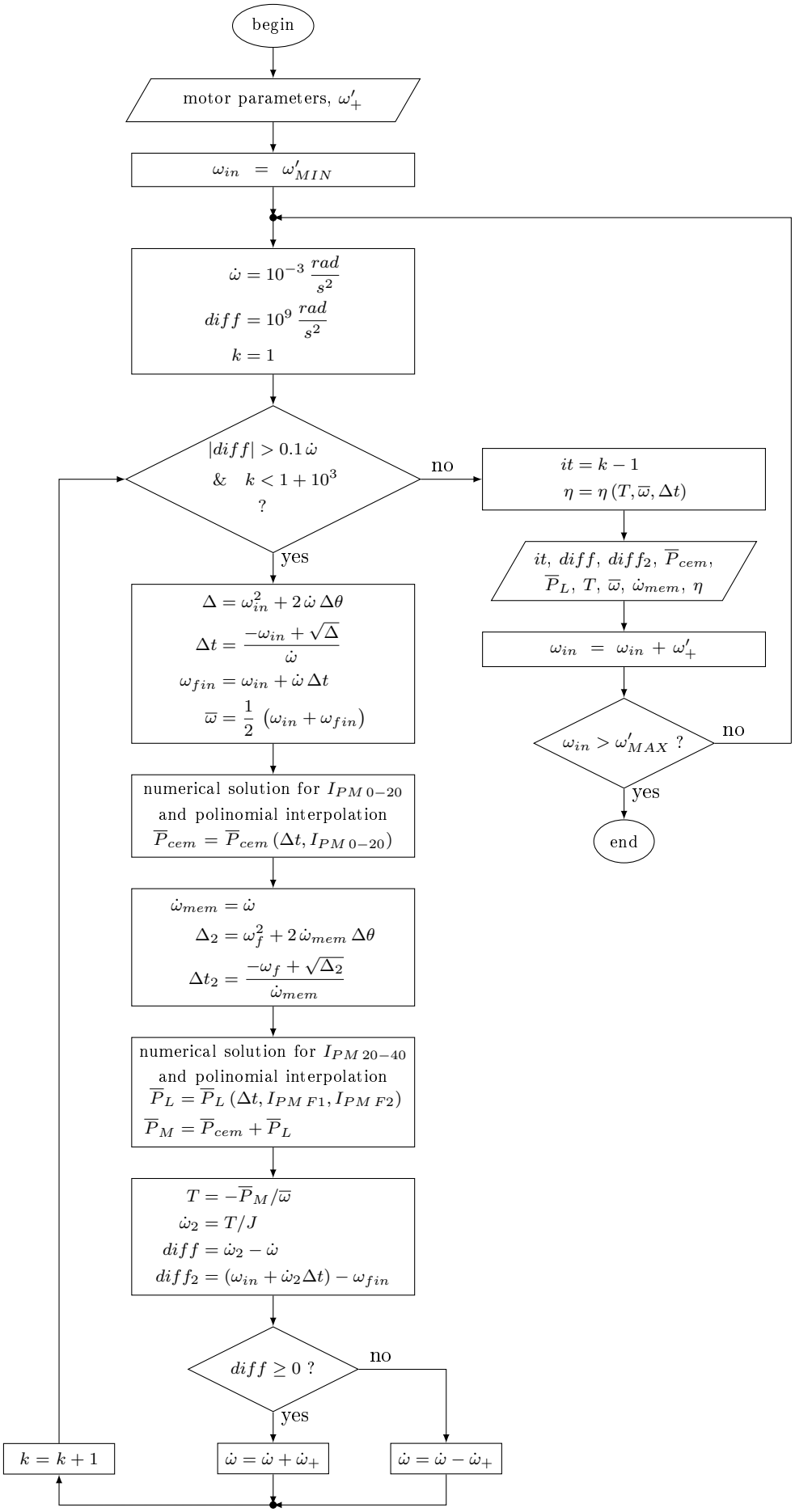

Figure 3.45: Flow chart for motor performance evaluation algorithm, for constant angular acceleration case.

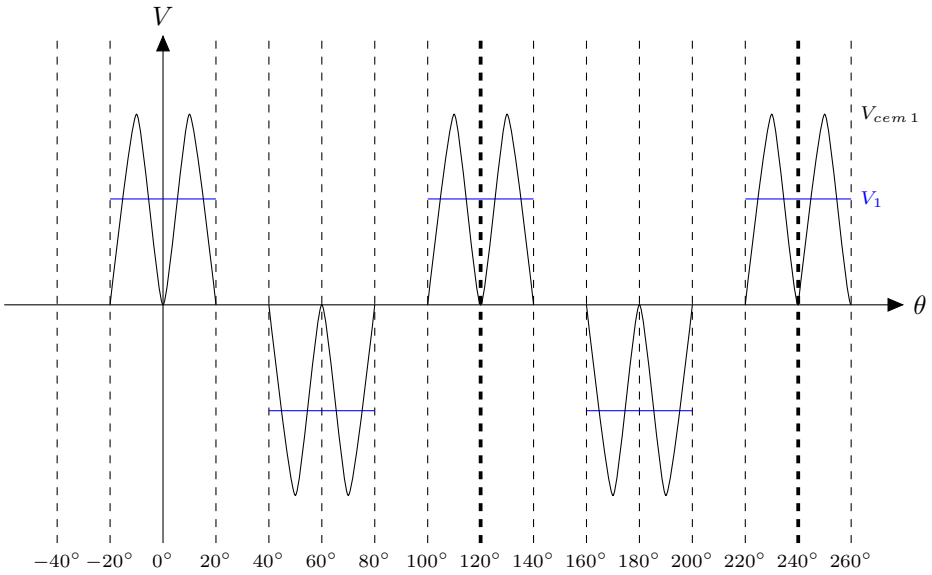

Figure 3.46: Proposed counter-electromotive force $V_{cem\,1}$ and coil voltage V_1 qualitative scheme for phase 1 as a function of mechanical angle θ. Bold dashed lines indicate currents working cycles.

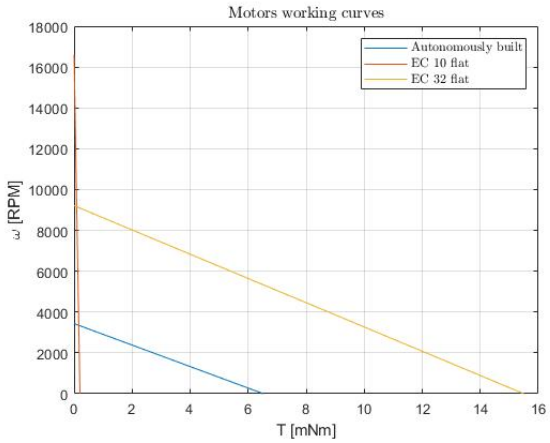

Figure 3.47: Motors working curves. Torques T are given in milli-newton-metres.

Chapter 4

Thermal analysis

A preliminary thermal analysis of the reaction wheel tile is performed adopting the models assumed for the entire AraMiS CubeSat. The objectives of the analysis are:

1. To provide thermal resistances values of the tile to complete the entire CubeSat thermal model;
2. To verify components thermal power fluxes and working temperatures, to verify their compatibility with allowable components temperatures, in two different working conditions. Payload is considered at a nominal temperature of $20\,^{\circ}C$ in both cases. The cold case considers the tile irradiated by Earth's albedo and reaction wheel motor turned off, the hot case considers the tile irradiated by the Sun at a distance of $1\,AU$ and motor in maximum continuous working condition. The top-bottom model is exploited to obtain these results.

The simplifying hypotheses assumed in all models are:

1. Models are unidimensional. Heat transfer is considered along a chosen direction and separate analyses are conducted for each direction of heat transfer. Heat transfer direction is identified with an x axis for top-bottom model and with radial direction and r axis for centre-edge model. Thermal component properties and their temperatures are considered constant on each cross section, at a given coordinate along the x axis for top-bottom model and at a given radius for centre-edge model;
2. Heat transfer among components consists in sole conduction. It is also shown that radiation is negligible in the cases under examination in the top-bottom model;
3. Steady state regime is considered. As a consequence, components thermal capacities are not involved in the analyses;
4. Components have homogeneous thermal and geometric properties. Thus for top-bottom model, components cross sections, perpendicular to x axis, have constant area, and for centre-edge model, components thicknesses are constant along r axis.

Configuration chosen for the examination is version 4, and in particular the following features are considered:

- The PCBs are soldered together with epoxy resin;
- Carbon fiber collar is considered.

Electronic components and thermal powers produced by their operations have been neglected in the analysis. In the first place, theoretical model descriptions are given at sections 4.1.1 and 4.2.1, and then calculations and results are presented at sections 4.1.2 and 4.2.2. Conclusions are reported at section 4.3.

4.1 Top-bottom model

4.1.1 Thermal model description

A generic thermal component C is shown in figure 4.1(a). Its lateral faces are adiabatic and its front ($x = 0$) and end ($x = L$) faces are isothermal and able to exchange heat, as will be assumed for the remainder of present section. It has an homogeneous thermal conductivity K, the area of any cross section perpendicular to x axis (including the external faces) is S, and its length along x axis is L. Entering thermal power $\dot{Q}_e$ and outgoing thermal power $\dot{Q}_o$ parallel to x axis are considered. Temperature of the section at $x = 0$ ($x = L$) is T_0 (T_L).

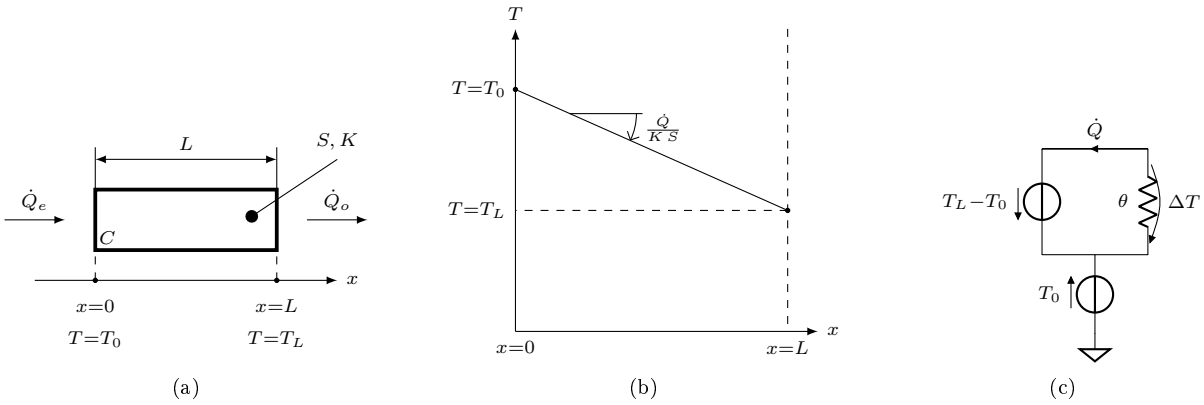

Figure 4.1: Physical diagram for generic thermal component C (a), possible temperature profile with $\dot{Q} > 0$ (b) and relative thermal schematic (c).

According to steady state hypothesis, temporal derivative of component thermal energy E is null:

$$\frac{dE}{dt} = 0 \tag{4.1}$$

Thus thermal energy balance, relating entering thermal power $\dot{Q}_e$, outgoing thermal power $\dot{Q}_o$ and component thermal energy E, becomes:

$$\dot{Q}_e - \dot{Q}_o = \frac{dE}{dt} = 0 \tag{4.2}$$

Thus there is no thermal energy accumulation or release within the component, the thermal power $\dot{Q}$ is conserved and flows through the component:

$$\dot{Q}_e = \dot{Q}_o = \dot{Q} \tag{4.3}$$

For a component with thermal conductivity K and length L, unidimensional Fourier's law for heat conduction states that:

$$\dot{Q} = -KS\,\frac{dT(x)}{dx} \tag{4.4}$$

where $T(x)$ is the temperature of the cross section whose coordinate is x. It can easily be shown from this law that temperature variation along x is linear, as shown in figure 4.1(b):

$$\frac{dT}{dx} = -\frac{\dot{Q}}{KS} \tag{4.5}$$

$$T_L = T_0 - \frac{\dot{Q}}{KS}\,L \tag{4.6}$$

If front or end face temperature is known, temperature profile is completely defined. When thermal power $\dot{Q}$ is positive (negative), temperature T_0 (T_L) is maximum and decreases (increases) with increasing coordinate x, as in figure. Another form of Fourier's law 4.4 can be found by integration:

$$\int_0^L \dot{Q}dx = -\int_{T_0}^{T_L} KSdT \tag{4.7}$$

$$\dot{Q} = KS\,\frac{T_0 - T_L}{L} = KS\,\frac{\Delta T}{L} \tag{4.8}$$

Where ΔT is the temperature difference between component ends. Equation 4.8 is formally comparable to Ohm's first law. It is obtained under a set of hypotheses analogous to hypotheses for the thermal problem under discussion, in fact it is valid for homogeneous electric conductor with constant cross section in a steady state condition. For a current I flowing through a resistor whose resistance is R and whose ends at $x = 0$ and $x = L$ are, respectively, at electrical potentials V_0 and V_L, so that the potential difference is $\Delta V = V_0 - V_L$, Ohm's law is given in the form:

$$I = \frac{V_0 - V_L}{R} = \frac{\Delta V}{R} \tag{4.9}$$

Thus current I is comparable to the thermal power flowing through the thermal component $\dot{Q}$, electric potentials V_0 and V_L are the analogous, respectively, of temperatures T_0 and T_L and the potential difference at resistor ends ΔV is comparable to temperature difference at thermal component ends, ΔT. The analogy allows to conceive the thermal component as a conductive thermal resistor and to define a conductive thermal resistance θ as

$$\theta = \frac{L}{K \cdot S} \tag{4.10}$$

Hence the thermal problem can easily be described by a lumped parameter model. If convection or radiation where considered under the same conditions, different expressions for thermal resistances could be found. Fourier's law for heat conduction 4.8 can be further developed as:

$$\dot{Q} = \frac{T_0 - T_L}{\theta} = \frac{\Delta T}{\theta} \tag{4.11}$$

The system can be represented with thermal schematic, similar to an electric schematic, shown in figure 4.1(c). The electrical symbol for the ground represents a $0\,K$ thermostat, symbols for wires represent a null temperature difference, and symbol for resistor represents the thermal resistor under examination. Symbols for voltage generators represent temperature differences constant in time and will be called temperature generators in the remainder of the chapter. The symbol for current generator represents a flux of thermal power constant in time and will be called thermal power generator in the remainder of the chapter.
The analogy can be expanded to thermal components networks and allows to easily evaluate thermal power exchanges among adjacent components and components temperatures. In the case of figure 4.2(a) components C_1 and C_2 have respectively the end face and the front face in contact. Their front and end faces are isothermal and able to exchange heat, while their lateral faces are adiabatic. Their contact is perfect, with no other materials between them, i.e. faces surfaces are perfectly smooth, thus there is no temperature drop between faces. This hypothesis will be adopted in the remainder of present section.

Under the same simplifying hypotheses, Fourier's law can be written for each component:

$$\dot{Q}_1 = K_1 S_1 \frac{T_0 - T_1}{L_1} = \frac{\Delta T_1}{\theta_1} \tag{4.12}$$

$$\dot{Q}_2 = K_2 S_2 \frac{T_1 - T_2}{L_2} = \frac{\Delta T_2}{\theta_2} \tag{4.13}$$

Clearly, thermal power is conserved and flows through both components:

$$\dot{Q}_1 = \dot{Q}_2 = \dot{Q} \tag{4.14}$$

Equation for temperature profile 4.6, applied to each component, yields:

$$T_1 = T_0 - \frac{\dot{Q}}{K_1\, S_1} L_1 \tag{4.15}$$

$$T_2 = T_1 - \frac{\dot{Q}}{K_2\, S_2} L_2 = T_0 - \frac{\dot{Q}}{K_1\, S_1} L_1 - \frac{\dot{Q}}{K_2\, S_2} L_2 = T_0 - \dot{Q}\left(\frac{L_1}{K_1\, S_1} + \frac{L_2}{K_2\, S_2}\right) \tag{4.16}$$

And the graph for temperature profile is shown with the black lines in figure 4.2(b), with the segments relative to different components having, in general, different slopes.
Temperature difference ΔT across faces at $x = L_2$ and $x = 0$, the temperature difference for the set of two components, can be written as:

$$\Delta T = T_0 - T_2 = (T_0 - T_1) + (T_1 - T_2) = \Delta T_1 + \Delta T_2 \tag{4.17}$$

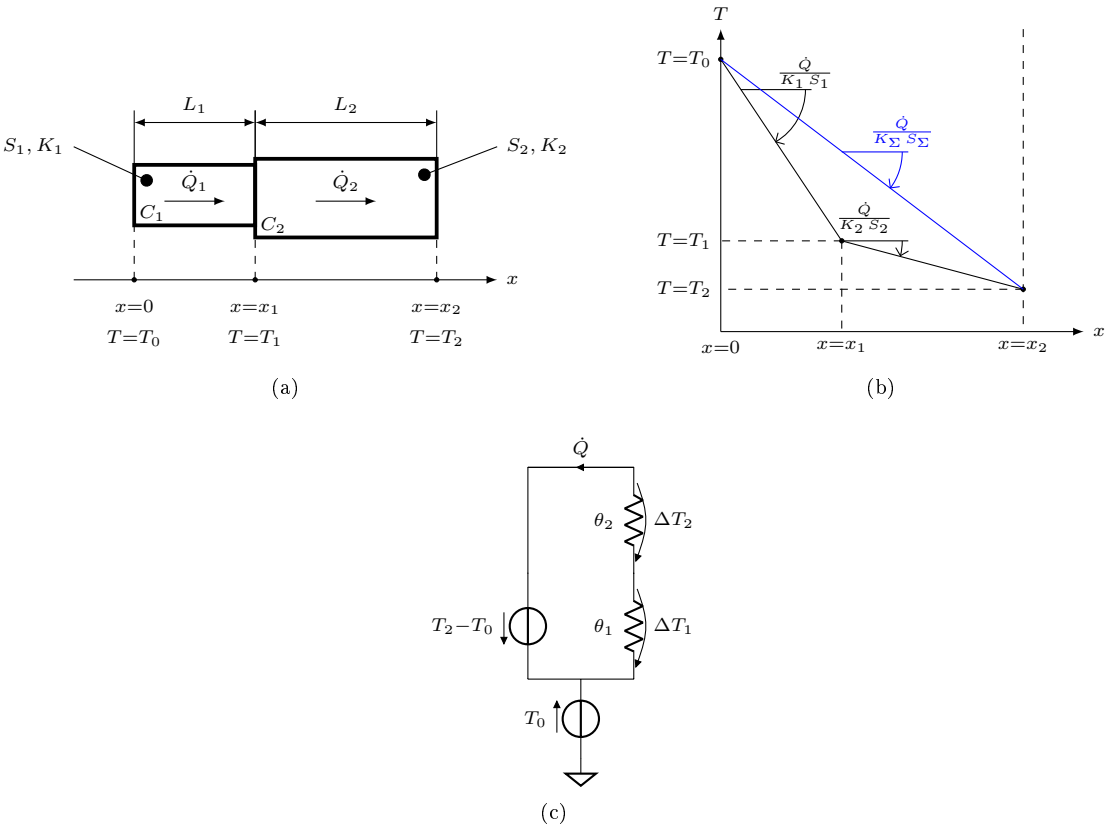

Figure 4.2: Physical diagram for thermal components C_1 and C_2 in series (a), possible temperature profile with $\dot{Q} > 0$ (temperature profile for model with equivalent resistor is shown in blue) (b) and relative thermal schematic (c).

Using Fourier's law for each component 4.12 and 4.13 it becomes:

$$\Delta T = \dot{Q}\,(\theta_1 + \theta_2) = \dot{Q}\,\theta_\Sigma \tag{4.18}$$

$$\dot{Q} = \frac{T_0 - T_2}{\theta_\Sigma} = \frac{\Delta T}{\theta_\Sigma} \tag{4.19}$$

And the set of two components can be interpreted as a single component with a conductive thermal resistance equal to θ_Σ, having a temperature difference across its faces of ΔT and experiencing a thermal power $\dot{Q} = \dot{Q}_1 = \dot{Q}_2$. The hypothesis of perfect contact implies that thermal contact resistance is null, as it is assumed in the remainder of present section. Exploiting the electric analogy, thermal resistors can be represented as they were connected in series, as shown in figure 4.2(c). From the laws of electrotechnics it is immediately clear that the same thermal power $\dot{Q}$ flows through the resistors and the total conductive thermal resistance θ_Σ is the sum of the single conductive thermal resistances θ_1 and θ_2.
Equivalent resistor length can be imagined to be the sum of components lengths, while only the product of its thermal conductivity and cross section area $K_\Sigma\,S_\Sigma$ can be defined:

$$\theta_\Sigma = \frac{L_1 + L_2}{K_\Sigma\,S_\Sigma} \tag{4.20}$$

$$K_\Sigma\,S_\Sigma = \frac{L_1 + L_2}{\theta_\Sigma} = \frac{L_1 + L_2}{\frac{L_1}{K_1\,S_1} + \frac{L_2}{K_2\,S_2}} \tag{4.21}$$

Equation for temperature profile 4.6 can be applied to thermal circuit with the equivalent resistor, to obtain:

$$T_2 = T_0 - \frac{\dot{Q}}{K_\Sigma\,S_\Sigma}\,(L_1 + L_2) = T_0 - \dot{Q}\left(\frac{L_1}{K_1\,S_1} + \frac{L_2}{K_2\,S_2}\right) \tag{4.22}$$

Which is equal to temperature T_2 already obtained at equation 4.16. Obviously, knowledge of exact temperature profile shown with the black lines in figure 4.2(b), and in particular knowledge of temperature T_1, is lost with the adoption of the equivalent conductive resistor, which leads to the temperature profile shown with the blue line in figure 4.2(b). It can be shown that the slope of the equivalent resistor line is intermediate between the slope of two components lines:

$$\frac{\dot{Q}}{K_1\,S_1} > \frac{\dot{Q}}{K_2\,S_2} \iff K_1\,S_1 < K_2\,S_2 \tag{4.23}$$

$$\frac{\dot{Q}}{K_\Sigma\,S_\Sigma} = \frac{\dot{Q}}{\frac{L_1+L_2}{\frac{L_1}{K_1\,S_1}+\frac{L_2}{K_2\,S_2}}} = \dot{Q}\left(\frac{L_1}{K_1\,S_1}+\frac{L_2}{K_2\,S_2}\right)\frac{1}{L_1+L_2} =$$

$$= \frac{\dot{Q}}{K_1\,S_1}\frac{L_1+L_2\frac{K_1\,S_1}{K_2\,S_2}}{L_1+L_2} < \frac{\dot{Q}}{K_1\,S_1} \tag{4.24}$$

$$\frac{\dot{Q}}{K_\Sigma\,S_\Sigma} = \frac{\dot{Q}}{K_2\,S_2}\frac{L_1\frac{K_2\,S_2}{K_1\,S_1}+L_2}{L_1+L_2} > \frac{\dot{Q}}{K_2\,S_2} \tag{4.25}$$

Similar conclusions can be drawn with a number N of components in series in perfect contact. It must be noticed that components thermally in series are not necessarily physically arranged in a straight row. The $i-th$ component has length L_i, lies between coordinates x_i and x_{i-1} and its faces are at temperatures, respectively, T_i and T_{i-1}, with a temperature difference ΔT_i:

$$L_i = x_i - x_{i-1} \qquad i = 1, 2, \ldots, N \tag{4.26}$$

$$\Delta T_i = T_{i-1} - T_i \qquad i = 1, 2, \ldots, N \tag{4.27}$$

With x_0 and T_0 being respectively the coordinate and the temperature of the front face of the first component. The $i-th$ component has thermal conductivity K_i and cross section area S_i, thus its conductive resistance θ_i is:

$$\theta_i = \frac{L_i}{K_i\,S_i} \qquad i = 1, 2, \ldots, N \tag{4.28}$$

And thermal power $\dot{Q}_i = \dot{Q}$ flowing through all the components is, according to Fourier's law 4.11:

$$\dot{Q} = \frac{\Delta T_i}{\theta_i} \qquad i = 1, 2, \ldots, N \tag{4.29}$$

Equation for temperature profile 4.6 can be applied again at the i-th component, yielding:

$$T_i = T_0 - \dot{Q}\sum_{j=1}^{i}\frac{L_j}{K_j\,S_j} \qquad i = 1, 2, \ldots, N \tag{4.30}$$

Temperature difference ΔT between temperatures at end face of the last component T_N and at front face of the first component T_0 is:

$$\Delta T = T_0 - T_N = \sum_{i=1}^{i=N}\Delta T_i \tag{4.31}$$

Hence applying Fourier's law in the form of equation 4.29:

$$\Delta T = \dot{Q}\sum_{i=1}^{i=N}\theta_i = \dot{Q}\,\theta_{\Sigma,\,N} \tag{4.32}$$

With $\theta_{\Sigma,\,N}$ being the sum of components resistances θ_i.
Equivalent resistor length is equal to the sum of all components lengths, the product of its thermal conductivity and cross section area $K_{\Sigma,\,N}\,S_{\Sigma,\,N}$ can be found as for the two components case:

$$\theta_{\Sigma,\,N} = \frac{\sum_{i=1}^{N}L_i}{K_{\Sigma,\,N}\,S_{\Sigma,\,N}} \tag{4.33}$$

$$K_{\Sigma,\,N}\,S_{\Sigma,\,N} = \frac{\sum_{i=1}^{N}L_i}{\theta_{\Sigma,\,N}} = \frac{\sum_{i=1}^{N}L_i}{\sum_{i=1}^{N}\frac{L_i}{K_i\,S_i}} \tag{4.34}$$

Equation for temperature profile 4.6 can be applied again to thermal circuit with the equivalent resistor, to obtain temperature at $x = x_N$:

$$T_N = T_0 - \frac{\dot{Q}}{K_{\Sigma,N}\, S_{\Sigma,N}} \sum_{i=1}^{N} L_i = T_0 - \dot{Q} \sum_{i=1}^{N} \frac{L_i}{K_i\, S_i} \tag{4.35}$$

That in equal to temperature T_N obtained with previous equation 4.30. Clearly, the exact temperature profile, which in general has $N-2$ singular points at the interface between components, is lost with the adoption of the equivalent conductive resistor, that gives a temperature profile with a straight line between T_0 and T_N. It can be shown that there may be components whose line slope is equal to equivalent resistor line slope, and the other lines have slopes major or minor than equivalent resistor line slope.

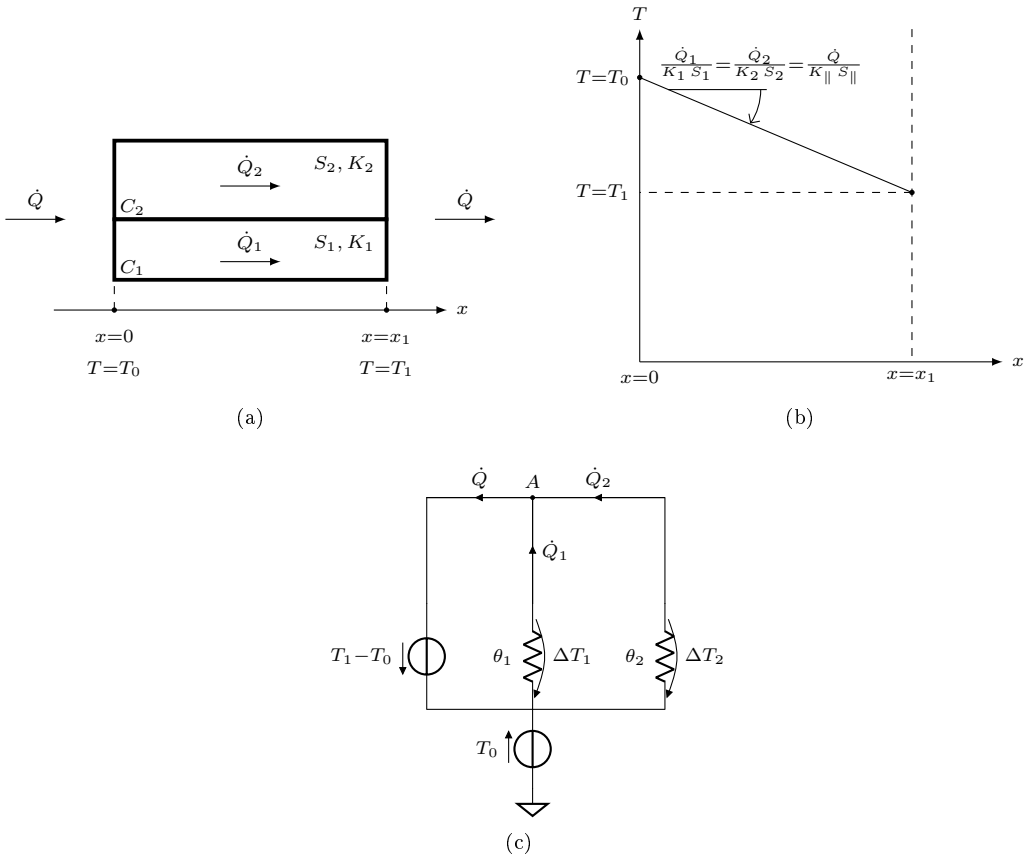

Figure 4.3: Physical diagram for thermal components C_1 and C_2 in parallel (a), possible temperature profile with $\dot{Q} > 0$ (components profiles and profile of model with equivalent resistor are coincident) (b) and relative thermal schematic (c).

The second fundamental case involves components C_1 and C_2, separated by an adiabatic wall, between two temperature sources, as shown in figure 4.3(a). Again, their faces are able to exchange heat, while their lateral walls are adiabatic, thus heat does not flow through the faces between C_1 and C_2. They have the same length L and temperature difference between front and end faces ΔT:

$$L_1 = L_2 = L = x_1 - 0 \tag{4.36}$$

$$\Delta T_1 = \Delta T_2 = \Delta T = T_1 - T_0 \tag{4.37}$$

Temperature profiles are shown in figure 4.3(b). Components thermal resistances θ_1 and θ_2 are different due to different thermal conductivities, respectively K_1 and K_2, and different cross section areas, respectively S_1 and

S_2:

$$\theta_1 = \frac{L}{K_1 S_1} \tag{4.38}$$

$$\theta_2 = \frac{L}{K_2 S_2} \tag{4.39}$$

Fourier's law can be applied to both components 1 and 2, giving expression for their thermal powers, respectively $\dot{Q}_1$ and $\dot{Q}_2$:

$$\dot{Q}_1 = K_1 S_1 \frac{T_0 - T_1}{L} = \frac{\Delta T}{\theta_1} \tag{4.40}$$

$$\dot{Q}_2 = K_2 S_2 \frac{T_0 - T_1}{L} = \frac{\Delta T}{\theta_2} \tag{4.41}$$

The total thermal power $\dot{Q}$ flowing through the system is the sum of components thermal powers $\dot{Q}_1$ and $\dot{Q}_2$:

$$\dot{Q}_1 + \dot{Q}_2 = \dot{Q} \tag{4.42}$$

Obviously, temperature profiles for components are coincident since they are both linear and between the same temperature sources. Lines slopes are given by temperature profiles in equation 4.5:

$$\frac{\dot{Q}_1}{K_1 S_1} = \frac{\dot{Q}_2}{K_2 S_2} \tag{4.43}$$

Fourier's law in form of equation 4.4 can be applied for each component in preceding equation to get:

$$\dot{Q} = \dot{Q}_1 + \dot{Q}_2 = -K_1 S_1 \frac{dT}{dx} - K_2 S_2 \frac{dT}{dx} = -\left(K_1 S_1 + K_2 S_2\right) \frac{dT}{dx} \tag{4.44}$$

From which temperature T_1 can be obtained by integration:

$$T_1 = T_0 - \frac{\dot{Q}}{K_1 S_1 + K_2 S_2} L \tag{4.45}$$

The entire temperature profile is shown in figure 4.3(b).
Substituting in equation 4.42 Fourier's laws 4.40 and 4.41 for separate components, Fourier's law for the entire system is obtained:

$$\dot{Q} = \Delta T \left(\frac{1}{\theta_1} + \frac{1}{\theta_2}\right) = \frac{\Delta T}{\theta_\parallel} \tag{4.46}$$

The resistance $\theta_\parallel$ can be imagined as the equivalent conductive resistance of the entire system:

$$\theta_\parallel = \left(\frac{1}{\theta_1} + \frac{1}{\theta_2}\right)^{-1} = \frac{\theta_1 \theta_2}{\theta_1 + \theta_2} \tag{4.47}$$

The system can be imagined with the lumped parameter model of the two components in parallel, as shown in figure 4.3(c).
The length of the equivalent conductive resistor can be imagined to be equal to L, while only the product of its conductivity and cross section area $K_\parallel S_\parallel$ can be defined:

$$\theta_\parallel = \frac{L}{K_\parallel S_\parallel} \tag{4.48}$$

$$K_\parallel S_\parallel = \frac{L}{\theta_\parallel} = K_1 S_1 + K_2 S_2 \tag{4.49}$$

As for the series case, equation for temperature profile 4.6 can be applied to thermal circuit with the equivalent resistor, to obtain:

$$T_1 = T_0 - \frac{\dot{Q}}{K_1 S_1 + K_2 S_2} L \tag{4.50}$$

Which is equal to temperature T_1 already obtained at equation 4.45. In this case, temperature profiles for equivalent resistor and separate components are all coincident and the exact shape of temperature profile is not lost with the adoption of the equivalent conductive resistor. Temperature profile gradient with equivalent resistor is indeed, in modulus:

$$\begin{aligned} \frac{\dot{Q}}{K_{\parallel}\, S_{\parallel}} &= \frac{\dot{Q}_1 + \dot{Q}_2}{K_1\, S_1 + K_2\, S_2} = \frac{\dot{Q}_1}{K_1\, S_1}\,\frac{K_1\, S_1}{K_1\, S_1 + K_2\, S_2} + \frac{\dot{Q}_2}{K_2\, S_2}\,\frac{K_2\, S_2}{K_1\, S_1 + K_2\, S_2} = \\ &= \frac{\dot{Q}_1}{K_1\, S_1} = \frac{\dot{Q}_2}{K_2\, S_2} \end{aligned} \tag{4.51}$$

The generalized case with N components thermally in parallel, as for the series case with N components, does not include only the physical situation of a stack of N components between the same temperature sources and separated by adiabatic walls. The lengths L_i and temperatures differences ΔT_i are all equal:

$$L_i = L = x_1 - 0 \qquad i = 1, 2, \ldots, N \tag{4.52}$$

$$\Delta T_i = \Delta T = T_1 - T_0 \qquad i = 1, 2, \ldots, N \tag{4.53}$$

Temperature profiles slopes of all components are equal:

$$\frac{\dot{Q}_1}{K_1\, S_1} = \frac{\dot{Q}_2}{K_2\, S_2} = \cdots = \frac{\dot{Q}_N}{K_N\, S_N} \tag{4.54}$$

Fourier's law in form of equation 4.4 can be applied, as in the previous case, for each component to get:

$$\dot{Q} = \sum_{i=1}^{N} \dot{Q}_i = -\sum_{i=1}^{N} K_i\, S_i\, \frac{dT}{dx} \tag{4.55}$$

From which temperature T_1 can be obtained again by integration:

$$T_1 = T_0 - \frac{\dot{Q}}{\sum_{i=1}^{N} K_i\, S_i}\, L \tag{4.56}$$

Thermal resistances θ_i are given by:

$$\theta_i = \frac{L}{K_i\, S_i} \qquad i = 1, 2, \ldots, N \tag{4.57}$$

And Fourier's law applied to each component gives the relative thermal power $\dot{Q}_i$:

$$\dot{Q}_i = \frac{\Delta T}{\theta_i} \qquad i = 1, 2, \ldots, N \tag{4.58}$$

By observing that the total thermal power $\dot{Q}$ flowing through the system is the sum of partial thermal powers $\dot{Q}_i$, one obtains Fourier's law for the entire system:

$$\dot{Q} = \sum_{i=1}^{N} \dot{Q}_i = \Delta T \sum_{i=1}^{N} \frac{1}{\theta_i} = \frac{\Delta T}{\theta_{\parallel,\, N}} \tag{4.59}$$

From which system conductive resistance $\theta_{\parallel,\, N}$ expression, as a function of components resistances θ_i, can be extracted:

$$\theta_{\parallel,\, N} = \left(\sum_{i=1}^{N} \theta_i^{-1} \right)^{-1} \tag{4.60}$$

The length of the equivalent conductive resistor can be imagined to be, as in previous case, equal to L, and the product of its conductivity and cross section area $K_{\parallel,\, N}\, S_{\parallel,\, N}$ can be found to be:

$$\theta_{\parallel,\, N} = \frac{L}{K_{\parallel,\, N}\, S_{\parallel,\, N}} \tag{4.61}$$

$$K_{\parallel,\, N}\, S_{\parallel,\, N} = \frac{L}{\theta_{\parallel,\, N}} = \sum_{i=1}^{N} K_i\, S_i \tag{4.62}$$

As for the previous case, equation for temperature profile 4.6 can be applied to thermal circuit with the equivalent resistor, to obtain:

$$T_1 = T_0 - \frac{\dot{Q}}{\sum_{i=1}^{N} K_i\, S_i}\, L \tag{4.63}$$

Which is equal to temperature T_1 already obtained at equation 4.56. As for the two components case, temperature profiles for equivalent resistor and separate components are all coincident. It can be shown that the slope of the equivalent resistor temperature profile is equal to the slopes of all components:

$$\begin{aligned} \frac{\dot{Q}}{K_{\parallel,\,N}\, S_{\parallel,\,N}} &= \frac{\sum_{i=1}^{N} \dot{Q}_i}{\sum_{i=1}^{N} K_i\, S_i} = \frac{\dot{Q}_1}{K_1\, S_1}\,\frac{K_1\, S_1}{\sum_{i=1}^{N} K_i\, S_i} + \frac{\dot{Q}_2}{K_2\, S_2}\,\frac{K_2\, S_2}{\sum_{i=1}^{N} K_i\, S_i} + \cdots + \frac{\dot{Q}_N}{K_N\, S_N}\,\frac{K_N\, S_N}{\sum_{i=1}^{N} K_i\, S_i} = \\ &= \frac{\dot{Q}_1}{K_1\, S_1} = \frac{\dot{Q}_2}{K_2\, S_2} = \cdots = \frac{\dot{Q}_N}{K_N\, S_N} \end{aligned} \tag{4.64}$$

Exploiting the electrical analogy, it is possible to solve complex thermal networks of components in perfect contact with thermal circuit laws, that are equivalent to electrotechnics laws. For example, the equivalent of Kirchhoff's law for currents states that, at any given time t, in each node of the thermal network, the sum of N_e entering thermal powers $\dot{Q}_{e,\,i}$ is equal to the sum of N_o outgoing thermal powers $\dot{Q}_{o,\,i}$:

$$\sum_{i=1}^{N_e} \dot{Q}_{e,\,i} = \sum_{i=1}^{N_o} \dot{Q}_{o,\,i} \qquad \forall\, t \tag{4.65}$$

It is deduced from conservation of energy and is a consequence of steady state regime considered with hypothesis number 3. The equivalent of Kirchhoff's voltage law states that, at any given time t, in each loop of the thermal network, the sum of the N_R temperature drops $\Delta T_{R,\,i}$ due to thermal resistors must be equal to the sum of the N_G temperature differences $\Delta T_{G,\,i}$ given by the temperature generators:

$$\sum_{i=1}^{N_R} \Delta T_{R,\,i} = \sum_{i=1}^{N_G} \Delta T_{G,\,i} \qquad \forall\, t \tag{4.66}$$

It is a consequence of the fact that temperature in each point of each loop must have a unique value. Topology assures that circuital laws 4.65 and 4.66, applied to each node and loop in the thermal schematic, provide enough independent equations to solve any thermal network, i.e. it is possible to find thermal powers and temperature drops for every discrete element.
However, as suggested by Çengel[1], there is an ambiguity in the passage from the physical diagram of a thermal network to its thermal schematic. It is well explained with the simple example in figure 4.4. The same thermal network can be assumed to have isothermal walls at faces orthogonal to x axis (as was assumed in all previous cases), as in the physical diagram in figure 4.4(a). The resulting thermal schematic is represented in figure 4.4(b), and has an equivalent conductive resistance $\theta_{eq\,1}$:

$$\theta_{eq\,1} = \theta_3 + \frac{\theta_1\, \theta_2}{\theta_1 + \theta_2} \tag{4.67}$$

However, the same system can be assumed to have adiabatic walls at faces parallel to x axis, as shown in physical diagram at figure 4.4(c) with the thin line between components. The resulting thermal schematic is different from the preceding and is shown in figure 4.4(d). The relative conductive resistance $\theta_{eq\,2}$ is different from the preceding one $\theta_{eq\,1}$:

$$\theta_{eq\,2} = \frac{(\theta_1 + \theta_4)\,(\theta_2 + \theta_5)}{(\theta_1 + \theta_4) + (\theta_2 + \theta_5)} \neq \theta_{eq\,1} \tag{4.68}$$

Thus total thermal power crossing the system is different. Moreover, components 1 and 2, in the different models, are crossed by different thermal powers and experience different temperature drops. However, Çengel assures[2] that the real value for thermal resistance θ_{eq} is between the two found with the different models, which are numerically close, and that both represent acceptable approximations. Obviously, the same conclusions can be made for total power crossing the system.

[1] See [6, p. 339-342].
[2] ibidem.

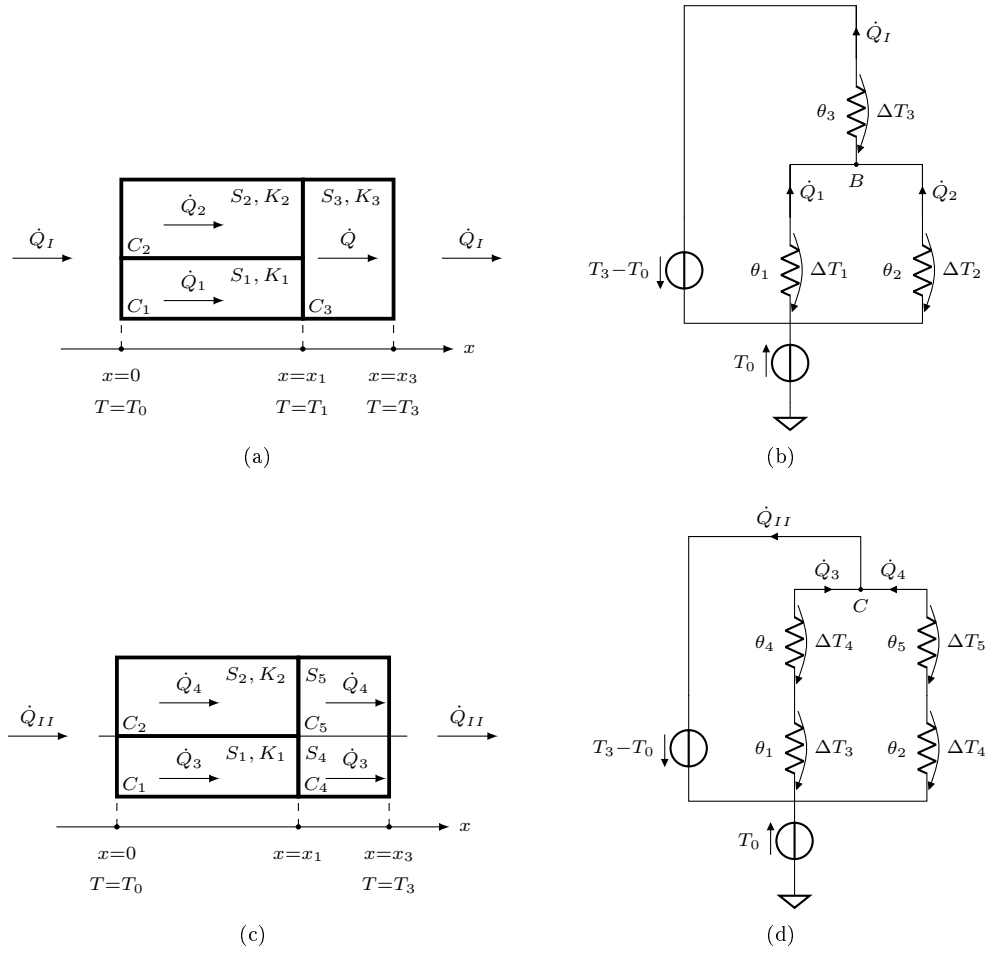

Figure 4.4: Thermal network showing ambiguity in passage from physical diagram to thermal schematic. The same system, shown in (a) and (c), can be represented with two corresponding thermal schematics, respectively shown in (b) and (d), due to different thermal hypotheses, leading to different results.

4.1.2 Top-bottom model description

The top-bottom model deals with thermal power fluxes $\dot{Q}$ orthogonal to PCB plates, as shown by the arrows in figure 4.5. As shown in figure, in the present section, the word "top" refers to the payload side, and the word "bottom" refers to the space side. In Fourier's law equation with thermal resistance 4.11:

$$\dot{Q} = \frac{T_0 - T_L}{\theta} = \frac{\Delta T}{\theta}$$

Temperature difference ΔT, as every temperature difference in the present section, is measured in the indicated direction of $\dot{Q}$, hence T_0 represents temperature of the component face towards the top and T_L represents temperature of the face towards the bottom. In the expression of conductive resistance at equation 4.10:

$$\theta = \frac{L}{K \cdot S}$$

Component length L is meaasured along the direction of thermal power flux, and the area S is referred to cross section perpendicular to thermal power flux. Firstly, top-bottom conductive resistance θ_{tb} of the entire reaction wheel tile is calculated.

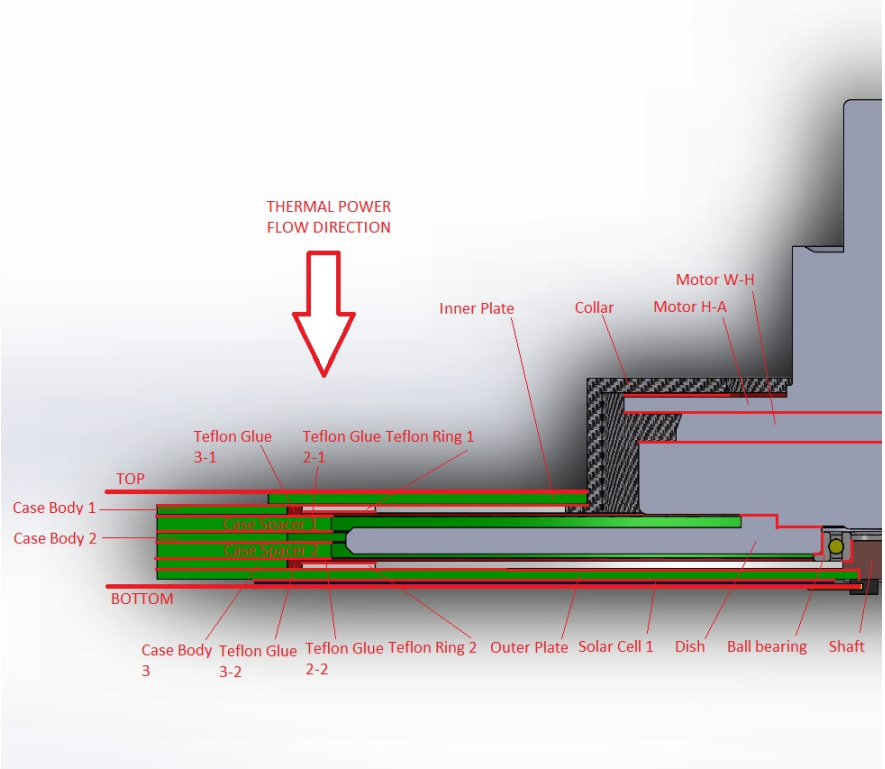

Figure 4.5: Top-bottom model. Thermal power flux direction is indicated by the red arrow.

4.1.2.1 Equivalent resistance

Reaction wheel tile components are conceived as thermal components and their conductive resistance θ can be calculated with the expression of equation 4.10:

$$\theta = \frac{L}{K \cdot S}$$

Components lengths L and cross section areas S are taken from CAD model, and their thermal conductivities K are taken from datasheets, where possible. In a few cases, external sources are used to find components materials conductivities. These are:

- FR4 for PCBs[3];
- Epoxy resin for solderings[4];
- PTFE for teflon rings[5];
- Copper for shaft[6];
- Aluminum for dish[7];
- Stainless steel for ball bearing[8];
- Carbon fiber plain weave for collar[9].

[3] [7, p. 127].
[4] Data about similar epoxy resins were taken from http://www.matweb.com/search/DataSheet.aspx?MatGUID=7edc700f902841f29d5578fd5f182f5b
[5] [6, p. 673]
[6] https://en.wikipedia.org/wiki/Copper
[7] [6, p. 666]
[8] [6, p. 667]
[9] [8].

In some cases, geometrical simplifications have been introduced. In particular:

- For collar and shaft, a mean area was obtained computing an arithmetic mean weighted with each section length;
- The dish has been treated as a cylinder with a central hole, neglecting its chamfers and the ring around central hole;
- Ball bearing shape has been simplified. Its balls and flange have been neglected and the sum of inner and outer ring sections areas has been considered.

Collar thermal conductivity θ_{Collar} has been evaluated combining CFRP conductivities through-the-tickness, $0.6\,W/m/K$, and in fibers plane, $2.5\,W/m/K$. For the cylindrical part of the collar, in top-bottom direction, in-plane conductivity has been considered, while for flanges, which are orthogonal to top-bottom direction, through-the-thickness conductivity has been employed. Thus, using CAD model, conductivity θ_{Collar} is:

$$\theta_{Collar} = \frac{7.71 \cdot 2.5 + (1 + 0.5) \cdot 0.6}{7.71 + 1 + 0.5} = 2.190\,\frac{W}{m\,K} \tag{4.69}$$

Resulting resistances values are given in table 4.1. In some cases, resistance value is given directly, as for the motor, where the sum of the housing-ambient resistance, θ_{H-A},and winding-housing resistance, θ_{W-H}, is considered:

$$\theta_{Motor} = \theta_{H-A} + \theta_{W-H} = 8.25\,\frac{K}{W} + 6.21\,\frac{K}{W} = 1.446 \cdot 10^{1}\,\frac{K}{W} \tag{4.70}$$

Resistances for solar cells and their resin are taken from literature[10].

	$L\,[mm]$	$S\,[mm^2]$	$K\,[W/m/K]$	$\theta\,[K/W]$
Ball Bearing	2.000	1.886×10^{1}	1.400×10^{1}	7.574
Case Body	0.630	2.882×10^{3}	2.400×10^{-1}	9.108×10^{-1}
Case Soldering Inner	0.100	2881.934	1.110	3.126×10^{-2}
Case Spacer	1.000	3.608×10^{3}	2.400×10^{-1}	1.155
Collar	9.210	2.124×10^{2}	2.190	1.980×10^{1}
Glue Solar Cell	—	—	—	2.360
Inner Plate	0.800	5.312×10^{3}	2.400×10^{-1}	6.276×10^{-1}
Motor	—	—	—	1.446×10^{1}
Outer Plate	0.630	7.908×10^{3}	2.400×10^{-1}	3.319×10^{-1}
Outer Soldering	0.100	284.972	1.110	3.161×10^{-1}
Shaft	2.630	7.384	4.010×10^{2}	8.882×10^{-1}
Solar Cell	—	—	—	9.700×10^{-4}
Teflon Glue 1	0.100	1.147×10^{3}	2.000×10^{-1}	4.360×10^{-1}
Teflon Glue 2	0.230	4.775×10^{2}	2.370×10^{2}	2.032×10^{-3}
Teflon Glue 3	0.830	2.482×10^{2}	2.370×10^{2}	1.411×10^{-2}
Teflon Ring	0.500	2.482×10^{2}	3.500×10^{-1}	5.756
Wheel	1.800	4.033×10^{3}	2.370×10^{2}	1.883×10^{-3}

Table 4.1: Top-bottom conductive resistances of tile components.

Top-bottom thermal schematic is presented in figure 4.6(a). Obviously, some components are repeated. Repetitions are indicated with a number at the end of the resistor's name. For example, "$Teflon\,Glue\,1-1$" and "$Teflon\,Glue\,1-2$" are two repetitions of the same component, Teflon Glue 1, whose resistance is indicated in table 4.1. To obtain tile top-bottom resistance, the schematic is simplified by substituting some components resistors with equivalent resistors θ_1-θ_7.

[10] [7, p. 127]

The simplified schematic is represented in figure 4.6(b), expressions for resistance of equivalent resistors are given in equations 4.71-4.76 and the relative results are reported in table 4.2.

$$\theta_1 = \theta_{Collar} + \theta_{Motor} + \theta_{Wheel} + \theta_{Ball\,Bearing} + \theta_{Shaft} \tag{4.71}$$

$$\theta_2 = \theta_7 = \frac{\left(\theta_{Teflon\,Glue\,1} + \theta_{Teflon\,Ring} + \theta_{Teflon\,Glue\,2}\right)\theta_{Teflon\,Glue\,3}}{\theta_{Teflon\,Glue} + \theta_{Teflon\,Ring} + \theta_{Teflon\,Glue\,2} + \theta_{Teflon\,Glue\,3}} \tag{4.72}$$

$$\theta_3 = \frac{1}{2}\left(\theta_{Glue\,Solar\,Cell} + \theta_{Solar\,Cell}\right) \tag{4.73}$$

$$\theta_4 = \theta_{Case\,Body} + \theta_{Case\,Soldering\,Inner} + \theta_{Outer\,Soldering} \tag{4.74}$$

$$\theta_5 = \theta_{Case\,Body} + 2\,\theta_{Case\,Spacer} + 2\,\theta_{Outer\,Soldering} \tag{4.75}$$

$$\theta_6 = \theta_{Case\,Body} + 2\,\theta_{Outer\,Soldering} \tag{4.76}$$

	$\boldsymbol{\theta}\,[\boldsymbol{K/W}]$
$\boldsymbol{\theta_1}$	4.273×10^1
$\boldsymbol{\theta_2}$	3.286
$\boldsymbol{\theta_3}$	1.180
$\boldsymbol{\theta_4}$	1.258
$\boldsymbol{\theta_5}$	3.853
$\boldsymbol{\theta_6}$	1.543
$\boldsymbol{\theta_7}$	3.286

Table 4.2: Equivalent resistors for top-bottom model thermal schematic.

Finally, expression for tile top-bottom resistance and the relative result is given in equation 4.77.

$$\theta_{tb} = \theta_{Inner\,Plate} + \theta_{Outer\,Plate} + \theta_3 + \frac{\theta_1\left(\frac{\theta_2\,\theta_4}{\theta_2+\theta_4} + \theta_5 + \frac{\theta_6\,\theta_7}{\theta_6+\theta_7}\right)}{\theta_1 + \frac{\theta_2\,\theta_4}{\theta_2+\theta_4} + \theta_5 + \frac{\theta_6\,\theta_7}{\theta_6+\theta_7}} = 7.257\,\frac{K}{W} \tag{4.77}$$

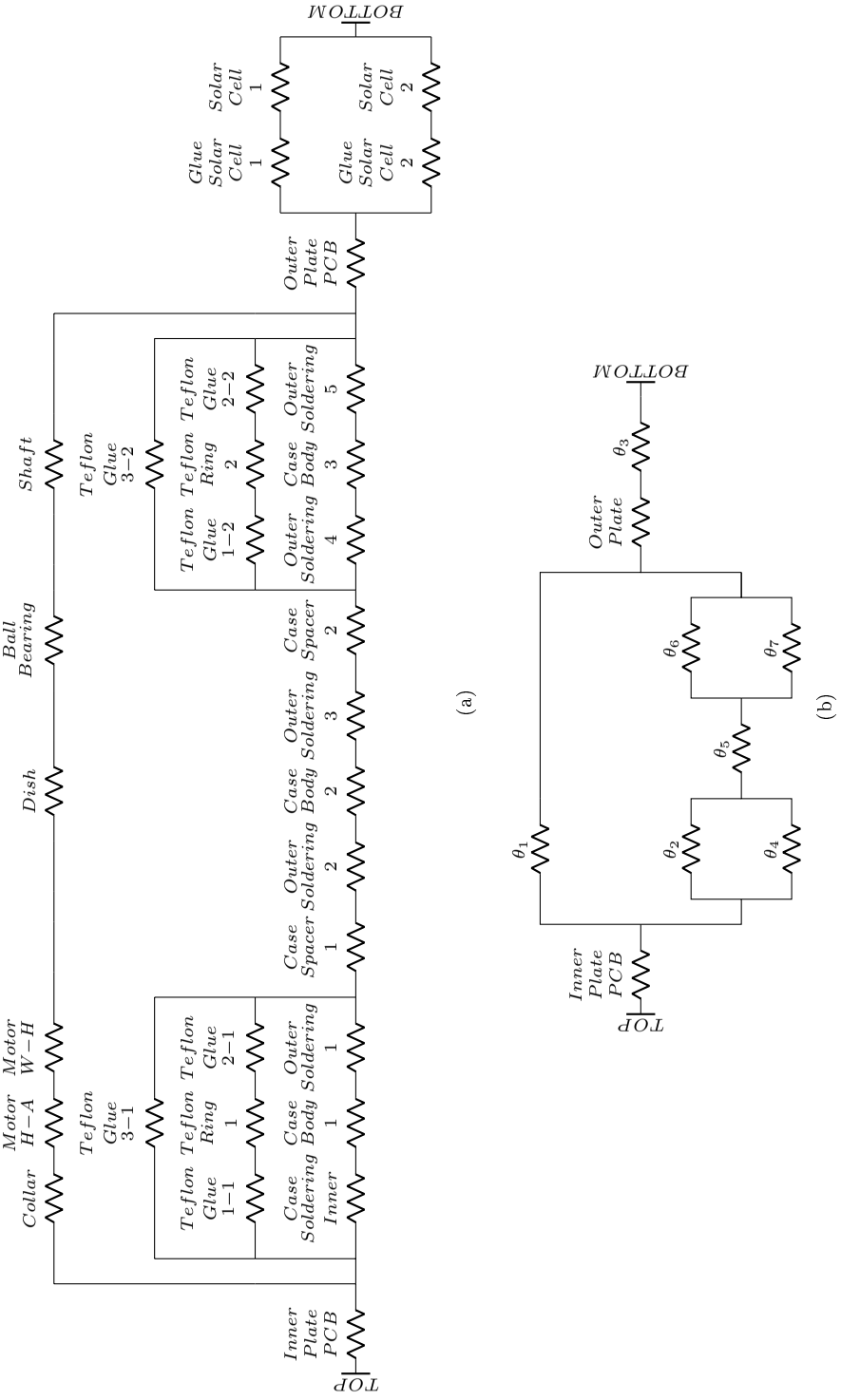

Figure 4.6: Top-bottom model thermal schematic for conductive resistance calculation (a) and relative simplification (b).

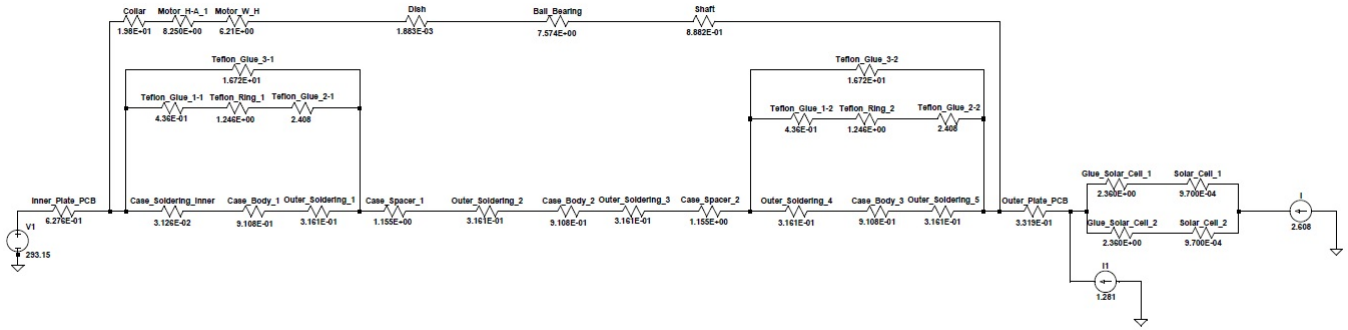

Figure 4.7: Top-bottom model thermal schematic for cold case. Resistances values are given in K/W, temperature difference given by the generator is in K and thermal powers are in W.

4.1.2.2 Cold case

As mentioned above, thermal simulations are performed in the top-bottom model. With the assumed lumped parameter model, simulation consists in the resolution of a thermal resistive network in stationary conditions, aimed at obtaining components faces temperatures and their thermal power fluxes. To solve the network, LTspice® software has been employed. For the cold case, the following conditions have been considered:

- Solar cells and outer plate outermost faces are considered to be heated by terrestrial albedo;
- Temperature on payload side (at top) has been assumed to be equal to $20\,°C = 293.150\,K$;
- Motor has been considered to be turned off and thus it does not produce additional heat.

Cold model thermal schematic is shown in figure 4.7. Clearly, ground is directly connected with the voltage generator in figure. Entering powers are evaluated using solar constant P_{sol} and terrestrial albedo α_{earth}:

$$P_{sol} = 1366\,W/m^2 \tag{4.78}$$
$$\alpha_{earth} = 0.400 \tag{4.79}$$

Solar cells power P_s is obtained from their absorbance α_{cells} and surface S_{cells}, evaluated with CAD model:

$$\alpha_{cells} = 0.900 \tag{4.80}$$
$$S_{cells} = 2651.504\,mm^2 \tag{4.81}$$
$$P_s = P_{sol}\,\alpha_{earth}\,\alpha_{cells}\,2S_{cells} = 2.608\,W \tag{4.82}$$

Outer plate power P_o is obtained from its absorbance $\alpha_{outer\,plate}$ and surface, excluding solar cells $S_{outer\,plate}$, evaluated with CAD model:

$$\alpha_{outer\,plate} = 0.900 \tag{4.83}$$
$$S_{outer\,plate} = 2605.481\,mm^2 \tag{4.84}$$
$$P_o = P_{sol}\,\alpha_{earth}\,\alpha_{outer\,plate}\,S_{outer\,plate} = 1.281\,W \tag{4.85}$$

Absorbance are taken from previous work on AraMiS[11].
Results of the simulation run are reported in table 4.3. Components allowable temperature ranges are reported in table 4.4 where they are matched with simulation results. Where possible, temperature limits have been taken from datasheet, although some data had to be taken elsewhere. These are indicated at table 4.5. Since temperature within components is assumed to vary linearly between faces temperatures T_0 and T_L (referring to equation 4.11), temperature check is straightforward, once component temperature limits T_{min} and T_{max} are known:

$$T_{min} < \min(T_0, T_L) \tag{4.86}$$
$$T_{max} > \max(T_0, T_L) \tag{4.87}$$

All tile components are within prescribed temperature limits, as long as the simplifying hypotheses described above are valid.

[11] [7, p. 129].

	$T_1\,[K]$	$T_2\,[K]$	$\dot{Q}\,[W]$
Ball Bearing	311.548	315.076	0.466
Case Body PCB 1	295.668	297.923	2.475
Case Body PCB 2	303.741	306.859	3.423
Case Body PCB 3	312.631	314.753	2.329
Case Soldering Inner	295.591	295.668	2.475
Case Spacer PCB 1	298.705	302.659	3.423
Case Spacer PCB 2	307.941	311.895	3.423
Collar	295.591	304.813	0.466
Glue Solar Cell 1	316.780	319.858	1.304
Glue Solar Cell 2	316.780	319.858	1.304
Inner Plate PCB	293.150	295.591	3.889
Motor H-A	304.813	308.655	0.466
Motor W-H	308.655	311.547	0.466
Outer Plate PCB	315.489	316.780	3.889
Outer Soldering 1	297.923	298.705	2.475
Outer Soldering 2	302.659	303.741	3.423
Outer Soldering 3	306.859	307.941	3.423
Outer Soldering 4	311.895	312.631	2.329
Outer Soldering 5	314.753	315.489	2.329
Shaft	315.076	315.489	0.466
Solar Cell 1	319.858	319.859	1.304
Solar Cell 2	319.858	319.859	1.304
Teflon Glue 1-1	295.591	295.923	0.762
Teflon Glue 1-2	311.895	312.278	0.879
Teflon Glue 2-1	296.872	298.705	0.762
Teflon Glue 2-2	313.373	315.489	0.879
Teflon Glue 3-1	295.591	298.705	0.186
Teflon Glue 3-2	311.895	315.489	0.215
Teflon Ring 1	295.923	296.872	0.762
Teflon Ring 2	312.278	313.373	0.879
Wheel	311.547	311.548	0.466

Table 4.3: Cold case simulation results. T_1 is temperature of component face towards the top and T_2 is temperature of component face towards the bottom.

4.1.2.3 Hot case

For the hot case the following conditions are imposed:

- As for previous case, payload side is assumed to be at $20\,^{\circ}C = 293.150\,K$;
- Motor is assumed to work in maximum contiuous conditions;
- Solar radiation at a distance of $1\,AU$ has been considered, adding to model schematic thermal power fluxes $P_{s,\,sun}$ towards solar cells and $P_{o,\,sun}$ towards outer plate PCB.

Additional themal powers are calculated from solar constant P_{sol}, absorbivities and surfaces of outer plate and solar cells:

$$P_{o,\,sun} = P_{sol}\,\alpha_{outer\,plate}\,S_{outer\,plate} = 3.203\,W \tag{4.88}$$

$$P_{s,\,sun} = P_{sol}\,\alpha_{cells}\,2S_{cells} = 6.520\,W \tag{4.89}$$

	$T_1\,[^\circ C]$	$T_2\,[^\circ C]$	$T_{max}\,[^\circ C]$	$T < T_{max}$?	$T_{min}\,[^\circ C]$	$T > T_{min}$?
Ball Bearing	38.398	41.926	150	***OK***	−30	***OK***
Case Body PCB 1	22.518	24.773	130	***OK***	—	***OK***
Case Body PCB 2	30.591	33.709	130	***OK***	—	***OK***
Case Body PCB 3	39.481	41.603	130	***OK***	—	***OK***
Case Soldering Inner	22.441	22.518	149	***OK***	−20	***OK***
Case Spacer PCB 1	25.555	29.509	130	***OK***	—	***OK***
Case Spacer PCB 2	34.791	38.745	130	***OK***	—	***OK***
Collar	22.441	31.663	150	***OK***	−100	***OK***
Glue Solar Cell 1	43.630	46.708	149	***OK***	−20	***OK***
Glue Solar Cell 2	43.630	46.708	149	***OK***	−20	***OK***
Inner Plate PCB	20.000	22.441	130	***OK***	—	***OK***
Motor H-A	31.663	35.505	—	***OK***	—	***OK***
Motor W-H	35.505	38.397	125	***OK***	—	***OK***
Outer Plate PCB	42.339	43.630	130	***OK***	—	***OK***
Outer Soldering 1	24.773	25.555	149	***OK***	−20	***OK***
Outer Soldering 2	29.509	30.591	149	***OK***	−20	***OK***
Outer Soldering 3	33.709	34.791	149	***OK***	−20	***OK***
Outer Soldering 4	38.745	39.481	149	***OK***	−20	***OK***
Outer Soldering 5	41.603	42.339	149	***OK***	−20	***OK***
Shaft	41.926	42.339	150	***OK***	—	***OK***
Solar Cell 1	46.708	46.709	125	***OK***	−40	***OK***
Solar Cell 2	46.708	46.709	125	***OK***	−40	***OK***
Teflon Glue 1	22.441	22.773	300	***OK***	−50	***OK***
Teflon Glue 2	38.745	39.128	300	***OK***	−50	***OK***
Teflon Glue 2–1	23.722	25.555	300	***OK***	−50	***OK***
Teflon Glue 2–2	40.223	42.339	300	***OK***	−50	***OK***
Teflon Glue 3-1	22.441	25.555	300	***OK***	−50	***OK***
Teflon Glue 3-2	38.745	42.339	300	***OK***	−50	***OK***
Teflon Ring 1	22.773	23.722	260	***OK***	−200	***OK***
Teflon Ring 2	39.128	40.223	260	***OK***	−200	***OK***
Wheel	38.397	38.398	200	***OK***	—	***OK***

Table 4.4: Comparison of cold case temperatures with allowed ranges.

For motor, maximum continuous working conditions are assumed. Its input voltage and current and output angular speed and torque are taken from datasheet:

$$V_{MAX} = 6.000\,V \tag{4.90}$$
$$I_{MAX} = 1.370\,A \tag{4.91}$$
$$\omega_{MAX} = 3860\,RPM \tag{4.92}$$
$$T_{MAX} = 7.61 \cdot 10^{-3}\,Nm \tag{4.93}$$

Thus electrical power P_{el}, mechanical power P_{mech} and thermal power P_{th} can be evaluated:

$$P_{el} = V_{MAX}\,I_{MAX} = 8.220\,W \tag{4.94}$$
$$P_{mech} = \omega_{MAX}\,T_{MAX} = 3.076\,W \tag{4.95}$$
$$P_{th} = P_{el} - P_{mech} = 5.144\,W \tag{4.96}$$

Thermal schematic is presented in figure 4.8(a). Simulation with LTspice® software has been performed, and the results are shown in table 4.6. Resulting temperatures are checked against prescribed temperature limits in table 4.7. Comparisons are made with equations 4.86-4.87. All temperatures are within allowed temperature ranges, although it must be remembered that the results are limited by the validity of the presented simplifying hypotheses.

	T_{max} source	T_{min} source
Case Bodies	From PCBway	Could not find on PCBway
Case Soldering Inner, Outer Solderings	From matweb[a]	From matweb
Case Spacers	From PCBway	Could not find on PCBway
Shaft	Supposed from wikipedia[b]	Could not find
Glue Solar Cell 1, 2	Supposed equal to solderings	From matweb
Inner Plate PCB	From PCBway	Could not find on PCBway
Motor_H-A	Could not find	Could not find
Motor_W-H	From datasheet	Not given
Outer Plate PCB	From PCBway	Could not find on PCBway
Solar Cell 1, 2	Taken from Isis[c]	Taken from Isis
Teflon Ring 1, 2	From Guarniflon[d]	From datasheet
Wheel	From common aluminum alloys	Not given

Table 4.5: Components allowed temperature ranges sources. The same source corresponds to the same URL indicated in the footnote.

[a] http://www.matweb.com/search/DataSheet.aspx?MatGUID=7edc700f902841f29d5578fd5f182f5b.
[b] https://en.wikipedia.org/wiki/Copper.
[c] https://www.isispace.nl/product/isis-cubesat-solar-panels/.
[d] http://www.guarniflon.com/it/catalogo-materiali/ptfe/ptfe-g400.

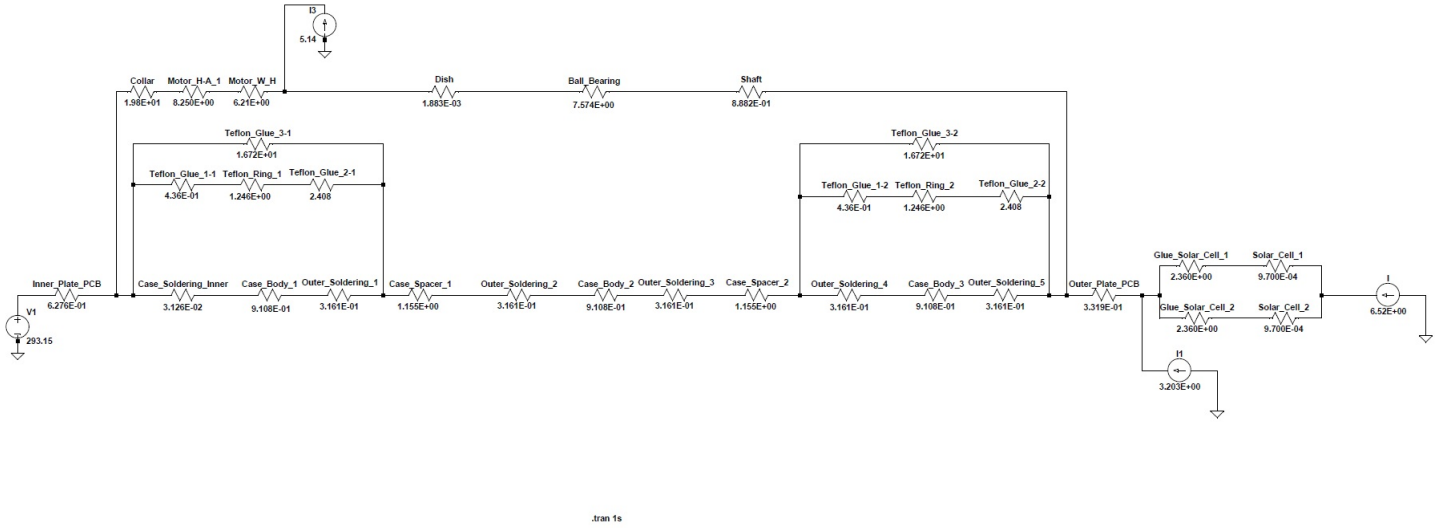

(a)

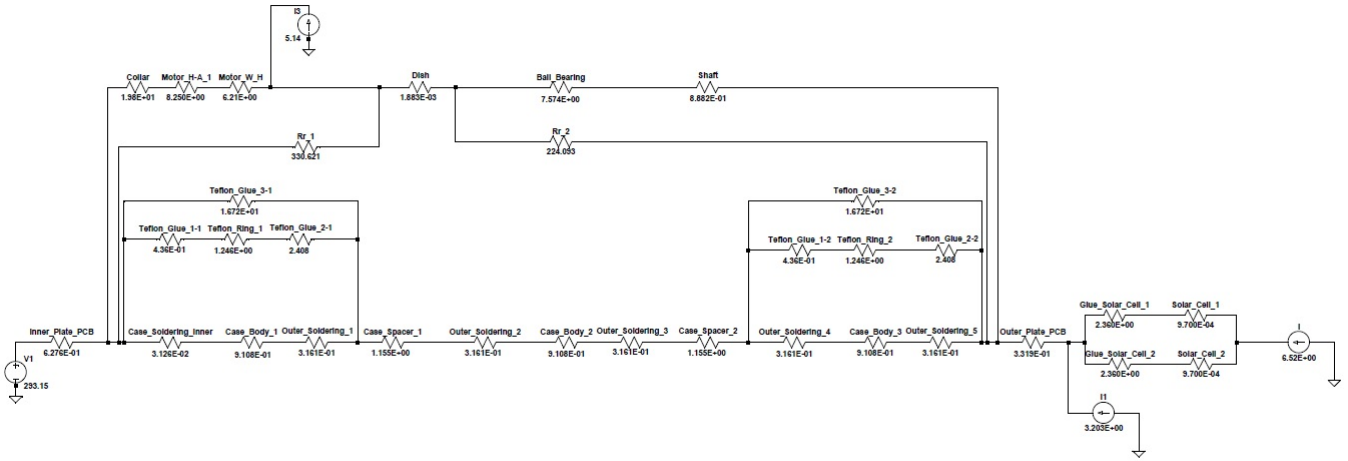

(b)

Figure 4.8: Top-bottom model thermal schematic for hot case, without contribution of radiation (a) and with contribution of radiation (b). Resistances values are given in K/W and temperature difference given by the generator is in K.

	$T_1\,[K]$	$T_2\,[K]$	$\dot{Q}\,[W]$
Ball Bearing	394.165	375.505	2.676
Case Body PCB 1	302.754	310.780	8.813
Case Body PCB 2	331.493	342.593	12.187
Case Body PCB 3	363.142	370.695	8.293
Case Soldering Inner	302.478	302.754	8.813
Case Spacer PCB 1	313.566	327.641	12.187
Case Spacer PCB 2	346.445	360.521	12.187
Collar	302.478	355.470	2.676
Glue Solar Cell 1	376.544	384.237	3.260
Glue Solar Cell 2	376.544	384.237	3.260
Inner Plate PCB	293.150	302.478	14.863
Motor H-A 1	355.470	377.549	2.676
Motor W-H	377.549	394.169	2.676
Outer Plate PCB	373.316	376.544	9.723
Outer Soldering 1	310.780	313.566	8.813
Outer Soldering 2	327.641	331.493	12.187
Outer Soldering 3	342.593	346.445	12.187
Outer Soldering 4	360.521	363.142	8.293
Outer Soldering 5	370.695	373.317	8.293
Shaft	375.505	373.317	2.676
Solar Cell 1	384.237	384.241	3.260
Solar Cell 2	384.237	384.241	3.260
Teflon Glue 1-1	302.478	303.660	2.711
Teflon Glue 1-2	360.521	361.885	3.129
Teflon Glue 2–1	307.038	313.566	2.711
Teflon Glue 2–2	365.783	373.317	3.129
Teflon Glue 3-1	302.478	313.566	0.663
Teflon Glue 3-2	360.521	373.317	0.765
Teflon Ring 1	303.660	307.038	2.711
Teflon Ring 2	361.885	365.783	3.129
Wheel	394.169	394.165	2.676

Table 4.6: Hot case simulation results. T_1 is temperature of component face towards the top and T_2 is temperature of component face towards the bottom.

4.1.2.4 Radiation

Radiation was neglected with hypothesis 2. It is possible to verify this hypothesis with some simple calculations, in the hot model, in which radiation is more critical. Radiation from surface 1 to surface 2 is considered. A possible expression for radiative thermal resistance R_r is taken from literature[12]:

$$R_r = \frac{\frac{1-\varepsilon_1}{\varepsilon_1 A_1} + \frac{1}{A_1 F_{12}} + \frac{1-\varepsilon_2}{\varepsilon_2 A_2}}{\sigma (T_1 + T_2)(T_1^2 + T_2^2)} \tag{4.97}$$

$$\sigma = 5.670 \cdot 10^{-8} \frac{W}{m^2 K^4} \tag{4.98}$$

[12] [6, p. 268]

	$T_1\,[°C]$	$T_2\,[°C]$	$T_{max}\,[°C]$	$T < T_{max}$?	$T_{min}\,[°C]$	$T > T_{min}$?
Ball Bearing	121.015	102.355	150	***OK***	−30	***OK***
Case Body PCB 1	29.604	37.630	130	***OK***	—	***OK***
Case Body PCB 2	58.343	69.443	130	***OK***	—	***OK***
Case Body PCB 3	89.992	97.545	130	***OK***	—	***OK***
Case Soldering Inner	29.328	29.604	149	***OK***	−20	***OK***
Case Spacer PCB 1	40.416	54.491	130	***OK***	—	***OK***
Case Spacer PCB 2	73.295	87.371	130	***OK***	—	***OK***
Collar	29.328	82.320	542	***OK***	—	***OK***
Glue Solar Cell 1	103.394	111.087	149	***OK***	−20	***OK***
Glue Solar Cell 2	103.394	111.087	149	***OK***	−20	***OK***
Inner Plate PCB	20.000	29.328	130	***OK***	—	***OK***
Motor H-A 1	82.320	104.399	—	***OK***	—	***OK***
Motor W-H	104.399	121.019	125	***OK***	—	***OK***
Outer Plate PCB	100.167	103.394	130	***OK***	—	***OK***
Outer Soldering 1	37.630	40.416	149	***OK***	−20	***OK***
Outer Soldering 2	54.491	58.343	149	***OK***	−20	***OK***
Outer Soldering 3	69.443	73.295	149	***OK***	−20	***OK***
Outer Soldering 4	87.371	89.992	149	***OK***	−20	***OK***
Outer Soldering 5	97.545	100.167	149	***OK***	−20	***OK***
Shaft	102.355	100.167	542	***OK***	—	***OK***
Solar Cell 1	111.087	111.091	125	***OK***	−40	***OK***
Solar Cell 2	111.087	111.091	125	***OK***	−40	***OK***
Teflon Glue 1	29.328	30.510	300	***OK***	−50	***OK***
Teflon Glue 2	87.371	88.735	300	***OK***	−50	***OK***
Teflon Glue 2–1	33.888	40.416	300	***OK***	−50	***OK***
Teflon Glue 2–2	92.633	100.167	300	***OK***	−50	***OK***
Teflon Glue 3-1	29.328	40.416	300	***OK***	−50	***OK***
Teflon Glue 3-2	87.371	100.167	300	***OK***	−50	***OK***
Teflon Ring 1	30.510	33.888	260	***OK***	−200	***OK***
Teflon Ring 2	88.735	92.633	260	***OK***	−200	***OK***
Wheel	121.019	121.015	200	***OK***	—	***OK***

Table 4.7: Comparison of hot case temperatures with allowed ranges.

The subscripts refer to surfaces. In this expression:

- σ is the Stefan-Boltzmann constant;
- A_1 and A_2 are surfaces areas respectively of components 1 and 2;
- T_1 and T_2 are surfaces temperatures;
- ε_1 and ε_2 are surfaces emissivities;
- F_{12} is the view factor.

Two pairs of radiating surfaces are considered, as they are among the hottest and those with the major areas. Thus two radiative resistors will be introduced in the cold model thermal schematic:

- $R_{r\,1}$, to consider radiation between part of inner plate PCB surface towards space, that is assumed to be surface 1, and part of dish surface towards payload, assumed to be surface 2;
- $R_{r\,2}$ to consider radiation between part of dish surface towards space, that is assumed to be surface 1, and part of outer plate PCB surface towards payload, that is assumed to be surface 2.

View factors are assumed to be unitary in both cases. Only parts of the above mentioned surfaces are considered, since other components absorb radiation. They are annular surfaces and their areas are calculated from their diameters for resistor $R_{r\,1}$:

$$A_1 = \frac{\pi}{4}\left[(68\,mm)^2 - (42\,mm)^2\right] = 2246.239\,mm^2 \tag{4.99}$$

$$A_2 = \frac{\pi}{4}\left[(71\,mm)^2 - (18\,mm)^2\right] = 3704.723\,mm^2 \tag{4.100}$$

And for resistor $R_{r\,2}$:

$$A_1 = \frac{\pi}{4}\left[(71\,mm)^2 - (8.1\,mm)^2\right] = 3907.662\,mm^2 \tag{4.101}$$

$$A_2 = \frac{\pi}{4}\left[(68\,mm)^2 - (4.1\,mm)^2\right] = 3618.479\,mm^2 \tag{4.102}$$

Data for resistances calculation are reported in table 4.8. FR4 emissivity is taken from literature[13] and aluminum emissivity is taken from Çengel[14]. Indicated temperatures are taken from cold case simulation. Obviously, the introduction of radiation changes actual surface temperatures and convergence must reached. Results are shown in table 4.9.

Surface	ε [ ]	$A\,[mm^2]$	$T\,[K]$
$R_{r\,1}$ **− 1**	0.900	2246.239	302.478
$R_{r\,1}$ **− 2**	0.090	3704.723	394.169
$R_{r\,2}$ **− 1**	0.090	3907.662	394.165
$R_{r\,2}$ **− 2**	0.900	3618.479	373.317

Table 4.8: Data for calculation of radiative resistances in top-bottom model.

	$\theta\,[K/W]$
$R_{r\,1}$	330.621
$R_{r\,2}$	224.093

Table 4.9: Radiative resistances values for top-bottom model.

The two radiative resistors are inserted in hot case thermal schematic as shown in figure 4.8(b). The simulation run with LTspice® provides the following thermal powers across radiative resistors:

$$\dot{Q}_{r\,1} = 0.268\,W \tag{4.103}$$

$$\dot{Q}_{r\,2} = 0.083\,W \tag{4.104}$$

A comparison of components temperatures with and without radiation effect is presented in table 4.10.

The following conclusions can be drawn:

- Thermal schematic for hot case, without considering radiation, represents well the real physical situation with radiative exchange, and there is no need to proceed with further iterations since convergence is reached;
- Radiative heat exchanges can be neglected, since considering the hottest and biggest surfaces in the hot model, these introduce small variations in results.

Hence radiation can be considered negligible for cold case as well.

[13] http://webparts.mentor.com/flotherm/support/supp/mm/pcb_modelling/.
[14] [6, p. 681]

	T_1 [K]	T_2 [K]
Inner plate with rad	293.150	302.478
Inner plate without rad	293.150	302.478
Outer plate with rad	372.303	375.530
Outer plate without rad	373.317	376.544
Wheel with rad	390.974	390.970
Wheel without rad	394.169	394.165

Table 4.10: Comparison of components temperatures with and witohut radiation effect.

4.2 Centre-edge model

4.2.1 Thermal model description

The model deals with heat conduction. Component C has circular simmetry and is shown in figure 4.9(a).The component has constant thickness h and conductivity K. Temperature at its inner margin $r = r_1$ is T_1 and temperature at outermost radius $r = r_2$ is T_2.

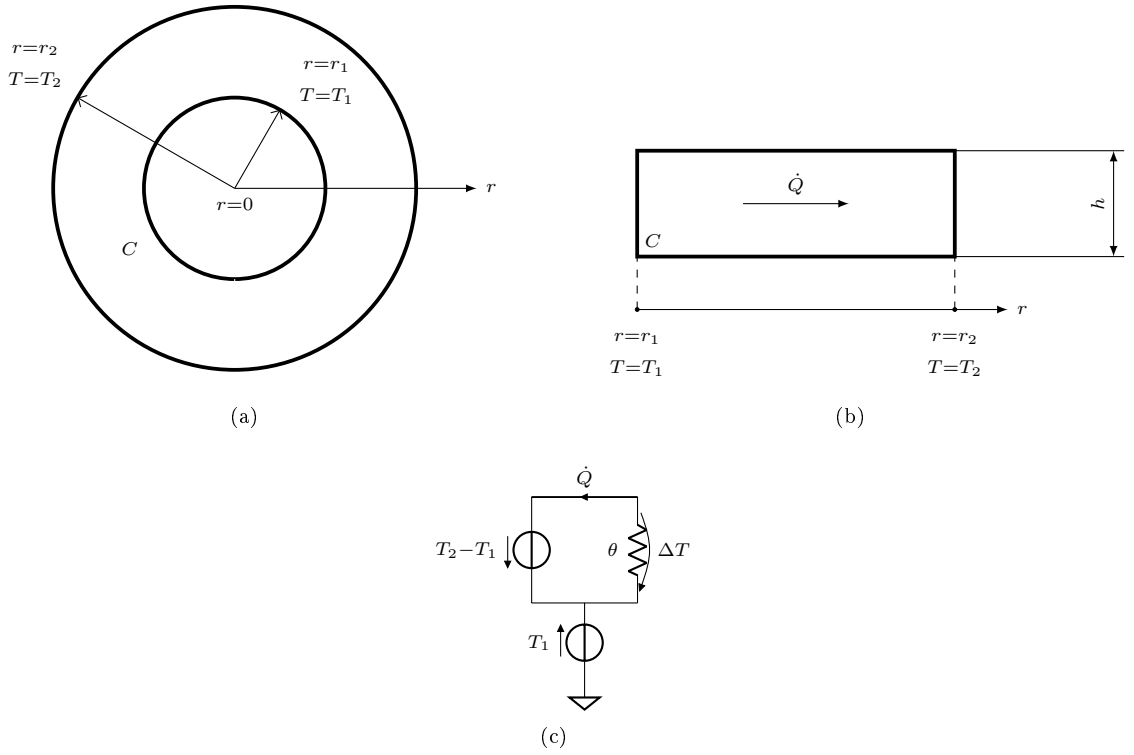

Figure 4.9: Centre-edge model physical diagrams (a and b), possible temperature profile with $\dot{Q} > 0$ (c) and relative thermal schematic (d).

Thermal power $\dot{Q}$ is assumed to flow radially from the origin of the axis towards increasing radii, as shown in figure 4.9(b). Application of Fourier's law with radial coordinates leads to:

$$\dot{Q} = -K\, 2\,\pi\, r\, h \frac{dT}{dr} \tag{4.105}$$

Which can easily be integrated to obtain thermal resistance θ:

$$d\theta = \frac{-dT}{\dot{Q}} = \frac{dr}{r\,2\pi\,h\,K} \tag{4.106}$$

$$\theta = \int_{r=r_1}^{r=r_2} \frac{dr}{r\,2\pi\,h\,K} = \frac{1}{2\pi\,h\,K} \log\left(\frac{r_2}{r_1}\right) \tag{4.107}$$

The final equation can be compared to Fourier's law form with thermal resistance θ at equation 4.11:

$$\theta\,\dot{Q} = \Delta T \tag{4.108}$$

And thus the system can be represented with the usual thermal schematic shown in figure 4.9(c), imagined with $\dot{Q} > 0$.
For networks of thermal components, their resistances can be combined as shown for the top-bottom model. Heat is assumed to flow from a central component, shown in black in figure 4.10.

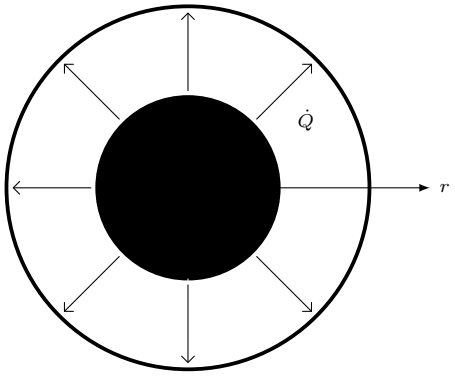

Figure 4.10: Heat source for centre-edge model.

4.2.2 Centre-edge model description

In the centre-edge model the radial axis lies in a plane parallel to PCBs. The components excluded from computation are: collar, motor, wheel and ball bearing. Motor could be included in the model as a thermal power source. Model centre and edge are shown in figure 4.11, along with thermal components. Clearly, thermal power flow direction is parallel to radial axis.

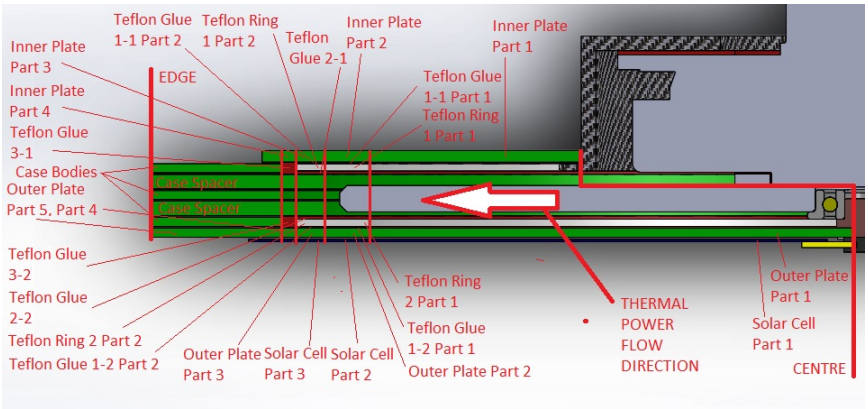

Figure 4.11: Centre-edge model thermal components.

As a consequence, in Fourier's law in the form with thermal resistance θ at equation 4.108:

$$\theta \dot{Q} = \Delta T = T_0 - T_R \tag{4.109}$$

Temperature drop ΔT represents a difference between temperatures of an inner surface, closer to shaft axis, and an outer surface, further from shaft axis. In the expression of conductive resistance θ at equation 4.107:

$$\theta = \frac{1}{2\pi\, h\, K} \log\left(\frac{r_2}{r_1}\right)$$

Component thickness h is measured in a direction parallel to shaft axis. Tile centre-edge conductive resistance is calculated in the remainder of the chapter.

4.2.2.1 Equivalent resistance calculation

To evaluate tile centre-edge conductive resistance, the formula at equation 4.107 is considered:

$$\theta = \frac{1}{2\pi\, h\, K} \log\left(\frac{r_2}{r_1}\right)$$

Components thicknesses h are taken from CAD model and their thermal conductivities K are chosen as explained for top-bottom model equivalent resistance calculation, at section 4.1.2.

	$K\ [W/m/K]$	$h\ [mm]$	$r_1\ [mm]$	$r_2\ [mm]$	$\theta\ [K/W]$
Case body	2.400×10^{-1}	6.300×10^{-1}	4.000×10^{1}	4.890×10^{1}	2.115×10^{2}
Case spacer part 1	2.400×10^{-1}	1.000	3.700×10^{1}	3.900×10^{1}	3.491×10^{1}
Case spacer part 2	2.400×10^{-1}	1.000	3.900×10^{1}	4.000×10^{1}	1.679×10^{1}
Case spacer part 3	2.400×10^{-1}	1.000	4.000×10^{1}	4.890×10^{1}	1.332×10^{2}
Glue solar cell part 1	1.460	1.000×10^{-1}	1.000	3.400×10^{1}	3.844×10^{3}
Glue solar cell part 2	1.460	1.000×10^{-1}	3.400×10^{1}	3.700×10^{1}	9.218×10^{1}
Glue solar cell part 3	1.460	1.000×10^{-1}	3.700×10^{1}	3.900×10^{1}	5.739×10^{1}
Glue solar cell part 4	1.460	1.000×10^{-1}	3.900×10^{1}	4.000×10^{1}	2.760×10^{1}
Inner plate part 1	2.400×10^{-1}	8.000×10^{-1}	1.950×10^{1}	3.400×10^{1}	4.608×10^{2}
Inner plate part 2	2.400×10^{-1}	8.000×10^{-1}	3.400×10^{1}	3.700×10^{1}	7.009×10^{1}
Inner plate part 3	2.400×10^{-1}	8.000×10^{-1}	3.700×10^{1}	3.900×10^{1}	4.364×10^{1}
Inner plate part 4	2.400×10^{-1}	8.000×10^{-1}	3.900×10^{1}	4.000×10^{1}	2.099×10^{1}
Outer plate part 1	2.400×10^{-1}	6.300×10^{-1}	1.000	3.400×10^{1}	3.712×10^{3}
Outer plate part 2	2.400×10^{-1}	6.300×10^{-1}	3.400×10^{1}	3.700×10^{1}	8.901×10^{1}
Outer plate part 3	2.400×10^{-1}	6.300×10^{-1}	3.700×10^{1}	3.900×10^{1}	5.541×10^{1}
Outer plate part 4	2.400×10^{-1}	6.300×10^{-1}	3.900×10^{1}	4.000×10^{1}	2.665×10^{1}
Outer plate part 5	2.400×10^{-1}	6.300×10^{-1}	4.000×10^{1}	4.890×10^{1}	2.115×10^{2}
Outer soldering	1.110	1.000×10^{-1}	4.000×10^{1}	4.890×10^{1}	2.881×10^{2}
Solar cell part 1	5.500×10^{1}	1.600×10^{-1}	1.000	3.400×10^{1}	6.378×10^{1}
Solar cell part 2	5.500×10^{1}	1.600×10^{-1}	3.400×10^{1}	3.700×10^{1}	1.529
Solar cell part 3	5.500×10^{1}	1.600×10^{-1}	3.700×10^{1}	3.900×10^{1}	9.521×10^{-1}
Solar cell part 4	5.500×10^{1}	1.600×10^{-1}	3.900×10^{1}	4.000×10^{1}	4.579×10^{-1}
Teflon glue 1 part 1	2.000×10^{-1}	1.000×10^{-1}	3.400×10^{1}	3.700×10^{1}	6.729×10^{2}
Teflon glue 1 part 2	2.000×10^{-1}	1.000×10^{-1}	3.700×10^{1}	3.900×10^{1}	4.189×10^{2}
Teflon glue 2	2.000×10^{-1}	2.300×10^{-1}	3.700×10^{1}	3.900×10^{1}	1.821×10^{2}
Teflon glue 3	2.000×10^{-1}	8.300×10^{-1}	3.900×10^{1}	4.000×10^{1}	2.427×10^{1}
Teflon ring part 1	3.500×10^{-1}	5.000×10^{-1}	3.400×10^{1}	3.700×10^{1}	7.690×10^{1}
Teflon ring part 2	3.500×10^{-1}	5.000×10^{-1}	3.700×10^{1}	3.900×10^{1}	4.788×10^{1}

Table 4.11: Centre-edge resistances of tile components.

Results are shown in table 4.11. Some components have been divided in parts, to better represent thermal schematic.
Thermal schematic is shown in figure 4.12(a). As for top-bottom schematic, some components are repeated. To distinguish repetitions, a number is added at the end of the resistor name, for example $Teflon\,Glue\,1-1$ and $Teflon\,Glue\,1-2$ are two repetitions of the teflon glue 1 component. The schematic has been simplified to reckon tile equivalent resistance θ_{ce}. Simplified schematic is shown in figure 4.12(b). Correspondingly, equivalent resistances θ_1-θ_8 are computed using expressions in equations 4.110-4.117.

$$\theta_1 = \left(\frac{1}{\theta_{Inner\,Plate\,Part\,2}} + \frac{1}{\theta_{Teflon\,Glue\,1-1\,Part\,1}} + \frac{1}{\theta_{Teflon\,Ring\,1\,Part\,1}}\right)^{-1} \tag{4.110}$$

$$\theta_2 = \left(\frac{1}{\theta_{Inner\,Plate\,Part\,3}} + \frac{1}{\theta_{Teflon\,Glue\,1-1\,Part\,2}} + \frac{1}{\theta_{Teflon\,Ring\,1\,Part\,2}} + \right.$$
$$\left. + \frac{1}{\theta_{Teflon\,Glue\,2}} + \frac{1}{\theta_{Case\,Spacer\,1\,Part\,1}}\right)^{-1} \tag{4.111}$$

$$\theta_3 = \left(\frac{1}{\theta_{Inner\,Plate\,Part\,4}} + \frac{1}{\theta_{Teflon\,Glue\,3-1}} + \frac{1}{\theta_{Case\,Spacer\,1\,Part\,2}}\right)^{-1} \tag{4.112}$$

$$\theta_4 = \left(\frac{1}{\theta_{Outer\,Plate\,Part\,1}} + \frac{1}{\theta_{Glue\,S\,Cell\,Part\,1}} + \frac{1}{\theta_{Solar\,Cell\,Part\,1}}\right)^{-1} \tag{4.113}$$

$$\theta_5 = \left(\frac{1}{\theta_{Teflon\,Ring\,2\,Part\,1}} + \frac{1}{\theta_{Teflon\,Glue\,1-2\,Part\,1}} + \frac{1}{\theta_{Outer\,Plate\,Part\,2}} + \right.$$
$$\left. + \frac{1}{\theta_{Glue\,S\,Cell\,Part\,2}} + \frac{1}{\theta_{Solar\,Cell\,Part\,2}}\right)^{-1} \tag{4.114}$$

$$\theta_6 = \left(\frac{1}{\theta_{Case\,Spacer\,2\,Part\,1}} + \frac{1}{\theta_{Teflon\,Glue\,2-2}} + \frac{1}{\theta_{Teflon\,Ring\,2\,Part\,2}} + \right.$$
$$+ \frac{1}{\theta_{Teflon\,Glue\,1-2\,Part\,2}} + \frac{1}{\theta_{Outer\,Plate\,Part\,3}} + \frac{1}{\theta_{Glue\,S\,Cell\,Part\,3}} +$$
$$\left. + \frac{1}{\theta_{Solar\,Cell\,Part\,3}}\right)^{-1} \tag{4.115}$$

$$\theta_7 = \left(\frac{1}{\theta_{Case\,Spacer\,2\,Part\,2}} + \frac{1}{\theta_{Teflon\,Glue\,3-2}} + \frac{1}{\theta_{Outer\,Plate\,Part\,4}} + \right.$$
$$\left. \frac{1}{\theta_{Glue\,S\,Cell\,Part\,4}} + \frac{1}{\theta_{Solar\,Cell\,Part\,4}}\right)^{-1} \tag{4.116}$$

$$\theta_8 = \left(\frac{3}{\theta_{Case\,Body}} + \frac{2}{\theta_{Case\,Spacer\,Part\,3}} + \frac{5}{\theta_{Outer\,Soldering}} + \right.$$
$$\left. + \frac{1}{\theta_{Outer\,Plate\,Part\,5}}\right)^{-1} \tag{4.117}$$

Results are presented in table 4.12.

Finally, tile centre-edge conductive resistance can be computed:

$$\theta_{ce} = \theta_8 + \frac{\left(\theta_{Inner\,Plate\,Part\,1} + \theta_1 + \theta_2 + \theta_3\right)\left(\sum_{i=4}^{7}\theta_i\right)}{\theta_{Inner\,Plate\,Part\,1} + \sum_{i=1}^{7}\theta_i} = 7.677 \cdot 10^1\,\frac{K}{W} \tag{4.118}$$

	$\theta\,[K/W]$
θ_1	3.477×10^1
θ_2	1.245×10^1
θ_3	6.738
θ_4	6.169×10^1
θ_5	1.448
θ_6	8.747×10^{-1}
θ_7	4.240×10^{-1}
θ_8	1.950×10^1

Table 4.12: Equivalent resistors for centre-edge model thermal schematic.

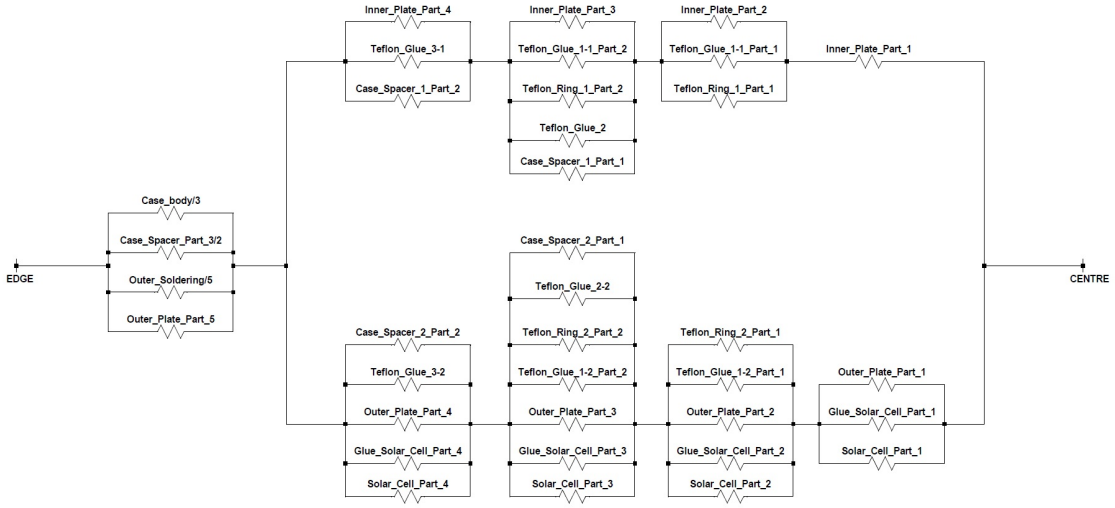

(a)

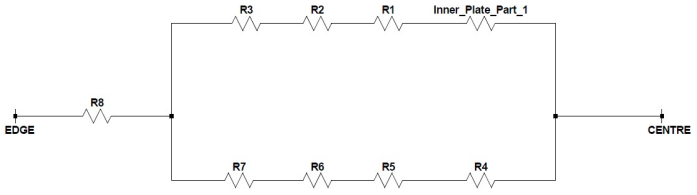

(b)

Figure 4.12: Centre-edge model thermal schematic for conductive resistance calculation (a) and relative simplification (b).

4.3 Conclusions

Numerical results for reaction wheel tile preliminary thermal analysis are shown in table 4.13.

Model	$\boldsymbol{\theta}\,[\boldsymbol{K/W}]$
Top-bottom	7.257
Centre-edge	7.677×10^{1}

Table 4.13: Reaction wheel tile thermal resistances.

Moreover, preliminary thermal simulations with top-bottom model have shown that:

1. Most of tile components temperatures are within allowable ranges for the cold case. Only solar cells and their resins temperatures are below minimum limits. However, these values could become major by taking into account heating produced by electronic components, which has been neglected in present preliminary analysis. Anyway, the problem could be easily solved by placing heaters underneath solar cells;
2. All tile components temperatures are within allowable ranges for the hot case;
3. Radiation can be neglected in thermal simulations.

Clearly, the field of validity of conclusions is limited by the simplifying assumptions.

Chapter 5

Structural analysis

A preliminary structural analysis of reaction wheel tile has been performed. The chosen launch vehicle is Arianespace© Vega and applicable launch conditions are described in section 5.1. The objectives of present chapter are:

1. To choose the best junction between Printed Circuit Boards (PCBs), from a mechanical point of view. The choice is between traditional PCB soldering made with SAC 305 solder paste (version 3 of the reaction wheel) and an epoxy resin (version 4). This is done in section 5.2.1. Then an estimate of reaction wheel tile mass is made, along with a preliminary mean stress evaluation in the bonding for two load conditions;

2. To evaluate tile stresses and strains under inertial loads, and verify their compatibility with material proportional limit stress. This is done preliminarily with a simple spreadsheet analysis, described in section 5.2, and then with a finite elements linear static analysis, described in section 5.3.2;

3. To evaluate tile resonance frequencies to verify compatibility with mechanical requirements imposed by the launcher. This is done with a finite elements modal analysis, described in section 5.3.1.

An analytical approach to stress and strain determination was not attempted, due to the complexity of tile geometry.
Since reaction wheel tile can be placed on any face of CubeSat structure, chosen inertial loads are applied on each of the tile axis and boundary conditions are set according to tile position on CubeSat structure.

5.1 Launch conditions

Applicable launch conditions are described in Vega User's Manual[1] at section 3.2. In that section, for a spacecraft in single launch configuration, limit inertial loads are given in tabular form, as shown in figure 5.1(a) and as a diagram, as shown in figure 5.1(b). These loads should be taken into account for primary structure design and will be considered as an input for structural analysis. A typical longitudinal acceleration profile for Sun-Synchronous Orbit (SSO) mission is also shown, and is reproduced in figure 5.1(c). The chosen Safety Factor (SF) is 1.8, thus the Ultimate Load (UL, in gs) is obtained as the maximum Limit Load (LL, in absolute value in gs) multiplied by the safety factor:

$$UL = SF \cdot LL = 1.8 \cdot 7\,g = 12.6\,g \simeq 13\,g \tag{5.1}$$

As a result, a ultimate load of $13\,g$ is used in present structural analysis. Since the tile can be mounted on any of the CubeSat structure faces, the ultimate load is applied along each axis (shown in figures 5.3(b) and 5.3(c)), in positive and negative directions.

[1] [9]

5.2 Preliminary analysis

In the present section, firstly the choice between soldering with SAC 305 solder paste and epoxy resin bonding is made, i.e. choice between version 3 and 4 of the tile, respectively, is made. Then total tile mass is estimated and a simple evaluation of mean stress in the bondings is made.

5.2.1 PCB junction type choice

The alternatives for joining PCB pairs are two:

1. Soldering. The solder paste, SAC 305[2], is distributed in discrete points and then heated in a oven, where it solidifies. Solder paste composition, which is the reason for its name, is 0.5% copper, 3% silver, and 96.5% tin (percentages are in weight);
2. Bonding. A classical epoxy resin could be used, producing a continuous bonding.

In the first place, the weight of the two solutions is evaluated. For the soldering solution, SAC 305 density $\rho_{SAC\,305}$ is known[3], and the volume involved in each soldering $V_{SAC\,305}$ is known as well, since it can be regulated by machine:

$$\rho_{SAC\,305} = 7.380\,g/cm^3 \tag{5.2}$$

$$V_{SAC\,305} = 0.3\,mm^3 \tag{5.3}$$

The number of solderings for each pair of PCBs is known and reported in the first column of table 5.1. The weight of each joint can then easily be evaluated:

$$\text{Weight SAC 305} = \text{Number of solderings} \cdot \rho_{SAC\,305} \cdot V_{SAC\,305} \tag{5.4}$$

And is reported in the second column of the table. The total weight is simply the sum of each joint's weight.
For the bonding solution, the density of a mean epoxy resin is chosen, ρ_{epoxy}, and a mean thickness t_{epoxy} is supposed:

$$\rho_{epoxy} = 1.200\,g/cm^3 \tag{5.5}$$

$$t_{epoxy} = 100\,\mu m \tag{5.6}$$

To estimate the weight of each joint, its area is estimated from CAD model and reported in table. Thus the weight can be estimated:

$$\text{Weight epoxy} = \text{Area epoxy} \cdot \rho_{epoxy} \cdot t_{epoxy} \tag{5.7}$$

And is shown in table. Total weight is again the sum of each joint's weight.
On the basis of pure weight, epoxy bonding seems not convenient. However, this solutions provides a more uniform stress field with respect to soldering solution, which would produce a non uniform stress field with numerous areas with high stress intensities. For this reason epoxy bonding, and consequently version 4 of reaction wheel tile, is chosen.

The remaining columns in table 5.1 refer to inertial loads induced by aforementioned weights. They can easily be evaluated remembering that supposed acceleration intensity was $13\,g$:

$$\text{Load SAC 305/epoxy} = \text{Weight SAC 305/epoxy} \cdot 13 \cdot 9.806\,m/s^2 \tag{5.8}$$

Total load is simply the sum of each load induced by individual joints.

[2] http://www.chipquik.com/datasheets/SMD291SNL10T5.pdf.
[3] http://www.matweb.com/search/datasheet.aspx?matguid=d1fb83962e5445859d408356bfa18bc7&ckck=1.

PCB	Number of solderings [ ]	Weight SAC 305 $[g]$	Load SAC 305 $[N]$	Area epoxy $[mm^2]$	Weight epoxy $[g]$	Load epoxy $[N]$
Inner plate						
	53	1.009×10^{-1}	1.290×10^{-2}	284.972	3.420×10^{-2}	4.360×10^{-3}
Case body						
	92	1.752×10^{-1}	2.230×10^{-2}	2881.934	3.458×10^{-1}	4.410×10^{-2}
Case spacer						
	92	1.752×10^{-1}	2.230×10^{-2}	2881.934	3.458×10^{-1}	4.410×10^{-2}
Case body						
	92	1.752×10^{-1}	2.230×10^{-2}	2881.934	3.458×10^{-1}	4.410×10^{-2}
Case spacer						
	92	1.752×10^{-1}	2.230×10^{-2}	2881.934	3.458×10^{-1}	4.410×10^{-2}
Case body						
	92	1.752×10^{-1}	2.230×10^{-2}	2881.934	3.458×10^{-1}	4.410×10^{-2}
Outer Plate						
Total weight		9.768×10^{-1}			1.763	
Total load			1.250×10^{-1}			2.250×10^{-1}

Table 5.1: Evaluation of weight and load induced by SAC 305 solderings and epoxy bonding.

5.2.2 Mass and mean stress evaluation

Tile mass evaluation can be made adding up weights of the joints (evaluated above) and weights of the components. This is done evaluating density and volume of each component and the results are shown in table 5.2. Ball bearings and motor masses are known from datasheet, for the remaining components:

- FR4 density for case body, case spacer, inner plate and outer plate are supposed to be equal to the density of epoxy resin[4];
- Collar density is supposed to be equal to density of typical a carbon fiber-epoxy material;
- Wheel density is assumed to be the density of aluminum;
- Motor glue, teflon glue and pad 2 densities are taken from datasheet;
- Shaft density is assumed to be the density of copper[5];
- Teflon ring density is taken from datasheet.

Components volumes can easily be estimated from CAD model. Thus components weight can be estimated:

$$\text{Component weight} = \text{Component density} \cdot \text{Component volume} \tag{5.9}$$

Loads reported in the last column are weights multiplied by the $13\,g$ acceleration, as made for joints weights in equation 5.8. Tile weight breakdown is reported in table 5.3 and shown in figure 5.2. Tile weight is clearly dominated by contribution of the motor, being greater than wheel weight.

A simple evaluation of mean stresses in each PCB junction is made and reported in table 5.4. Two kinds of bondings are considered: the case soldering inner, between inner plate and a case body, and the outer soldering, representing the rest of the bondings. In the first column, PCB loads are reported, they are the sum of loads given by inner plate, case bodies, case spacers and outer plate. In the second column, other components weights are summed and in the third column, loads due to epoxy bondings are summed. The sum of these columns is divided by epoxy areas given in table 5.1 to obtain mean stresses. These stresses can be interpreted as normal loads (σ) or shear loads (τ).

[4] http://www.matweb.com/search/datasheet.aspx?matguid=1de6952e06274961a1dfc1bb54f45337.
[5] https://it.wikipedia.org/wiki/Rame

Component	Density $[g/cm^3]$	Volume $[mm^3]$	Weight $[g]$	Load $[N]$
Ball Bearing	—	—	0.370	0.047
Case Body	1.890	1815.620	3.432	0.437
Case Spacer	1.890	3607.642	6.818	0.869
Collar	1.800	1955.971	3.521	0.449
Glue motor	1.100	24.891	0.027	0.003
Inner Plate	1.890	4078.900	7.709	0.983
Motor	—	—	32.000	4.080
Outer Plate	1.890	4980.405	9.413	1.200
Pad 2	1.100	196.040	0.216	0.027
Shaft	8.920	19.408	0.173	0.022
Teflon Glue	1.100	114.668	0.126	0.016
Teflon ring	2.180	573.340	1.250	0.159
Wheel	2.700	7296.797	19.701	2.512

Table 5.2: Evaluation of weights and loads induced by tile components.

Component	Weight $[g]$	Breakdown [ ]
Ball Bearing	0.370	0.364%
Case Body	3.432	10.135%
Case Spacer	6.818	13.425%
Collar	3.521	3.466%
Glue motor	0.027	0.027%
Glue PCB	1.763	1.736%
Inner Plate	7.709	7.589%
Motor	32.000	31.503%
Outer Plate	9.413	9.267%
Pad 2	0.216	0.212%
Shaft	0.173	0.170%
Teflon Glue	0.126	0.248%
Teflon Ring	1.250	2.461%
Wheel	19.701	19.395%
Tile weight	101.577	100.000%

Table 5.3: Evaluation of tile weight and weight breakdown.

Finally, an estimate of mean stresses at the junction between inner plate and collar is made and reported in table 5.5. For different bonding external diameters (first column), bonding area is measured from CAD model (second column). Compression (σ_c) or shear (τ) stresses are obtained by dividing the load induced by motor, wheel, collar, ball bearing and shaft by bonding area. The tensile stress (σ_t) is obtained by dividing collar load by bonding area. An external bonding diameter of $42\,mm$ is chosen, to save room for electronic components with acceptable stresses.
All the obtained mean stresses are considerably inferior to maximum shear load for a typical epoxy resin, which is $1\,kg/mm^2$ and inferior to adopted epoxy resin tensile strength, $37\,Mpa$.

Bonding	**Load (PCBs)** $[N]$	**Load (Components)** $[N]$	**Load (Epoxy)** $[N]$	**Mean** σ/τ $[MPa]$
Outer soldering	5.234	7.491	0.225	4.493×10^{-3}
Case soldering inner	5.234	7.491	0.225	4.544×10^{-2}

Table 5.4: Evaluation of total loads and mean stresses acting on soldering.

External diameter $[mm]$	**Bonding area** $[mm^2]$	**Mean** σ_c/τ $[MPa]$	**Mean** σ_t $[MPa]$
39	119.381	5.978×10^{-2}	3.760×10^{-3}
42	310.232	2.300×10^{-2}	1.447×10^{-3}
57	1476.549	4.833×10^{-3}	3.040×10^{-4}

Table 5.5: Evaluation of mean stresses acting on collar bonding.

5.3 Finite elements analysis

A simplified finite elements analysis is performed with MSC Nastran and Patran softwares, in order to evaluate tile stresses and displacements and its resonance frequencies. Information on analysis hypotheses and inputs are given below.

A perfect bonding was assumed among FR4 panels, since evaluation of stresses and strains in bonding requires a non linear analysis. A simplified SOLIDWORKS® CAD model is thus used for geometry, as shown in figure 5.3(a). All electronic components are neglected for finite elements analysis, including solar cells.

Tile mesh involves tetrahedral elements with 10 nodes (Tet10 elements) and is shown in figures 5.3(b) and 5.3(c). 141 887 elements and 238 224 nodes are employed. In the same figures, Cartesian reference frame for structural analysis is shown, in which X and Y axes lie in the plane of the tile and Z axis is orthogonal to tile plane.

The electric motor, the collar, the wheel, the shaft and the ball bearing have been considered as a unique rigid body and included in structural model as a point mass, with the mass of the above mentioned components, located at the estimated position of components center of gravity. The point mass has been supposed to be connected with rigid links to nodes belonging to inner and outer plate central hole. An RBE2 has been made to connect the above mentioned nodes with the point mass.

Since no information on FR4 material properties was given by the producer, PCBWay, it was decided to adopt typical epoxy resin properties as an input, adopting this isotropic material as a conservative hypothesis. Indeed, fibers contribution should be considered negligible since most probably short fibers are employed for FR4. Adopted properties are density ρ, Young modulus E, tensile strength σ_U and Poisson ratio ν:

$$\rho = 1.2\, g/cm^3 \tag{5.10}$$

$$E = 3000.0\, MPa \tag{5.11}$$

$$\sigma_U = 37.0\, MPa \tag{5.12}$$

$$\nu = 0.39 \tag{5.13}$$

Shear modulus G can then be evaluated:

$$G = \frac{E}{2\,(1+\nu)} = 1079.137\, MPa \tag{5.14}$$

Boundary conditions depend on which side of CubeSat structure the tile is mounted on. Groups of four mounting holes accommodate screws that connect the tile with the structure.

Referring to holes numbering in figures 5.3(b) and 5.3(c), these groups are:

- Holes 1, 2, 11, 12 (called external holes);
- Holes 3, 4, 9, 10 (called intermediate holes);
- Holes 5, 6, 7, 8 (called internal holes).

Translations and rotations of nodes belonging to holes accommodating a screw have been set to null values.

5.3.1 Modal analysis

For each boundary condition described in previous section, a modal analysis has been performed. Fundamental resonance frequencies have been found and are listed in table 5.6.

Boundary condition	**Fundamental resonance frequency [Hz]**
External holes fixed	598.320
Intermediate holes fixed	611.590
Internal holes fixed	611.000

Table 5.6: Reaction wheel tile fundamental resonance frequencies calculated with possible boundary conditions.

Requirements for fundamental frequencies imposed by Vega launch vehicle can be found in Vega User's Manual[6]. These apply to the entire spacecraft, cantilevered at the interface and employing one of the prescribed off-the-shelf adapters. For the lateral axis, the frequency f_{Lat} must be equal to or greater than $15\,Hz$:

$$f_{Lat} \geq 15\,Hz \tag{5.15}$$

And for longitudinal axis allowable values for fundamental frequency f_{Long} are:

$$20\,Hz < f_{Long} < 45\,Hz \quad \vee \quad f_{Long} > 60\,Hz \tag{5.16}$$

Since the tile can be mounted on any of the CubeSat structure faces, both requirements apply, and both are satisfied by the tile.

[6] [9, p. 4-3,4-4]

5.3.2 Linear static analysis

The linear static analysis employs load conditions described in section 5.1 and boundary conditions described at section 5.3. A preliminary analysis is made with $10\,g$ loads along all axes, in positive and negative directions. Once compatibility with these loads is verified, $13\,g$ loads along positive and negative axes are introduced.
Results for displacements are given in table 5.7 and in figures 5.4-5.7. For a given load intensity, displacement fields are very similar for the two directions in each axis, and maximum displacement magnitudes are the same. As expected, maximum displacements occur for loads along $\pm Z$ axes, and they appear to be contained for the maximum value corresponding to $13\,g$ loads. External holes fixing produces major displacements between the possible boundary conditions, thus analysis with internal holes fixed has been neglected for $13\,g$ loads.
Results for equivalent Von Mises stresses are given in table 5.8 and figures 5.8-5.11. As expected, maximum stresses occur in fixed holes nodes. As for the displacements, for a given load intensity stress fields are very similar for the two directions in each axis, and maximum and minimum values are the same. Clearly, maximum stresses are found for $\pm Z$ loads. Internal holes fixing produces lower stresses with respect to external holes fixing, thus it has been neglected for $13\,g$ case. Finally, it is clear that maximum stresses are well below epoxy resin tensile strenght σ_U, thus material can withstand the prescribed launch loads.
In conclusion, the proposed structural configuration appears to be suitable for Vega launch vehicle, within the validity of assumed hypotheses. However, perfect bondings have been assumed. It could be useful to evaluate stresses in the bondings with a non linear finite elements analysis.

Maximum displacements magnitude [μm]			
Load intensity	**Load direction**	**External holes fixed**	**Internal holes fixed**
$10\,g$	$\pm X$	0.178	0.078
	$\pm Y$	0.201	0.173
	$\pm Z$	11.800	11.100
$13\,g$	$\pm X$	0.232	—
	$\pm Y$	0.262	—
	$\pm Z$	15.300	—

Table 5.7: Maximum displacements magnitudes due to $10\,g$ and $13\,g$ loads, with different boundary conditions.

Von Mises stresses magnitude [MPa]				
Load intensity	**Load direction**	**Maximum/ minimum**	**External holes fixed**	**Internal holes fixed**
$10\,g$	$\pm X$	max	5.240×10^{-2}	3.760×10^{-2}
		min	1.560×10^{-5}	1.410×10^{-5}
	$\pm Y$	max	5.070×10^{-2}	4.450×10^{-2}
		min	1.500×10^{-5}	1.810×10^{-5}
	$\pm Z$	max	4.110×10^{-1}	3.890×10^{-1}
		min	4.100×10^{-5}	3.680×10^{-5}
$13\,g$	$\pm X$	max	6.810×10^{-2}	—
		min	2.030×10^{-5}	—
	$\pm Y$	max	6.590×10^{-2}	—
		min	1.950×10^{-5}	—
	$\pm Z$	max	5.340×10^{-1}	—
		min	5.330×10^{-5}	—

Table 5.8: Maximum and minimum equivalent Von Mises stresses magnitudes due to $10\,g$ and $13\,g$ loads, with different boundary conditions.

Load Event		QSL (g) (+ = tension ; - = compression)		
		Longitudinal		Lateral
		Compression	Tension	
1	Lift-off phase	-4.5	+3.0	±0.9
2	Flight with maximum dynamic pressure (Q_{max})	-3.0	N/A	±0.9
3	1st stage flight with maximal acceleration and tail off	-5.0	N/A	±0.7
4	2nd stage ignition and flight, 3rd stage ignition	-5.0	+3.0	±0.7
5	3rd stage maximal acceleration	-7.0 + M (1) / 1000	N/A	±0.2
6	AVUM flight	-1.0	+0.5	±0.7

(a)

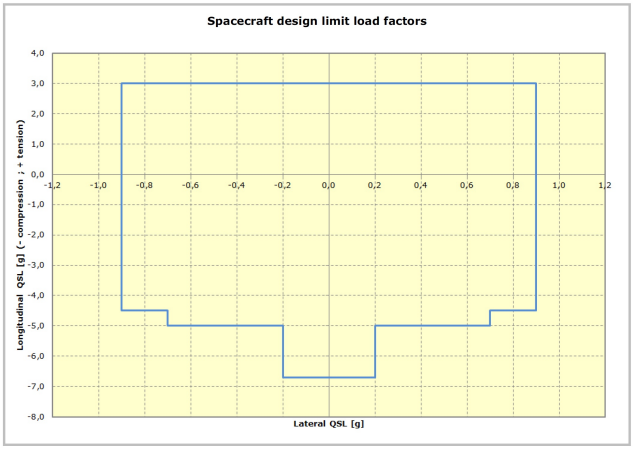

(b)

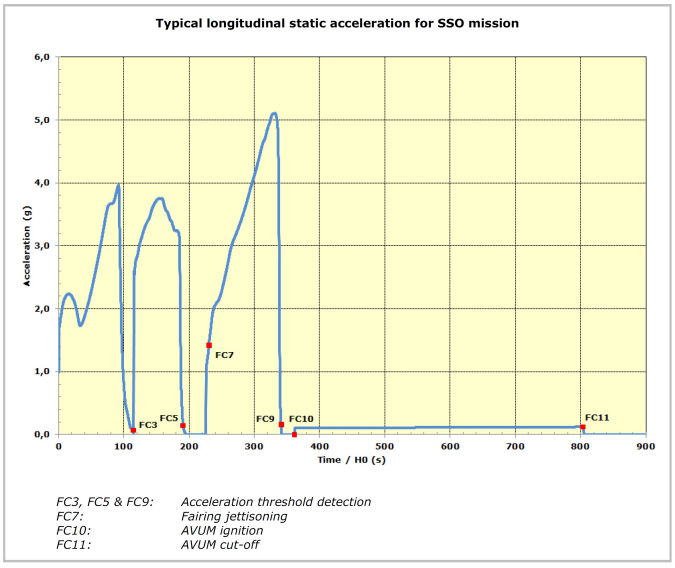

(c)

Figure 5.1: Recommended limit quasi-static loads table (a) and corresponding diagram (b), and typical time history for longitudinal static acceleration in Sun-Synchronous Orbit (SSO) mission (c), taken from Vega User's Manual[a].

[a] [9]

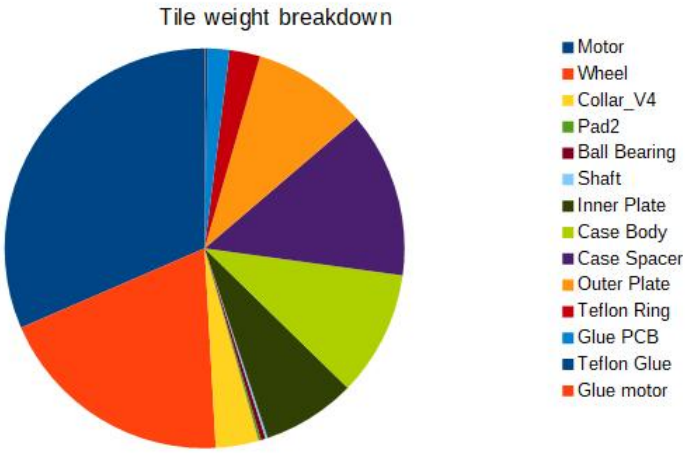

Figure 5.2: Tile weight breakdown.

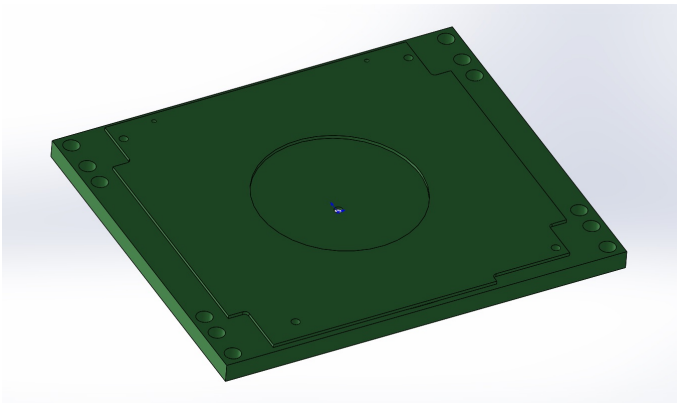

(a)

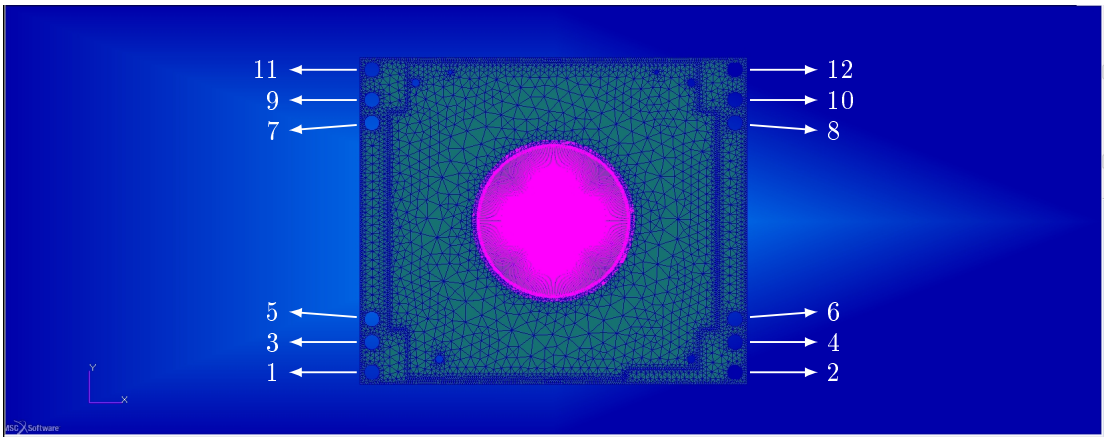

(b)

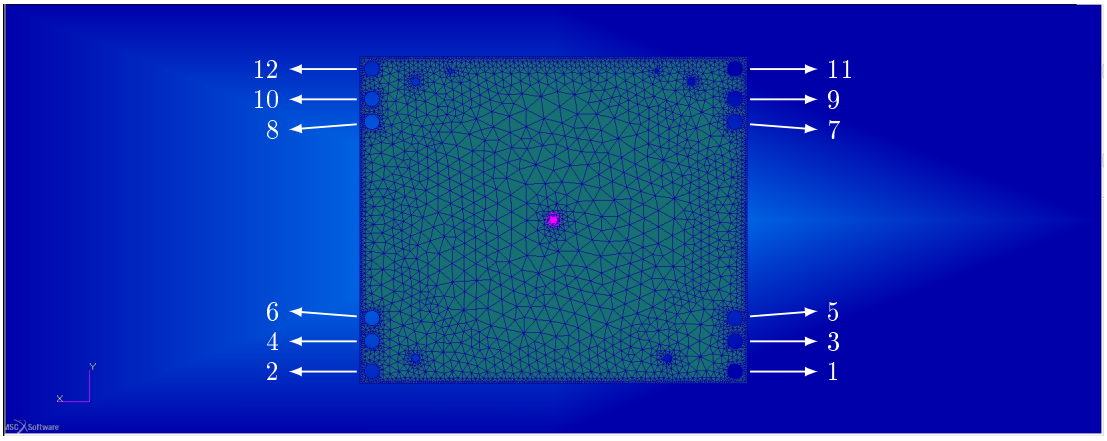

(c)

Figure 5.3: Tile simplified CAD model (a) and tile mesh seen from inner plate side (b) and outer plate side (c). The reference frame for structural analysis and mounting holes numbering are indicated in figures (b) and (c). The RBE connections are shown in pink.

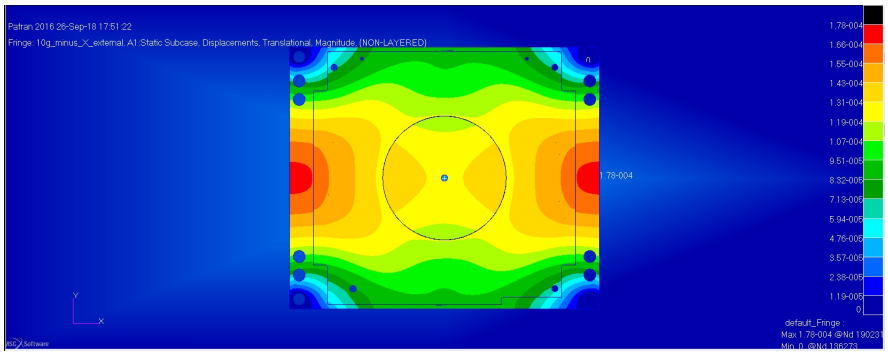

(a)

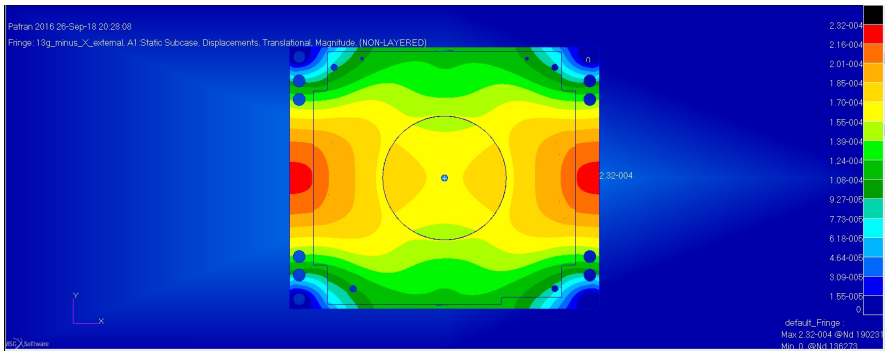

(b)

Figure 5.4: Tile displacements magnitudes with external holes fixed due to loads along $-X$ axis and intensity of $10\,g$ (a) and $13\,g$ (b). Displacements are given in millimeters.

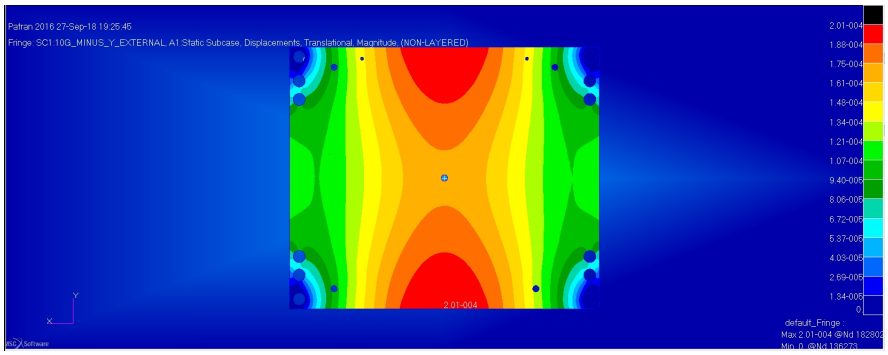

(a)

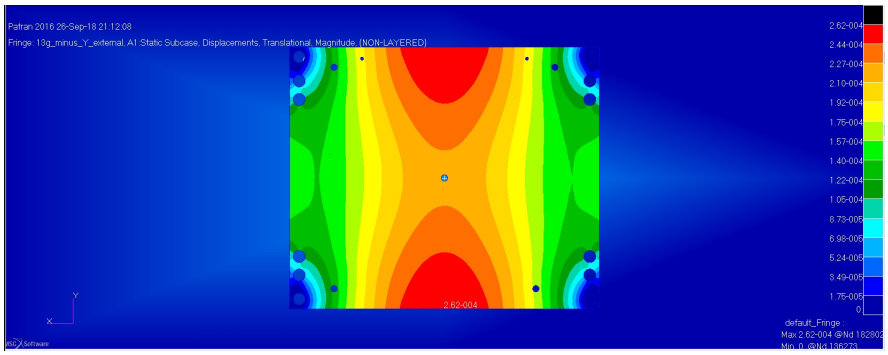

(b)

Figure 5.5: Tile displacements magnitudes with external holes fixed due to loads along $-Y$ axis and intensity of $10\,g$ (a) and $13\,g$ (b). Displacements are given in millimeters.

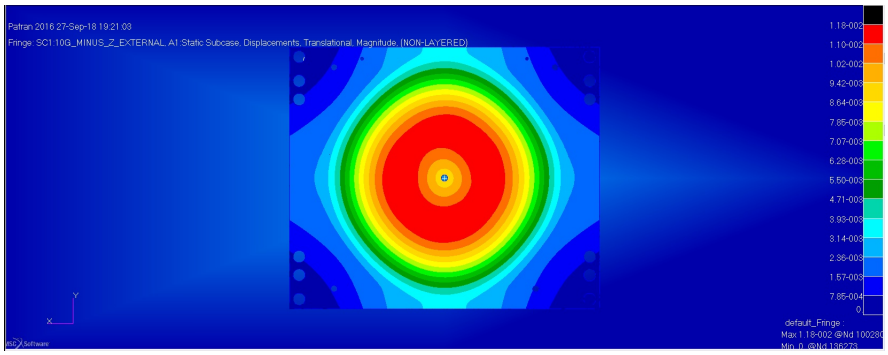

(a)

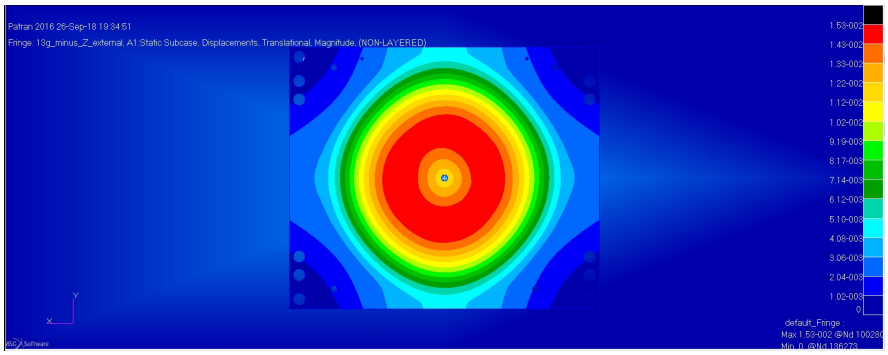

(b)

Figure 5.6: Tile displacements magnitudes with external holes fixed due to loads along $-Z$ axis and intensity of $10\,g$ (a) and $13\,g$ (b). Displacements are given in millimeters.

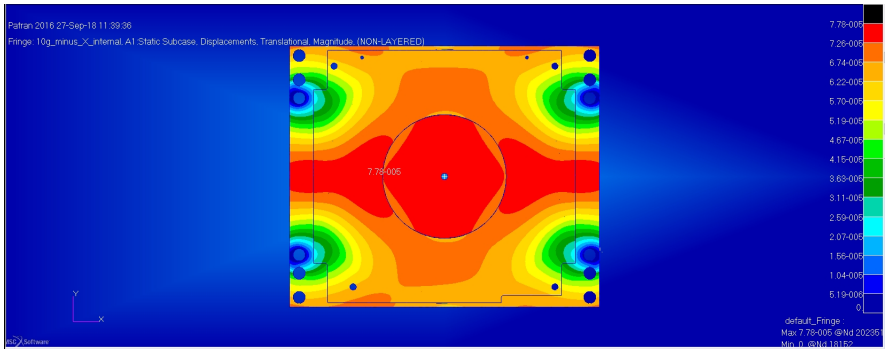

(a)

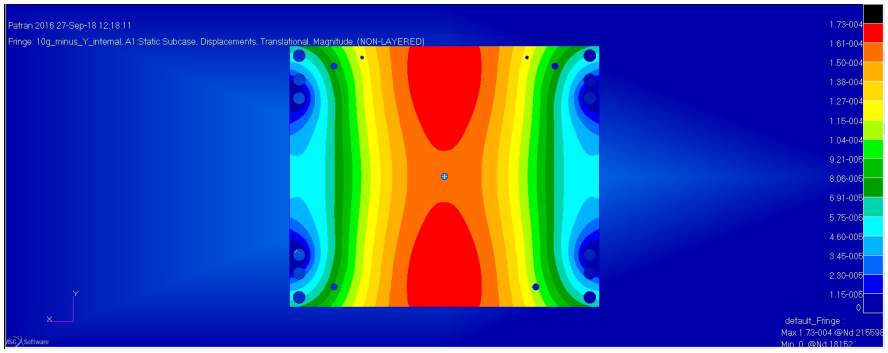

(b)

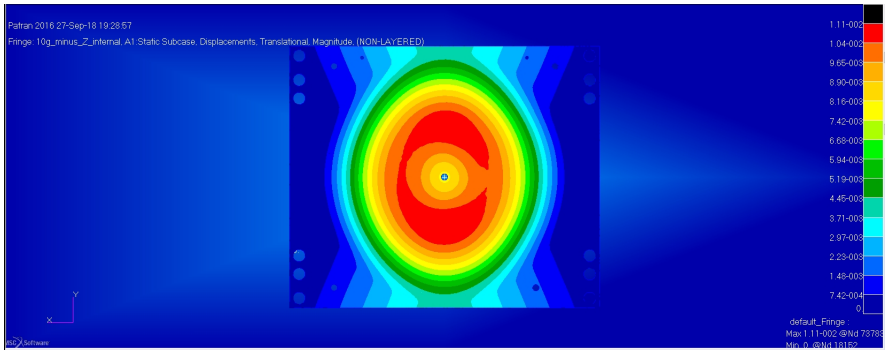

(c)

Figure 5.7: Tile displacements magnitudes with internal holes fixed due to $10\,g$ loads acting along $-X$ axis (a), $-Y$ axis (b) and $-Z$ axis (c). Displacements are given in millimeters.

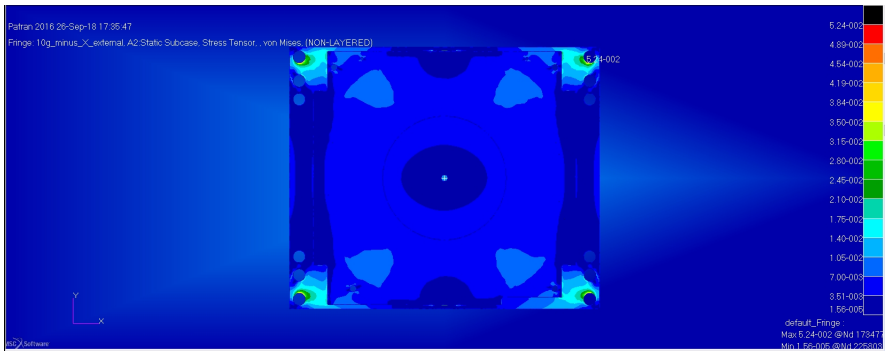

(a)

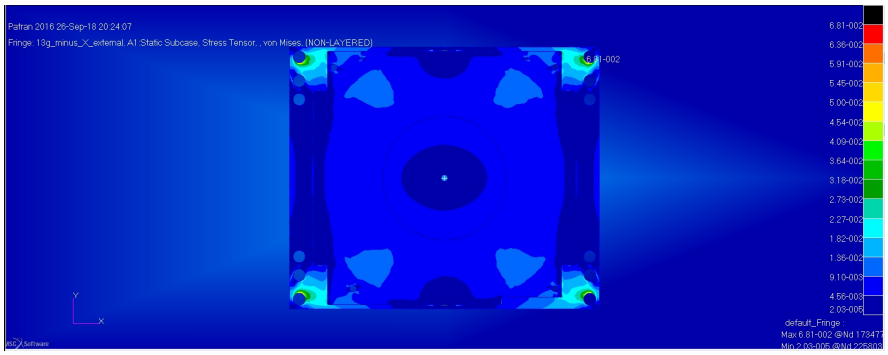

(b)

Figure 5.8: Tile stresses magnitudes with external holes fixed due to loads along $-X$ axis and intensity of $10\,g$ (a) and $13\,g$ (b). Stresses are given in megapascal.

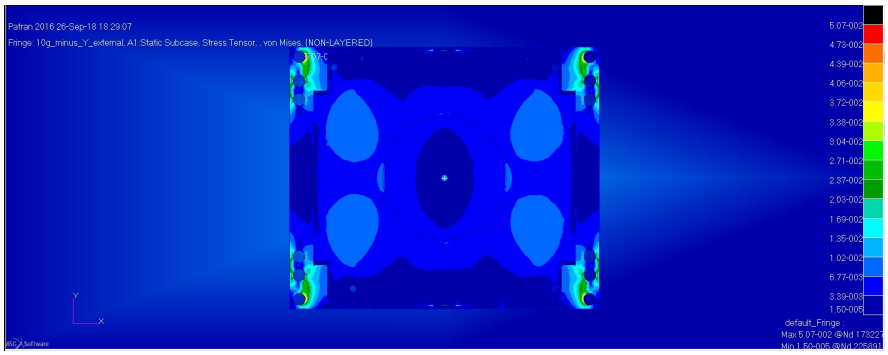

(a)

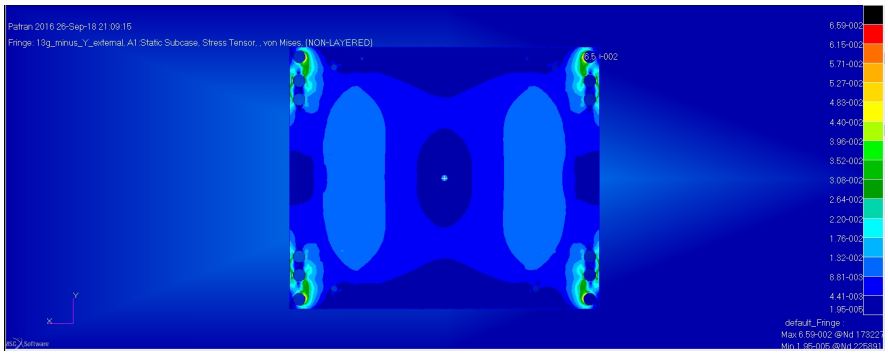

(b)

Figure 5.9: Tile stresses magnitudes with external holes fixed due to loads along $-Y$ axis and intensity of $10\,g$ (a) and $13\,g$ (b). Stresses are given in megapascal.

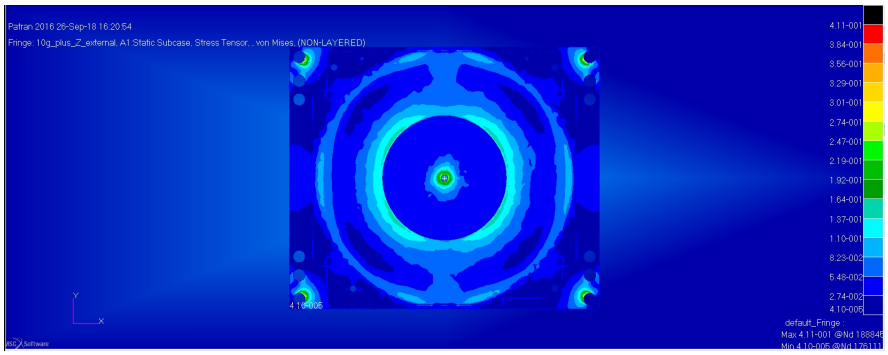

(a)

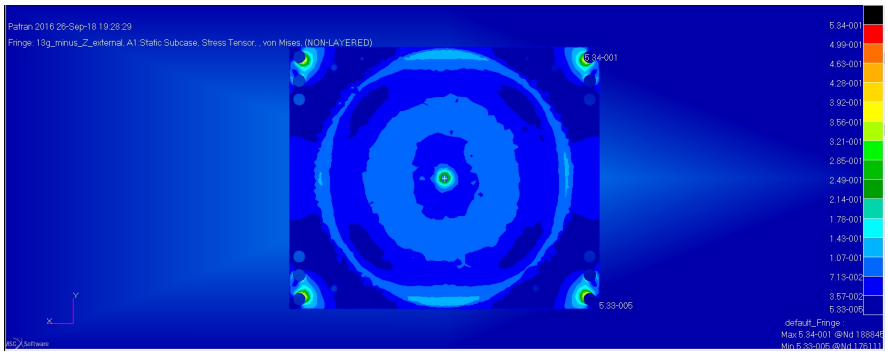

(b)

Figure 5.10: Tile stresses magnitudes with external holes fixed due to loads along $-Z$ axis and intensity of $10\,g$ (a) and $13\,g$ (b). Stresses are given in megapascal.

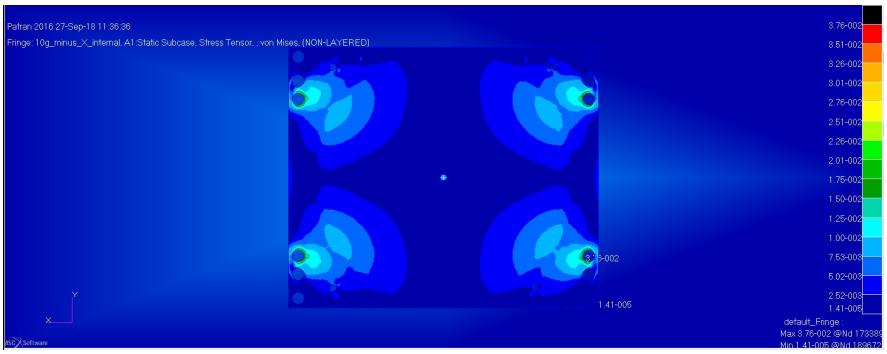

(a)

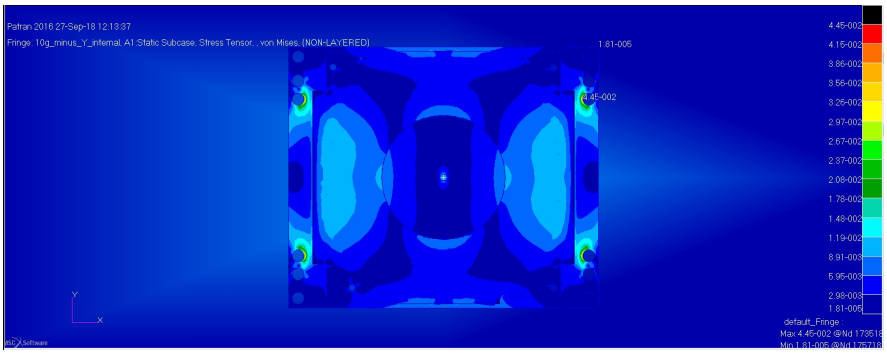

(b)

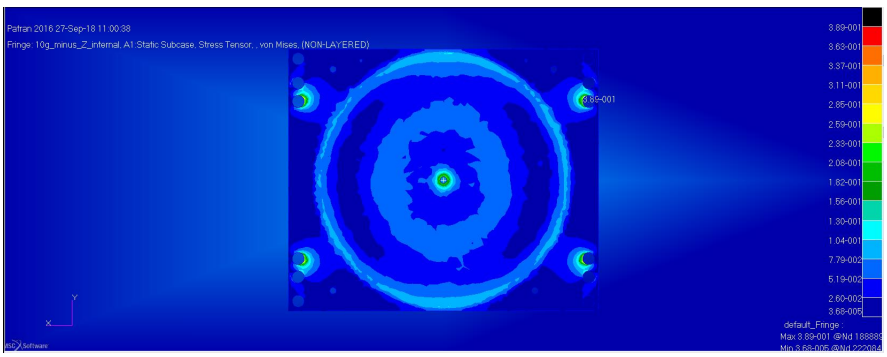

(c)

Figure 5.11: Tile stresses magnitudes with internal holes fixed due to $10\,g$ loads acting along $-X$ axis (a), $-Y$ axis (b) and $-Z$ axis (c). Stresses are given in megapascal.

Chapter 6

Conclusions and future work

In the present chapter, conclusions on the analyses are presented. Starting from these conclusions, future work is proposed.

6.1 Conclusions

Results from motor analysis are shown in tables 6.1 and 6.2 and in figure 6.1. Autonomously built motor weight and maximum input power were not evaluated due to poor efficiency, and commercial motors maximum input power were evaluated with voltages and currents in maximum continuous operation. All saturation momenta are acceptable, although maximum efficiency of autonomously built motor is excessively low. However, EC 10 flat motor has gone out of production, and mass of EC 32 motor appears excessive with respect to wheel mass, as shown in mass breakdown in figure 6.2. Moreover, motor architecture needs to be adapted to leave room for the payload.

Motor	**Version**	**Diameter** $[mm]$	**Weight** $[g]$	**Max input power** $[W]$
Autonomously built	1	—	—	—
EC 10 flat	2	10	0.82	0.488
EC 32 flat	3-4	32	32.00	8.220

Table 6.1: Motors characteristics.

Motor	**Max speed** $[RPM]$	**Max torque** $[mNm]$	**Saturation momentum** $[mNms]$
Autonomously built	3434	6.525	5.636
EC 10 flat	16 600	0.202	27.257
EC 32 flat	9210	15.500	16.455

Table 6.2: Motors performances.

Thermal analysis of version 4 has revealed that no component, in Low Earth Orbit, is outside of working temperatures range, when exposed to Sun and Earth radiation. However, in the solar radiation case, temperature margin appears scarce for motor windings.
The structural analysis, made on version 4, assured that launch on a Vega launch vehicle is feasible. Under a $13\,g$ inertial load there is no structural failure, since stresses are well below yeld strength.

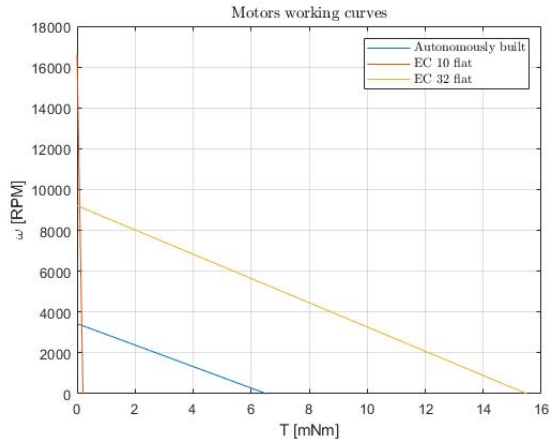

(a)

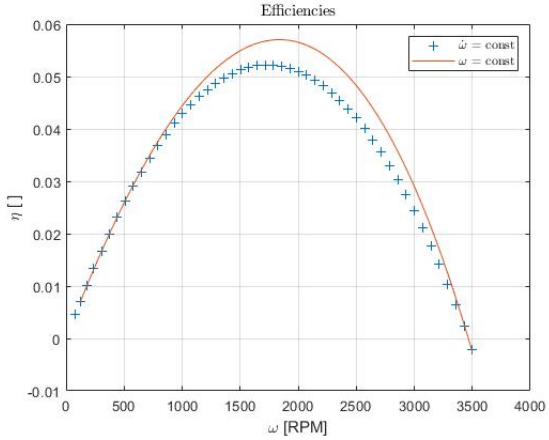

(b)

Figure 6.1: Motors working curves (a) and efficiencies for autonomously built motor (b).

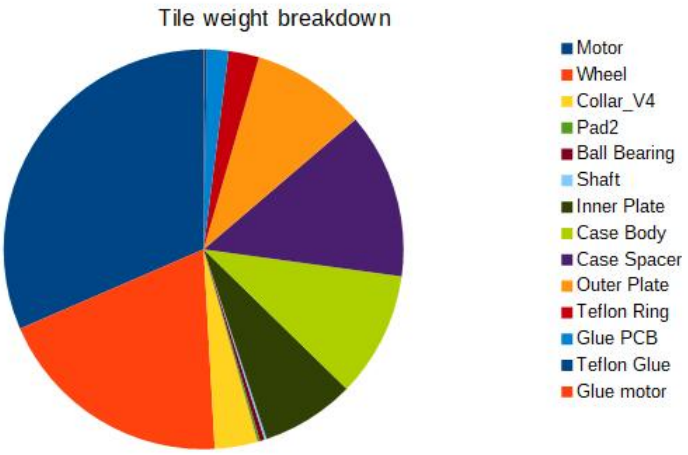

Figure 6.2: Tile version 4 mass breakdown.

In conclusion, tables can be compared with their correspondents in the state of the art description. Values appear to be in the same orders of magnitude, although weight for proposed solutions appears inferior.

Recalling proposed objectives in the problem statement at section 1.3:

- Designed reaction wheel is flat and mounted on CubeSat external faces;
- The design integrates magnetic torquers, magnetometers and solar cells, that are not described in this thesis;
- The reaction wheel is modular;
- Versions 2-4 characteristics appear to be in line with state of the art devices.

6.2 Future works

Version 4, based on analyses and conclusions, seems to have a satisfying design. However, design cold be improved with the following future works:

- Motor weight could be improved by developing a second autonomously built motor. Low efficiency problems can be solved by changing permanent magnets distribution in the wheel, as shown in the motor analysis chapter. This would give more control on weight, performances, and as a consequence on saturation momentum;
- Thermal analysis could be improved by including a thermal model for the whole CubeSat. Thus temperature generators could be avoided and the real thermal behavior could be studied. It is possible that some adaptation may be required to avoid components maximum temperatures;
- Tile structure could be improved by employing CFRP for the whole tile, instead of using carbon-epoxy fiber just for the collar. With a proper material tailoring, tile mass could be reduced. Moreover, a more tight integration among structure, reaction wheel and its motor, electronics, magnetorquer and electrical power system components could be obtained.

Appendices

Appendix A

Motor performances script

MATLAB script written for autonomously built motor performances evaluation, described at sections 3.4.1 and 3.4.2, is reproduced below.

```
clear all
close all
clc
% all parameters are in SI, except where specified
m1=3;
theta_max=2*asin(5/28);%20*pi/180;
D_theta=20*pi/180;
V=2;
% variables for K
n_c=3;
n=40;
Phi_M=2.9715*10^(-5);
% variables for K1=K'
R=1.007*n_c;
L=1.068*10^(-4);
tau=L/R;
%% electrical parameters for proposal_2
% current I_c due to coils, in stage I
%
N=3434;
omega=[1,100,1000,N]*2*pi/60;
theta=0:0.001:6*D_theta;
I_c=zeros(length(theta),4);
figure(3);
hold on;
for j=1:length(omega)
for i=1:length(theta)
if theta(i)<D_theta
I_c(i,j)=V/R*(1-exp(-theta(i)/tau/omega(j)));
I0=I_c(i,j);
else
I_c(i,j)=I0*exp(-(theta(i)-D_theta)/tau/omega(j));
end
end
end
% stages III-IV current
for j=1:length(omega)
for i=1:length(theta)
if i+2*349 <= length(theta)
```

```
% Delta theta=20 deg=.349 rad = 349 steps in theta
if (theta(i+2*349)-2*20*pi/180)<(40*pi/180)
I_c(i+2*349,j)=-V/R*(1-exp(-(theta(i))/tau/omega(j)));
I0=I_c(i+2*349,j);
else
I_c(i+2*349,j)=I0*exp(-(theta(i)-40*pi/180)/tau/omega(j));
end
end
end
end
% stage VI current
for j=1:length(omega)
for i=1:length(theta)
if i+5*349 <= length(theta)
I_c(i+5*349,j)=V/R*(1-exp(-theta(i)/tau/omega(j)));
end
end
plot(theta*180/pi,I_c(:,j));
end
%
grid on;
hold off;
title('I_{C} - Phase 1');
xlabel('\theta [deg]');
ylabel('I_{C} [A]');
legend('\omega=1 RPM', '\omega=100 RPM', '\omega=1000 RPM',
'\omega=3434 RPM','Location','southeast');
%
% I_PM with right phase
I_PM2=zeros(length(theta),length(omega));
figure(4);
hold on;
for i=1:length(omega)
K(i)=n_c*n*0.5*Phi_M*pi*omega(i)/theta_max;
K1(i)=R/L*theta_max/pi/omega(i);
for j=1:2*349+1
I_PM2(j,i)=K(i)/L*theta_max/pi/omega(i)/(1+K1(i)^2)*(exp(-(theta(j)+
(theta_max-D_theta)/2)/omega(i)/tau)-cos(pi/theta_max*(theta(j)+
(theta_max-D_theta)/2))+K1(i)*sin(pi/theta_max*(theta(j)+(theta_max-D_theta)/2)));
end
for j=2*349+1:3*349-1
I_PM2(j,i)=I_PM2(2*349+1,i)*exp(-theta(j-(2*349))/omega(i)/tau);
end
I_PM2((3*349:1:end),i)=-I_PM2((1:1:3*349+2),i);
plot(theta*180/pi,I_PM2(:,i));
end
hold off;
grid on;
title('I_{PM} - Phase 1');
xlabel('\theta [deg]');
% xticklabels({'x = 0','x = 5','x = 10'});
ylabel('I_{PM} [A]');
% yticks(-3:0.5:3);
% yticklabels(-3:0.5:3);
legend('\omega=1 RPM', '\omega=100 RPM', '\omega=1000 RPM',
'\omega=3434 RPM','location','southeast');
```

```
%
% total current I=I_c-I_PM2
I=I_c-I_PM2;
figure (5);
hold on;
for i=1:length(omega)
plot(theta*180/pi,I(:,i));
end
grid on;
hold off;
title('I - Phase 1');
xlabel('\theta [deg]');
% xticklabels({'x = 0','x = 5','x = 10'});
ylabel('I [A]');
% yticks(-3:0.5:3);
% yticklabels(-3:0.5:3);
legend('\omega=1 RPM', '\omega=100 RPM', '\omega=1000 RPM',
'\omega=3434 RPM','Location','southeast');
%
% counterelectromotive force V_cem
V_cem=zeros(length(theta),length(omega));
figure (6);
hold on;
for i=1:length(omega)
for j=1:2*349+1
V_cem(j,i)=K(i)*sin(pi/theta_max*(theta(j)+(theta_max-D_theta)/2));
end
V_cem(2*349+1:1:3*349-1,i)=zeros(349-1,1);
V_cem((3*349:1:end),i)=-V_cem((1:1:3*349+2),i);
plot(theta*180/pi,V_cem(:,i));
end
hold off;
grid on;
title('V_{cem} - Phase 1');
xlabel('\theta [deg]');
% xticklabels({'x = 0','x = 5','x = 10'});
ylabel('V_{cem} [V]');
% yticks(-3:0.5:3);
% yticklabels(-3:0.5:3);
legend('\omega=100 RPM', '\omega=100 RPM', '\omega=1000 RPM',
'\omega=3434 RPM','Location','southeast');
%
% power P_cem=V_cem*I
figure(7);
hold on;
for i=1:length(omega)
for j=1:length(theta)
P_cem(j,i)=V_cem(j,i)*I(j,i);
end
plot(theta*180/pi,-P_cem(:,i));
end
hold off;
grid on;
title('P_{cem} - Phase 1');
xlabel('\theta [deg]');
% xticklabels({'x = 0','x = 5','x = 10'});
```

```
ylabel('-P_{cem} [W]');
% yticks(-3:0.5:3);
% yticklabels(-3:0.5:3);
legend('\omega=1 RPM', '\omega=100 RPM', '\omega=1000 RPM',
'\omega=3434 RPM','Location','northwest');
%
% inductive power P_L=L*I*I_dot
d_theta=theta(2)-theta(1);
figure(8);
hold on;
for i=1:length(omega)
for j=1:length(theta)
if j <= (length(theta)-1)
I_dot(j,i)=(I(j+1,i)-I(j,i))/d_theta*omega(i);
P_L(j,i)=L*I(j,i)*I_dot(j,i);
end
end
plot(theta(1:end-1)*180/pi,P_L(:,i));
end
hold off;
grid on;
title('P_L - Phase 1');
xlabel('\theta [deg]');
% xticklabels({'x = 0','x = 5','x = 10'});
ylabel('P_L [W]');
% yticks(-3:0.5:3);
% yticklabels(-3:0.5:3);
legend('\omega=1 RPM', '\omega=100 RPM', '\omega=1000 RPM',
'\omega=3434 RPM','Location','southwest');
%
% resistive power P_R=R*I^2
P_R=zeros(length(theta),length(omega));
figure(9);
hold on;
for i=1:length(omega)
for j=1:length(theta)
P_R(j,i)=R*I(j,i)^2;
end
plot(theta*180/pi,P_R(:,i));
end
hold off;
grid on;
title('P_R - Phase 1');
xlabel('\theta [deg]');
ylabel('P_R [W]');
legend('\omega=1 RPM', '\omega=100 RPM', '\omega=1000 RPM',
'\omega=3434 RPM','Location','northwest');
%
% total P_cem power from m1 phases
P_cem_tot=zeros(6*349,length(omega));
figure(10);
hold on;
for i=1:length(omega)
P_cem_tot([1:349],i)=P_cem([1:349],i)+P_cem([2*349+1:3*349],i)+
P_cem([4*349+1:5*349],i);
P_cem_tot([349+1:2*349],i)=P_cem([349+1:2*349],i)+
```

```
P_cem([3*349+1:4*349],i)+P_cem([5*349+1:6*349],i);
P_cem_tot([2*349+1:3*349],i)=P_cem_tot([1:349],i);
P_cem_tot([3*349+1:4*349],i)=P_cem_tot([349+1:2*349],i);
P_cem_tot([4*349+1:5*349],i)=P_cem_tot([1:349],i);
P_cem_tot([5*349+1:6*349],i)=P_cem_tot([349+1:2*349],i);
plot(theta([1:6*349])*180/pi,-P_cem_tot(:,i));
end
hold off;
grid on;
title('P_{cem} - sum');
xlabel('\theta [deg]');
% xticklabels({'x = 0','x = 5','x = 10'});
ylabel('-P_{cem, tot} [W]');
% yticks(-3:0.5:3);
% yticklabels(-3:0.5:3);
legend('\omega=1 RPM', '\omega=100 RPM', '\omega=1000 RPM',
'\omega=3434 RPM','Location','southwest');
%
% total P_L power from m1 phases
P_L_tot=zeros(6*349,length(omega));
figure(11);
hold on;
for i=1:length(omega)
P_L_tot([1:349],i)=P_L([1:349],i)+P_L([2*349+1:3*349],i)+
P_L([4*349+1:5*349],i);
P_L_tot([349+1:2*349],i)=P_L([349+1:2*349],i)+
P_L([3*349+1:4*349],i)+P_L([5*349+1:6*349],i);
P_L_tot([2*349+1:3*349],i)=P_L_tot([1:349],i);
P_L_tot([3*349+1:4*349],i)=P_L_tot([349+1:2*349],i);
P_L_tot([4*349+1:5*349],i)=P_L_tot([1:349],i);
P_L_tot([5*349+1:6*349],i)=P_L_tot([349+1:2*349],i);
plot(theta([1:6*349])*180/pi,P_L_tot(:,i));
end
hold off;
grid on;
title('P_L - sum');
xlabel('\theta [deg]');
% xticklabels({'x = 0','x = 5','x = 10'});
ylabel('P_{L, tot} [W]');
% yticks(-3:0.5:3);
% yticklabels(-3:0.5:3);
legend('\omega=1 RPM', '\omega=100 RPM', '\omega=1000 RPM',
'\omega=3434 RPM','Location','southeast');
%
%
% total P_R power from m1 phases
P_R_tot=zeros(6*349,length(omega));
figure(12);
hold on;
for i=1:length(omega)
P_R_tot([1:349],i)=P_R([1:349],i)+P_R([2*349+1:3*349],i)+
P_R([4*349+1:5*349],i);
P_R_tot([349+1:2*349],i)=P_R([349+1:2*349],i)+
P_R([3*349+1:4*349],i)+P_R([5*349+1:6*349],i);
P_R_tot([2*349+1:3*349],i)=P_R_tot([1:349],i);
P_R_tot([3*349+1:4*349],i)=P_R_tot([349+1:2*349],i);
```

```
P_R_tot([4*349+1:5*349],i)=P_R_tot([1:349],i);
P_R_tot([5*349+1:6*349],i)=P_R_tot([349+1:2*349],i);
plot(theta([1:6*349])*180/pi,P_R_tot(:,i));
end
hold off;
grid on;
title('P_R - sum');
xlabel('\theta [deg]');
% xticklabels({'x = 0','x = 5','x = 10'});
ylabel('P_{R, tot} [W]');
% yticks(-3:0.5:3);
% yticklabels(-3:0.5:3);
legend('\omega=1 RPM', '\omega=100 RPM', '\omega=1000 RPM',
'\omega=3434 RPM','Location','southeast');
%
% Electrical powers
V=[1,1.5,2];
I_c_p=V(end)/R;% peak value of I_c
K_omega=n_c*n*0.5*Phi_M*pi/theta_max;% K(i)=K_omega*omega(i);
K1_omega=R/L*theta_max/pi;% K1(i)=K1_omega/omega(i);
% P_cem-omega plot
% these quantities have to be set with excel
% spreadsheet "Calcoli_magnetici_aggiornati"
n=[40,30,20,10,9,8];
R=n_c*[1.007,0.755,0.503,0.252,0.227,0.201];
L=[1.068*10^(-4),6.008*10^(-5),2.67*10^(-5),6.675*10^(-6),5.407*10^(-6),
4.272*10^(-6)];
I_c_p=V(end)./R;
tau=L./R;
%
%% mean powers
%
x=linspace(0,4000*2*pi/60,100);% motor speeds
figure(20);
hold on;
for i=1:length(n)
K_omega(i)=n_c*n(i)*0.5*Phi_M*pi/theta_max;% K(i)=K_omega*omega(i);
K1_omega(i)=R(i)/L(i)*theta_max/pi;% K1(i)=K1_omega/omega(i);
P_1(i)=-2/pi*I_c_p(i)*K_omega(i);% coefficient for P_cem
P_2(i)=(K_omega(i)).^2*K1_omega(i)./L(i)*theta_max/pi;% coefficient for P_cem
P(:,i)=P_1(i).*x+P_2(i)./(1+(K1_omega(i))^2./x.^2);% P_cem
P_omega2(:,i)=-P(:,i)./x'.^2;
plot(x*60/2/pi,-P(:,i));
end
legend('n=40','n=30','n=20','n=10','n=9','n=8','Location','southwest');
grid on;
hl=title('$\overline{P}_{cem}$ - $\omega$');
set(hl, 'Interpreter', 'latex');
xlabel('\omega [RPM]');
h2=ylabel('-$\overline{P}_{cem}$ [W]');
set(h2, 'Interpreter', 'latex');
ylim([-1 1]);
%
figure(21);
hold on;
for i=1:length(n)
```

```
plot(x*60/2/pi,P_omega2(:,i));
end
legend('n=40','n=30','n=20','n=10','n=9','n=8','Location','northeast');
grid on;
xlabel('\omega [RPM]');
h2=ylabel('-$\overline{P}_{cem}/\omega^2\,[Ws^2]$');
set(h2, 'Interpreter', 'latex');
ylim([-1 1]);
%
% P_L plot
figure(22);
hold on;
P_L=zeros(length(x),length(n));
for i=1:length(n)
K_omega(i)=n_c*n(i)*0.5*Phi_M*pi/theta_max;% K(i)=K_omega*omega(i);
K1_omega(i)=R(i)/L(i)*theta_max/pi;% K1(i)=K1_omega/omega(i);
P_L(:,i)=2*L(i)/D_theta*(K_omega(i).*x/L(i)*theta_max/pi./x./(1+
(K1_omega(i)./x).^2)).^2.*x.*exp(-D_theta/tau(i)./x);
plot(x*60/2/pi,P_L(:,i));
end
legend('n=40','n=30','n=20','n=10','n=9','n=8','Location','northwest');
grid on;
hold off;
hl=title('$\overline{P}_L$ - $\omega$ = const');
set(hl, 'Interpreter', 'latex');
xlabel('\omega [RPM]');
h2=ylabel('-$\overline{P}_L$ [W]');
set(h2, 'Interpreter', 'latex');
% additional terms in P_cem
figure(23);
hold on;
for i=1:length(n)
K_omega(i)=n_c*n(i)*0.5*Phi_M*pi/theta_max;% K(i)=K_omega*omega(i);
K1_omega(i)=R(i)/L(i)*theta_max/pi;% K1(i)=K1_omega/omega(i);
P_cem_II(:,i)=K_omega(i).*x/pi/(1+(D_theta./(x(i).*pi.*tau(i)))^2).*
(1+exp(-D_theta./x(i)/tau(i))).*(I_c_p(i).*(1+exp(-D_theta./x(i)/tau(i))-
exp(-2.*D_theta./x(i)/tau(i)))+(K_omega(i).*x/L(i)*theta_max/pi./x./
(1+(K1_omega(i)./x).^2)).*(1-exp(-D_theta./x(i)/tau(i))));
plot(x*60/2/pi,P_cem_II(:,i));
end
legend('n=40','n=30','n=20','n=10','n=9','n=8','Location','northwest');
grid on;
hl=title('$\overline{P}_{cem,\,II}$ - $\omega$ = const');
set(hl, 'Interpreter', 'latex');
xlabel('\omega [RPM]');
h2=ylabel('-$\overline{P}_{cem,\,II}$ [W]');
set(h2, 'Interpreter', 'latex');
%
%% working curve evaluation assuming constant angular velocity
%
J=pi/2*2700*(2.2*10^(-3))*(36*10^(-3))^4;
n=n(end-1);% n(1);
R=R(end-1);% R(1);
L=L(end-1);% L(1);
I_c_p=V(end)./R;% I_c_p(1);
tau=tau(end-1);% tau(1);
```

```
K_omega=n_c*n*0.5*Phi_M*pi/theta_max;% K(i)=K_omega*omega(i);
K1_omega=R/L*theta_max/pi;% K1(i)=K1_omega/omega(i);
%
Omega=linspace(7,3500*2*pi/60,100);
% there is no acceptable solution under 5.9 rad/s = 56.3408 RPM
for j=1:length(Omega)
omega_in=Omega(j);
omega_m=omega_in+10^(-1);
d_omega_m=10^(-1);
diff=10^9;
omega_mem=10^(-6);
k=1;% index to count number of iterations
while abs(diff)>0.01*omega_in && (k<5*10^6+1)
Delta_omega=2*(omega_m-omega_in);
omega_f=omega_in+Delta_omega;
P_cem=-I_c_p*K_omega/pi*2*omega_m+(K_omega)^2*K1_omega/L*theta_max/pi*
(1+K1_omega/Delta_omega*(atan(omega_in/K1_omega)-atan(omega_f/K1_omega)));

M=-P_cem/omega_m;
omega_dot=M/J;
D_t=D_theta/omega_m;
omega_f2=omega_in+omega_dot*D_t;

omega_mem=omega_m;

diff=omega_f2-omega_f;
if diff>=0
omega_m=omega_m+d_omega_m;
else
omega_m=omega_m-d_omega_m;
end
k=k+1;% number of iterations is k-1
end
it(j)=k-1;
diff_mem(j)=diff;
P_cem_const(j)=P_cem;
P_L_const(j)=2*L/D_theta*(K_omega*theta_max/pi/L/(1+(K1_omega/omega_mem)^2))^2*
omega_mem*exp(-D_theta/tau/omega_mem);
M_const(j)=M;
omega_const(j)=omega_mem;
eta_const(j)=M*omega_mem/(2*I_c_p*V(end)/D_t*(D_t+tau*(exp(-D_t/tau)-1))-
V(end)/D_t*K_omega*omega_mem/L*theta_max/pi/omega_mem/(1+
(K1_omega/omega_mem)^2)*(K1_omega/omega_mem*2*theta_max/pi/omega_mem+tau*
(1-exp(-D_t/tau))*(2-exp(-2*D_t/tau))));
end
figure(25);
plot(Omega*60/2/pi,0.01*Omega*60/2/pi,'*');
hold on;
grid on;
plot(Omega*60/2/pi,diff_mem*60/2/pi,'+');
hl=title('Error check - $\omega$ = const');
set(hl,'Interpreter','latex');
xlabel('\omega_{in} [RPM]');
ylabel('diff [RPM]');
hl=legend('max error','diff','Location','northwest');
set(hl,'Interpreter','latex');
```

```
%
figure(26);
semilogy(Omega*60/2/pi,it);
grid on;
hl=title('Iterations - $\omega$ = const');
set(hl, 'Interpreter', 'latex');
xlabel('\omega_{in} [RPM]');
ylabel('iterations number [ ]');
%
figure(27);
plot(omega_const*60/2/pi,-P_cem_const);
hold on;
grid on;
plot(omega_const*60/2/pi,P_L_const);
hl=title('Powers - $\omega$ = const');
set(hl, 'Interpreter', 'latex');
xlabel('\omega [RPM]');
ylabel('P [W]');
ylim([-0.05 0.65])
hl=legend('$-P_{cem}$','$P_L$','Location','northeast');
set(hl, 'Interpreter', 'latex');
%
figure(28);
plot(omega_const*60/2/pi,eta_const);
grid on;
xlabel('\omega [RPM]');
ylabel('\eta [ ]');
hl=title('Efficiency - $\omega$ = const');
set(hl, 'Interpreter', 'latex');
%
%% numerical solution taking angular acceleration into account
%
K_omega=n_c*n*0.5*Phi_M*pi/theta_max;% K(i)=K_omega*omega(i);
K1_omega=R/L*theta_max/pi;% K1(i)=K1_omega/omega(i);
%
Omega_2=linspace(3500*2*pi/60,0.0001,50);
delta_omega_dot=0.5;
D_theta=20*pi/180;
for i=1:length(Omega_2)
omega_0=Omega_2(i);
omega_dot=10^(-3);
k=1;
diff=10^9;
while abs(diff)>0.1*omega_dot && k<10^3+1
%      I_PMs evaluation
Delta=omega_0^2+2*omega_dot*D_theta;
dt=(-omega_0+sqrt(Delta))/omega_dot;
omega_f=omega_0+omega_dot*dt;
omega_m=0.5*(omega_0+omega_f);
fun=@(t,u) -u/tau+1/L*n_c*n*0.5*Phi_M*sin(pi/theta_max*
(omega_0*t+0.5*omega_dot*t^2))*pi/theta_max*(omega_0+omega_dot*t);
[t,I_PM]=ode15s(fun,[0 dt],0);%I_PM in 0 deg-20 deg
p=polyfit(t,I_PM,10);
%      % plot of I_PM
x=linspace(t(1),t(end),100);
py=polyval(p,x);
```

```
figure(30);
plot(t,I_PM,'LineWidth',2);
hold on;
grid on;
plot(x,py);
%       %
%       Delta2=omega_f^2+2*omega_dot*D_theta;
%       dt2=(-omega_f+sqrt(Delta2))/omega_dot;
%       [t2,I_PM2]=ode15s(fun,[dt  dt+dt2],I_PM0);%I_PM in 20 deg-40 deg
%       p2=polyfit(t2,I_PM2,10);
%       % plot of I_PM
%       x2=linspace(t2(1),t2(end),100);
%       py2=polyval(p2,x2);
%       figure(5);
%       plot(t2,I_PM2,'LineWidth',2);
%       hold on;
%       grid on;
%       plot(x2,py2);
%       P_cems evaluation (includes minor terms in P_cemII)
Pow=@(x) (-(n_c*n*0.5*Phi_M.*sin(pi/theta_max.*(omega_0.*x+0.5*omega_dot.*x.^2)).*
pi/theta_max.*(omega_0+omega_dot.*x))).*(-2*(p(1).*x.^10+p(2).*x.^9+p(3).*x.^8+p(4).*
x.^7+p(5).*x.^6+p(6).*x.^5+p(7).*x.^4+p(8).*x.^3+p(9).*x.^2+p(10).*x+p(11))+I_c_p);
%
P_cem=1/dt*integral(Pow,t(1),t(end));
omega_dot_mem=omega_dot;
I_PMf1=I_PM(end);
Delta2=omega_f^2+2*omega_dot_mem*D_theta;
dt2=(-omega_f+sqrt(Delta2))/omega_dot_mem;
[t2,I_PM2]=ode15s(fun,[dt  dt+dt2],I_PMf1);%I_PM in 20 deg-40 deg
I_PMf2=I_PM2(end);
P_L=L/2/dt*(2*I_PMf1^2+I_PMf2^2*(exp(-2*dt/tau)-1)+2*I_c_p*
(-I_PMf1+I_PMf2*exp(-dt/tau)));
%
Pow_m=P_cem+P_L;
M=-Pow_m/omega_m;
omega_dot2=M/J;
diff=omega_dot2-omega_dot;
diff_2=(omega_0+omega_dot2*dt)-omega_f;
if diff>=0
omega_dot=omega_dot+delta_omega_dot;
else
omega_dot=omega_dot-delta_omega_dot;
end
k=k+1;% number of iterations is k-1
end
i
P_cem_acc(i)=P_cem;
P_L_acc(i)=P_L;
diff_vel(i)=diff_2;
diff_acc(i)=diff;
it_acc(i)=k-1;
omega_dot_acc(i)=omega_dot_mem;
omega_acc(i)=omega_m;
M_acc(i)=M;
eta(i)=M*omega_m/(2*I_c_p*V(end)/dt*(dt+tau*(exp(-dt/tau)-1)));
%
```

```
end
figure(31);
% plot([0,M1],[N,0]);
hold on;
plot(M_const*10^3,omega_const*60/2/pi);
plot(M_acc*10^3,omega_acc*60/2/pi,'+');
grid on;
hl=title('Working curves');
set(hl, 'Interpreter', 'latex');
xlabel('T [mNm]');
ylabel('\omega [RPM]');
hl=legend('$\omega$ = const','$\dot{\omega}$ = const',
'Location','northeast');
set(hl, 'Interpreter', 'latex');
%
figure(32);
plot(Omega_2*60/2/pi,0.1*omega_dot_acc*60/2/pi,'*');
hold on;
grid on;
plot(Omega_2*60/2/pi,diff_acc*60/2/pi,'+');
hl=title('Error check - $\dot{\omega}$ = const');
set(hl, 'Interpreter', 'latex');
xlabel('\omega_{in} [RPM]');
ylabel('diff [RPM/s]');
hl=legend('max error','diff','Location','northeast');
set(hl, 'Interpreter', 'latex');
%
figure(33);
% plot(Omega_2*60/2/pi,0.01*omega_0*60/2/pi,'*');
% hold on;
plot(Omega_2*60/2/pi,diff_vel*60/2/pi,'+');
grid on;
hl=title('Velocity difference check - $\dot{\omega}$ = const');
set(hl, 'Interpreter', 'latex');
xlabel('\omega_{in} [RPM]');
ylabel('diff_2 [RPM]');
% hl=legend('max error','diff','Location','northeastoutside');
% set(hl, 'Interpreter', 'latex');
%
figure(34);
semilogy(Omega_2*60/2/pi,it_acc);
grid on;
hl=title('Iterations - $\dot{\omega}$ = const');
set(hl, 'Interpreter', 'latex');
xlabel('\omega_{in} [RPM]');
ylabel('iterations number [ ]');
%
figure(35);
semilogy(Omega_2*60/2/pi,it_acc);
hold on;
grid on;
semilogy(Omega*60/2/pi,it);
hl=title('Iterations');
set(hl, 'Interpreter', 'latex');
xlabel('\omega_{in} [RPM]');
ylabel('iterations number [ ]');
```

```
hl=legend('$\dot{\omega}$ = const','$\omega$ = const',
'Location','northeast');
set(hl, 'Interpreter', 'latex');
%
figure(36);
plot(omega_acc*60/2/pi,-P_cem_acc,'+');
grid on;
hold on;
plot(omega_acc*60/2/pi,P_L_acc,'*');
hl=title('Powers - $\dot{\omega}$ = const');
set(hl, 'Interpreter', 'latex');
xlabel('\omega [RPM]');
ylabel('P [W]');
hl=legend('$-\overline{P}_{cem}$','$\overline{P}_L$','Location','northeast');
set(hl, 'Interpreter', 'latex');
%
figure(37);
plot(omega_acc*60/2/pi,eta,'+');
grid on;
hold on;
plot(omega_const*60/2/pi,eta_const);
hl=title('Efficiencies');
set(hl, 'Interpreter', 'latex');
xlabel('\omega [RPM]');
ylabel('\eta [ ]');
hl=legend('$\dot{\omega}$ = const','$\omega$ = const', 'Location','northeast');
set(hl, 'Interpreter', 'latex');
%
%% wheel performances evaluation
%
omega_MAX=3434*2*pi/60;
H_sat=J*omega_MAX;
J_R_EC10=0.08*10^(-7);
J_R_EC32=13.9*10^(-7);
omega_MAX_EC10=16600*2*pi/60;
omega_MAX_EC32=9210*2*pi/60;
H_sat_EC10=(J+J_R_EC10)*omega_MAX_EC10;
H_sat_EC32=(J+J_R_EC32)*omega_MAX_EC32;
T_MAX=6.525*10^(-3);
T_MAX_EC10=0.202*10^(-3);
T_MAX_EC32=15.5*10^(-3);
%
figure (38);
plot([0,T_MAX*10^3],[omega_MAX*60/2/pi,0]);
hold on;
plot([0,T_MAX_EC10*10^3],[omega_MAX_EC10*60/2/pi,0]);
plot([0,T_MAX_EC32*10^3],[omega_MAX_EC32*60/2/pi,0]);
grid on;
hl=title('Motors working curves');
set(hl, 'Interpreter', 'latex');
xlabel('T [mNm]');
% xticklabels({'x = 0','x = 5','x = 10'});
ylabel('\omega [RPM]');
% yticks(-3:0.5:3);
% yticklabels(-3:0.5:3);
hl=legend('Autonomously built','EC 10 flat','EC 32 flat', 'Location','northeast');
```

```
set(h1, 'Interpreter', 'latex');
```

Appendix B

Mechanical drawings

Mechanical drawings of autonomously built components, described in section 2.2, are reproduced below.

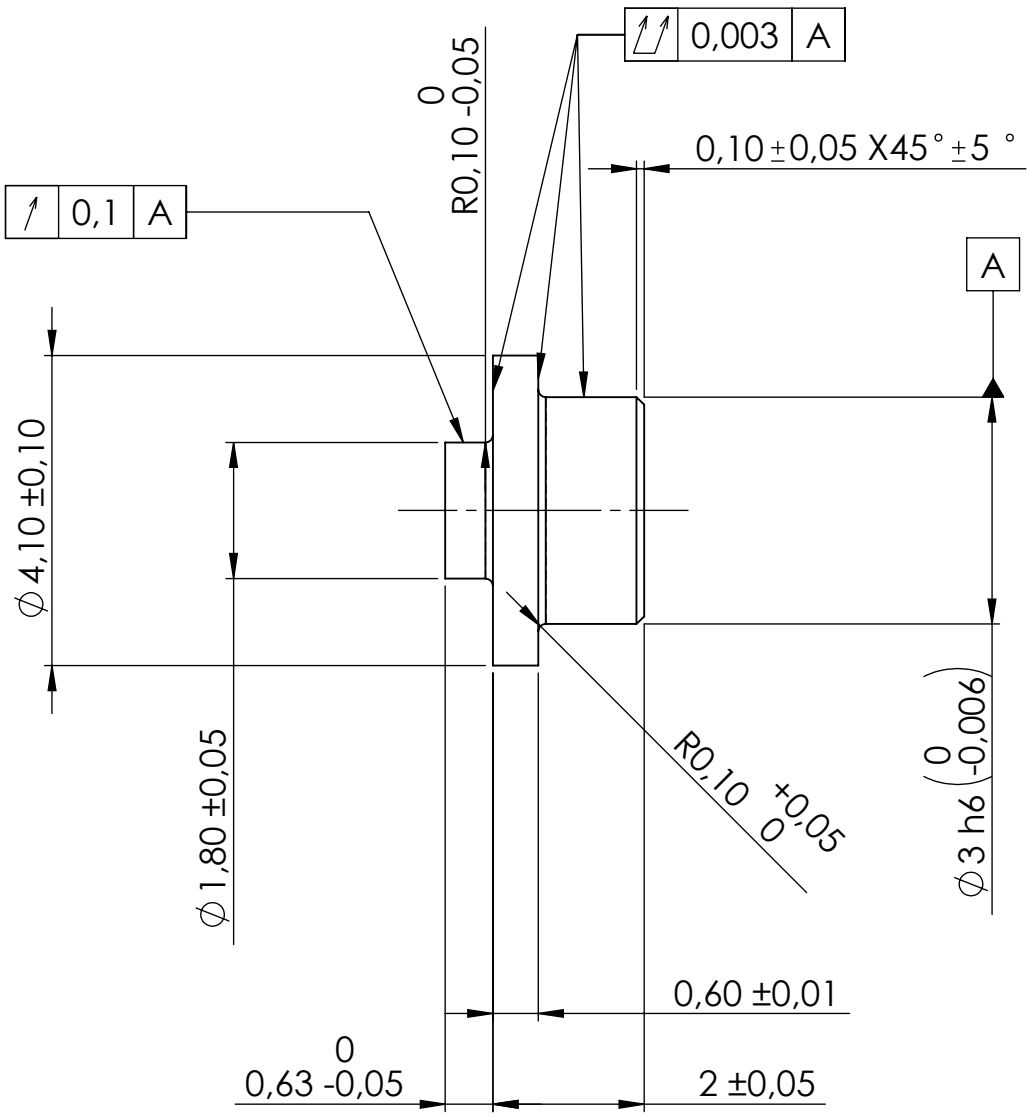

Tolleranze secondo UNI ISO 8015

Tolleranze generali ISO 2768-fH

SE NON SPECIFICATO: QUOTE IN MILLIMETRI FINITURA SUPERFICIE: TOLLERANZE: LINEARE: ANGOLARE:	FINITURA:	INTERRUZIONE BORDI NETTI	NON SCALARE DISEGNO	REVISIONE	

	NOME	FIRMA	DATA
DISEG.			
VERIF.			
APPR.			
FABB.			
Qual.			

TITOLO: Shaft_V2

MATERIALE:

N. DISEGNO 1

A4

PESO:

SCALA:20:1

FOGLIO 1 DI 1

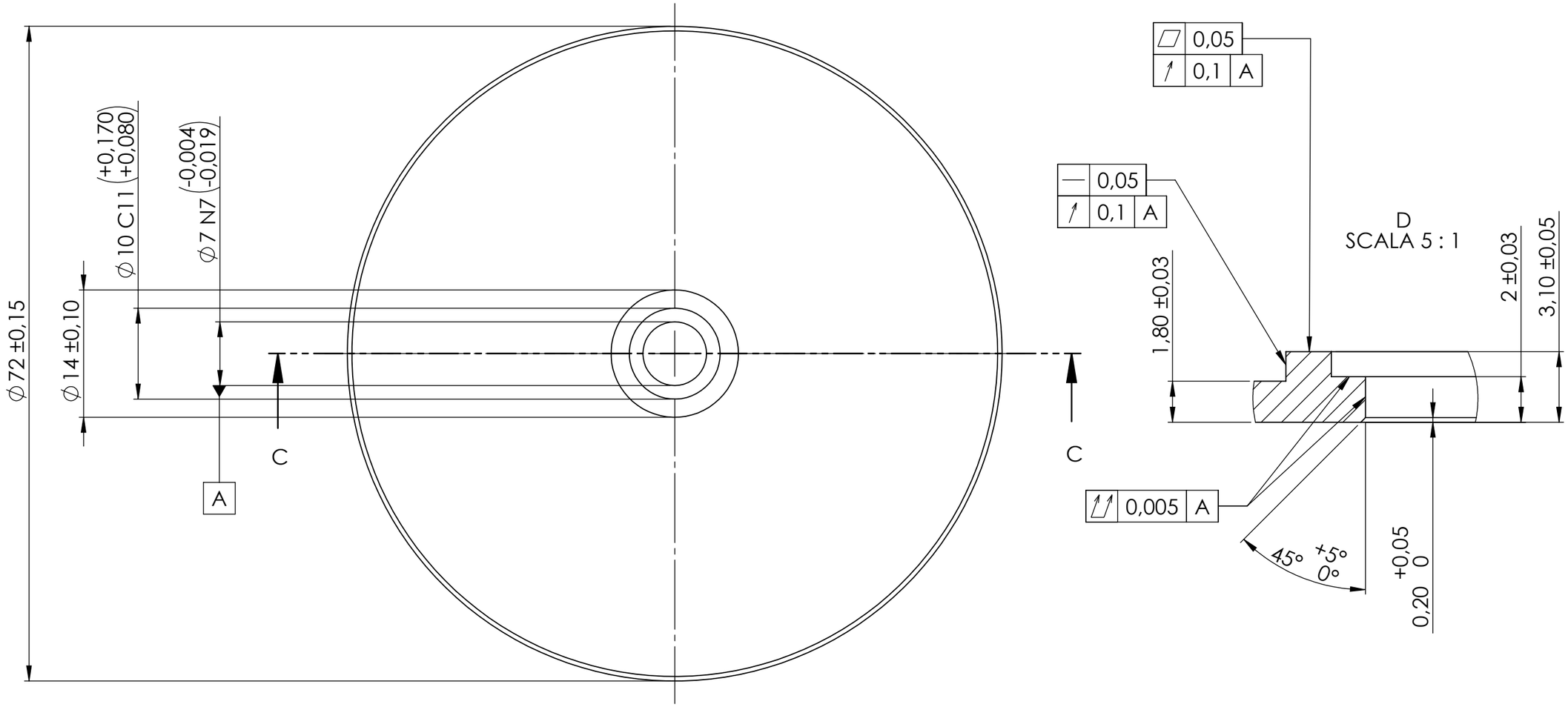

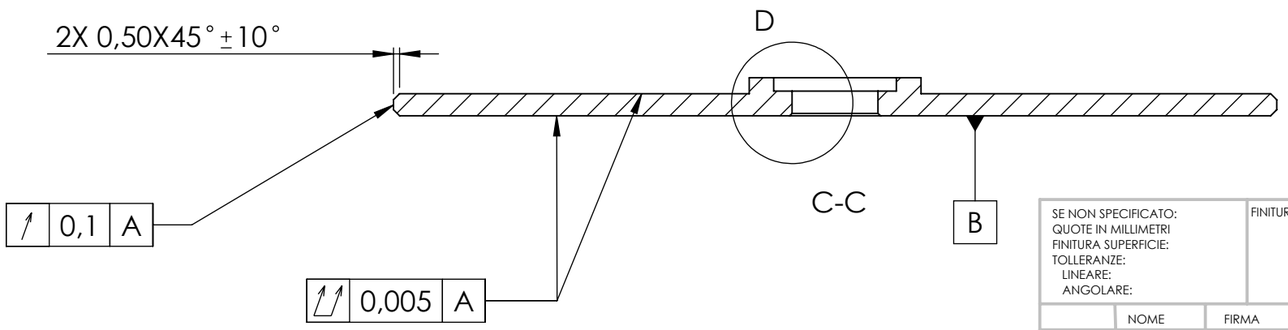

Tolleranze secondo UNI ISO 8015

Tolleranze generali ISO 2768-fH

SE NON SPECIFICATO: QUOTE IN MILLIMETRI FINITURA SUPERFICIE: TOLLERANZE: LINEARE: ANGOLARE:	FINITURA:			SBAVATURA E INTERRUZIONE DEI BORDI NETTI	NON SCALARE IL DISEGNO	REVISIONE
	NOME	FIRMA	DATA		TITOLO:	
DISEGNATO					Wheel_V2	
VERIFICATO						
APPROVATO						
FATTO						
QUALITA'				MATERIALE: Al	N. DISEGNO 2	A3
PESO:					SCALA:2:1	FOGLIO 1 DI 1

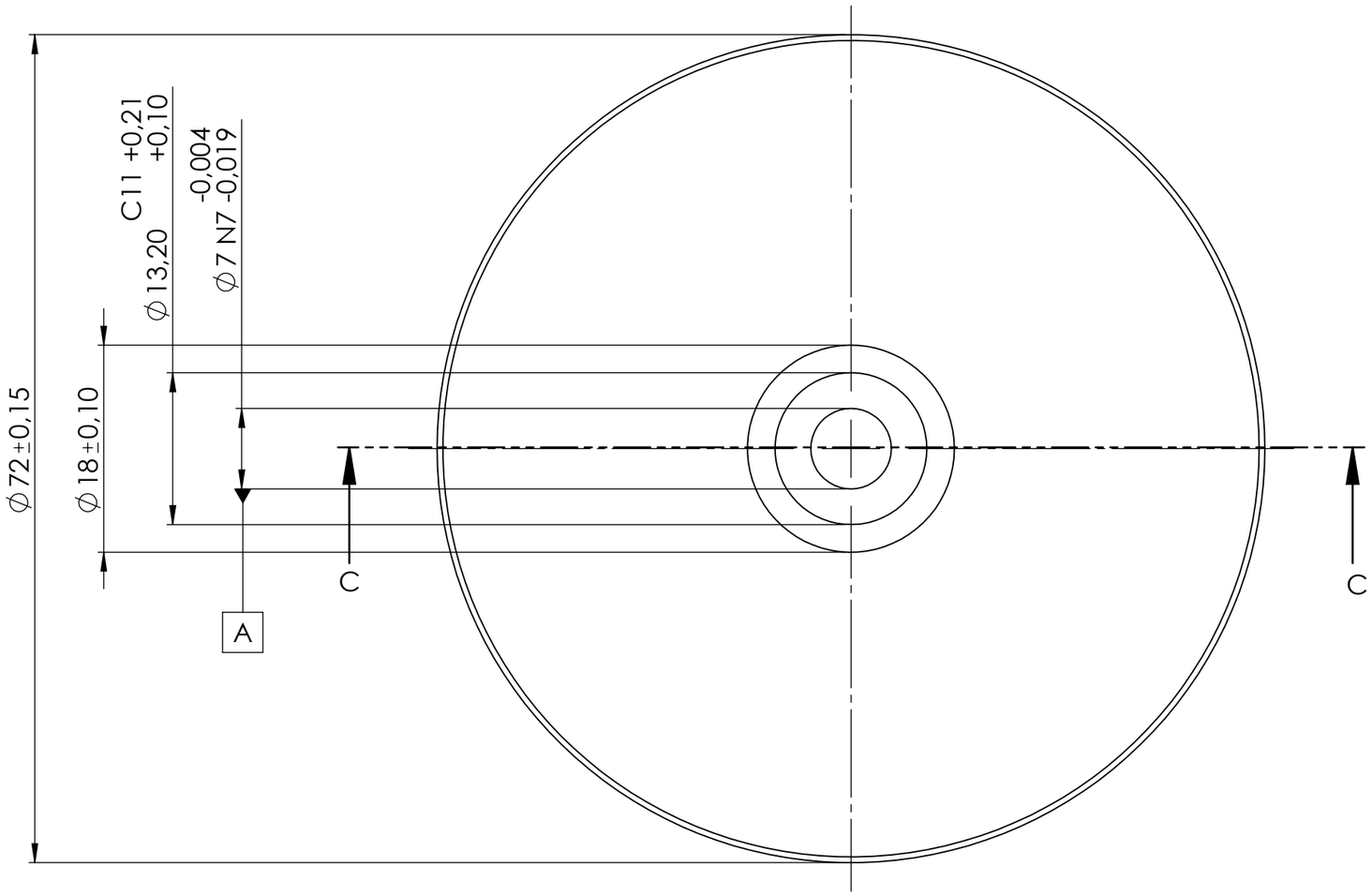

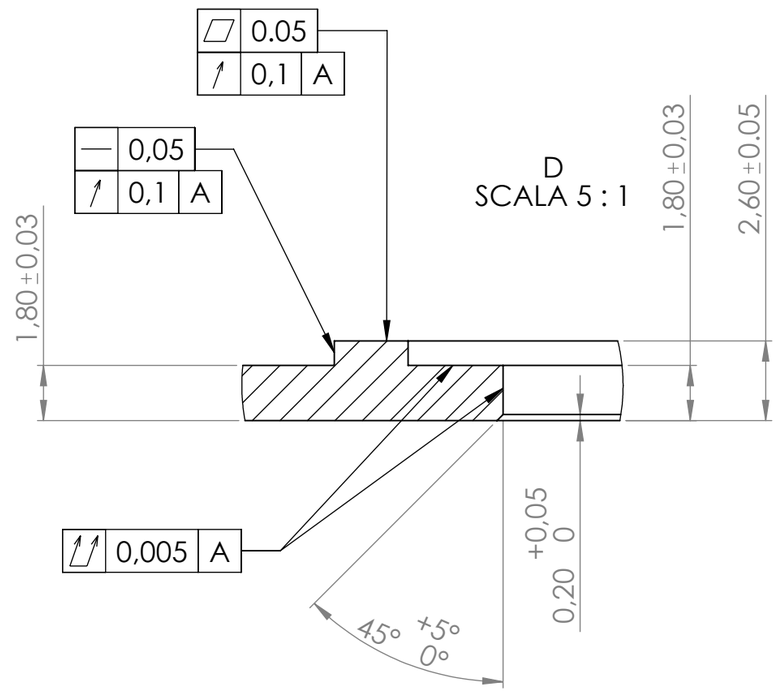

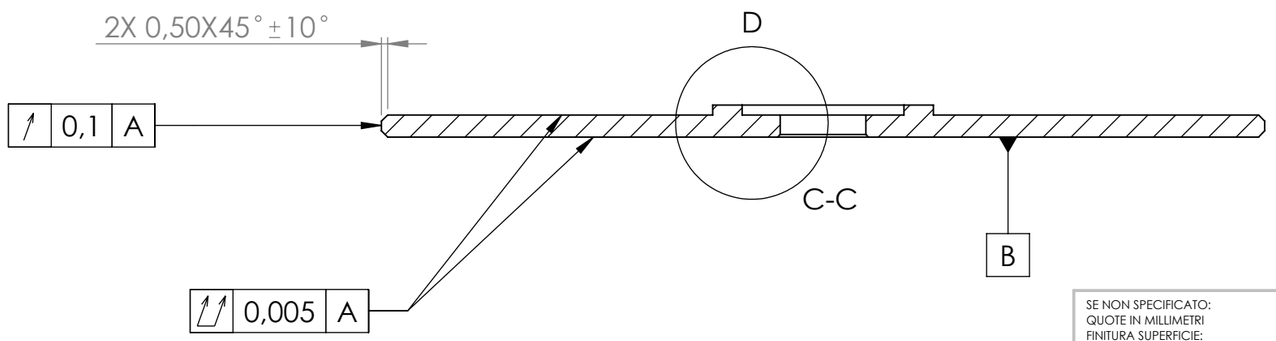

Tolleranze secondo UNI ISO 8015

Tolleranze generali ISO 2768-fH

SE NON SPECIFICATO: QUOTE IN MILLIMETRI FINITURA SUPERFICIE: TOLLERANZE: LINEARE: ANGOLARE:	FINITURA:			SBAVATURA E INTERRUZIONE DEI BORDI NETTI	NON SCALARE IL DISEGNO	REVISIONE
	NOME	FIRMA	DATA		TITOLO: Wheel_V3	
DISEGNATO						
VERIFICATO						
APPROVATO						
FATTO						
QUALITA'				MATERIALE: Al	N. DISEGNO 3	A3
				PESO: $PRPSHEET:{Peso}	SCALA:2:1	FOGLIO 1 DI 1

Bibliography

[1] Fortescue P., Swinerd G., Stark J., *Spacecraft systems engineering*, 4. ed, Singapore, John Wiley & Sons, 2011

[2] The CubeSat Program, *CubeSat Design Specification Revision 13*, February 2014
URL: https://static1.squarespace.com/static/5418c831e4b0fa4ecac1bacd/t/56e9b62337013b6c063a655a/1458157095454/cds_rev13_final2.pdf

[3] The CubeSat Program, *6U CubeSat Design Specification Revision 1.0*, June 2018
URL: https://static1.squarespace.com/static/5418c831e4b0fa4ecac1bacd/t/5b75dfcd70a6adbee5908fd9/1534451664215/6U_CDS_2018-06-07_rev_1.0.pdf

[4] Bouwmeester J., Guo J., "Survey of worldwide pico- and nanosatellite missions, distributions and subsystem technology" in *Acta Astronautica*, Volume 67, Issues 7–8, October–November 2010, Pages 854-862
URL: https://doi.org/10.1016/j.actaastro.2010.06.004

[5] Gieras J., Wang R., Kamper M., *Axial Flux Permanent Magnet Brushless Machines*, 2 ed., the Netherlands, Kluwer Academic Publishers, 2008

[6] Çengel Y., *Termodinamica e trasmissione del calore*, 1 ed., Milan, McGraw-Hill, 1998

[7] Ali A., *Power management, attitude determination and control systems of small satellites*, PhD thesis, February 2014

[8] Joven R., Das R., Ahmed A., Roozbehjavan P., Minaie B., *Thermal properties of carbon fiber-epoxy composites with different fabric weaves* in SAMPE international symposium proceedings, Charleston, SC, 2012
URL: https://www.researchgate.net/publication/262007032_Thermal_properties_of_carbon_fiberepoxy_composites_with_different_fabric_weaves

[9] Arianespace, *Vega User's Manual Issue 4 Revision 0*, April 2014
URL: http://www.arianespace.com/wp-content/uploads/2015/09/Vega-Users-Manual_Issue-04_April-2014.pdf